Stabilité en extrusion des polymères fondus. Effets de la pression et de la structure des copolymères triblocs de type ABA

Enric Santanach Carreras

THESE

présentée par

Enric SANTANACH CARRERAS

pour obtenir le grade de DOCTEUR de

L'UNIVERSITE JOSEPH FOURIER-GRENOBLE I

(Arrêtés ministériels du 5 juillet 1984 et du 25 avril 2002)

Formation doctorale « Mécanique et Energetique »
Spécialité : Mécanique des Fluides et Transferts

STABILITE EN EXTRUSION DES POLYMERES FONDUS. EFFETS DE LA PRESSION ET DE LA STRUCTURE DES COPOLYMERES TRIBLOCS DE TYPE ABA

Soutenue le 3 Octobre 2005 devant le jury composé de

M	Pierre ATTANE	Président
M.	Christian BAILLY	Rapporteurs
M.	Antxon SANTAMARIA	
Mme.	Nadia EL KISSI	Co-directeur
M.	Jean-Michel PIAU	Directeur

Thèse préparée au sein du Laboratoire de Rhéologie (UJF – INPG – CNRS)

REMERCIEMENTS

Ce travail a été réalisé dans le Laboratoire de Rhéologie, dirigé actuellement par Monsieur A. MAGNIN, directeur de recherche au CNRS, et lors de mon arrivée par Monsieur J-M. PIAU, professeur à l'INPG. Je les remercie de m'avoir accueilli au Laboratoire, de leur soutien pendant ces années de thèse et pour tous les moyens mis à ma disposition. En particulier, je tiens à exprimer toute ma reconnaissance au Professeur Piau, mon directeur de thèse, pour m'avoir confié ce sujet et pour son encadrement. Je ne peux pas oublier tous les fructueux échanges, ainsi que sa rigueur scientifique communicative. J'ai beaucoup appris à son contact au cours de ces années passées au Laboratoire, et en travaillant avec lui.

Cette thèse a été effectuée aussi sous la direction de Madame N. EL KISSI, chargée de recherche au CNRS. Je tiens à la remercier particulièrement pour son encadrement pendant la durée de ma thèse. J'ai trouvé auprès d'elle une disponibilité, des conseils et une rigueur scientifique qui m'ont beaucoup encouragé à mener ce travail.

Je suis très reconnaissant envers Monsieur P. ATTANE, Professeur à l'Université Joseph Fourier-Grenoble I, de me faire l'honneur de présider ce jury. Je voudrais aussi le remercier pour les nombreux conseils et discussions qui m'ont permis d'améliorer cette thèse.

J'exprime aussi ma gratitude à Monsieur C. BAILLY, Professeur à l'Université Catholique de Louvain, qui a accepté de s'intéresser à ce travail et de trouver le temps pour en être rapporteur.

Je remercie Monsieur A. SANTAMARIA, Professeur à l'Euskal Herriko Unibertsitatea, qui malgré ses nombreuses fonctions s'est intéressé à ce travail en acceptant aussi d'en être rapporteur.

Je voudrais aussi exprimer toute ma gratitude à Monsieur F. PIGNON, chargé de recherche au CNRS, qui a participé activement à l'organisation des mesures à l'ESRF de Grenoble. Pour ces mesures, et leur interprétation, je suis très reconnaissant à T. NARAYANAN, P. PANINE, et G. BELINA qui m'ont accueilli sur la ligne ID02 de l'ESRF et ont toujours été disponibles.

Je voudrais aussi remercier l'équipe ELSA du Laboratoire d'Electrochimie et de Physico-chimie des Matériaux et des Interfaces, LEPMI, pour l'aide lors des mesures de caractérisation structurelle des polymères.

Je n'oublierai pas tous ceux qui, au sein du Laboratoire de Rhéologie, ont apporté leur contribution à ce travail en leur exprimant toute ma gratitude.
Mesdames H. GALLIARD et C. COULAUD, Messieurs D. BLESES, M. KARROUCH et F. HUGENELL ont contribué à la conception et la réalisation du rhéomètre capillaire portable, ainsi que pour réaliser les mesures expérimentales. Tous leurs conseils qu'ils ont apportés au quotidien ont été extrêmement précieux.
Mesdames S. FAURE et S. GAROFALO, Monsieur F. BERGEROT ont été toujours aimables, souriants et disponibles. Par leur travail, ils facilitent la vie quotidienne au Laboratoire.
L'ensemble des chercheurs, doctorants, et stagiaires rencontrés tout au long de ma thèse ont aussi contribué à rendre ces années agréables avec leur bonne humeur et leur sympathie.

Enfin, je remercie mes parents et ma famille pour tout leur soutien.

RESUME

L'extrusion est un procédé de mise en forme très répandu dans des industries variées telles que la plasturgie, la métallurgie, les céramiques, ou encore l'industrie agroalimentaire. Les matériaux doivent cependant être soumis à des niveaux de pression et de contrainte élevés pour être extrudés à des débits suffisants.

La présente thèse a pour objectif de mieux connaître l'influence des paramètres de pression et contrainte sur les propriétés des polymères et la stabilité de leurs écoulements, et ce en relation avec leur structure mésoscopique.

Les effets de la pression ont été étudiés sur quatre polyéthylènes (PE) de structures différentes. D'abord, des conditions expérimentales précises ont été définies pour isoler les effets de la pression des effets de la température et pour différencier les écoulements stables ou instables. Nos résultats montrent que les effets de la pression sont les mêmes en cisaillement et en élongation, sauf pour l'un des PE où ils sont 30% supérieurs en cisaillement. En outre, c'est un critère de contrainte critique qui caractérise l'apparition des instabilités viscoélastiques quelle que soit la pression moyenne.

Dans la deuxième partie de cette thèse, trois copolymères de la famille des SEBS montrant une séparation de phase aux échelles nanoscopiques ont été considérés. L'étude des défauts macroscopiques d'extrusion, et de la propagation des fissures surfaciques, pour ces copolymères à blocs a permis d'identifier l'origine du défaut dit de « refente d'extrudat » ainsi qu'un nouveau régime d'extrusion : le « pelage continu ». Ces défauts ont été mis en relation avec la structure mésoscopique par des essais de diffusion de rayons-X aux petits angles. Pour cela, un rhéomètre portable équipé d'une filière en béryllium transparente aux rayons-X et pouvant atteindre des températures de 150°C et des pressions de 200 bars a été développé.

ABSTRACT

Extrusion is a processing operation widely used in various industries such as polymer processing, metallurgy, ceramics or still in the food industry. Materials undergo high pressures and stresses when extruded at acceptable rates. The aim of this thesis is to gain some knowledge on the pressure and stress conditions and to better understand theirs effects on the properties and extrusion stability of polymers. Moreover, these effects will be related to the mesoscopic structure of polymers.

Four polyethylenes with different structures have been considered to study the effects of pressure. Firstly, the precise experimental conditions allowing to isolate pressure effects from temperature effects and the distinction between stable and unstable flows have been established. Our results show that pressure effects in shear and in elongation can be considered as equal for three out of the four polyethylenes. In the case of the fourth one, pressure effects in shear were found to be 30% higher than in elongation.
Our results also show that a critical shear stress criterion characterizes the appearance of viscoelastic instabilities. Moreover, we show that this critical shear stress is independent of mean pressure.

In the second part of this thesis, three block copolymers, of the SEBS family, which show microphase separation, have been considered. Firstly, the macroscopic defects and the propagation of surface cracks during extrusion have been studied. We have shown the origin of flow split at the die exit and a new extrusion regime has been identified: “continuous peeling”. Then, the defects and the structure at the nanometric scale are related by using a capillary rheometer equipped with a Be die allowing for in-situ SAXS observations that has been developed. It can operate at temperatures and pressures as high as 150°C and 200 bar. SAXS experiments at the ESRF, Grenoble, have been performed and have allowed identification of the structure deformation and the consequences of this on macroscopic defects.

TABLE DES MATIERES

INTRODUCTION GENERALE

INTRODUCTION GENERALE

L'extrusion est un procédé de mise en forme très répandu dans de nombreuses industries telles que la plasturgie, la métallurgie, les céramiques, ou encore l'industrie agroalimentaire. Les différents défauts susceptibles d'apparaître pendant l'extrusion des matériaux limitent souvent les débits de production. Compte tenu de l'importance de ce procédé, on comprend l'intérêt de toute thèse visant à mieux comprendre les mécanismes et la physique causant les défauts.

Les premières études au niveau mondial ont commencé il y a plus d'un demi siècle et plusieurs revues ont été écrites, (Denn 1990, 2001 ; Piau 1995 ; Hatzikiriakos et Migler, 2005). Plusieurs types de défauts susceptibles d'apparaître lors de l'extrusion ont été identifiés. De nombreuses études ont été menées en utilisant principalement des thermoplastiques commerciaux, polystyrène (PS) et polyéthylène (PE). Cependant des élastomères ont progressivement été aussi considérés, principalement du polybutadiène (PB) dans les pays influencés par l'ancienne union soviétique. L'avantage de ces derniers est la clarté avec laquelle les défauts d'extrusion sont observés sur le PB. Les temps de relaxation des fluides utilisés, particulièrement longs, facilitent l'observation des différents défauts.

Depuis plus d'une vingtaine d'années, l'extrusion a été un des thèmes centraux de la recherche dirigée par J-M Piau au sein du Laboratoire de Rhéologie. Les études réalisées peuvent être divisées en deux groupes : d'un côté celles qui utilisent des fluides modèles avec une structure bien définie et connue et de l'autre coté les études qui utilisent des matériaux industriels commerciaux. Les premiers ont l'intérêt de permettre l'observation de phénomènes propres, et clairs qui mènent à comprendre la physique sous-jacente. Evidemment, les deuxièmes sont intéressants car on retrouvera les mêmes phénomènes que les industriels doivent éviter sur leurs lignes de production.

Ceci explique qu'une grande partie des travaux de recherche conduits au Laboratoire de Rhéologie sur les polymères a été associée à des polybutadiènes (PB), et des polydimethylsiloxanes (PDMS) en tant que fluides modèles, ou encore à des familles de polyéthylènes (PE) avec des structures moléculaires différentes et à des caoutchoucs comme produits industriels plus complexes.

On sait actuellement que la même séquence de défauts est observée pour un grand nombre de polymères relativement ou fortement enchevêtrés : c'est la physique des chaînes polymères qui prime.

Pour des débits suffisamment faibles, l'extrudat est lisse, transparent et exempt de défauts.

Lorsque le débit augmente, la surface de l'extrudat devient matte et des fissures sur la surface de plus en plus prononcées apparaissent progressivement à la sortie de la filière. Ce phénomène de fissuration, historiquement dénommé « peau de requin » même si cette appellation est physiquement injustifiée, a été le sujet de nombreuses études. Actuellement, on sait que cette fissuration de l'extrudat est un défaut surfacique du à la singularité, et à la concentration de contraintes associée, présente en sortie de filière où le polymère passe d'un écoulement confiné à un jet à surface libre (Cogswell 1977 ; Denn 1990 ; Piau *et al.* 1995). Cette fissuration du polymère, même si elle est d'origine surfacique, peut être très sévère quant à l'amplitude des fissures, et distordre complètement l'aspect visuel de l'extrudat. Néanmoins, il est bien connu que même dans les cas d'une fissuration surfacique sévère, l'écoulement à l'intérieur de la filière peut être complètement stable (Piau *et al.* 1995)

Si le débit est encore augmenté, l'écoulement de polymères fondus devient soudain instable en entrée de la filière (Piau *et al.* 1990 ; Legrand et Piau 1998). Cette instabilité en amont, qui résulte du comportement viscoélastique des polymères, se traduit en sortie de la filière par le défaut dit (de façon encore peu justifiée) de « rupture d'extrudat ». La terminologie plus correcte et qui devient de plus en plus courante dénomme ces défauts comme « instabilité viscoélastique en amont ».

Aux grands débits, un glissement permanent à la paroi accompagne souvent le déclenchement de l'instabilité viscoélastique en amont des polymères très enchevêtrés, même si pour certains PEHD cette instabilité peut avoir lieu en même temps que le défaut de fissuration surfacique (Piau *et al.* 1995) et avant que le glissement n'apparaisse finalement.

Dans le cas des extrusions à débit moyen imposé et pour des polymères fortement enchevêtrés, les « régimes oscillants » se déclenchent généralement en même temps que l'instabilité viscoélastique en amont. Ces régimes oscillants sont des écoulements instationnaires où l'on relève des oscillations de la pression et du débit instantanées. Pour ces régimes la compressibilité du polymère n'est plus négligeable et doit être prise en considération.

Une fois que les défauts, ainsi que leurs origines, sont déterminés, il doit être plus facile d'agir sur les formulations et les procédés en vue d'améliorer le rendement de l'opération d'extrusion.

Ainsi, il a été montré que le phénomène de fissuration surfacique peut être éliminé en utilisant des filières avec parois glissantes (Piau et al. 1995).

Ensuite, l'atténuation des défauts dus à l'instabilité viscoélastique en amont été envisagée. Après avoir étudié le champ d'écoulement au voisinage de l'entrée de la filière, la géométrie de la zone juste en amont de la contraction a été modifiée à l'aide de différentes grilles jouant le rôle de filtres. Les

résultats ont montré que les défauts dus à l'instabilité viscoélastique en amont sont fortement atténués par la présences de ces milieux filtrants qui modifient le champ d'écoulement, et de contraintes, en amont de l'entrée de la filière (Done *et al.* 1983 ; Piau *et al.* 2000 ; Goutille et Guillet 2002).

La présente thèse porte sur deux points qui n'ont pas été étudiés auparavant en détail au sein du laboratoire. D'une part les effets de la pression sur la stabilité d'écoulement ainsi que sur la viscosité des polymères fondus seront étudiés. D'autre part, les défauts susceptibles d'avoir lieu ainsi que la transition stable/instable pendant l'extrusion de copolymères séquentiels seront examinés. Dans les deux cas, les effets possibles de la structure des chaînes polymères sur les phénomènes observés à l'échelle macroscopique seront pris en compte.

Le problème des effets de la pression sur la viscosité des polymères fondus a été étudié depuis plus de 50 ans. Les premiers articles présentaient une gamme de dispositifs expérimentaux et les analyses des données expérimentales. Des ordres de grandeurs des effets de la pression sur la viscosité exprimés par le coefficient β ont ainsi été rapportés pour différentes familles de polymères. Les résultats publiés montrent que la structure des macromolécules joue un rôle décisif sur la piézodépendance de la viscosité.
Ici nous avons considéré 4 polyéthylènes (PE) de structures différentes : un polyéthylène haute densité (PEHD), un polyéthylène basse densité linéaire (PEBDL), et deux polyéthylènes synthétisés par catalyse métallocène (mPE). L'un des deux contient de longues ramifications (LCB) tandis que l'autre contient de nombreuses ramifications courtes (SCB).
Tout d'abord, des conditions expérimentales précises ont été définies pour isoler les effets de la pression des effets de la température et pour différencier les écoulements stables ou instables. Nos résultats montrent que c'est un critère de contrainte critique qui caractérise l'apparition des instabilités viscoélastiques quelle que soit la pression moyenne. Pour les régimes d'écoulement stables, nous avons mesuré les effets de la pression en cisaillement et en élongation pour les 4 PE. Cette étude fait l'objet de la première partie de ce mémoire.

La deuxième partie de ce mémoire porte sur les défauts d'extrusion caractéristiques des copolymères à blocs dans leur état ordonné. Pour cette deuxième partie, nous avons considéré 3 copolymères commerciaux de la famille des SEBS : polystyrène-*bloc*-poly(éthylène-*co*-butylène)-*bloc*-polystyrène.
Dans le Chapitre 2, nous avons porté un regard macroscopique sur l'apparition et l'évolution des défauts d'extrusion, et en particulier sur la propagation des fissures surfaciques, de ces copolymères à blocs. Nous présentons dans ce chapitre l'origine du défaut dit de « refente d'extrudat » et un nouveau régime d'extrusion : le pelage continu. Les différences de microstructure entre ces SEBS et les homopolymères expliquent les différences d'aspect des défauts constatés.
Le Chapitre 3 de ce mémoire vise à analyser précisément la structure mésoscopique des SEBS et à la mettre en relation avec les propriétés macroscopiques. Pour cela, nous avons fait appel au grand instrument de mesure de l'ESRF et nous avons développé un rhéomètre équipé d'une filière en béryllium transparente aux rayons-X. Grâce a des mesures de diffusion de rayons-X aux petits angles (SAXS), nous avons pu suivre les changements structuraux subis par les SEBS au long du chemin

d'extrusion. Ces observations ont permis d'identifier les effets de la déformation de la structure sur les défauts macroscopiques.

Enfin, le dernier chapitre de ce mémoire présente mes conclusions. Il ouvre aussi un grand éventail de perspectives pour des recherches futures concernant chacun des chapitres cette thèse.

REFERENCES BIBLIOGRAPHIQUES

Cogswell FN (1977) Stretching flow instabilities at the exits of extrusion dies. J Non-Newtonian Fluid Mech 3:37-47.

Denn, MM (1990) Issues in viscoelastic fluid mechanics. Ann Rev Fluid Mech 22:13-34.

Denn, MM (2001) Extrusion instabilities and wall slip, Ann Rev Fluid Mech 33:265-297.

Done DS, Baird DG, Average AE (1983) The influence of porous media on the flow of polymer melts in capillaries. Chem. Eng. Commun 21:293-309.

Goutille Y, Guillet J (2002) Disentanglement of polymer melts flowing through porous medium before entering a capillary die. J. Rheol 46 :1307-1323.

Hatzikiriakos SG, Migler KB, editors, Polymer processing instabilities-Control and understanding, Marcel Dekker, New York, 2005.

Legrand F, Piau JM (1998) Spatially resolved stress birefringence and flow visualization in the flow instabilities of a polydimethylsiloxane extruded through a slit die. J Non-Newtonian Fluid Mech 77:123-150.

Piau JM, El Kissi N, Tremblay B (1990) Influence of upstream instabilities and wall slip on melt fracture and sharkskin phenomena during silicones extrusion through orifice dies. J Non-Newtonian Fluid Mech 34:145-180.

Piau JM, El Kissi N; Toussaint F, Mezghani A (1995) Distortions of polymer melt extrudates and their elimination using slippery surfaces. Rheol Acta 34:40-57.

Piau JM, Nigen S, El Kissi N (2000) Effect of die entrance filtering on mitigation of upstream instability during extrusion of polymer melts. J Non-Newtonian Fluid Mech 91:37-57.

CH. 1

Chapitre 1

Effets de la pression sur la viscosite et la stabilite en ecoulement pendant l'extrusion des polyethylenes

[Version abregee]

Les polymères fondus peuvent être soumis à de très hautes pressions (~2000 bar) pendant les opérations de mise en forme. A ces niveaux de pression, leurs propriétés et leurs lois d'écoulement diffèrent de celles utilisés à pressions modérées. D'après les travaux de Couch et Binding (2000), il est possible de décrire les effets de la pression et de la température sur la contrainte de cisaillement grâce à la relation

$$\sigma_s(\dot{\gamma}, T, P) = \sigma_s\left(a_{TP}^s \dot{\gamma}, T_R, P_R\right) \quad (1)$$

où $\dot{\gamma}$ est le gradient de cisaillement, T et T_R sont respectivement la température absolue et la température de référence, P et P_R sont la pression relative et la pression relative de référence. Finalement, a_{TP}^s est un facteur de translation empirique qui a été modélisé de façon satisfaisante à l'aide de l'équation (2)

$$a_{TP}^s = \exp\left[\beta_S (P - P_R) + \frac{E_S}{R}\left(\frac{1}{T} - \frac{1}{T_R}\right)\right] \quad (2)$$

Les effets de la pression sont décrits par le coefficient β_s. La sensibilité aux changements de température sont pris en compte par le rapport entre l'énergie d'activation, E_S, et la constante universelle des gaz, R.

Ce même principe de superposition temps-température-pression peut être a priori utilisé dans le cas des propriétés élongatonelles si l'on remplace $\dot{\gamma}$ par $\dot{\varepsilon}$, et a_{TP}^s par a_{TP}^E. Un coefficient de pression en élongation, β_E, remplace β_S et une énergie d'activation en élongation E_E remplace E_S.

Les effets de la pression sur la viscosité des polymères fondus ont été étudiés depuis une cinquantaine d'années. Les premiers travaux présentaient une gamme de dispositifs expérimentaux et l'analyse des données expérimentales. Les différentes techniques ont fait l'objet d'une étude comparative publiée par Goubert *et al.* (2001). Des valeurs du coefficient de pression en cisaillement ont été publiées par un grand nombre d'auteurs. Les résultats les plus significatifs pour notre propre étude sont présentés dans le Tableau 1 (p. 22). En général, des résultats voisins ont été obtenus pour les différentsauteurs pour un même type de polymère. De plus, on observe que les effets de la pression sont plus importants pour les molécules avec les chaînes principales les plus volumineuses. Pour les PEs, β_S est de l'ordre de 10-15x10^{-9} Pa^{-1}. Cette valeur est d'environ la moitié de celle couramment trouvée pour le PS (~30x10^{-9} Pa^{-1}) dans la littérature.

En élongation, les effets de la pression ont aussi été mesurés (Couch et Binding, 2000). Ces auteurs ont trouvé que pour un PEHD, un PEBD, un PP, et un PMMA, les effets de pression en élongation et en cisaillement étaient égaux aux incertitudes de mesure près. Par contre, dans le cas d'un PS les effets de pression en élongation étaient 30% plus importants que les effets de pression en cisaillement. Ceci pose la question de savoir pourquoi les effets de pression ne sont pas égaux en cisaillement et en élongation et, quel est le rôle de la structure moléculaire sur une telle différence ?

La plupart des études sur les effets de la pression ont ignoré l'existence des instabilités d'écoulement susceptibles d'apparaître lors de l'extrusion des polymères, même lorsque les expériences avaient lieu à des gradients de cisaillement 10 fois plus importants que le gradient critique au-delà duquel l'instabilité viscoélastique en amont est déclenchée à pression atmosphérique. On sait que le champ d'écoulement en entrée et dans la filière est très complexe (fortement viscoélastique et turbulent) une fois que l'instabilité amont est présente. A cause de cela, on peut se demander quelles sont les différences entre les valeurs de β_S obtenues en écoulements instables et les valeurs de β_S obtenues sous écoulement stable et établi.

La stabilité en écoulement a été l'objet de plusieurs articles de revue parmi lesquels on peut citer ceux de Denn 1990, 2001 et ceux de Piau *et al.* 1995. Le déclenchement de l'instabilité viscoélastique en amont se traduit par un changement de pente sur la courbe d'écoulement. Ceci est d'autant plus marqué que la filière utilisée est courte.

Jusqu'à présent et à notre connaissance, l'influence des hautes pressions sur l'existence des instabilités d'écoulement (régimes oscillatoires, instabilité viscoélastique en amont) susceptibles d'avoir lieu lors de la mise en forme des polymères fondus n'a pas fait l'objet d'études spécifiques.

Ainsi, dans les travaux de Hatzikiriakos et Dealy (1992), les auteurs concluaient que les effets de la pression n'existaient pas et que les déviations observées sur les courbes d'écoulement étaient dues à un glissement du polymère à la paroi déclenché au-delà d'une certaine pression. En effet, dans ces expériences, le glissement correspondait au déclenchement de l'instabilité viscoélastique en amont (Figure 1, p. 24). Hatzikiriakos et Dealy n'ont pas observé les effets de la pression car les pertes de charges n'étaient pas suffisamment importantes. Ces effets ont était observés quelques années plus tard par le même groupe avec une nouvelle version de leur rhéomètre à plats glissants à haute pression (Koran et Dealy 1999).

Les travaux du groupe d'Aberyswith (Binding *et al.* 1998, Couch et Binding 2000) ne mentionnent pas la présence d'instabilités d'écoulement même si leurs expériences sont faites à gradients de cisaillement apparent allant jusqu'à 2500 s^{-1}. Cependant, l'examen de leurs courbes révèle bien le changement de pente caractéristique du déclenchement des instabilités. De plus, ce changement de pente a lieu au même niveau de contrainte critique que celui rapporté par Laun (2003, 2004) pour le même PEBD.

Les effets de la pression et de la température sont couplés (Denn 1981 et Hay e al. 1999). Ceci implique que pour déterminer les effets de la pression il est nécessaire de les isoler. Toute perte de charge dans une filière entraîne une augmentation de la température due à la dissipation visqueuse. Ce changement de température doit être pris en compte lors de l'étude des effets de la pression. Denn (1981) a proposé une première solution du profil de pression dans une filière pour le cas adiabatique qui tenait compte des effets de la température et de la pression. Ensuite le problème a été repris par Hay *et al.* (1999) pour inclure les transferts de chaleurs entre le polymère et les parois. Plus récemment Laun (2003) a adapté l'analyse de Hay *et al.* au cas de la perte de charge totale dans une filière. Dans les travaux de Laun, les échauffements visqueux sont estimés, de façon trop simpliste, par des simulations numériques avec POLYFLOW. Néanmoins, la valeur de β_S obtenue par Laun est inférieure à celle obtenue par Couch et Binding (2000) qui n'avaient pas tenu compte de la

dissipation visqueuse. Les différences entre les valeurs du coefficient de pression ne peuvent pas être expliquées par les incertitudes expérimentales rapportées par les auteurs. Comme on verra par la suite, ces différences seront expliquées par la prise en compte des instabilités en écoulement.

D'après l'équation (4) (p. 26), extraite des travaux de Laun (2003), le coefficient de pression déterminé expérimentalement, $\beta_{S,exp}$, est égal au coefficient de pression apparent, $\beta_S(\dot{\gamma})$, pourvu que la quantité $(\beta_S(\dot{\gamma}) + \alpha\varepsilon)\Delta P/2$ soit « suffisamment » petite. Si, l'on entend par « suffisamment petite » une quantité inférieure à 5%, on obtient une perte de charge admissible maximale de 170×10^5 Pa en utilisant les valeurs typiques d'un PE quelconque. Donc, dans le cas des expériences où la perte de charge est inférieure à 170×10^5 Pa, les effets de la dissipation visqueuse seront négligeables.

Le dispositif expérimental utilisé est présenté en Figure 2 (p. 27). Nous avons adapté sur un rhéomètre capillaire Göttfert 2001, une pièce cylindrique munie d'une chambre, d'un capteur de pression et d'un piston, qui est une tige filetée pouvant être déplacée perpendiculairement au sens de l'écoulement. Ainsi, à débit moyen donné, on peut augmenter la pression en sortie de filière en obturant plus ou moins la chambre du fait du déplacement du piston.
En utilisant des filières axisymétriques de diverses longueurs et diamètres on peut alors caractériser les effets de la pression tant en cisaillement (L/D>>1) qu'en élongation (L/D~0). Les mesures avec les filières orifices minces (L/D~0) ont aussi permis de corriger les effets d'entrée dans les capillaires longs.
Les pertes de charge à travers les filières ont été mesurées à l'aide des deux capteurs de pression placés en amont et en aval de la filière. Les signaux des capteurs ont été enregistrés en fonction du temps. Ceci a permis d'identifier les régimes stables et les régimes instables.

Quatre polyéthylènes commerciaux ont été testés dont un polyéthylène de basse densité linéaire (PEBDL) classique type Ziegler et Natta, un polyéthylène de haute densité (PEHD) et deux polyéthylènes produits par catalyse métallocène: l'un avec des ramifications courtes (mPE-SCB) et l'autre avec des ramifications courtes et longues (mPE-LCB). Les caractéristiques structurales de ces quatre polyéthylènes sont résumées dans le Tableau 2 (p. 29).

Le PEBDL et le mPE-LCB sont les deux PE qui ont présenté les instabilités les plus évidentes parmi les quatre produits étudiés. Ces instabilités comprenaient successivement un régime oscillatoire et un régime avec glissement pour le PEBD, ou bien un changement de pente avec déclenchement du glissement, pour le mPE-LCB. Le changement de comportement associé au déclenchement des instabilités peut être observé de façon nette en Figures 3 et 4 (p. 30-31). Dans les deux cas, ce changement se produit à des pressions moyennes d'autant plus faibles que le gradient de cisaillement augmente. Cependant, la perte de charge, proportionnelle au niveau de contrainte à la paroi, reste constante indépendamment de la pression moyenne. De plus cette valeur de la contrainte critique est la même que celle trouvée sous pression atmosphérique. Le Tableau 3 (p. 35) présente les valeurs de contrainte critique pour le PEBDL et le mPE-LCB.

Les effets de la structure sur la piézodependance des polyéthylènes ont été aussi étudiés tant en cisaillement qu'en élongation. Pour ceci, il a été nécessaire de déterminer les coefficients de pression du PEBDL, du PEHD, et des deux mPE tout en tenant compte des instabilités d'écoulement mises en évidence pour la première fois pour ces écoulements à hautes pressions.

La méthode la plus appropriée est la superposition temps-pression (Couch et Binding 2000) car elle permet de privilégier les points expérimentaux obtenus avec des régimes stables et elle permet un comparaison facile avec des données obtenues sous pression atmosphérique. L'application de cette méthode consiste à tracer des courbes maîtresses à une pression de référence en translatant horizontalement, de façon empirique, les courbes d'écoulement obtenues à différentes pressions moyennes. Le coefficient de pression, β_S, peut alors être extrait à partir de l'évolution des coefficients de translation avec la pression moyenne.

Les courbes obtenues en cisaillement sont présentées en Figures 8-11 (p. 37-38) pour les quatre PE étudiés. Ces courbes montrent un bon accord entre les expériences à hautes pressions et les valeurs obtenues en rhéométrie capillaire conventionnelle (pression atmosphérique en sortie de filière). De plus les valeurs des coefficients de pression en cisaillement, rapportées dans le Tableau 4 (p. 39), sont en bon accord avec celles publiées ailleurs (Couch et Binding 2000, Goubert et al. 2001, Koran et Dealy 1999) pour différents polyéthylènes, dans la gamme 10-20x10^{-9} Pa^{-1}. On observe également que la valeur de β_S augmente avec le nombre de ramifications.

Le même principe de superposition temps-pression a été appliqué sur les données obtenues avec des orifices minces. Les courbes maîtresses qui en résultent sont présentées en Figures 13-16 (p. 40-41). De nouveau, les données obtenues à hautes pressions et ramenées à la pression atmosphérique sont en bon accord avec les valeurs obtenues en rhéométrie capillaire conventionnelle aux incertitudes de mesure près. Ces courbes permettent d'accéder aux coefficients de pression en élongation, β_E, dont les valeurs sont rapportées dans le Tableau 3, pour les quatre PE. On y observe que les valeurs de β_E peuvent être considérées comme égales aux valeurs de β_S pour le PEBDL, le PEDH et le mPE-SCB. Ceci n'est pas le cas pour le mPE-LCB où $\beta_S > \beta_E$. Ce résultat va dans le sens opposé de celui de Couch et Binding pour le PS. Les différences doivent être relatives à la longueur des ramifications. Pour comprendre ces différences, des expériences complémentaires visant à voir l'organisation des chaînes pendant l'écoulement seraient nécessaires.

Cette étude nous a permis de montrer également, dans des conditions expérimentales avec dissipation visqueuse négligeable, que les instabilités d'extrusion ont aussi lieu pour ces écoulements à hautes pressions. Nous avons trouvé que le niveau de contrainte critique au-delà de laquelle les instabilités amont se déclenchent est indépendant de la pression moyenne.

Finalement, tenir compte des instabilités d'écoulement permet d'expliquer les différences entre les coefficients de pression rapportés par Couch et Binding (2000) et ceux de Laun (2003) qui restent en dehors des incertitudes expérimentales. Ceci est expliqué par la Figure 17 (p. 43) où nous avons rapporté les données de ces deux auteurs. En effet, en considérant les pentes des courbes a 50 et 100 s^{-1} (écoulement stable), le coefficient de pression est d'environ 17x10^{-9} Pa^{-1}, une valeur qui, aux incertitudes de mesure près, est égale à la valeur trouvée par la méthode de superposition temps-

température. Par contre lorsque les courbes obtenues à des régimes fortement instables sont considérées, la valeur du coefficient de pression calculée est de l'ordre de $11x10^{-9}$ Pa^{-1}. Cette différence des valeurs (35%) montre clairement l'importance de tenir compte de la stabilité des écoulements dans, et à l'entrée, de la filière.

CHAPTER 1

PRESSURE EFFECTS ON VISCOSITY AND FLOW STABILITY OF POLYETHYLENE MELTS DURING EXTRUSION

E. SANTANACH CARRERAS, N. EL KISSI, J-M. PIAU(✉), F. TOUSSAINT, AND S. NIGEN

*Laboratoire de Rhéologie**, B.P. 53, Domaine Universitaire, 38041 Grenoble cedex 9 (France)*

Key words: *extrusion, PE, pressure dependence, shear viscosity, flow stability, entrance flow*

This chapter is an article currently in press at Rheologica Acta.

✉ Author to whom all correspondence should be addressed. Electronic mail: jmpiau@ujf-grenoble.fr
** *Université Joseph Fourier-Grenoble I, Institut National Polytechnique de Grenoble, CNRS (UMR 5520*)

Abstract:

In the present work, the effects of pressure on the viscosity and flow stability of four commercial grade polyethylenes have been studied: LLDPE, HDPE, mPE-SCB, and mPE-LCB. The range of shear rates considered covers both stable and unstable flow regimes. "Enhanced exit-pressure" experiments have been performed attaining pressures of the order of $500x10^5$ Pa at the die exit. The necessary experimental conditions have been clearly defined so that dissipative heating can be neglected and pressure effects isolated.

The results obtained show an exponential increase in both shear and entrance-flow pressure drop with mean pressure when shear rate is fixed and as long as flow is stable. These pressure effects are described by two pressure coefficients, β_S under shear and, β_E under elongation, that are calculated using time-pressure superposition and that are independent of mean pressure and flow rate. For three out of four PE, pressure coefficient values can be considered equal under shear and under elongation. However, for the mPE with long chain branching (LCB) the pressure coefficient under elongation is found to be about 30% lower than under shear.

Flow instabilities in the form of oscillating flows or of upstream instabilities appear at lower shear rates as mean pressure increases. Nevertheless, the critical shear stress at which they are triggered remains independent of mean pressure. Moreover, it is found that the β_S values obtained for stable flows do not differ much from the values obtained during upstream instability regimes, and differ really from pressure effects observed under oscillating flow and slip conditions.

1.1 Introduction

Very high pressures can be exerted on polymers during processing. At these pressure levels, polymer melt properties, and flow stability, evolve according to laws that are different from those used at moderate pressures. Following work by Couch and Binding (2000), temperature and pressure dependence of shear stress can be modeled as

$$\sigma_s(\dot{\gamma}, T, P) = \sigma_s\left(a_{TP}^s \dot{\gamma}, T_R, P_R\right) \quad (1)$$

where $\dot{\gamma}$ is the shear rate, T and T_R are the absolute temperature and reference temperature respectively. Similarly, P and P_R are the gauge and reference gauge pressures. a_{TP}^s is a shift factor that was found to be well approximated by

$$a_{TP}^s = \exp\left[\beta_S (P - P_R) + \frac{E_S}{R}\left(\frac{1}{T} - \frac{1}{T_R}\right)\right] \quad (2)$$

in which β_S is the pressure coefficient, E_S is the activation energy, and R is the gas constant. The reason for the good performances obtained when using Eq. (2) is the relatively limited range of pressure and temperature values finally considered, quite far from any phase change conditions. Moreover, Eq. (2) is ideally simple to allow analytical calculations to be made. Using any more complex empirical expression for a_{TP}^s would not have been justified in the work by Couch and Binding (2000), and it would not be either in the present paper.

The same time-temperature-pressure superposition principle can be applied for the elongation case if $\dot{\gamma}$ is replaced by $\dot{\varepsilon}$, and a_{TP}^s is replaced by a_{TP}^E where an elongational pressure coefficient β_E replaces β_S and an elongation activation energy E_E replaces E_S.

Numerous experimental studies (Maxwell and Jung 1957; Semjonow 1962; Choi 1968; Penwell *et al.* 1971; Hatzikiriakos and Dealy 1992; Kadjick and Van den Brule 1994; Binding *et al.* 1998; Koran and Dealy 1999; Hay *et al.* 1999; Couch and Binding 2000; Goubert *et al.* 2001; Laun 1983, 2003, 2004; Sedlacek 2004) have been carried out to quantify this coefficient β_S and values have been reported for a number of polymer grades. Papers on the subject by Binding *et al.* (1998) and Goubert *et al.* (2001) have already presented very good reviews of the historical background and the reader is encouraged to consult them for further insight. The different experimental techniques commonly used have also been reviewed in the work of Goubert *et al.* (2001). Thus, they will not be treated in the present paper. The more relevant results for our study are tabulated in Table 1. In general, acceptable agreement is observed for each type of polymer. Pressure effects are more important for those melts with bulkier backbones in their molecular structure: for most PEs, β_S is in the order of 10-15x10^{-9} Pa^{-1}, which is less than half of the β_S values reported for PS (β_S~30x10^{-9} Pa^{-1}). Increasing pressure, or decreasing temperature, reduces the amount of free volume available to molecules, resulting in an increase in intermolecular interactions, and thus in a viscosity increase. The number of interactions will be greater

for bulkier molecules, and therefore, so will be the temperature-pressure dependence of the material (Couch and Binding 2000).

Author	Material	β_S (10^{-9} Pa^{-1})	Quantity measured
Sedlacek *et al.* (2004)	HDPE (ExxonMobil HMA 014)	10.4	Pressure drop in capillary
	LLDPE (ExxonMobil LD 600 BA)	11.7	
	LDPE (ExxonMobil LL6101 XR)	18.3	
	PP (ExxonMobil PP1374 F1)	21±4.1	
	PC (Krasten 137, Kaucup-Unipetrol Group)	31.1	
	PS (DELPET 80N, Asahi Kasei Corp.)	43.5±12.1	
	PMMA (Panlite AD-5503, Teijin Chemicals)	43.6	
Laun (2003)	LDPE (BASF, Lupolen 1840H)	11.0	Pressure drop in capillary
Goubert *et al.* (2001)	LLDPE (Atofina)	15.3±1.5	Pressure drop in capillary
Couch and Binding (2000)	HDPE (BASF, Lupolen 1840H5431P)	10±0.5	Pressure drop in capillary
	LDPE (BASF, Lupolen 1840H)	16.5±0.8	
	PP (ICI, GWM 213)	22±1.1	
	PMMA (ICI, CLH374)	25±1.25	
	PS (BASF, Polystyrol 143E)	29±1.5	
Hay *et al.* (1999)	LLDPE (ICI 501)	16.4	Axial pressure profile in slit die
	PS (Dow 555 PS)	45	
Koran and Dealy (1999)	LLDPE (Dowlex™ 2049)	14	High pressure sliding plate rheometer
Kadijck and Van den Brule (1994)	PS	31	Flow rate in fixed pressure drop slit rheometer
	ABS	24	
	PP	16	
Laun (1983)	LDPE	7	Axial pressure profile in slit die
		20	Pressure drop in die
Penwell *et al.* (1971)	PS	29±1.4	Pressure drop in capillary
Choi (1968)	PE (Phillips type)	12	Pressure profile in melt barrel of capillary rheometer
Semjonow (1962)	PS (Polystyrol)	~ 10.4	Torque in pressurized Couette cell
	HDPE	~ 10.4	
Maxwell and Jung (1957)	PE	16	Pressure drop in capillary
	PS	37	

Table 1: Shear pressure coefficients reported in the literature.

Within experimental errors, Couch and Binding (2000) find β_S and β_E to be the same in four out of the five polymer grades studied (HDPE, LDPE, PP, and PMMA). On the other hand, for PS, β_E is 30% greater than β_S, leaving an interesting open question in the air: can the pressure coefficient depend on the type of flow?

Flow instabilities are an important aspect which seems to have been overlooked in several studies concerning the effects of pressure on viscosity (Hatzikiriakos and Dealy 1992; Binding *et al.* 1998; Couch and Binding 2000; Laun 2003, 2004; Sedlacek 2004). Experiments may take place at apparent shear rates 10 times greater than the critical shear rate at which upstream instabilities (also named melt fracture) appear under atmospheric pressure. In the presence of the upstream instability, the flow field in the die and near its entrance is highly viscoelastic and unsteady, rendering any numerical simulation extremely difficult. Couette-Bagley corrections used here may be several times larger (Laun 2003) than typical viscous Couette-Bagley corrections. Hence, it is possible to ask for a comparison of β_S values published so far from oscillating flow data with β_S values obtained from stable flow data.

Flow stability during extrusion has already been the subject of several reviews which are too numerous to list (Denn 1990, 2001 and Piau *et al.* 1995). It is clear that flow curves show a change in slope when upstream instabilities appear as shown in work by Piau *et al.* (1990) and by El Kissi and Piau (1990). The sharpness of this slope change depends on the nature of the polymer and on the length of the die used. In general, the shorter the die is, the more distinct the change in slope will be in the flow curve. Upstream instabilities and wall slip often appear simultaneously, though this is not always the case. Some HDPE can show upstream instabilities with the polymer adhering at the wall (Piau *et al.* 1995). It can be very difficult to determine precisely the critical shear stress at which upstream instabilities appear when the polymer melt exits the die freely under atmospheric pressure. High-pressure rheometry only increases the difficulty, since no visual observation of the unperturbed melt exiting the die is possible in experimental set ups.

To our knowledge, no work has focused on the effects of pressure on flow instabilities (oscillatory flow, upstream instability) prone to occur during polymer processing operations, which brings us to the following questions: do these instabilities still take place in flows under high pressures? And if so, how does pressure affect them in terms of stability criteria and in terms of pressure drop?

As an example to illustrate the relevance of accounting for flow instabilities, the work by Hatzikiriakos and Dealy (1992) can be considered. They calculated apparent slow slip laws by means of a sliding plate rheometer and capillary rheometry experiments. From their capillary rheometry measurements, they concluded that the effects of pressure on pressure drop were negligible and that any deviations in the flow curve were due to slip at the wall. It is true that the deviations observed in their study were not due to pressure effects, but only because the pressure drops were too small. The apparent slip calculated in their work seems to correspond to flow regimes presenting the upstream instability. In fact, a change in slope indicative of a possible upstream instability is observed near 30 s^{-1} in their Bagley correction curve, (Figure 2 in their paper). Additional confirmation is obtained by plotting their flow curves on logarithmic scales as Figure 1 shows for a die with a length-to-diameter ratio of 60 and the Bagley correction of the same diameter. The same slope change, around 30 s^{-1}, is observed in

both the Bagley correction curve and the long capillary one and would be observed for all other dies as well. The absence of any flow visualization proved to be a heavy handicap for the sliding plate rheometer and interpretation of capillary experiments in the work of Hatzikiriakos and Dealy (1992).
A few years later, the same group successfully determined a pressure coefficient of 14×10^{-9} Pa^{-1} for a LLDPE (Koran and Dealy 1999) using a new version of their high-pressure sliding plate rheometer. Since then, it has been well established that pressure affects viscosity.

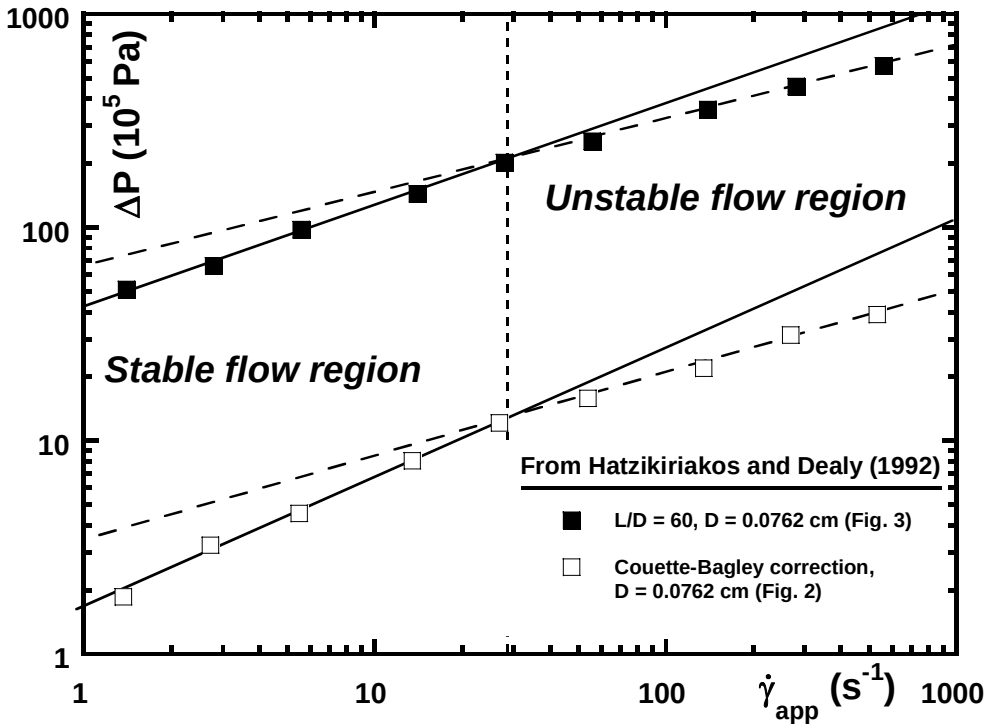

Figure 1: Pressure drop across a die with L/D = 60 (D = 0.0762 cm) recalculated from Figure 3 in Hatzikiriakos and Dealy (1992) as $\tau_w 4L/D$ and entry pressure drop for the same diameter from Figure 2 in the same reference on logarithmic scales.

In their work, Binding and his co-workers (1998, 2000) do not mention flow instabilities either, though they attain apparent shear rates as high as 2500 s^{-1}. For LDPE, and most noticeably for the short orifice curves, one observes sharp slope changes characteristic of the onset of upstream instabilities. Moreover, regardless of extrusion temperature, the slope change appears at the same critical shear stress level reported by Laun (2003, 2004) for the same LDPE.
Any pressure drop in a die will result in a temperature rise due to dissipative heating as pressure and temperature effects are coupled as shown explained by Denn (1981). The analysis of the pressure and temperature-dependence of the axial pressure profile in slit dies proposed by Hay *et al.* (1999) is adapted to the capillary rheometry case by Laun (2003, 2004), who concludes that differences in β_S and β_E are solely due to viscous dissipation. It is true that Binding and his co-workers (1998, 2000) consider viscous heating as negligible, but in this case their pressure coefficient values should be lower than those reported by Laun (2003, 2004).

The procedure to account for dissipative heating proposed by Laun (2003) is as follows: FEM numerical simulations performed using POLYFLOW give access to a dissipative heating coefficient, ε, that is then used to correct experimental data obtained with "enhanced exit-pressure" experiments.
In principle, the procedure outlined should work if experiments are performed under well-chosen conditions. So far, Laun has only been able to apply his procedure to a set of experimental data that does not seem to be the most relevant. Indeed, Laun calculates a Nahme number, Na, of 0.041 for the experimental conditions used, apparent shear rate, $\dot{\gamma}_{app}$, of 500 s^{-1}. Na is a dimensionless group that quantifies the importance of viscous heating (Winter 1977). It is defined as $\frac{\eta_0 \alpha \overline{V}^2}{kT}$ where η_0 is the zero shear viscosity, α is the thermal coefficient, $\overline{V}$ is a velocity characteristic of the flow, k is the fluid's thermal conductivity and T is the absolute temperature. For Nahme number values much smaller than 1, shear heating is negligible (Winter 1977).
Moreover, though numerical simulations may be a powerful tool, one must treat boundary conditions as well as flow conditions (i.e., steady or unsteady, laminar or turbulent) with extreme care. Steady flow numerical data can become irrelevant with respect to chaotic experimental conditions.
The Péclet number, Pe, expresses the ratio between heat transfer advected by the flow and heat transfer conducted at the die wall. For a die of diameter D, and in terms of the apparent shear rate, the melt's density ρ, its conductivity k, and its specific heat c_p, Pe is calculated as

$$Pe = \frac{\rho c_p}{k} \frac{\dot{\gamma}_{app} D^2}{8} \qquad (3)$$

Using $\dot{\gamma}_{app}$ = 500 s^{-1}, D = 10^{-3} m, and thermal properties reported by Laun (2003), (k = 0.24 $Wm^{-1}K^{-1}$, ρ = 780 kg m^{-3}, and c_p = 2600 J $kg^{-1}K^{-1}$), we obtain Pe ~ 530. Thus, heat transfer by conduction may be negligible and the die wall can be locally adiabatic. Moreover part of the die outer surface can be in contact with thermal resistances and with the open air. Using an isothermal wall boundary condition and forcing flow stability, as Laun (2003) proposes, may lead to an inaccurate dissipative heating coefficient ε, for the complex thermal problem at hand.

In the next section, following the analysis proposed by Hay *et al.* (1999), and extended by Laun (2003), we have determined the necessary experimental conditions in which viscous heating can be considered as negligible and thus, have been able to isolate the effects of pressure and measure them experimentally.
Then in the third section, the experimental set-up and products used are presented. "Enhanced exit-pressure" experiments were carried out on four commercial PE grades for mean pressures up to 700x10^5 Pa (exceptionally as high as 10^8 Pa). We worked with a LLDPE, a HDPE, and two mPEs, one with long ramifications (LCB) and one with short ones (SCB).
The results section is subdivided into two parts: the first one examines the existence of pressure effects on flow stability. To see the effects of pressure, we chose shear rates that lay on both sides of the stable/unstable flow transition under atmospheric pressure. Moreover, pressure drops were kept

small to ensure that viscous heating was negligible. Finally, the effect of pressure on flow stability is shown as upstream instabilities and/or oscillating flow conditions at the wall are observed.
The second part is devoted to the influence of ramifications on the effects of pressure under stable flow regime conditions. For stable flow regimes, these effects of pressure are measured and quantified in both shear and entrance flows. In contrast, and to complement work by Binding and his co-workers (1998, 2000) the backbones of the molecules are quite similar in our study but the number and length of these ramifications are changed.
A brief discussion of what we consider to be the most important points takes place in the last section. It is accompanied by some concluding remarks.

1.2 Negligible viscous heating conditions

It is well known that the pressure drop across a die causes a temperature rise in the melt due to dissipative heating; both pressure effects and dissipative heating are coupled (Denn 1981 and Hay *et al.* 1999). The purpose of this section is to determine those experimental conditions that will allow viscous heating effects to be neglected and thus the effects of pressure on viscosity to be isolated. In order to do this, we use work presented by Laun (2003) that is based on an analysis initially proposed by Denn (1981) for the adiabatic case and that was later extended by Hay *et al.* (1999) to include thermal heat flow from the melt to the die.
Let us recall equation (23) from Laun (2003):

$$\beta_{S,exp} = \frac{\beta_S(\dot{\gamma})}{1 + (\beta_S(\dot{\gamma}) + \alpha\varepsilon)\Delta P/2} \qquad (4)$$

$\beta_{S,exp}$ is the experimentally determined pressure coefficient. $\beta_S(\dot{\gamma})$ is a shear rate dependent coefficient equal to $n\beta_S$ (Couch and Binding 2000), n being the power law-index. α is the thermal coefficient and ε is a dissipative heating coefficient accounting for heat transfers between the melt and the die that will be maximum when the adiabatic condition at the die wall is considered. Then $\varepsilon = \frac{1}{\rho_0 c_P}$, with ρ_0 being the melt's density at atmospheric pressure, and c_P the specific heat at constant pressure. ΔP is the pressure difference between the inlet and outlet of the die.
When the quantity $(\beta_S(\dot{\gamma}) + \alpha\varepsilon)\Delta P/2$ is small enough, i.e.: less than 5%, it can be considered negligible and the experimentally determined pressure coefficient will be free of viscous heating effects.
With representative values of the different coefficients in (4), a limiting pressure drop, below which viscous heating effects will be insignificant, can be estimated. Common values for PE (Van Krevelen, 1990) are 8×10^{-3} K^{-1} for the thermal coefficient α, a pressure coefficient $\beta_S(\dot{\gamma})$ of the order of 5×10^{-9} Pa^{-1}, a specific heat c_v of 3000 J $kg^{-1}K^{-1}$, and a reference density ρ_0 of 900 kg m^{-3}. Using these values, a limiting pressure drop of 170×10^5 Pa is obtained. For flow conditions with pressure drops below this cutoff value, viscous heating effects will be negligible with respect to pressure effects. Couch and

Binding (1998, 2000) had assumed negligible viscous heating effects having maximum pressure drops in the vicinity of $200x10^5$ Pa. Their assumption thus seems quite justified.

1.3 Experimental means

1.3.1 Experimental bench and method

A Göttfert Reograph 2001 capillary rheometer was modified by attaching a cylindrical steel piece containing a chamber and a valve assembly at the die exit. A schematic drawing of the set-up is shown in Figure 2. Opening or tightening the valve regulated the pressure inside the chamber. Dynisco PT420 pressure transducers were used to measure the pressure near the die inlet and inside the downstream chamber. Transducers rated at 100, 500, 1000, and $2000x10^5$ Pa, having an accuracy better than $\pm 0.5\%$ of their full scale, were used according to the pressures measured. All pressure readings were plotted as a function of time on a multi-channel recorder during the experimental runs.

The barrel and die were kept at temperature by three independent heating coils controlled through the rheometer's interface. PT100-type resistance thermometers allowed the assembly to be kept within 0.5°C of the desired temperature. The section below the die was kept at the same temperature by a fourth heating coil controlled separately. Whenever possible, and depending on the length of the capillary, one or two type J thermocouples were used to check the temperature of the polymer melt during the experimental runs.

Axisymmetric dies having length-to-diameter (L/D) ratios of 5, 15, 20, and 30 as well as orifices of zero mm nominal length and diameters of 1 and 2 mm were used.

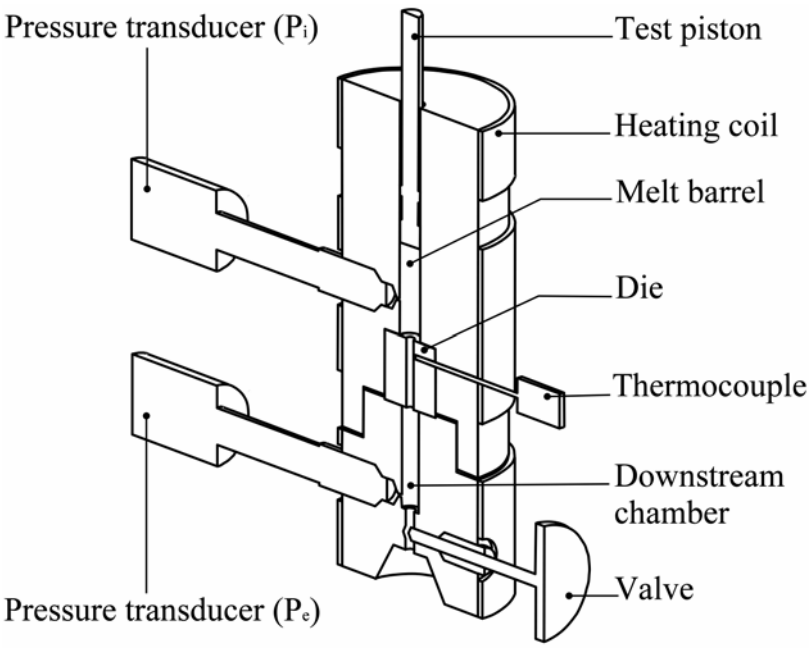

Figure 2: Experimental set-up

During the experimental runs, the test piston pushed the melt through the die at a constant mean flow rate, i.e. constant strain rate, with the valve fully opened. Once the pressure levels in both transducers stabilized with time, i.e. steady-state flow conditions, the pressure readings upstream of the die, P_i, and downstream of it, P_e, were recorded. The difference between P_i and P_e is used to calculate a pressure drop across the die, ΔP, defined by

$$\Delta P = P_i - P_e \tag{5}$$

The valve was then tightened, so pressure in the downstream chamber would increase. Pressure levels were allowed to stabilize and were recorded again. Repeating these steps, a curve describing the change in pressure drop across the die as a function of the upstream pressure was completed for a given flow rate.

The pressure drop across the capillary as defined in (5) includes entrance effects. To account for them, a simplified version of the Couette-Bagley (1957) correction is used. Basically, it states that the entrance effects, and their associated pressure drop, for an orifice and a capillary of the same diameter can be considered equal at a given flow rate (Binding *et al.* 1998; Couch and Binding 2000). It has already been recalled by Couch and Binding (2000) that the Couette-Bagley correction is normally carried out by substracting pressure losses from capillaries with the die exit at ambient pressure. It is preferred to compare pressure losses for the same values of entrance pressure when fluid physical properties are not constant.

The pressure drop across the orifice and the capillary are defined by

$$\Delta P_o = P_{i,o} - P_{e,o} \tag{6}$$

and

$$\Delta P_L = P_{i,L} - P_{e,L} \tag{7}$$

where P_i and P_e are the pressures measured upstream and downstream of the die respectively and the subscripts o and L stand for orifice and long-capillary. As long as the condition $P_{i,o} = P_{i,L}$ is respected, possible by regulating the die exit pressure with the valve, the Couette-Bagley corrected pressure-drop in the capillary can be rewritten as

$$\Delta P_{corr} = \Delta P_L - \Delta P_o \tag{8}$$

A mean pressure inside the capillary can be defined as

$$P_{ave,L} = P_{e,L} + \frac{\Delta P_{corr}}{2} \tag{9}$$

From the corrected pressure drop, the shear stress at the wall for each couple of mean pressure and wall shear rate can be calculated as

$$\tau_w(\dot{\gamma}, P_{ave,L}) = \frac{\Delta P_{corr}(\dot{\gamma}, P_{ave,L})}{4L/D} \tag{10}$$

Where L is the capillary's length and D its diameter. $\dot{\gamma}$ is related to the volumetric flow rate Q, the capillary's diameter, and the power-law index, n, by

$$\dot{\gamma} = \left(\frac{3n+1}{4n}\right)\frac{32Q}{\pi D^3} \tag{11}$$

Neglecting dissipation, the equation for momentum conservation can be solved to obtain the expression for pressure drop within a capillary:

$$\beta_S(\dot{\gamma})\,\Delta P_{corr}\left(P_{ave,L}\right) = \ln\left\{1+\beta_S(\dot{\gamma})\,\Delta P_{corr}(0)\exp\left(\beta_S(\dot{\gamma})\left(P_{ave,L}+0.5\,\Delta P_{corr}\left(P_{ave,L}\right)\right)\right)\right\} \tag{12}$$

A simple expression valid up to second order can be deduced from Eq. (12) in terms of shear stress at the wall:

$$\tau_w(\dot{\gamma}, P_{ave,L}) = \tau_w(\dot{\gamma},0)\exp\left(\beta_S(\dot{\gamma})\,P_{ave,L}\right) \tag{13}$$

If $\beta_S(\dot{\gamma})$ and a power-law index, n, are used, the expression for a_{TP}^{s} presented in (2) should be rewritten as

$$a_{TP}^{s} = \exp\left[\frac{\beta_S(\dot{\gamma})}{n}\left(P-P_R\right)+\frac{E_S}{R}\left(\frac{1}{T}-\frac{1}{T_R}\right)\right] \tag{14}$$

1.3.2 Products used

In Table 2, we present the principal characteristics of the four commercial grades of polyethylene (PE) used: A linear-low-density polyethylene copolymer (LLDPE), a high-density polyethylene (HDPE), and two low-density metallocene polyethylenes (mPE). One of them had short-chain branches only (mPE-SCB) whilst long-chain ramifications, about 1000 C in length, were also present in the other (mPE-LCB) every 1000 C. In both mPEs there is a percentage of octane present in the macromolecules, about 15% for the SCB and 5-10% for the LCB. The four of them have already been well characterized in shear conditions under atmospheric pressure conditions at the die exit.

Polyethylene type	Commercial Name	Producer	M_w (g/mol)	M_w/M_n	ρ (kg m^{-3})	Ramification Distribution	Extrusion T (°C)
LLDPE	Lotrex FC1010	Enichem	143.000	3.9	914	Statistic	190
HDPE	HD2i	Total-Fina-Elf	90,000	4.6	944	(≈ 0) Linear	185
mPE-LCB	Affinity™ PL1880	Dow Plastics	80,000	2.0	902	Long branches every 1000C	190
mPE-SCB	Engage® 8100	Dupont Dow	115,000	2.0	870	?	190

Table 2: Principal characteristics of the PE studied.

1.4 Results

1.4.1 Flow instabilities

With increasing mean pressure, flow instabilities were observed at lower shear rates in two different forms: as pressure oscillations typical of oscillating flow conditions (LLDPE) or as sharp slope changes in $\tau_w(P_{ave})$ curves typical of upstream instability conditions (mPE-LCB). In the case of HDPE, pressure oscillations were only observed for one single point and in the case of mPE-SCB, no instabilities were observed for the range of shear rates and mean pressures covered. Thus, the latter two will not be considered in this section.

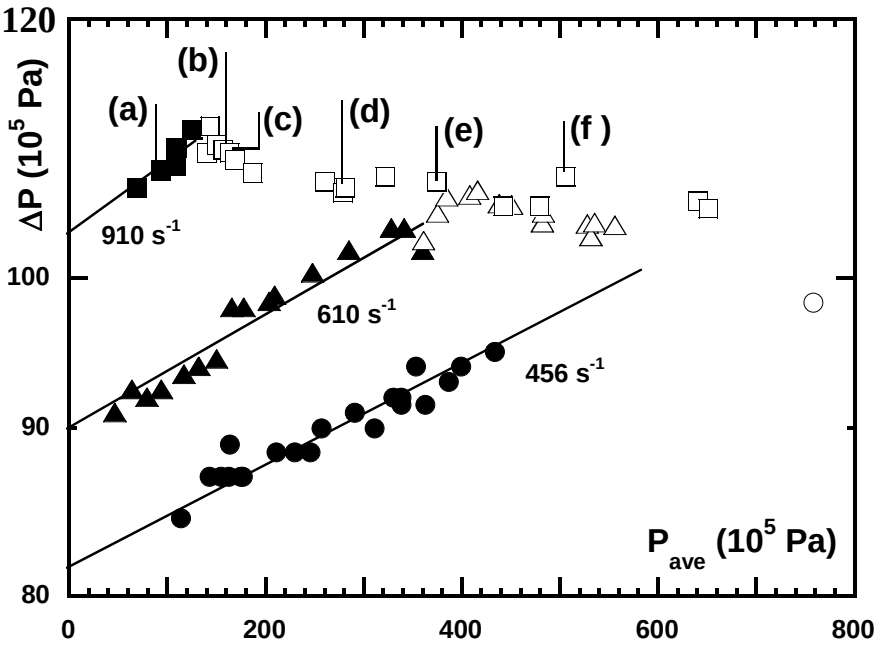

Figure 3: LLDPE at 190°C. Pressure difference measured across a capillary (L/D = 5/1) as a function of mean pressure for different shear rates. Stable flow regimes (filled marks) and unstable flow regimes (open marks) determined by the presence of oscillating flows.

Figure 3 and Figure 4 present experimental data obtained with LLDPE and mPE-LCB respectively. All curves correspond to a capillary with L/D = 5/1. Notice that dissipative heating is negligible since pressure drops are below 170×10^5 Pa. Thus, the change in slope observed in the different curves can be attributed solely to pressure. This distinct slope change coincides with the point at which pressure oscillations appeared for LLDPE (Figure 3), which means a stable flow region (filled marks), and an unstable flow region (open marks) can be determined for higher mean pressures. For mPE-LCB (Figure 4) no pressure oscillations were detected, but a clear slope change was observed. In the stable flow region, the pressure drop increases exponentially with the mean pressure, confirming theoretical predictions. For unstable regimes, variations in pressure drop with mean pressure are much more complex to predict.

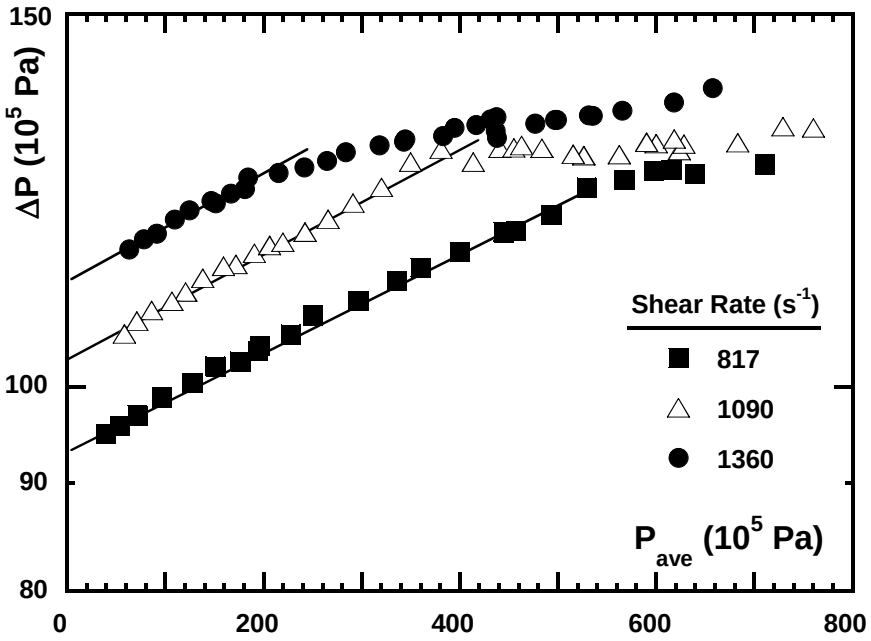

Figure 4: mPE-LCB at 190°C. Pressure difference measured across a capillary (L/D = 5/1) as a function of mean pressure for different shear rates.

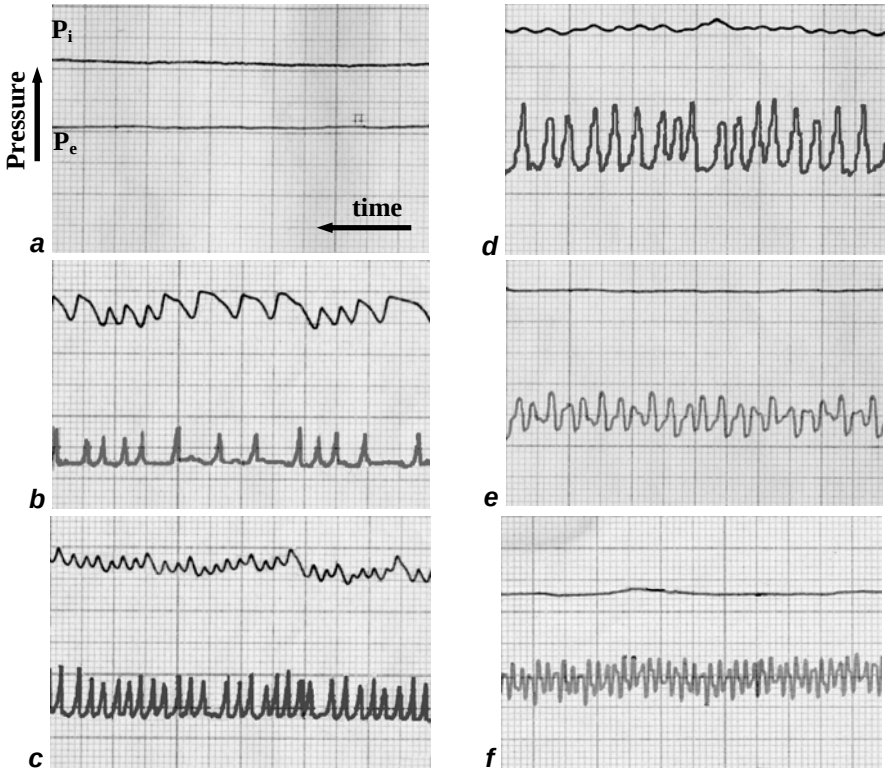

Figure 5: Variations in instability shape with mean pressure at 910 s^{-1} for LLDPE at 190 °C. Capillary with L/D *= 5. All pressures in 10^5 Pa. (a)* P_i *= 163.6,* P_e *= 54.0,* S_{paper} *= 2 mm/s, (b)* $P_{i,max}$ *= 211.9,* $P_{i,min}$ *= 211.3,* P_e *= 101.2,* S_{paper} *= 2 mm/s, (c)* $P_{i,max}$ *= 223.7,* $P_{i,min}$ *= 223.3,* $P_{e,max}$ *= 116.0,* $P_{e,min}$ *= 113.6,* S_{paper} *= 2 mm/s, (d)* $P_{i,max}$ *= 332.4,* $P_{i,min}$ *= 331.6,* $P_{e,max}$ *= 228.0,* $P_{e,min}$ *= 223.6,* S_{paper} *= 5 mm/s, (e)* P_i *= 428,* $P_{e,max}$ *= 322,* $P_{e,min}$ *= 320,* S_{paper} *= 10 mm/s, (f) Pi = 559.2,* $P_{e,max}$ *= 453.2,* $P_{e,min}$ *= 450.4 ,* S_{paper} *= 5 mm/s*

Figures 3 and 4 are strong evidence that data in the stable flow region must be used for an accurate determination of pressure coefficients.

Recordings of pressure-drops across a capillary with L/D = 5/1 as a function of mean pressure at 910 s^{-1} are presented in Figure 5. On the figure legends, we have noted the paper rolling speed as S_{paper}. Experimental points corresponding to the recordings are marked (a) through (f) on Figure 3.

Characteristic pressure readings as a function of time for the stable flow domain are presented in caption 5a, corresponding to a mean pressure of 108x10^5 Pa. The upper and lower traces are the signals from pressure transducers upstream (P_i) and downstream (P_e) of the die respectively. In all captions, time advances from right to left. The pens are offset by about 2.5 mm in the recorder. Thus, there will be a 2.5 mm difference between the recordings for an event occurring at a time t. While the flow is stable, both signals remain constant with time.

When the mean pressure is increased, oscillatory flow appears (see captions 5b through 5d) as evidenced by the sudden pressure drops of 0.6x10^5 Pa and oscillations detected upstream. These pressure oscillations occur at irregular frequencies, creating an asymmetric saw tooth-shaped curve. The downstream pressure transducer registers the signature of the slipping phase, which appears in the capillary, as quasi-instant pressure increases that mirror the corresponding P_i pressure drops. As mean pressure is increased, the frequency of the oscillations increases: 1 and 2.5 Hz for captions 5c and 5d respectively. A complete analysis of these pressure oscillations is beyond the scope of this paper and will not be treated.

In the case of mean pressures above 280x10^5 Pa, no more oscillations are recorded upstream of the die (captions 5e and 5f). Moreover, the pressure drop becomes independent of the mean pressure within experimental errors. A constant pressure drop across the die results from a permanent slip of the polymer at the die-melt interface. However, pressure oscillations were still detected downstream, although of slightly different shape. Now, they seem to be symmetric about an average value as opposed to the quasi-instant peaks. These oscillations, occurring at about 4 Hz, seem to become more chaotic with increasing mean pressure. They can be related to the natural frequency and its harmonics that are associated with the upstream instability causing melt fracture (Piau *et al.* 1990, 1995). These pressure oscillations, as well as permanent slippage of the polymer, are characteristic consequences of melt fracture, which would be observed if the die exit were free. Finally, changing the exit pressure provides a scan of the capillary die flow stability for a given mean rate of flow. It should be noticed that for experiments for a same shear rate but with two dies of same diameter and different length, pressure oscillations were initially detected at different downstream pressures P_e but equal shear stresses. Thus, pressure oscillations must correspond to the flow in the capillary.

Analysis of the pressure readings as a function of time shows how these pressure oscillations vary with shear rate. Figure 6 presents several pressure readings at different shear rates for two mean pressure levels: 150 and 400x10^5 Pa approximately.

This sequence of captions shows that, at a mean pressure of 400x10^5 Pa, pressure oscillations appear at a lower shear rate than they did at a mean pressure of 150x10^5 Pa. However, the wall shear stress at which these instabilities are triggered is independent of mean pressure. At 910 s^{-1} and 150x10^5 Pa, the pressure drop across the die is 110.7x10^5 Pa, while at 610 s^{-1} and a mean pressure

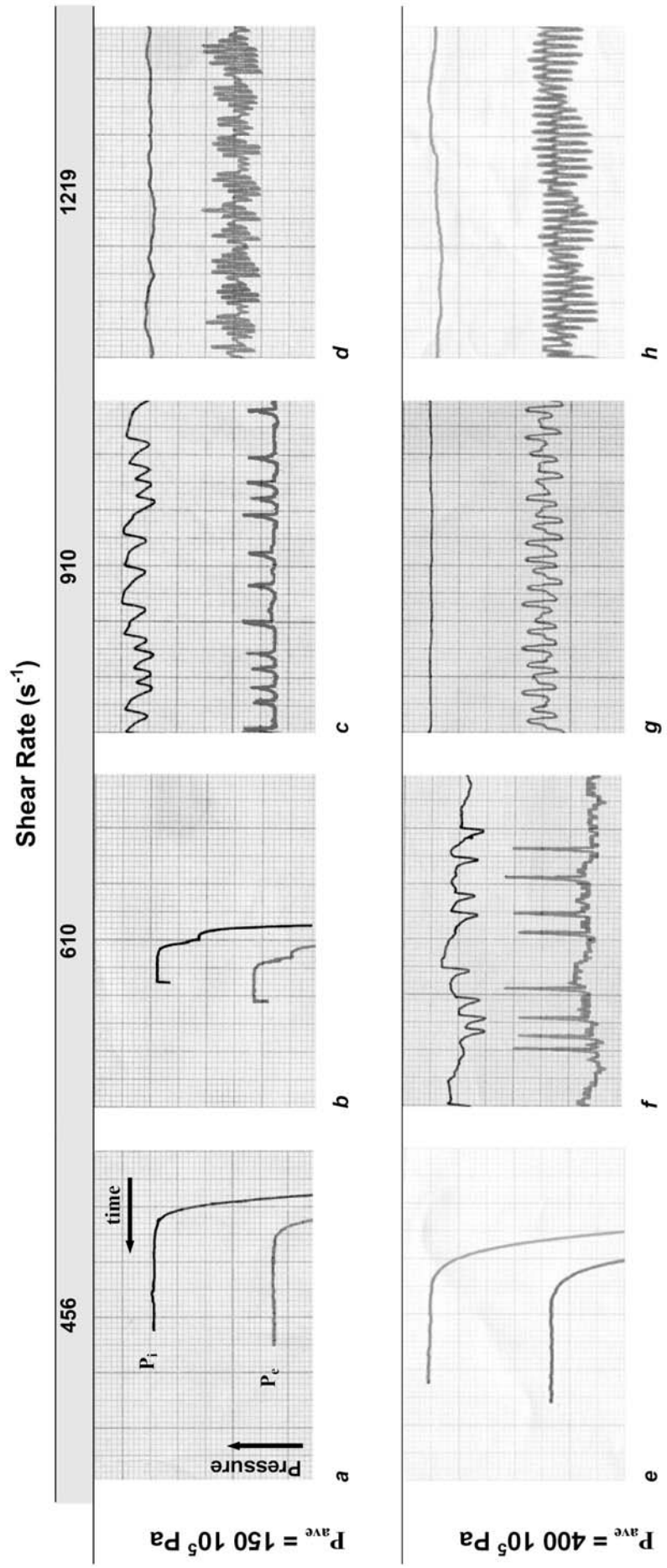

Figure 6: Variations in instability shape with shear rate for LLDPE at 190 °C and different mean pressures. Capillary with L/D = 5. All pressures in 10^5 Pa. (a) P_i *= 198,* P_e *= 111, Shear rate = 456* s^{-1}*,* S_{paper} *= 0.33 mm/s; (b)* P_i *= 197.5,* P_e *= 103, Shear rate = 611* s^{-1}*,* S_{paper} *= 0.083 mm/s; (c)* $P_{i,max}$ *= 211.9,* $P_{i,min}$ *= 211.3,* P_e *= 101.2, Shear rate = 910* s^{-1}*,* S_{paper} *= 2 mm/s; (d)* P_i *= 211,* $P_{e,max}$ *= 102.1,* $P_{e,min}$ *= 101, Shear rate = 1219* s^{-1}*,* S_{paper} *= 5 mm/s; (e)* P_i *= 481,* P_e *= 386, Shear rate = 456* s^{-1}*,* S_{paper} *= 0.33 mm/s; (f)* $P_{i,max}$ *= 491.6,* $P_{i,min}$ *= 490,* $P_{e,max}$ *= 387.4,* $P_{e,min}$ *= 383.4, Shear rate = 611* s^{-1}*,* S_{paper} *= 1 mm/s; (g)* P_i *= 428,* $P_{e,max}$ *= 322,* $P_{e,min}$ *= 320, Shear rate = 910* s^{-1}*,* S_{paper} *= 10 mm/s; (h)* P_i *= 445.3,* $P_{e,max}$ *= 340.6,* $P_{e,min}$ *= 339.2, Shear rate = 1219* s^{-1}*,* S_{paper} *= 5 mm/s.*

of $400x10^5$ Pa, the measured pressure drop is of $108.2x10^5$ Pa; less than a 2.5% difference. These results show that flow instabilities during extrusion result from the state of stress of the fluid. Indeed, at a fixed shear rate, increasing mean pressure results in an increase in shear stress. Thus, the critical shear stress at which flow instabilities occur will be reached at lower shear rates when mean pressure is increased.

Table 3 summarizes results for LLDPE and mPE-LCB that are necessary in order to quantify correctly the critical value of wall shear stress beyond which instabilities appear. The shear rate and critical shear stress determined with conventional capillary rheometry and considered to be under atmospheric pressure conditions are presented.

In the portion of the table entitled "Experimental data", we report the mean pressures at which flow instabilities were initially observed for different shear rates. The apparent shear stress, which does not account for entrance effects, is reported.

Equation (10) has been applied to correct for entrance effects with experimental data obtained when a short orifice die was used. Although within experimental errors of the critical shear stress values calculated can be considered equal to those determined using capillary rheometry experiments; they are consistently on the high side. This is particularly true for the data obtained with the 5/1 capillary. Thus, it seems that the Couette-Bagley correction with the short orifice die is not sufficient for dies with L/D of 5/1. With that in mind and for a given shear rate, when handling data for capillaries of the same diameter and different lengths L_1 and L_2 (with $L_1>L_2$), the simplified Couette-Bagley correction (Couch and Binding 2000) was applied and the shear stress calculated using (10) for a die of length L_1-L_2. The calculated values of the critical shear stress are presented in the table in bold italic characters. More than acceptable agreement is observed between these calculated values and shear stress values obtained with capillary rheometry experiments.

The critical shear stress was also calculated from master curves using atmospheric pressure as the reference state (Figures 8 and 10). The shear rates and shear stresses beyond which flow instabilities were observed are presented on the last row of the table.

The product between the shear rate and a_P^S has been calculated at the stable/unstable transition mean pressure. It represents the reduced shear rate under atmospheric pressure conditions and should be higher than the critical shear rate determined from capillary rheometry. This is the case.

It is clear from Table 3 that the shear stress level at which flow instabilities are observed is independent of mean pressure. Moreover, the stress level and flow instabilities observed for these flows under high mean pressures are the same as those observed under atmospheric pressure conditions.

We should comment that the HDPE used in our study is stable for shear rates as high as 2500 s^{-1}, too high for the current experimental set-up. In addition, we should note that at 190 °C and atmospheric pressure, the appearance of flow instabilities is marked neither by pressure oscillations nor by a clear discontinuity on the flow curve of the mPE-SCB used. The appearance of these flow instabilities needs to be determined visually at the die exit, which is an impossible task given our experimental set-up.

		LLDPE (190°C)				mPE-LCB (190°C)			
	Die (L/D)	$\dot{\gamma}$ (s^{-1})	Mean Pressure (10^5 Pa)	τ_w (10^5 Pa)	$a_p^* \dot{\gamma}$ (s^{-1})	$\dot{\gamma}$ (s^{-1})	Mean Pressure (10^5 Pa)	τ_w (10^5 Pa)	$a_p^* \dot{\gamma}$ (s^{-1})
Capillary rheometry		>1000	1	3.8±0.1	-	>1600	1	4.1±0.1	-
Experimental data (τ_w reported is apparent and equal to $\Delta P/(4L/D)$)	30/1	610	415±25	3.98±0.1	*1104±40*				
	20/1					1090	365±25	4.6±0.1	*1930±75*
	20/1					817	570±30	4.7±0.1	*2000±96*
	5/1	910	134±10	5.5±0.1	*1102±40*	1360	200±15	6.3±0.1	*1860±44*
	5/1	610	360±5	5.2±0.1	*1020±8*	1090	395±15	6.4±0.1	*2035±50*
	5/1	456	758	4.9±0.2	*1348*	817	550±20	6.2±0.1	*1940±62*
Calculated data (τ_w calculated with Equation (10) and orifice die data)	*30/1*	*610*	*415±25*	*3.8±0.2*	1104±40				
	20/1					*1090*	*365±25*	*4.2±0.3*	1930±75
	20/1					*817*	*570±30*	*4.25±0.3*	2000±96
	5/1	*910*	*134±10*	*3.98±0.5*	*1102±40*	*1360*	*200±15*	*4.5±0.5*	*1860±44*
	5/1	*610*	*360±5*	*3.95±0.5*	*1020±8*	*1090*	*395±15*	*4.7±0.5*	*2035±50*
	5/1	*456*	*758*	*3.7±0.5*	*1348*	*817*	*550±20*	*4.7±0.5*	*1940±62*
Calculated from two long capillaries*	***25/1***	***610***	***410±10***	***3.76±0.2***	***1096±15***				
	15/1					***1090***	***380±15***	***4.2±0.3***	***1980±50***
	15/1					***817***	***560±15***	***4.1±0.3***	***1968±50***
T-P Superposition	-	1025±10	1	3.76	-	1740±10	1	4.25	-

*e.g.: for LLDPE, capillaries of length 30 and 5 mm were used resulting in the pressure drop for a die of length 25 mm.

Table 3: Set of conditions that will trigger flow instabilities for LLDPE and mPE-LCB studied using different methods. Experimentally observed values are not corrected for entrance effects. An empty case means that no experiments were performed with the given die.

1.4.2 Effect of structure on the pressure-dependence of viscosity

Figure 7 presents flow curves at different mean pressures for LLDPE at 190°C. The effect of pressure on shear stress is observed by the upwards shift of the flow curve with increasing mean pressure. We are aware that the assumptions used to calculate shear stress and shear rate may not be valid for unstable regimes. Nevertheless, both stable and unstable regimes have been plotted on the graph so as to have a better view of pressure effects on flow stability.

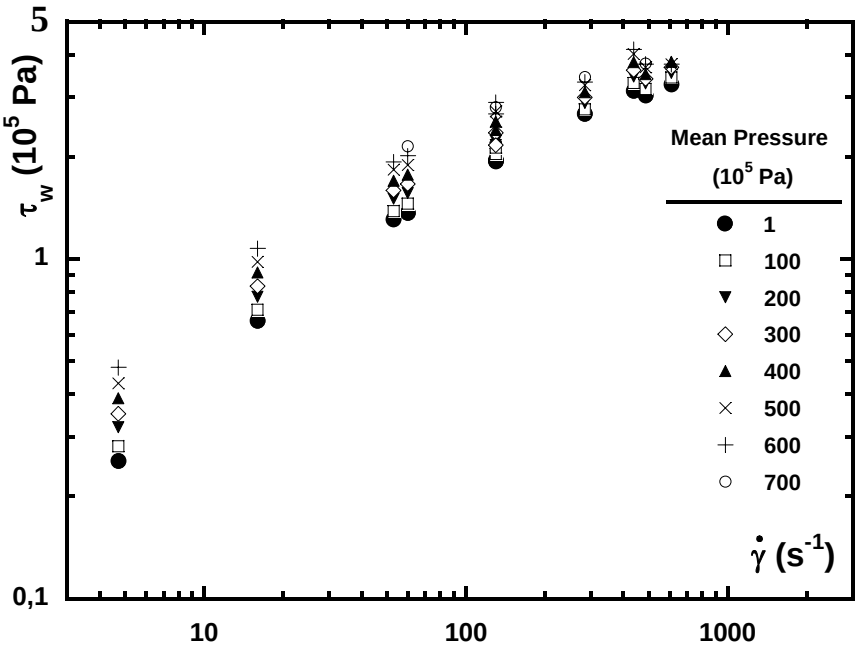

Figure 7: Flow curves, $\tau_w(\dot{\gamma})$, at different mean pressures for LLDPE at 190 °C.

The master curve for LLDPE using 10^5 Pa as reference pressure is given in Figure 8. The graph also includes the flow curve obtained from capillary rheometry experiments using a 2 mm diameter die. The inset on the right side zooms on the stable/unstable flow regime transition. It can be noticed that as the transition is approached, marked by a slope change in the curve, superposition of the different curves no longer holds. The master curve splits into two branches. The upper one corresponds to measurements obtained with a 30/2 die, whereas the lower one corresponds to a 20/1 capillary. This lack of superposition could be due to the appearance of slip at the wall.

Since each fluid was only characterized at one temperature ($T=T_R$), the temperature term in (1) reduces to zero. Thus, the shift factor only includes pressure effects and its variation with mean pressure (shown in the inset) can be used to determine β_S. Notice that data obtained at mean pressures of 600 and 700x10^5 Pa fall within the unstable flow region. Thus, great caution must be used when interpreting the results.

Master curves for HDPE at 185°C, mPE-LCB at 190°C, and mPe-SCB at 190°C, using 10^5 Pa as the reference pressure, are presented in Figure 9, Figure 10 and Figure 11 respectively. Flow curves

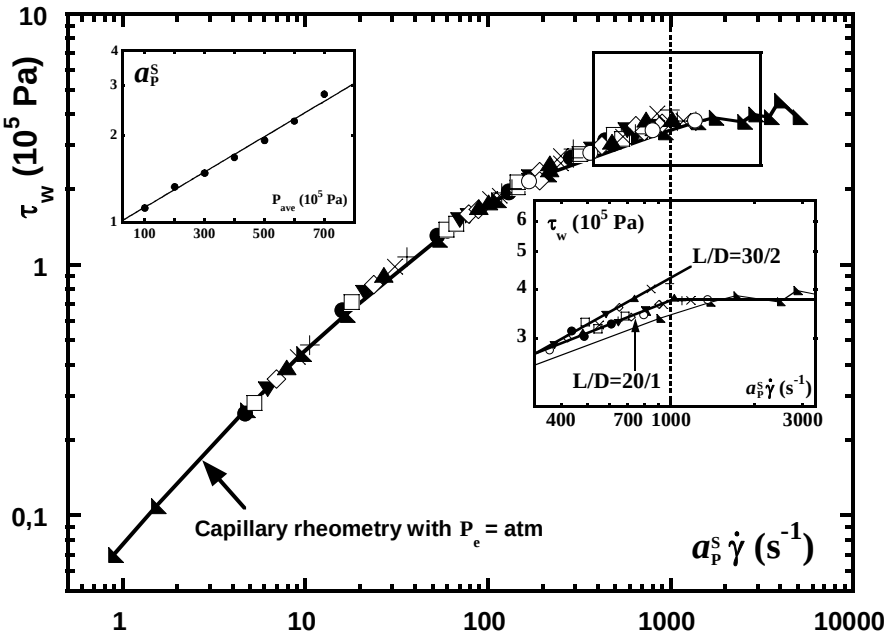

Figure 8: Master flow curve for LLDPE at 190 °C using atmospheric pressure as the reference state.

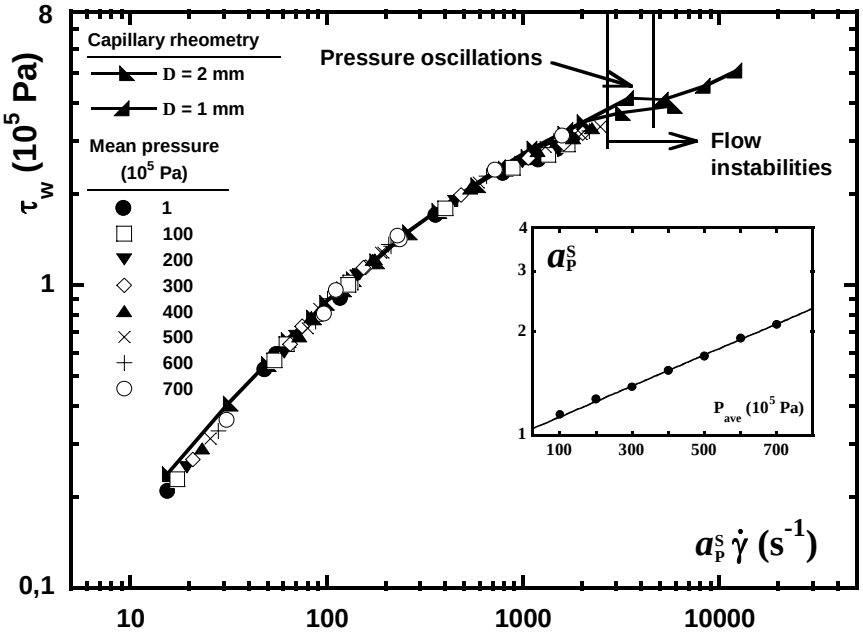

Figure 9: Master flow curve for HDPE at 185 °C using atmospheric pressure as the reference state.

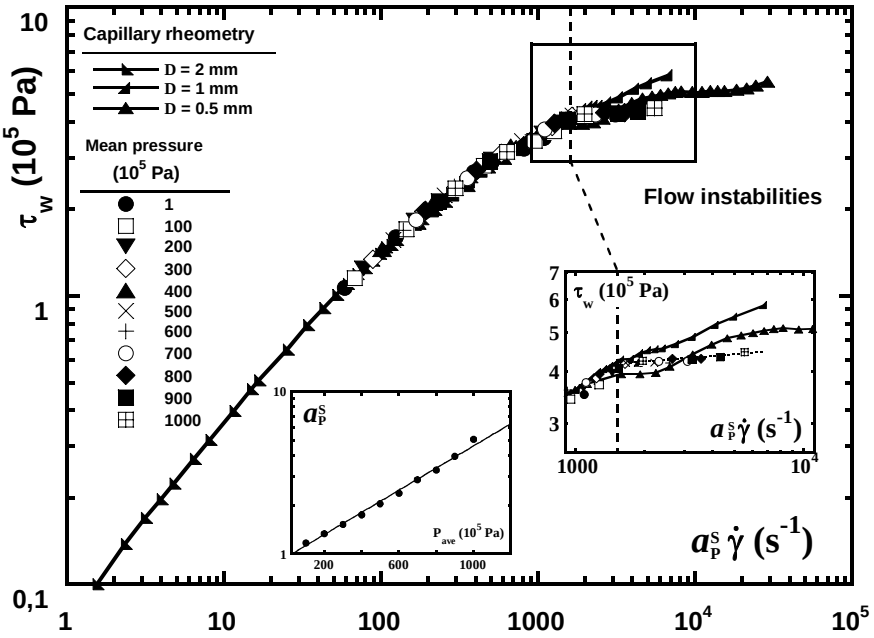

Figure 10: Master flow curve for mPE-LCB at 190 °C using atmospheric pressure as the reference state.

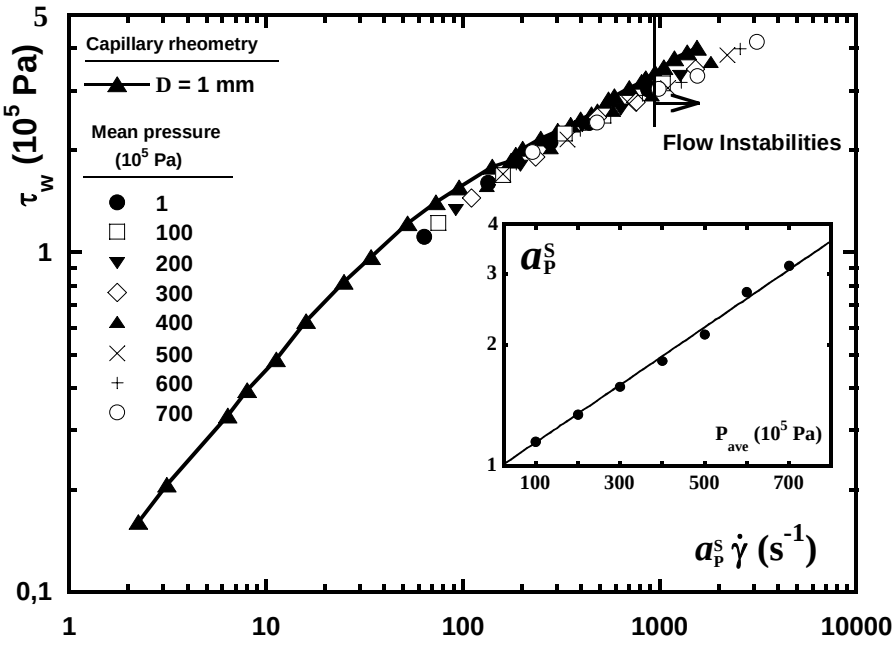

Figure 11: Master flow curve for mPE-SCB at 190 °C using atmospheric pressure as the reference state.

obtained using capillary rheometry with a free die exit under atmospheric pressure conditions are also included for all three fluids. In all three cases, time-pressure superposition works relatively well and master curves superpose well with conventional capillary rheometry flow curves for stable flow regimes.

	β_S (10^{-9} Pa^{-1})	β_E (10^{-9} Pa^{-1})
LLDPE	13.5±1.3	10.8±1.3
HDPE	10.7±1.8	10.1±1.8
mPE-LCB	14.6±1.8	9.8±1.8
mPE-SCB	18±1.8	16.1±1.8

Table 4: Comparison of pressure coefficient values obtained from superposition in shear flow (β_S) and in entrance flow (β_E).

Table 4 shows that β_S values for all 4 PE are in the 10-20x10^{-9} Pa^{-1} range. These values agree well with pressure coefficient values published elsewhere (Couch and Binding 2000; Goubert *et al.* 2001; Koran and Dealy 1999) for PE. If all 4 PE are classified by pressure coefficient in an increasing order, we obtain: HDPE, LLDPE, mPE-LCB, and mPE-SCB. The same order would have been obtained had the four melts been classified by their number of ramifications. Indeed, Sedlacek *et al.* (2004) have shown that the pressure sensitivity of polymers increases with the number of ramifications, more so than with the length of ramifications.

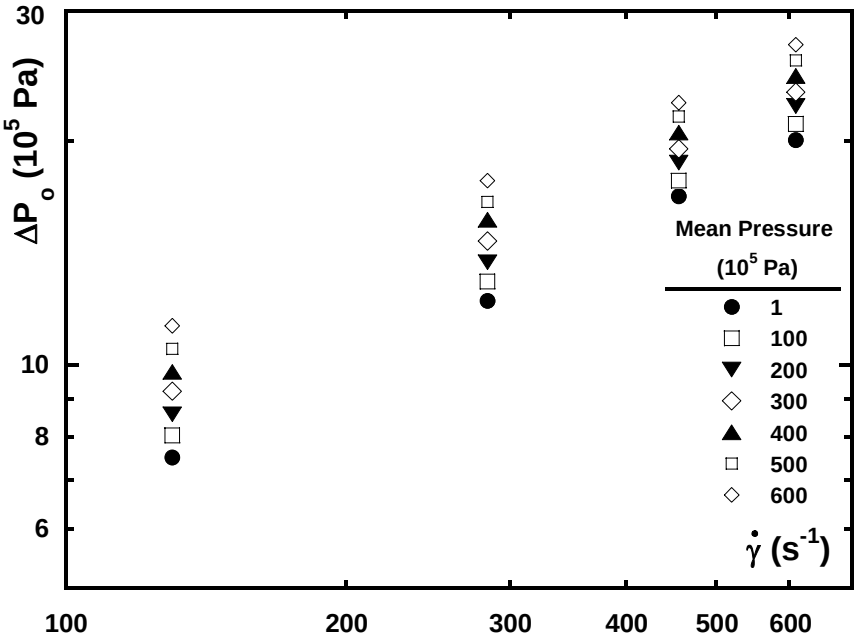

Figure 12: Pressure drop across the short orifice die as a function of shear rate at different mean pressures for LLDPE at 190°C.

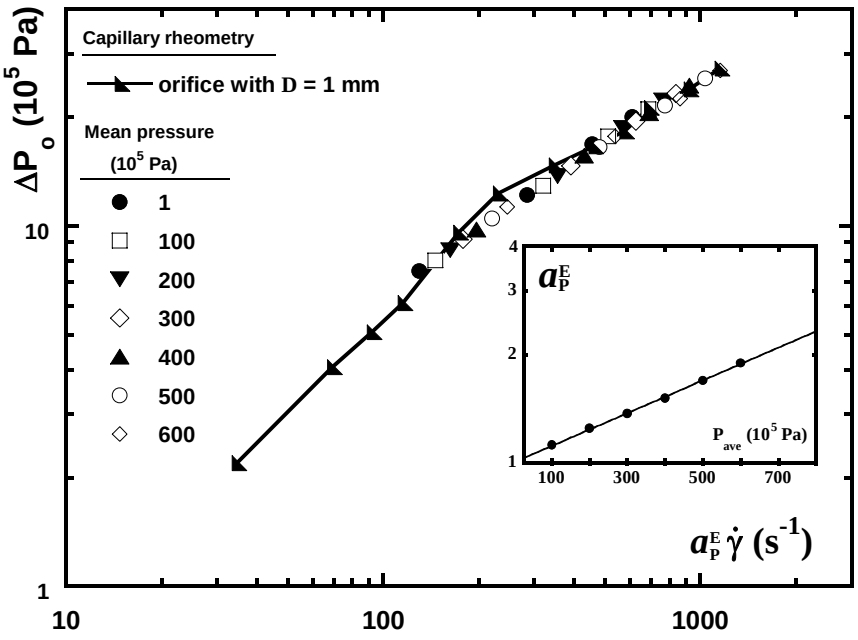

Figure 13: Entrance master flow curve for LLDPE at 190 °C using atmospheric pressure as the reference state.

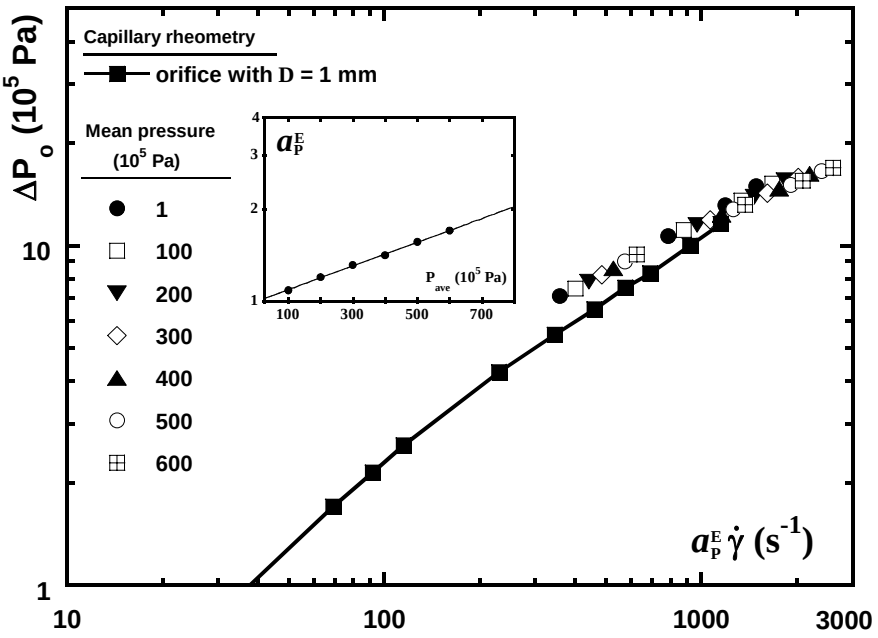

Figure 14: Entrance master flow curve for HDPE at 185 °C using atmospheric pressure as the reference state.

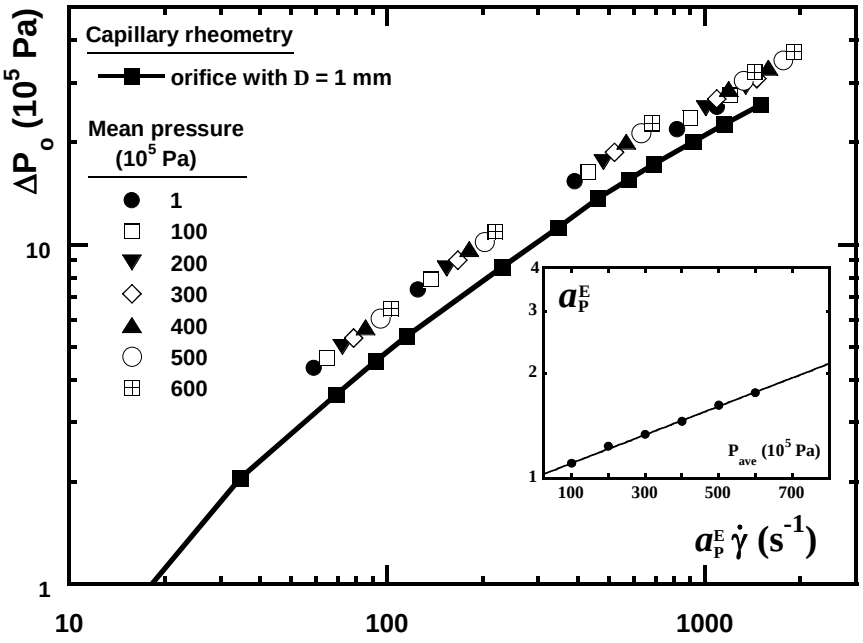

Figure 15: Entrance master flow curve for mPE-LCB at 190 °C using atmospheric pressure as the reference state.

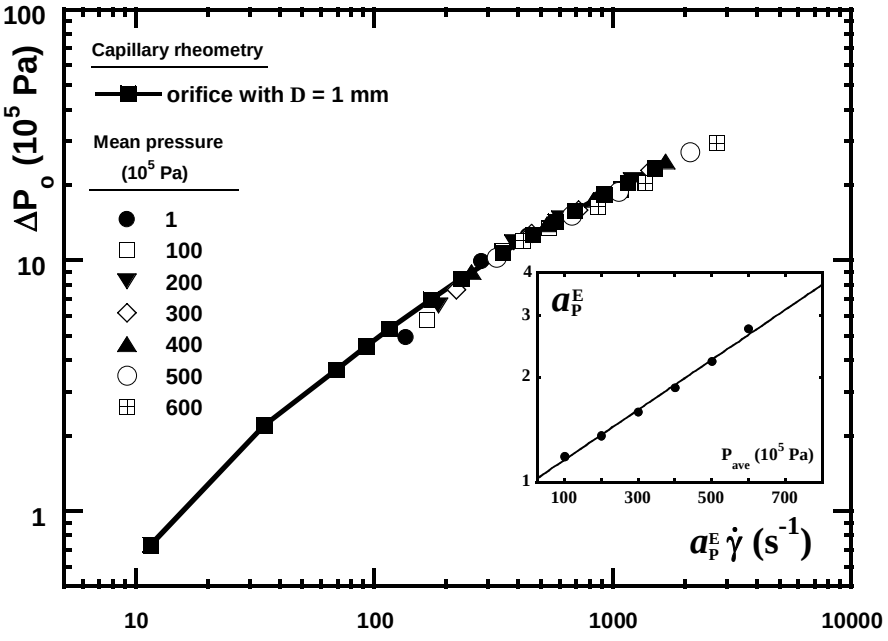

Figure 16: Entrance master flow curve for mPE-SCB at 190 °C using atmospheric pressure as the reference state.

Pressure drop versus shear rate data at different mean pressures obtained with a short orifice of 1 mm diameter are presented in Figure 12 for LLDPE at 190°C. Master curves using 10^5 Pa as the reference pressure are presented in Figures 13, 14, 15 and 16. Respectively, they correspond to LLDPE, HDPE, mPE-LCB, and mPE-SCB. The flow field in a short orifice die is representative of the fluid's extensional behavior. Thus, shift factors from these curves will give an "extensional" pressure coefficient (Binding *et al.* 1998, Couch and Binding 2000).

Table 4 also shows that for LLDPE, HDPE, and mPE-SCB both β_S and β_E can be considered equal within experimental uncertainties. This is not the case for mPE-LCB, whose β_E is about 30% lower than its β_S. This difference between pressure effects under shear and in entrance flows can be partially explained by the presence of long ramifications in the macromolecules. Indeed, these long branches have an effect on the elongational properties of the fluid (Gabriel and Münstedt 1999) and will modify entrance effects since their length will result in lower extensional gradients through the contraction.

1.5 Discussion and conclusions

This study examines the effects of pressure on the flow stability of four commercial grade polyethylenes under conditions relevant to those encountered during industrial processing operations. The effects of pressure on viscosity have been studied for over 50 years now. Most work has focused on the effect of macromolecular structure on piezodependence. As seen in Table 1, agreement is not always so bad for the same type of polymer in shear flows. Given the precision achieved in β_S values, 2 significant figures at most can be retained. In some cases there is no evaluation of the precision achieved. On other occasions, just the repeatability of the measurements, rather than the actual error in the pressure coefficient, is reported. It may be noticed that there is general agreement on a value of $\beta_S=\beta_E= 10^{-8}$ Pa^{-1} for HDPE. A fair agreement can also be noticed among the various measurements for LLDPE. The one shocking point is the 50% discrepancy between values supposed to be calculated with a precision better than 5% for the same LDPE polymer by Binding and co-workers (1998, 2000) and by Laun (2003, 2004).

Whether pressure effects depend on the type of flow (shear or extensional) is another question that still need to be clearly answered. Couch and Binding (2000) observe pressure effects to be equal in both shear and entrance flows for HDPE, LDPE, PP, and PMMA. However they were different for PS. Laun (2003) claims that the differences observed between curves obtained with a long capillary and a short orifice are solely due to viscous heating. And that when dissipative heating is accounted for, the same pressure coefficient in shear and in entrance flows is obtained. In this case one would expect Laun's pressure coefficient (11×10^{-9} Pa^{-1}) to be higher than Binding's (16×10^{-9} Pa^{-1}). Thus, the difference must be explained otherwise.

With that in mind, we determined experimental conditions for which viscous heating effects become non-negligible. When pressure drops reach a critical magnitude, dissipative heating needs to be accounted for as it can significantly contribute to the correction of the pressure coefficient β_S. The magnitude of this critical pressure drop depends on the physical characteristics of a given polymer, i.e.

density, specific heat, thermal viscosity coefficient, and pressure coefficient. For PE at 200 °C, this pressure-drop threshold is 170×10^5 Pa, which means that for smaller pressure drops viscous dissipation effects will be negligible.

Under experimental conditions with negligible viscous heating, our results show an exponential increase in the pressure drop across the die with mean pressure for a fixed mean shear rate as long as the flow is stable. However, once a critical wall shear stress is reached flow instabilities are triggered. These need to be taken into account when interpreting experimental results. For unstable flow domains common capillary rheometry relations cannot be used and are no longer appropriate for modeling variations in viscosity with pressure at fixed shear rate. These instabilities occur at lower shear rates as mean pressure increases. Moreover, they may explain the difference in the pressure coefficients reported by Laun (2003, 2004) and Binding and co-workers (1998, 2000).

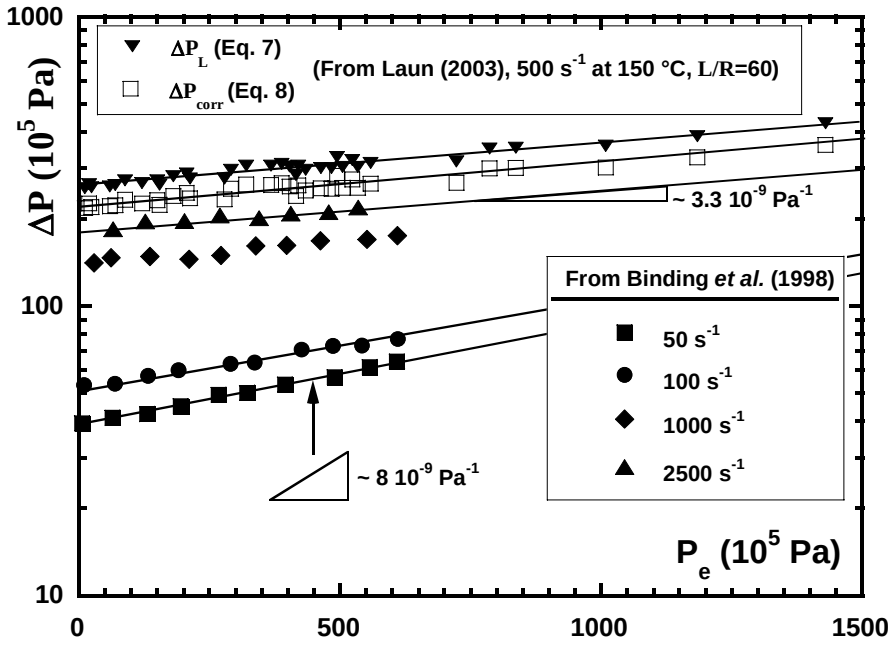

Figure 17: Pressure drop as a function of exit pressure (P_e) in long capillaries with L/R of 60 and 50. Data extracted from Binding et al. (1998) and Laun (2003).

Relevant data from Figure 8 in work by Laun (2003) and from Figure 3 in work by Binding *et al.* (1998) have been reported in Figure 17. Original data from Laun (2003) was not corrected for entrance effects and were obtained at 500 s^{-1} and 150°C. In Figure 17, entrance effects have been accounted for using short orifice data from Laun (2003) and equation (8). The corrected pressure-drops are represented by the hollow squares. Using the temperature-dependence of the viscosity of this branched LDPE given in Couch and Binding (2000), 500 s^{-1} at 150°C is equivalent to an apparent shear rate of 1750 s^{-1} at 200°C, the temperature used by Binding *et al.* (1998). Figure 3 in Binding *et al.* (1998) already presents Couette-Bagley corrected pressure drops. It can be noticed that the slope of the curves decreases with increasing shear rate. Moreover, the curve by Laun and those from Binding *et al.* at 1000 s^{-1} and 2500 s^{-1} have very similar slopes. They are all in highly unstable

regimes. An exponential fit leads to slopes of 3.4, 3.6, and $3x10^{-9}$ Pa^{-1} for the three curves respectively. The slope of these curves corresponds to $\beta_S(\dot{\gamma})$. The power-law index n for these rates, given by Laun and extracted from Figure 6 in Couch and Binding (2000) are respectively 0.33, 0.35, 0.3, which leads to a shear-rate independent pressure coefficient β_S of 10±1.

Let us now consider the curves at 50 s^{-1} and 100 s^{-1}. For all these experimental conditions, the wall shear stress remains below the critical shear stress that will trigger the upstream instability for this product. The slopes are 8.2 and $6.3x10^{-9}$ Pa^{-1} and n is in the order of 0.45 and 0.4 respectively, leading to β_S values of 18.2±2 and 16±2. These are in agreement with the values obtained by time-temperature-pressure superposition for this branched LDPE: $16.5x10^{-9}$ Pa^{-1} (Couch and Binding 2000).

So, this is strong evidence that measurements in stable flow regimes are necessary. Moreover, if macroscopic slip at the wall occurs (e.g. mPE-LCB) in the unstable flow regimes, the increase in pressure drop with mean pressure for a fixed flow rate will be further underestimated. This is clearly observed in Figures 3 and 4, where, for unstable regimes, the average pressure drop across the die remains constant.

For stable regimes, and using time-pressure superposition, pressure coefficients under shear are of the same order of magnitude for all four fluids (~10^{-8} Pa^{-1}) which agrees well with values published elsewhere (Couch and Binding 2000; Goubert *et al.* 2001; Koran and Dealy 1999). β_S orders the pressure-dependence of the 4 PE as: mPE-SCB>mPE-LCB>LLDPE>HDPE. Thus, β_S will increase with the number of ramifications present in the macromolecules, independently of their length.

Using data from orifices or short dies, the time-pressure superposition principle applies and an entrance-flow pressure coefficient, β_E, is obtained. Within experimental uncertainties, these entrance-flow pressure coefficients can be considered equal to those calculated under shear. However, for the mPE-LCB with long ramifications, the pressure-dependence of entrance flows can be significantly lower than in shear flows. β_E is found to be about 30% lower than β_S. Couch and Binding (2000) observed the opposite effect using a HDPE and a branched LDPE. Thus, it would be interesting to obtain microscopic PVT data and microscopic local polymer dynamics data for PS and the various PE considered in order to discuss and explain these findings as well as the results obtained by Couch and Binding (2000) in greater detail. Such work is well beyond the scope of this paper.

Summarizing, we have seen that flow instabilities upstream of the contraction also occur under pressure and thus they have to be taken into account when interpreting experimental results. In unstable flow domains, common capillary rheometry relations cannot be used and are no longer appropriate for modeling variations in viscosity with pressure at fixed shear rate. These instabilities occur at lower shear rates as mean pressure increases. The effects of pressure at fixed shear rate result in an increase in shear stress and thus the critical shear stress that will trigger flow instabilities is reached at lower rates when extruding at mean pressures higher than atmospheric. However, the critical shear stress at which flow instabilities are initiated remains independent of mean pressure. Moreover, the same critical shear stress will trigger flow instabilities under atmospheric exit pressure conditions. This confirms that flow instabilities are caused by the state of macroscopic stress of the fluid, which mimics the mean polymer chain conformation under flow conditions.

1.6 References

Bagley EB (1957) End corrections in the capillary flow of polyethylene. J App Phys 28:624-627.

Binding DM, Couch MA, Walters K. (1998) The pressure dependence of the shear and elongational properties of polymer melts. J Non-Newtonian Fluid Mech 79:137-155.

Choi SY (1968) Determination of melt viscosity as a function of hydrostatic pressure in an extrusion rheometer. J Polym Sci A-2 6:2043-2049.

Couch MA, Binding DM (2000) High-pressure capillary rheometry of polymeric fluids. Polymer, 41:6323-6334.

Denn MM (1981) Pressure drop-flow rate equation for adiabatic capillary flow with a pressure- and temperature-dependent Viscosity. Poly Eng Sci 21:65-68.

Denn, MM (1990) Issues in viscoelastic fluid mechanics. Ann Rev Fluid Mech 22:13-34.

Denn MM (2001) Extrusion instabilities and wall slip. Ann Rev Fluid Mech 33:265-297

El Kissi N, Piau JM (1990) The different capillary flow regimes of entangled polydimethylsiloxane polymers: macroscopic slip at the wall, hysteresis and cork flow. J Non-Newtonian Fluid Mech 37:55-94.

Gabriel C, Münstedt H (1999) Creep recovery behavior of metallocene linear low-density polyethylenes. Rheol Acta 38:393-403.

Goubert A, Vermant J, Moldenaers P, Göttfert A, Ernst B. (2001) Comparison of measurement techniques for evaluating the pressure dependence of viscosity. Appl Rheology 11:26-37.

Hatzikiriakos SG, Dealy JM (1992) Wall slip of molten high density polyethylenes. II. Capillary rheometer studies. J of Rheol 36:703-741.

Hay G, Mackay ME, Awati KM, Park Y (1999) Pressure and temperature effects in slit rheometry. J Rheol 43:1099-1116.

Kadjick SE, van den Brule BHAA (1994) On the pressure dependency of the viscosity of molten Polymers. Polym Eng Sci 34:1535-1546.

Koran F, Dealy JM (1999) A high pressure sliding plate rheometer for polymer melts. J Rheol 43:1279-1290.

Laun HM (1983) Polymer melt rheology with a slit die. Rheol Acta 22:171-185.

Laun, HM (2003) Pressure dependent viscosity and dissipative heating in capillary rheometry of polymer melts. Rheol Acta 42:295-308.

Laun HM (2004) Capillary rheometry for polymer melts revisited. Rheol Acta 43:509-528

Maxwell B, Jung A (1957) Hydrostatic pressure effects on polymer melt viscosity. Modern Plastics 35: 74-180.

Penwell RC, Porter RS, Middleman S (1971) Determination of the pressure coefficient and pressure effects in capillary flow. J Polym Sci A-2 9:731-745.

Piau JM, El Kissi N, Tremblay B (1990) Influence of upstream instabilities and wall slip on melt fracture and sharkskin phenomena during silicones extrusion through orifice dies. J Non-Newtonian Fluid Mech 34:145-180.

Piau JM, El Kissi N; Toussaint F, Mezghani A (1995) Distortions of polymer melt extrudates and their elimination using slippery surfaces. Rheol Acta 34:40-57.

Sedlacek T, Zatloukl M, Filip P, Boldizar A, Saha P (2004) On the effect of pressure on the shear and elongational viscosities of polymer melts. Polym Eng. Sci 44:1328-1337.

Semjonow V (1962) Über ein rotationsviskometer zur messun der druckabhägigkeit der viskositat hochpolmers schmelzen. Rheol Acta 2:138-143.

Van Krevelen DW (1990) Properties of Polymers. 3rd ed. Elsevier

Winter HH (1977) Viscous dissipation in shear flows of molten polymers. Adv Heat Transfer 13:205-267.

CH. 2

Chapitre 2

Defauts d'extrusion des copolymeres a blocs. Fissures primaires transversales en sortie de filiere et fissures secondaires longitudinales. Refente d'extrudat et pelage continu.

[Version abregee]

Les débits d'extrusion pendant la mise en forme des polymères fondus sont souvent limités par les différents défauts susceptibles d'apparaître lorsque que les contraintes dans le fluide sont suffisamment importantes.

La stabilité en écoulement a été le sujet de nombreux articles de revue dont on peut citer, parmi tous les travaux publiés, ceux de [1-4]. Les défauts d'extrusion des thermoplastiques ou des élastomères peuvent être classés en différentes catégories selon leur origine.

Au fur et à mesure que le débit d'extrusion est augmenté à partir de zéro, les régimes successivement observés pendant l'extrusion de polymères enchevêtrés sont les suivants :

- Extrudat lisse, transparent et exempt de défauts.
- Surface de l'extrudat matte et fissurée à la sortie de la filière.
- Ecoulement instable en entrée de la filière résultant du caractère viscoélastique des polymères.

Aux grandes masses molaires, un glissement à la paroi accompagne souvent le déclenchement de l'instabilité viscoélastique en amont. A débit moyen imposé, un « régime oscillant » se déclenche généralement en même temps que l'instabilité viscoélastique en amont.

Une dissection détaillée des ces instabilités en partant d'un polymère au comportement encore non identifié se révèle complexe car différents défauts peuvent se produire simultanément et/ou des confusions peuvent se produire. Seule la combinaison de plusieurs dispositifs expérimentaux donne accès à des preuves concluantes [2].

Ce chapitre porte sur les défauts d'extrusion caractéristiques de deux copolymères blocs dans leur état de séparation micronique. La séparation de phases et l'agencement naturel des copolymères blocs a fait l'objet de nombreux articles de revue et ouvrages [6-8]. Les deux systèmes considérés sont de la famille des SEBS. Ces copolymères sont constitués de trois blocs. Les deux blocs des extrémités sont du polytstyrene (PS) tandis que le bloc du milieu est du poly(ethylène-*co*-butylène). Le premier système (SEBS-1, SEBS-2) présente des domaines cylindriques de PS de quelques nanomètres (~18) de diamètre qui sont agencés de façon hexagonale. Dans le deuxième système (SEBS-3), les domaines de PS sont sphériques, avec un diamètre d'environ 15 nm. Ces domaines de PS sont immergés dans une matrice caoutchoutique de PEB. Il n'y a pas nécessairement d'ordre aux grandes échelles. Les caractéristiques des fluides étudiés sont rapportées sur le Tableau 1 (p. 62).

Après avoir présenté les dispositifs expérimentaux utilisés, nous examinerons le comportement viscoélastique de ces copolymères et les défauts d'extrusion qu'ils présentent. On verra deux systèmes de fissuration apparaître en sortie de filière. Un système de fissures secondaires sera à l'origine du défaut d'extrusion dit de « réfente d'extrudat » rapporté intialement par Fernández *et al.* [13] pour des copolymères statistiques et plus récemment par Zhu [26] pour des PB en étoile. Nos résultats montrent que ce défaut résulte en particulier d'une masse moléculaire « apparente » infinie.

Le comportement viscoélastique des différents SEBS dans le domaine linéaire a été étudié à des températures allant de 95°C jusqu'à 340°C avec un rhéomètre ARES de Rheometric Scientific en mode dynamique. Deux plans concentriques de diamètre 10 mm ou 25 mm ont été utilisés comme outils.
Les essais d'extrusion ont été menés avec un rhéomètre capillaire, le Rheograph 2001 de chez Göttfert fonctionnant à vitesse de piston contrôlée ou et à perte de charge fixée. La perte de charge dans les filières a été mesurée à l'aide de capteurs Dynisco de la classe 0.5 dont le signal était enregistré en fonction du temps. L'extrudat en sortie de filière a été filmé pendant les essais. Les filières utilisées étaient axisymétriques, avec des diamètres intérieurs de 1, 2 et 5 mm. Leurs rapports longueur sur diamètre étaient compris entre 0 et 15. L'écart entre la température d'extrusion affichée par l'interface du rhéomètre et la température de l'extrudat à l'intérieur de la filière était inférieure à 3°C. Ceci a été vérifié en insérant un thermocouple à l'intérieur de la filière remplie de polymère.

Les trois SEBS présentent une réponse viscoélastique dans le domaine linéaire qui est caractéristique des copolymères blocs. Leur module élastique et leur module de perte sont rapportés en Figure 1 pour le SEBS-1 et le SEBS-2 (p. 63) et en Figures 2 et 3 pour les SEBS-3 (p. 64).
Dans leur état avec séparation de phases à l'échelle nanoscopique deux plateaux caractéristiques sont observés. L'un, aux fortes fréquences, qui correspond au plateau caoutchoutique et qui est caractéristique de la matrice de PEB. Aux basses fréquences, un deuxième plateau de niveau de contrainte plus faible est remarqué. Ce plateau est caractéristique des domaines de PS. Le niveau de ce plateau décrit la quantité d'enchevêtrements, la forme des domaines et leur organisation dans l'espace.
Dans le cas du SEBS-3, compte tenu des températures d'observation, un comportement assez complexe est obtenu. On retrouve un comportement caractéristique du régime terminal des homopolymères et la transition ordre-desordre [17-20]. Les essais en régime dynamique, en combinaison avec des essais de calorimétrie différentielle à balayage, ont permis de déterminer les transitions de morphologie.
Pour une même morphologie, l'utilisation de températures adequates, a permis d'étudier toute la gamme des défauts d'extrusion avec des échelles de temps convenables pour l'observation aisée des phénomènes. Pour le SEBS-1 et le SEBS-2 nous avons considéré des températures qui correspondaient à la morphologie cylindrique. Dans le cas du SEBS-3, la morphologie sphérique à été étudiée.
Les courbes d'écoulement obtenues à partir des essais de rhéométrie capillaire sont présentées en Figures 5-7 (p. 68 et p. 70). Leur allure ne diffère pas de la courbe généralement obtenue pour des polymères fortement enchevêtrés.

La séquence d'images de l'extrudat en sortie de filière présentée en Figure 9 (p. 72-73) montre l'évolution des défauts susceptibles d'apparaître lors de l'extrusion du SEBS-2. Ces défauts sont comparables à ceux observés avec le SEBS-1.
Pour des débits suffisamment faibles, l'extrudat est lisse et transparent en sortie de filière.

Lorsque le débit augmente des fractures transversales apparaissent au voisinage de la sortie de la filière. Ces fractures primaires sont peu nombreuses au début, cependant, vu leur profondeur, elles peuvent distordre fortement l'aspect visuel de l'extrudat. On note leur forme caractéristique, en forme de V. De plus, et à la différence des fractures couramment observées avec des homopolymères, ces fissures primaires continuent à se propager dans l'extrudat y compris quand elles sont complètement à l'extérieur, et loin, de la sortie de la filière. Le nombre de ces fissures primaires, et leur vitesse de propagation augmente avec le débit. Eventuellement la vitesse de propagation des fissures est suffisamment rapide et elles font le tour complet de la sortie de la filière, formant ainsi une série d'anneaux successifs de polymère qui sont transportés par un noyau central. En augmentant le débit, les anneaux de polymère gonflent avant de se détacher. Le gonflement, et la déformation qu'il entraîne, génère des contraintes dans le polymère. Quand ces contraintes dépassent un seuil critique, un système de fissures secondaires, qui se propagent longitudinalement, est généré. Si les contraintes dans un anneau sont suffisamment importantes, plusieurs fissures secondaires peuvent se propager en même temps. Ces fissures secondaires multiples sont à l'origine du défaut d'extrusion dit de « refente d'extrudat ». En augmentant le débit, la refente de l'extrudat sera alors observée jusqu'au déclenchement des régimes oscillatoires. L'apparition des régimes oscillatoires coïncide avec le déclenchement de l'instabilité viscoélastique en amont. Si le débit est encore augmenté, les oscillations de pression cessent et un glissement macroscopique permanent à la paroi s'installe.
Le SEBS-3 ne présente pas le défaut dit de « refente d'extrudat ». La séquence des défauts d'extrusion pour le SEBS-3 est présentée en Figure 10 (p. 78).

Les copolymères étudiés ont des temps de relaxation longs. Ceci a permis pour la première fois de calculer la vitesse de propagation des fissures en sortie de la filière à partir des images enregistrées. Pour les fissures primaires, la Figure 13 (p. 82) montre l'évolution de la vitesse de propagation de la fissure, normalisée par la vitesse moyenne de l'écoulement à l'intérieur de la filière, en fonction du temps qui a été normalisé par un temps caractéristique du fluide, τ_p. Sur cette figure, on notera que la durée de vie d'une fissure primaire est divisée en quatre phases. La première phase correspond à la naissance. La deuxième et la troisième correspondent à la propagation de la fissure qui se fait à deux vitesses distinctes. Notons aussi que les durées de ces deux phases sont de l'ordre du temps caractéristique du fluide. Finalement, la quatrième phase correspond au transport de la fissure une fois qu'elle est complètement ouverte.
Des mesures de la vitesse de propagation des fissures secondaires on montré que sa dépendance en la vitesse moyenne d'écoulement dans la filière n'est pas la même que pour les fissures primaires au même niveau de contrainte. Ainsi, aux vitesses d'écoulement « faibles », les fissures secondaires se propagent plus rapidement que les fissures primaires. De cette façon, les différentes fissures secondaires qui se produisent sur un même anneau de polymère peuvent se joindre au centre de l'extrudat et le refendre. Aux « fortes » vitesses d'écoulement, ce sont les fissures primaires qui se propagent le plus rapidement. Cette différence de vitesse de propagation déclenche un nouveau régime d'extrusion : le pelage continu.

D'après les résultats en rhéométrie dynamique et en rhéométrie capillaire, et vu les caractéristiques des produits utilisés par [13] et [26] (voir Tableau 3, p. 89) on peut faire l'hypothèse qu'une masse moléculaire quasi infinie est une condition nécessaire pour avoir ce système de fissures secondaires. Cette hypothèse a été testée en extrudant un polybutadiène linéaire et monodiperse de grands poids-moléculaire (M_w=600000 g/mol) à température ambiante. Comme les photos présentées en Figure 19 (p. 90) le montrent, le système secondaire de fissuration existe aussi pour ce PB. Ceci nous permet de vérifier notre hypothèse d'une masse moléculaire apparente infinie.

CHAPTER 2

BLOCK COPOLYMER EXTRUSION DISTORTIONS. EXIT DELAYED TRANSVERSAL PRIMARY CRACKS AND LONGITUDINAL SECONDARY CRACKS. EXTRUDATE SPLITTING AND CONTINUOUS PEELING.

E. SANTANACH CARRERAS, N. EL KISSI, J-M. PIAU(✉)
Laboratoire de Rhéologie[**], B.P. 53, Domaine Universitaire, 38041 Grenoble cedex 9 (France)

Key words: *block copolymers, extrusion flow distortions, splitting, continuous peeling, cracking, structure*

This chapter is an article currently in press at the Journal of Non-Newtonian Fluid Mechanics.

✉ Author to whom all correspondence should be addressed. Electronic mail: jmpiau@ujf-grenoble.fr
** *Université Joseph Fourier-Grenoble I, Institut National Polytechnique de Grenoble, CNRS (UMR 5520*)

Abstract:

In the present work, we examine the different flow distortions that are prone to occur during the extrusion of microphase-separated block copolymer melts showing hexagonally packed cylindrical domains and spherical domains. The same successive distortions which appear for homopolymers were observed. Special attention is paid to the initiation of surface cracking, which can be severe enough for the extrudate to split at the die exit. Three SEBS in their microphase-separated state were extruded at several temperatures using a capillary rheometer. Pressure drops were recorded as a function of time, and the melt coming out of the die was filmed.

Dynamic rheometry experiments in the linear response region at different temperatures in conjunction with DSC revealed the different morphology transitions for the SEBS at hand. These were checked using SAXS. The results show that the Cox-Merx rule fails at frequencies below $1/\tau_p$, which represents a percolation time of the system. Extrusion of the SEBS forming hexagonally-packed cylinders of PS in a rubbery matrix showed flow split beyond a critical shear stress. In the case of the SEBS forming spherical PS microphases, no flow split was observed. Films of the melt exiting the die enabled the successive defects to be observed. Moreover, due to the slow relaxation times of block copolymers, initiation and propagation of surface cracks at the die exit were recorded and quantified. A secondary system of cracks that occur on the surfaces created by primary cracks transversal to the extrusion direction was also observed. In the case of high enough shear stresses, multiple secondary cracks occur simultaneously, leading to flow split. It was observed that at "low" mean velocities secondary cracks merge in the center of the core and *flow split* occurs in several branches. In the case of "high" mean velocities, primary cracks propagate faster than secondary cracks and a central, defect-free, polymer rod is observed at the center of the branches, resembling a *continuous peeling*.

To see if an "apparent" infinite molecular weight is responsible for this system of secondary cracks, a highly-entangled linear (M_w/M_e~400) PB was extruded. Secondary cracks were indeed also observed.

2.1 Introduction

Throughput rates during polymer processing operations, and extrusion in particular, are often limited by defects that are prone to occur when stresses in the fluid are sufficiently high.

Flow stability during extrusion and extrusion defects have already been the subject of many papers, which are too numerous to list. Several reviews on the subject have also been published, the most recent ones being references [1-4]. Extrusion defects in the case of elastomeric or thermoplastic homopolymers can be divided into several categories depending on their origin. It is useful to recall them, given the topic of the present paper.

The main trends can be summarized and examined successively, following the order in which they appear as flow rate is increased. A first type, extrudate surface cracking (also unphysically called sharkskin) is due to stress concentrations occurring at the die exit. The crack lips are oriented more or less perpendicular to the flow direction. No discontinuity in the flow curve is observed when extrudate surface cracking is initiated [2]. A second type, upstream instability (also unphysically called melt fracture), is of viscoelastic origin and is triggered at the die entrance. The appearance of upstream instability is observed by a distinct change in slope of the flow curve, which is stronger for short dies than for long ones, together with flow field instabilities upstream of the die, and extrudate shape distortions downstream.

In addition, highly entangled polymers show slip at the wall. Pressure controlled conditions lead to spurting whereas oscillating flows result from the combination of slip and compressibility during mean rate of flow controlled experiments [2]. These different instabilities are not mutually exclusive and they may or may not occur simultaneously. In addition, some other extrusion instability mechanisms have also been reported on in [5]. Detailed dissection of these instabilities is a complex task indeed, and safe conclusions are easier to reach when several techniques can be combined on the same experimental set-up [2].

When extruding other materials such as ceramics or metals, additional instability mechanisms appear. Reviews such as [1-4] do not pretend to cover all extrusion instabilities, even within the field of polymeric materials. The question of possible instabilities during the extrusion of polymeric materials at large is still an open problem, even if some reasonable answers can be expected.

The goal of the present paper is to study copolymer extrusion instabilities. Given the complexity of such materials, only one particular triblock copolymer system, which is of interest on account of their commercial application, will be studied. Parallels and differences with homopolymers will be carefully examined for two basic SEBS {polystyrene-*block*-poly(ethylene-*co*-butylene)-*block*-polystyrene } structures:

Hexagonally-packed cylindrical (HPC) Polystyrene (PS) sub-micronic domains in a rubbery PEB matrix.

Spherical (S) PS sub-micronic domains in the rubbery PEB matrix.

Microphase separation and self-ordering shown by block copolymers has been the subject of study for many years. Numerous review articles [6,7] as well as entire books [8] have been devoted to the different morphologies presented by these materials. Block copolymers are formed from segments of

chemically distinct covalently bonded polymers that would be immiscible otherwise. This chemical incompatibility leads to phase separation of the different components in the copolymer at a sub-micronic scale, historically called “microphase separation”. The size and spatial organization of the sub-micronic domain can be homogeneous inside relatively large grains, with characteristic length scales of the order of 100 µm.

Hence the material in hand is, in simple terms, composed of very small PS microphases in a sea of melted elastomer. Under particular conditions, these PS microphases may be organized within grains (possibly with a local mechanical re-enforcing capacity) separated by grain joints.

It can be expected, and needs to be checked, that the elastomer continuum itself may show the full range of flow distortions typical of homopolymers. Several authors [9-12] have studied the flow distortions presented by elastomers and showed that they can be quite severe. A central aspect is to examine the influence, if any, that re-enforced domains may have on distortions.

Fernández *et al.* [13] reported that three copolymers of ethane and propylene split into two branches at the die exit in the case of shear stresses higher than $3x10^5$ Pa when extruded through a capillary. Splitting was described in [13] as a new instability. However, little detail is available on the materials studied, on their flow distortions in general, or on the splitting phenomena.

In Section 2, important details will be given on the rheometers, extrusion systems and physico-chemistry equipment used to make the necessary measurements. A structural description of the two very similar SEBS showing HPC and the SEBS showing S morphology follows. Our results are compared to those already published by other groups, when applicable.

The flow curves obtained and linear viscoelastic properties measured will be described in section 3 and compared to those published elsewhere [14,15]. Our results agree with and extend those published in [14,15] for the same commercial SEBS.

Based on the flow curves, the range of flow distortions observed will be detailed in section 4 and will be put in perspective with relation, and in addition, to existing results for homopolymers. Particular attention will be paid to the appearance of extrudate splitting and of continuous peeling extrusion, a new regime which is discovered.

The rate of propagation of surface cracks will be examined in Section 5. This section will highlight the fact that the distortions are indeed similar to the extrusion distortions obtained for homopolymers. In particular, the case of a linear highly-entangled polybutadiene (PB) will be used for comparison. It will be shown that PB fractures at the die exit show delayed crack tip propagation. In addition, a new exit longitudinal secondary crack system may also appear with PB at the die exit. Its relation to the copolymer hexagonally-packed cylindrical structure will be discussed.

Finally, it will be concluded, in Section 6, that it is these primary and secondary cracks in combination which generate SEBS extrudate splitting and continuous peeling regimes.

2.2 Experiment

2.2.1 Rheometry

In the linear response domain, dynamic viscoelastic functions (G' and G") as a function of frequency were obtained using an ARES rheometer from Rheometric Scientific for temperatures as low as 95 °C and as high as 340 °C. Parallel plate tooling of 10 mm and 25 mm diameter were used. The range of frequencies covered was 10^{-2} – 10^{2} s^{-1}. Experiments at temperatures higher than 215 °C were performed under nitrogen purge to avoid thermal degradation.

Samples were prepared by initially compressing the SEBS in its solid state and then melting it in a mould. The procedure was as follows: the mold was filled with SEBS and closed as tight as possible at room temperature. The mold was then placed in an oven for approximately 45 minutes and the copolymer was allowed to melt and flow within the mold cavity. Sheets between 1 and 2 mm thick were obtained, from which disk-shaped samples were cut and used for dynamic rheometry experiments. This sample preparation method produced macroscopically isotropic samples as shown in SAXS experiments that will be detailed in a forthcoming paper.

No pre-shearing of the samples was performed before the isothermal frequency sweep tests, thus the storage (G') and loss (G") moduli measured are characteristic bulk properties of a randomly oriented sample.

A Göttfert Rheograph 2000 was used for the capillary rheometry experiments. Both fixed piston speed and fixed pressure drop experiments were performed, allowing a flow curve spanning over 5 decades to be plotted. Fixed pressure drop experiments were used to obtain data at mean flow rates lower than 5.65×10^{-11} m^3 s^{-1}, attainable at the lowest piston speed. During the fixed pressure drop experiments, a small floating PTFE piston was placed between the molten copolymer and the nitrogen gas used to force it through the die. This piston ensured that the pushing force was applied uniformly over the entire cross-section of the melt. The pressure was fixed with a valve and read on a manometer. In addition, the output voltage of a class 0.5 Dynisco PT420 pressure transducer, placed near the capillary entrance, was traced as a function of time by means of a recorder. Two pressure transducers were used, depending on the pressure drops measured: one was rated at 100×10^{5} Pa and the other at 500×10^{5} Pa.

The dies used had diameters of 1, 2 and 5 mm. Capillaries with length-to-diameter (L/D) ratios of 15, 10 and 5 were used to keep dissipative heating low yet allowing characterization in shear. In addition, short orifice dies of negligible length were used to correct for entrance effects, unless indicated otherwise.

In addition, before the experimental runs, the temperature of the melt was registered along the entire die axis and probed after inserting a thermocouple inside the capillary filled with polymer. The temperature was measured while the thermocouple and some polymer were extruded simultaneously. Thanks to the use of a controlled pulsed air heating system blowing at the die exit, temperatures were found to be within 3°C of the nominal temperature at the beginning of the experimental runs.

During the experimental runs, the melt coming out of the die was filmed with a Sony IRIS-CCD high-resolution video camera that was connected to a Wild M-540 macroscope.

2.2.2 Materials

Three linear SEBS triblock copolymers were used for this study. One of them was kindly supplied by Polimeri Europa SpA whereas the other two came from Kraton® Polymers. Table 1 summarizes the principal characteristics of the fluids used. It was with SEBS-1 that flow split was initially observed. SEBS-2 and SEBS-3 were chosen because they present typical structures. Moreover, their behavior has already been studied elsewhere [14, 15].

	Material	Producer	PS weight content (%)	M_w* (g/mol)	M_w/Mn *	$T_{g,PS}$ (°C)	$T_{g,PEB}$ (°C)	Morphology		
								T_{room}	OOT	ODT
SEBS-1	SEBS 30%PS	Polimeri Europa SpA	~30	44400	1.09	100	-40	HPC	~280 °C	N/R‡
SEBS-2	G-1650	Kraton® Polymers	30	*75000*[14]	*1.12*[14]	*96*[14]	-42**	HPC	~280 °C	N/R‡
SEBS-3	G-1657	Kraton® Polymers	13	37600 *70000*[14]	1.10 *1.05*[14]	*75*[14]	-42**	S	-	140 °C

* Values obtained with LALS measurements

** Values obtained from manufacturer

‡ N/R stands for "Not Reached" before thermal degradation of the copolymer

Table 1: Principal characteristics of the ABA triblock copolymers used in this study.

Molecular weights were determined at room temperature in tetrahydrofuran with a classical SEC apparatus coupled to a multiangle light-scattering device. PS standards were used. The M_w and M_w/M_n values reported come from the multiangle light-scattering device. The table also lists M_w values obtained from existing literature [14] where neither the solvent nor the standards used are indicated. These are about twice as much as those found in our measurement, but relative to each other, the values are consistent within the same technique. Thus, these values should not be used from an absolute point of view, but rather from a relative one. In the case of all three SEBS, the M_w of the PEB block is highly entangled since its molecular weight for entanglement, M_e, is between 3000 and 3400 g/mol at the temperatures covered [16]. On the other hand, the molecular weight of the end PS blocks is slightly below the M_e of 13000 g/mol [16] and thus they are not expected to be entangled.

SEBS-1 and SEBS-2 form hexagonally-packed cylinders (HPC) of PS inside the rubbery PEB matrix at room temperature. This has been confirmed with SAXS experiments for SEBS-1 and by SANS experiments in the case of SEBS-2 [14]. SEBS-3, which contains 13% PS, forms spherical (S) PS microphases under room temperature conditions. For this grade of SEBS in particular, Daniel and Hamley [14] report that the PS spherical microphases are organized in a BCC lattice. However, other studies have shown that for copolymers with less that 20% in end-blocks, a polydisperse population of more microphases with no long range order can be expected [8].

Using differential scanning calorimetry, the order-order transition temperature between cylindrical and spherical microdomains for SEBS-1 has been determined to be 280°C. As can be seen in Table 1 as well as in Figure 1, SEBS-2 is nearly identical to SEBS-1, and thus its transition temperatures must be similar to those of SEBS-1.

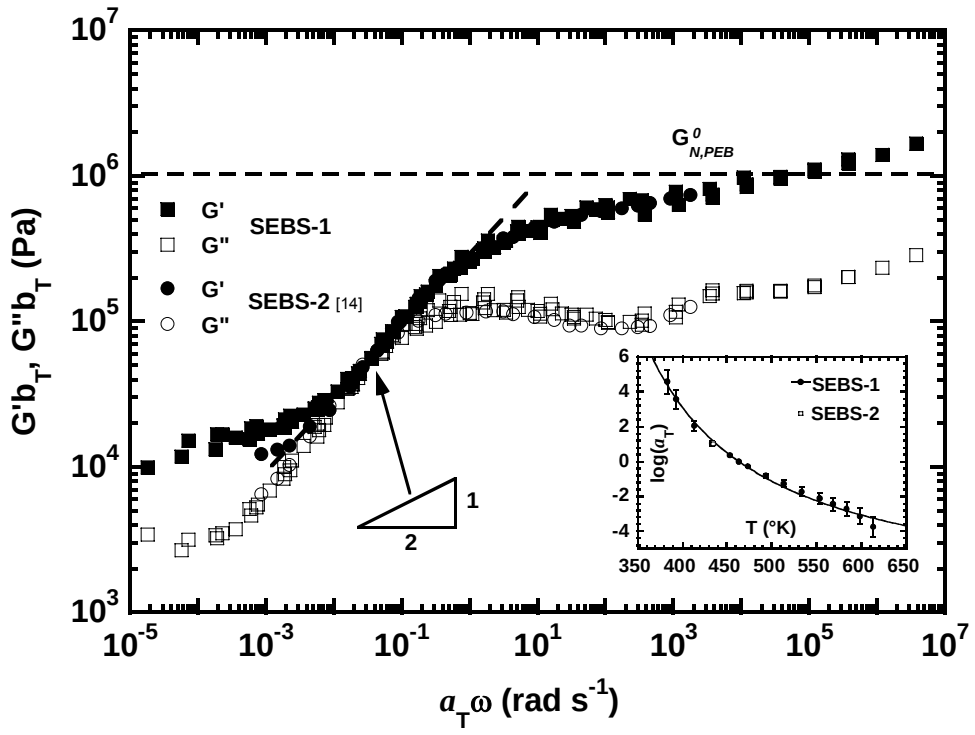

Figure 1: Reduced storage modulus ($G'b_T$) and reduced loss modulus ($G"b_T$) as a function of reduced frequency ($a_T\omega$) for SEBS-1 and SEBS-2 with cylindrical PS microphases using 190°C as reference temperature.

In the case of SEBS-3, superposition of isothermal small-strain oscillatory shear frequency sweeps revealed the order-disorder transition [17-20]. It starts in the temperature range 135-140°C. This temperature is in excellent agreement with the one reported by Daniel and Hamley [14] for this same grade of SEBS. They found that time-temperature superposition did not hold for curves obtained at temperatures higher than 140°C. Figure 2 and Figure 3 show the change in behavior between microphase-separated copolymer and the disordered state. For clarity, master curves for the storage modulus (G') and for the loss modulus (G") have been represented in different plots.

The time-temperature superposition (TTS) principle was applied to all master curves, as described in [21]. A vertical shift factor b_T equal to T_{ref}/T was applied. Changes in density were neglected. The inset in the different figures shows the empirical shift factor, a_T, used to reduce shear rates. The solid line represents a fit using the WLF-equation. The fit parameters C_1 and C_2 used for each fluid are presented in Table 2.

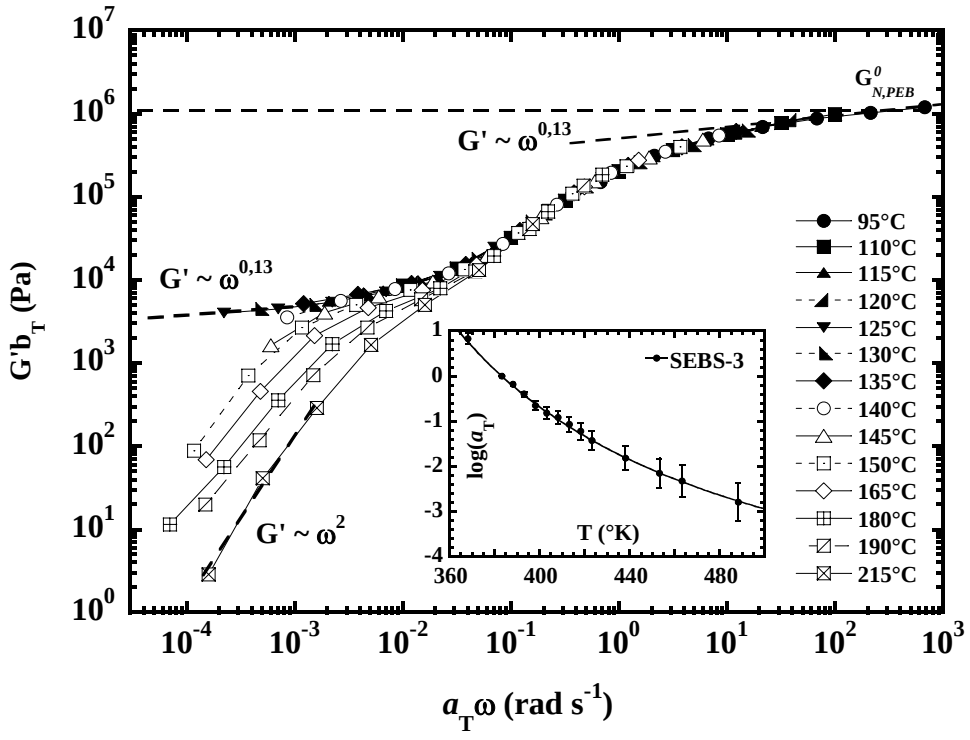

Figure 2: Reduced storage modulus ($G'b_T$) as a function of reduced frequency ($a_T\omega$) for SEBS-3 using 110°C as reference temperature.

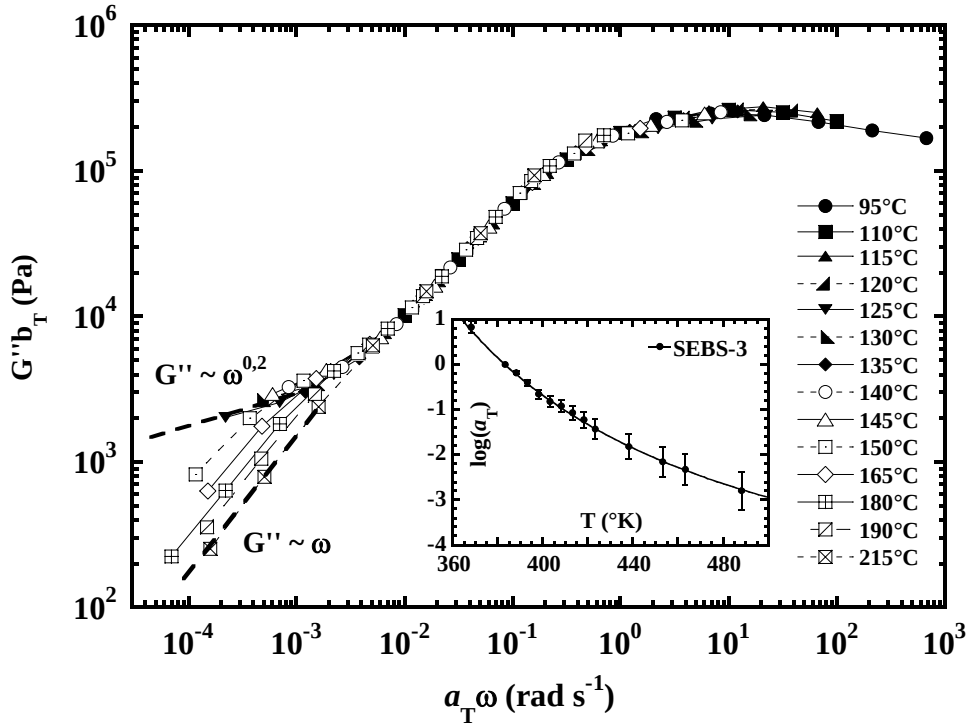

Figure 3: Reduced loss modulus ($G''b_T$) as a function of reduced frequency ($a_T\omega$) for SEBS-3 using 110°C as reference temperature.

	SEBS-1 (T_{ref} = 190°C)	SEBS-2 (T_{ref} = 190°C)	SEBS-3 (T_{ref} = 90°C)
C_1	8.2	7.1	9.4
C_2 (°K)	230.4	229.4	198.9
WLF-equation: $\log(a_T) = \frac{-C_1(T - T_{ref})}{C_2 + T - T_{ref}}$			

Table 2: WLF equation parameters used to fit the shift factor, a_T, for the three SEBS studied.

Notice that for both the cylindrical and spherical domains the curves are qualitatively similar and can be divided into three different regions. At high frequencies the storage modulus increases roughly as $\sim\omega^{0,1}$. This portion corresponds to the entanglement plateau , G_N^0, that is related to the density, ρ, the absolute temperature, T, the universal gas constant, R, and to M_e by $G_N^0 \sim \frac{\rho RT}{M_e}$. The value of the entanglement plateau, calculated using data for PEB only as it is the main component, is shown by the dashed horizontal lines in Figure 1 and in Figure 2. The molecular weight between the entanglements used is 3400 g/mol for PEB [16]. A ρ of 800 kg m^{-3} and a temperature of 463.2 °K were also used. The resulting value of G_N^0 is of the order of 10^6 Pa, which is slightly lower than the G' values measured at the highest frequencies studied. Moreover this value is of the same order of magnitude as the values reported in the literature for polybutadiene (PB) homopolymers [22]. As one moves towards lower frequencies, G' becomes tangent and superposes with G" and both moduli decrease as $\sim\omega^{0.5}$ for SEBS-1 and SEBS-2. This slope is characteristic of a system at its gelation threshold [23]. In the case of SEBS-3 in its microphase-separated state, it is important to notice that G' and G" cross over twice in the range of frequencies covered, with G" overtaking G' in the range of frequencies 0.007-0.7 s^{-1}. Hence, SEBS-3 represents a system in which percolation has not yet been reached.

As frequency is further decreased, the storage modulus evolves again roughly as $\sim\omega^{0,1}$. Similar behavior is observed in elastic gels and in polymer blends. In the case of perfect crystals, i.e. PS glassy microphases assembled with long-range order in a cubic lattice, one would expect to find a perfect elastic solid behavior [19] and thus a storage modulus independent of frequency. In our case, the PS microphases do not extend over the entire sample on a single lattice. Moreover, in the case of SEBS-1, though experiments at temperatures higher than the cylinder-to-sphere transition were carried out, they were sufficiently rapid to prevent a long-range order from being established in the spherical domains. From the superposition of the curves, the response obtained still seems characteristic of the hexagonally-packed morphology.

With all three SEBS, the copolymer presents the characteristic behavior of the PEB matrix at high frequencies. This matrix is highly entangled via mobile interchain elastomeric links, and by the PS microphases. The latter have an effect similar to that of a curing agent, increasing the apparent molecular weight of the elastomer. At low frequencies, or long times, below 10^{-1} rad s^{-1}, PS domains become more mobile and their influence on the shape of the curves becomes increasingly important. Using elongational flow optical rheometry, Kotaka *et al.* [24] showed that at extension strain rates of the order of 1 s^{-1}, only the PEB matrix of a SEBSEB was deformed and the spherical domains

remained unchanged. When the strain rate was reduced to 10^{-2} s^{-1}, the spherical domains transformed into cylinders aligned in the flow direction.

The frequencies covered in this study are not low enough to observe terminal region behavior for these microphase-separated block copolymers. The master curves presented in Figure 1, Figure 2, and Figure 3 were successfully modeled from the combination of two independent box-type relaxation spectrums. In the case of the modeled curves, the crossover point below which viscous behavior will be observed is expected to neighbor 10^{-6} s^{-1} (SEBS-1 and SEBS-2) and $4x10^{-5}$ s^{-1} (SEBS-3) at the reference temperatures used. Experiments at such low rates are practically impossible to perform (with respect to time, thermal degradation problems, etc.) at one fixed temperature. In order to attain such low rates, the use of the TTS principle is necessary. However, the experimental temperature window available for experiments is limited because of the temperature-dependence of morphology. In homogeneous polymeric materials the different components display a different temperature-dependent rheometry so that time-temperature superposition does not hold.

The extrusion temperatures considered in this study correspond in all cases to microphase-separated morphologies. Capillary rheometry experiments at 190°C were performed for SEBS-1. SEBS-2 was extruded at 170, 190, 210, and 230°C; all in the HPC morphology. SEBS-3 was extruded at 90°C in its microphase-separated state.

2.3 Flow curves

2.3.1 SEBS-2

Figure 4 presents a master curve of pressure drops measured across capillaries with L/D of 10/2, and 0/2 as a function of apparent shear rate for temperatures of 170, 190, 210, and 230 °C. For clarity, data obtained with other dies are presented in the form of shear stress in Figure 5. The time-temperature superposition principle has been applied as described in [21] using 190°C as the reference temperature. Again, a vertical shift factor, b_T, equal to T_{ref}/T was used. Changes in density due to temperature have been neglected. The inset shows the empirical shift factors, a_T, used to reduce the shear rates. Pressure drops for a short orifice die of negligible length are also presented for a temperature of 190°C. In this temperature range, SEBS-2 has a hexagonally-packed arrangement of PS cylinders in a rubbery PEB matrix. The apparent shear rate, $\dot{\gamma}_{app}$, is calculated as a function of the mean volumetric flow rate, Q, and the diameter of the die, D, by

$$\dot{\gamma}_{app} = \frac{32Q}{\pi D^3} \qquad (1)$$

In all four curves obtained with the 10/2 capillary, it can be seen that the measured pressure drop across the die increases initially with apparent shear rate until it reaches a value of about $92.5x10^5$ Pa. This pressure drop corresponds to a shear stress at the wall of $3.3x10^5$ Pa once entrance effects have been taken into account. This value is not far from the critical one reported in the literature of $3x10^5$ Pa that will trigger the upstream instability for PB [9,11]. At this point a change in slope is observed.

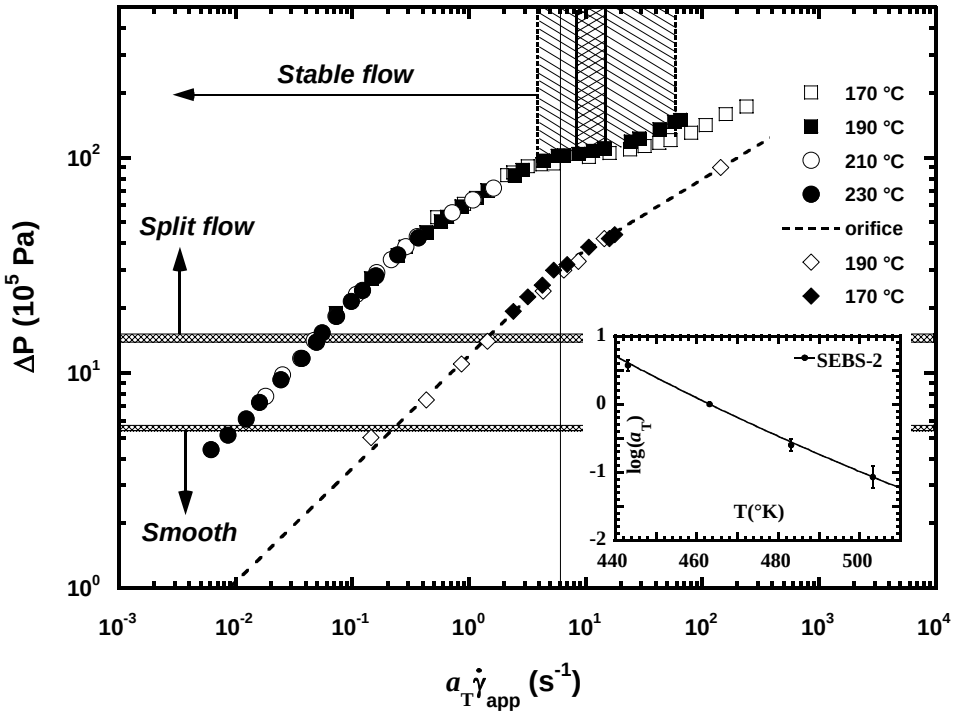

Figure 4: Pressure drop across a capillary with L/D *of 10/2 and a short orifice die of negligible length as a function or reduced apparent shear rate ($a_T \dot{\gamma}_{app}$) using 190°C as reference temperature with SEBS-2.*

Roughly, the slope of the curve for stable flows is 0.57 on average, whereas after the change in slope, it falls to roughly 0.09. Soon after this change in slope, oscillating flow, in the form of regular pressure fluctuations of 5x10^4 Pa in amplitude, was observed for experiments at 170°C and 190°C. At this point, the graph no longer represents $\Delta P(Q)$, but rather $\overline{\Delta P}(\overline{Q})$ where $\overline{Q}$ indicates an arithmetic mean rate of flow and $\overline{\Delta P}$ is an unclear mean value that depends on the equipment used to measure the pressure drop [3]. The range of apparent shear rates showing oscillating flows is represented on the graph by the cross-hatched regions. At 170°C, oscillating flow was observed for the apparent shear rate range of 1.44-11.5 s^{-1} inclusive. If a reference temperature of 190°C were used, the equivalent reduced apparent shear rate range would be 4.2-54 s^{-1}. However, during experiments at 190°C, oscillating flow was only observed for the range 8.6-14.4 s^{-1}.

In the case of even greater apparent shear rates, pressure oscillations stop and the pressure drop again increases [2]. An average slope of the curve is estimated at about 0.33; this is an intermediate value if compared to those found for stable flow regimes and in oscillating flows. High shear rate conditions are not the focus of this paper; therefore this region of the flow curve will not be explored any further. However, it seems that the flow curve obtained with SEBS-2 does not differ much from the general case flow curve for moderate to highly-entangled polymer melts reported in the literature [1,2].

Flow split at the capillary exit was observed to appear at pressure drops that can be considered equal within the transducer accuracy for both 210°C (14.2x10^5 Pa) and 230°C (13.9x10^5 Pa). Thus, the use

of time-temperature superposition to describe the development of extrusion defects seems justified, the more so since it works correctly for G', G" diagrams for the same range of ω.

The curve corresponding to a short orifice die of 2 mm diameter and negligible length is shown on the same plot. The characteristic change in slope corresponding to the appearance of the viscoelastic upstream instability can be seen to occur at the same shear rate for which long dies show oscillating flow. Data for short orifice dies are used to correct for entrance effects [25] and to calculate the shear stress at the capillary wall by

$$\tau_w(Q) = \frac{(\Delta P_L(Q) - \Delta P_o(Q))}{4L/D} \qquad (2)$$

where $\Delta P_L(Q)$ and $\Delta P_o(Q)$ are respectively the pressured drops measured across the long capillary and the short orifice die for the same flow rate.

Average wall shear stress plotted as a function of reduced apparent shear rate is presented in Figure 5 together with the complex modulus G* from [14]. The inset shows the shift factors used for superposition of the curves at different temperatures. Notice that superposition between τ_w and G* only occurs for the higher end of the apparent shear rates corresponding to stable flows within the die (without or in the presence of cracks) with the exception of low frequency-low rate of flow regimes. At rates lower than approximately 0.015 s^{-1}, PS domains are solicited and the bulk can no longer be considered as homogenous. The difference in deformation amplitude in the capillary ($\gamma \geq 40$) and during oscillatory shear experiments ($\gamma \leq 0.05$) may explain the different behavior. The solid horizontal line shows the critical shear stress, $\tau_{w,UI}$ beyond which the viscoelastic upstream instability is triggered for PB [9,11] (~$3x10^5$ Pa); this is of the same order of magnitude as the critical wall shear stress determined for SEBS-2.

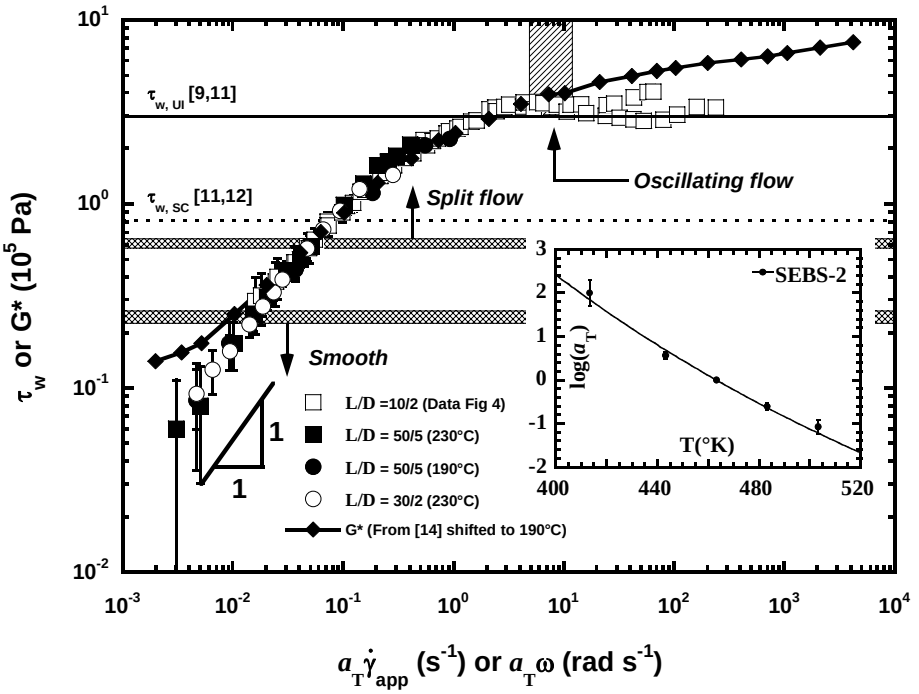

Figure 5: Wall shear stress (τ_w) and reduced complex modulus (G) from [14] as a function of reduced apparent shear rate ($a_T\dot{\gamma}_{app}$) for SEBS-2 using 190°C as reference temperature.*

During extrusion of SEBS-2, initial signs of surface cracking and flow split were observed visually at wall shear stresses of 0.21 and $0.6x10^5$ Pa respectively. These critical shear stresses are lower than that of $0.8x10^5$ Pa reported for surface cracking of PB in the literature [11,12] and represented by the dotted line labeled $\tau_{w,SC}$ in Figure 5.

It is known that visual observation of crack initiation is not objective, as it depends on the method (at the die exit or on relaxed samples) and the equipment used (naked eye, zoom, microscope). Nevertheless, crack initiation and propagation are clearly modified in these materials. Two factors need to be considered: these materials are formed by multiple grains and the PS microphases may give them infinite apparent molecular weight as they play a role similar to that of cross-links.

To observe the formation and birth of flow split at the capillary exit, the melt exiting the die was filmed with a camera using a macroscope as the lens. The development of the different defects observed is discussed in section 4 entitled “Flow visualization at the die exit”.

Notice that the curves obtained with different diameters superpose, thus indicating that no macroscopic slip occurs at the die wall in the case of stable flows.

2.3.2 Other SEBS

Figure 6 and Figure 7 present wall shear stress for SEBS-1 and SEBS-3 together with the complex modulus G* as a function of apparent shear rate, reduced to 190°C and 90°C respectively. Data for SEBS-1 were obtained with capillaries having a L/D ratio of 10 and diameters of 1 and 2 mm. Short orifices of these same diameters were used to correct for entrance effects. Again, as for SEBS-2, superposition of G* and τ_w does not hold at low shear rates. SEBS-3 was extruded through a 50 mm long capillary, 5 mm in diameter. A short orifice die of negligible length and diameter 5 mm allowed correcting for entrance effects. In the case of SEBS-1 and SEBS-3, surface cracking was first observed at shear stresses of 0.2 and $0.3x10^5$ respectively. However, differences in crack propagation and shape were observed. They will be discussed in section 4. SEBS-1 also showed flow split, which was observed in the case of shear stresses above $0.5x10^5$ Pa. SEBS-3 did not show flow split.

Just as in the case of SEBS-2, the viscoelastic upstream instability during the flow of SEBS-1 and SEBS-3 occurs at shear stress levels similar to the one reported in the literature for PB of $3x10^5$ Pa [9,11,12], again indicating that at high shear rates, the PS domains merely flow and that the block copolymer’s behavior is characteristic of its matrix constituent.

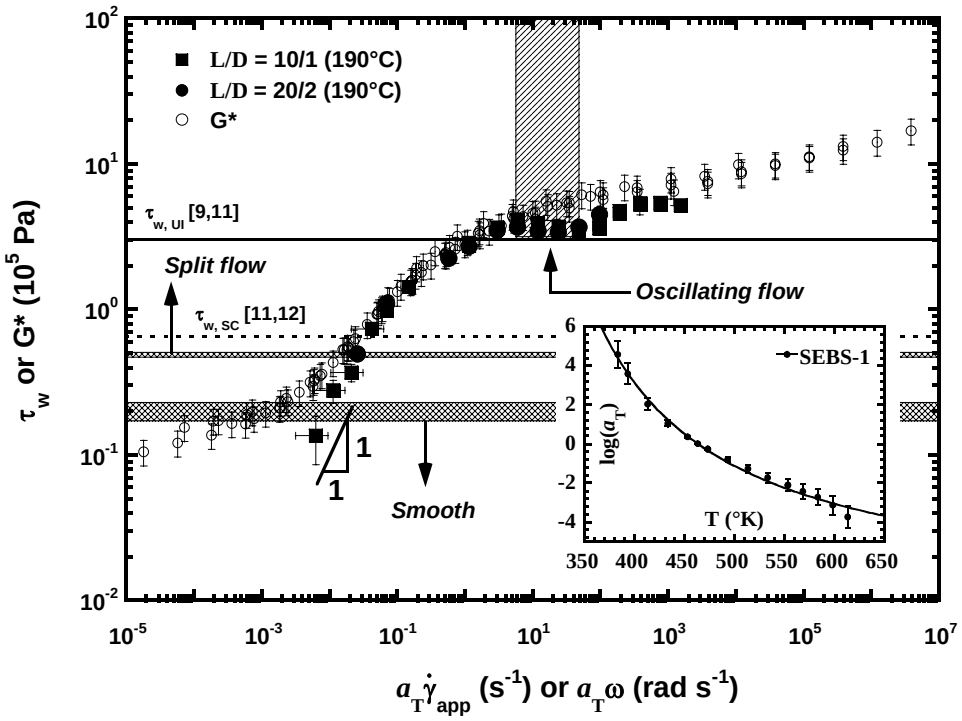

Figure 6: Wall shear stress (τ_w) and reduced complex modulus (G) as a function of reduced apparent shear rate ($a_T\dot{\gamma}_{app}$) for SEBS-1 using 190°C as reference temperature.*

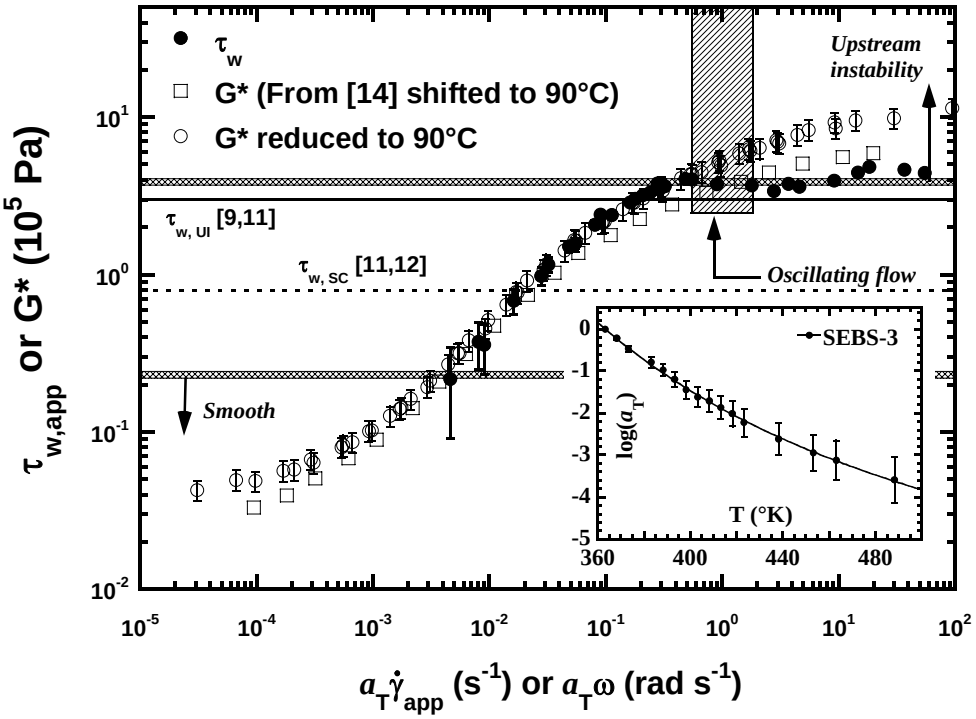

Figure 7: Wall shear stress (τ_w), and reduced complex modulus (G) as a function of reduced apparent shear rate ($a_T\dot{\gamma}_{app}$) for SEBS-3 using 90°C as reference temperature.*

2.4 Flow visualization at the die exit

2.4.1 SEBS-2

As stated in the previous subsection, the development of the defects observed during the extrusion of SEBS-2 will be described with curves obtained at different temperatures and with dies of different diameters in order to cover a larger range of shear rates. All frames have been extracted from experiments using a capillary with L/D ratios of 10/2 and 50/5. Figure 8 shows the nomenclature used to describe the different cases of surface cracking observed during extrusion of SEBS-2 (and SEBS-1) as their shape is complex and difficult to explain in words. This figure will also be used in the discussion to explain the mechanism leading to secondary fractures.

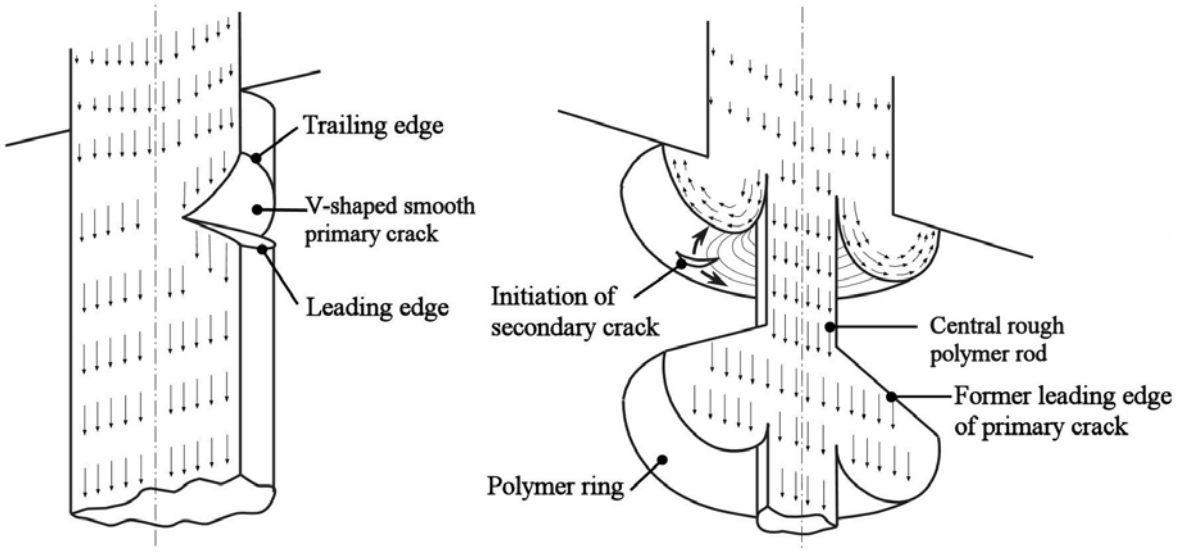

Figure 8: Principal nomenclature used to describe extrusion defects observed at the capillary exit. Primary crack on the left hand side (See Figure 11 for experimental pictures) and Secondary crack initiation on the right hand side (See Figures 16 or 18 for experimental pictures).

Three different levels of defects can be distinguished to describe the development of extrusion defects with increasing shear rate (for the range covered). At the lowest shear rates the smooth extrudate regime is apparent. If shear rate is increased, *primary cracks* are observed. They are initiated on the surface of the melt at the die exit and can propagate deep into the polymer stem. Their appearance is not gradual and they will cause severe distortions to the extruded melt. With increasing shear rate, the shape of the primary cracks will evolve until successive rings, or a helix, of polymer melt are formed.

Excess stresses in these rings will be eliminated by means of a system of longitudinal secondary cracks. To our knowledge, this type of crack has not been reported before. In the case of high enough stresses, simultaneous secondary cracks will lead to flow split at the capillary exit. It should be noticed, as will be shown in Figure 9, that under given conditions two stable solutions exist for flow

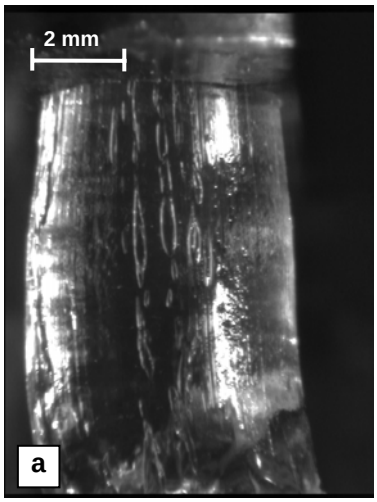

(a) U_p = 0.01, ΔP = 3.2
$a_T\dot{\gamma}_{app}$ = 0.005 s^{-1}

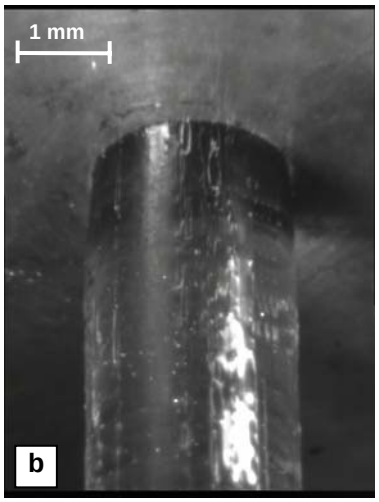

(b) U_p = 0.0007, ΔP = 5.13
$a_T\dot{\gamma}_{app}$ = 0.0085 s^{-1}

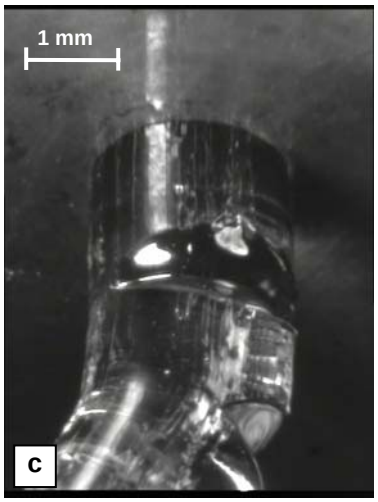

(c) U_p = 0.001, ΔP = 6.1
$a_T\dot{\gamma}_{app}$ = 0.012 s^{-1}

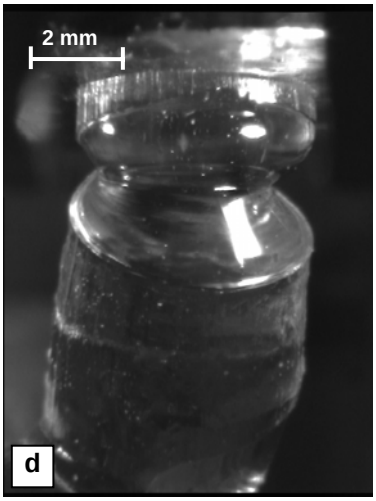

(d) U_p = 0.02, ΔP = 7
$a_T\dot{\gamma}_{app}$ = 0.01 s^{-1}

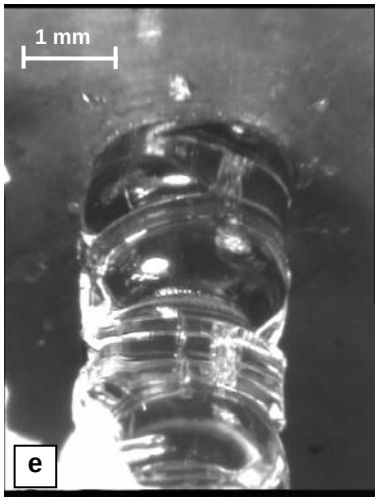

(e) U_p = 0.0013, ΔP = 7.3
$a_T\dot{\gamma}_{app}$ = 0.016 s^{-1}

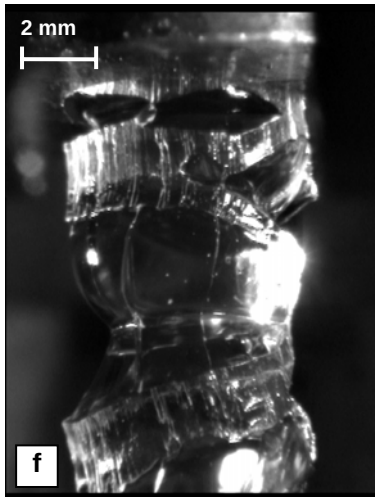

(f) U_p = 0,03, ΔP = 10.1
$a_T\dot{\gamma}_{app}$ = 0.015 s^{-1}

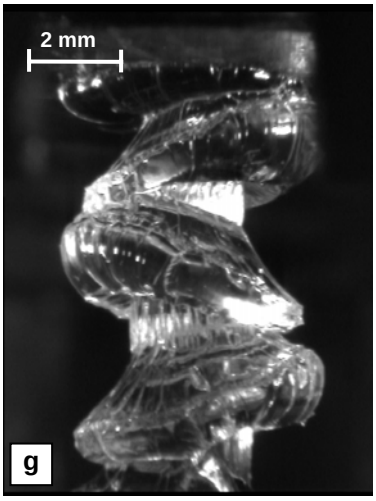

(g) U_p = 0.04, ΔP = 12.5
$a_T\dot{\gamma}_{app}$ = 0.02 s^{-1}

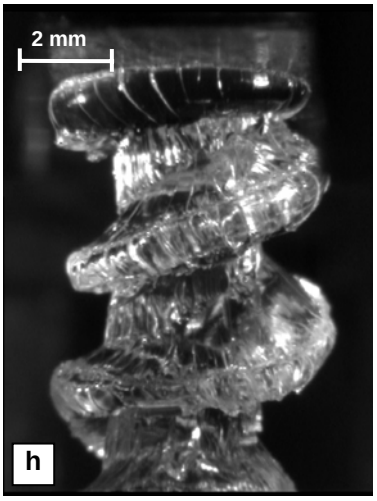

(h) U_p = 0.06, ΔP = 17.4
$a_T\dot{\gamma}_{app}$ = 0.03 s^{-1}

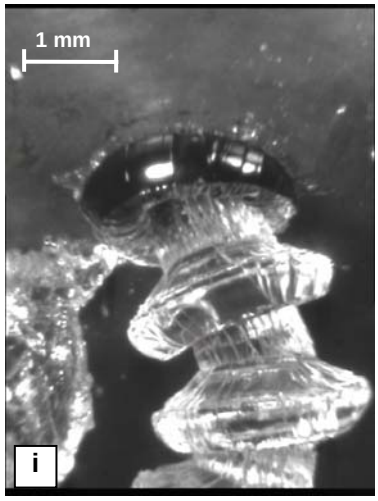

(i) U_p = 0.004, ΔP = 13.9
$a_T\dot{\gamma}_{app}$ = 0.049 s^{-1}

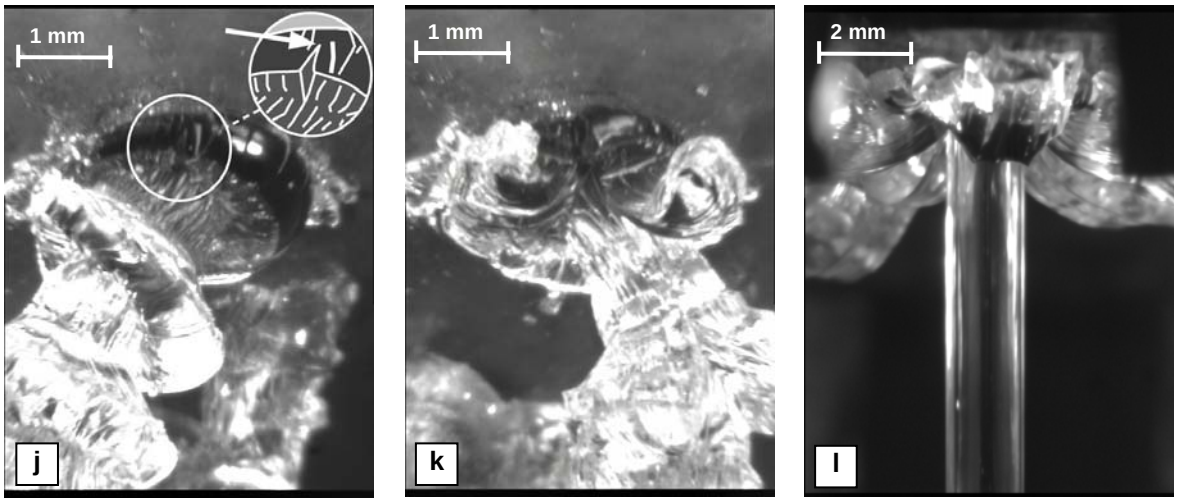

(j) U_p = 0.0045, ΔP = 14.1 $a_T\dot{\gamma}_{app}$ = 0.055 s^{-1}

(k) U_p = 0.0045, ΔP = 14.1 $a_T\dot{\gamma}_{app}$ = 0.055 s^{-1}

(l) U_p = 0.6, ΔP = 73 $a_T\dot{\gamma}_{app}$ = 0.3 s^{-1}

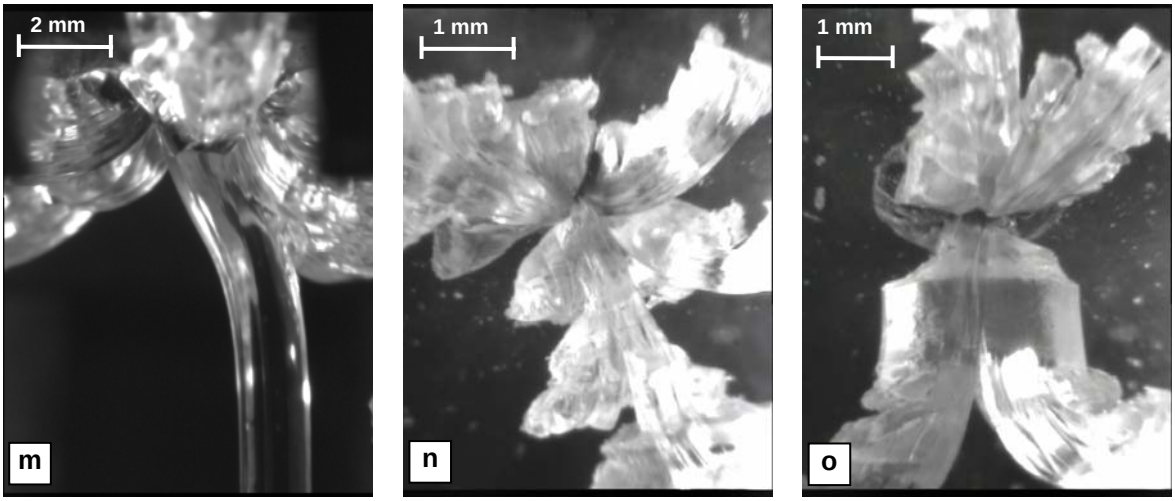

(m) U_p = 0.6, ΔP = 73 $a_T\dot{\gamma}_{app}$ = 0.3 s^{-1}

(n) U_p = 0.0045, ΔP = 85.8 $a_T\dot{\gamma}_{app}$ = 2.4 s^{-1}

(o) U_p = 0.008, ΔP = 93.3 $a_T\dot{\gamma}_{app}$ = 4.26 s^{-1}

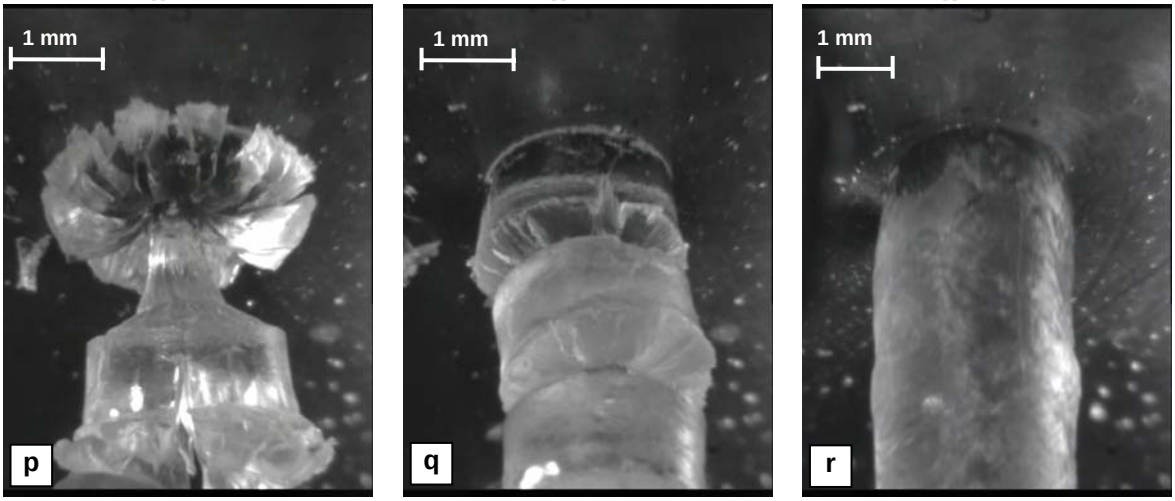

(p) U_p = 0.01, ΔP = 94.3 $a_T\dot{\gamma}_{app}$ = 5.33 s^{-1}

(q) U_p = 0.02, ΔP = 101.1 $a_T\dot{\gamma}_{app}$ = 10.66 s^{-1}

(r) U_p = 0.1, ΔP = 121 $a_T\dot{\gamma}_{app}$ = 53.3 s^{-1}

Figure 9: SEBS-2 exiting the die. L/D = 50/5 and 230°C for (a,d,f,f-h,l,m). L/D = 10/2 and 230°C for (b,c,e,i-k) and 170°C (n- r). U_p is the piston speed in 10^{-3} m s^{-1}. ΔP is the pressure drop in 10^5 Pa. $a_T\dot{\gamma}_{app}$ is the reduced apparent shear rate using 190°C as the reference temperature

split. We have kept the name *"flow split"* for the most general case. The more uncommon type has been labeled *"continuous peeling"* (from its physical resemblance).
Under fixed mean flow rate conditions, oscillating flow follows flow splitting. It is important to notice that secondary cracks continue to propagate during the slipping phase. Flow split and oscillating flows can occur simultaneously.
If shear rate is further increased, pressure oscillations cease and permanent slip at the wall is triggered. This regime coincides with the appearance of the upstream instability, detected by a slope change in the experimental curves obtained with orifice dies of negligible length.

Smooth extrudate regime

The first two captions in Figure 9, obtained at 230°C through dies with L/D of 50/5 and 10/2 respectively, show that the melt comes out of the die as a clear single-stem extrudate. This type of extrudate was observed for the lowest shear rates studied. The use of the macroscope during recording at the die exit reveals some small shallow ellipsoid-shaped defects on the surface of the extruded rod that would be undetected by the naked eye. In addition, several longitudinal scratches covering the surface of the extruded SEBS can be observed. These are similar to the surface scratches responsible for a loss of glossiness during the extrusion of homopolymers. However, with the SEBS considered, the extruded rod is still transparent in the presence of these longitudinal scratches. The caption also shows that melt swelling is nearly non-existent. The diameter of the cylindrical extrudates was measured with a caliper several days after extrusion to account for any deferred relaxation, and the increase in diameter was less than 10% even after heating them again at 150 and 230 °C for several hours.

Primary cracks

When the pressure drop reaches a value of 5.13×10^5 Pa ($\tau_w = 0.21 \times 10^5$ Pa) for the 10/2 and of 7×10^5 Pa ($\tau_w = 0.17 \times 10^5$ Pa) for the 50/5 (captions (c) and (d) in Figure 9), the first deep cracks are observed. These are V-shaped and perpendicular to the extrusion direction and, though they do not occur regularly, they can severely distort the extrudate when they do occur. As for homopolymers [2], the extrudate takes the appearance of a rod consisting of a cracked shell filled with a flowing melted core. Notice that for similar wall stress extrusion conditions, the depths and length of the primary cracks are much greater in the case of the 50/5 capillary. The mean velocity in the 50/5 capillary is three times higher than in the capillary with L/D of 10/2. Thus, the final extent of these cracks is proportional on the mean flow velocity in the die. The films of the melt flowing out the die show that these primary cracks are initiated at the die exit on small surface defects that induce stress concentrations. Moreover, it was possible to observe that the primary fractures continue to open when their trailing edge is no longer in contact with the die, under the influence of high core flow velocities as compared to much slower shell velocities. Differences between core and shell flow velocities are seen to have a strong influence on the final shape of the primary crack, in particular, on the shape of its trailing edge. The energy in the fluid will be dissipated by deformation and swelling of the trailing part of the newly created surface. Since the core fluid's velocity along the axis of symmetry is greater than that of the

shell fluid near the wall, the shape of the trailing edge will be curvilinear. This is illustrated in captions (c) and (d): the primary crack can be considered to be V-shaped in (c) but it is already rather swollen in (d) and will be more curved on the upstream side of this crack after an additional delay. Also notice that the new surfaces created by the crack are smooth and free of any defects and/or fibrils, which is usually typical of slow crack tip velocities. The development of these primary cracks is significantly different from that commonly observed in the case of homopolymers, where surface cracks relax rather than develop at the surface of the free rod. The differences can be explained by the long relaxation times characteristic of microphase-separated block copolymers.

With increasing apparent shear rate, these transversal cracks appear more frequently and cover the entire extrudate, as shown in captions (e) and (f) obtained at reduced apparent shear rates of 0.016 s^{-1} (τ_w = 0.3x10^{5}Pa) and 0.015 s^{-1} (τ_w = 0.25x10^{5}Pa). Both the new surfaces created by the primary fracture are curved, but are still smooth. However, it is possible to observe some localized scratches that result from the merging of two distinct primary cracks, as can be seen near the die exit in caption (f). In caption (e), it is also possible to observe a zone in the deepest part of the crack where multiple scratches are formed in the direction of crack penetration.

Better observation of this redirection of cracks is possible with a further increase in the apparent shear rate, when submerged jet conditions are obtained, similar to those for homopolymer cracking [2]. In caption (g), corresponding to a reduced apparent shear rate of 0.02 s^{-1} (τ_w = 0.31x10^{5}Pa), the redirection of the primary crack towards the extrusion direction as it penetrates deeper upstream into the flowing polymer is evident. The redirected primary crack leaves a series of vertical scratches in its wake. The beginning of this redirected fracture can be observed in the lower part of the disks as a circle: the outer part being nearly smooth and the inner surface being scratched. Notice that the transversal primary crack nearly propagates over the whole length of the extrudate circumference at the die exit and that the trailing edge swells. At this point, the flowing polymer turns around the die exit corner and the melt exiting along the die exit corner belongs to a submerged jet rather than a free surface jet.

When primary cracks propagate around the entire circumference of the die, a series of successive rings (or a helix under the influence of erratic free extrudate motions), are formed as shown in captions (h) and (i). They were obtained respectively at apparent reduced shear rates of 0.03 s^{-1} (τ_w = 0.43x10^{5}Pa) and 0.049 s^{-1} (τ_w = 0.57x10^{5}Pa). The shape of these defects is very similar to the one reported elsewhere for entangled polydimethylsiloxane (PDMS) polymers and PB [10]. The successive rings or helix are transported by a central core of diameter 0.6 D, where D is the die diameter.

As caption (h) shows, several small, shallow longitudinal cracks are observed on the new surfaces created by the primary V-shaped cracks. These defects extend radially on the newly created surfaces and their number increases with increasing shear rate.

Secondary cracks and continuous flow splitting

If stress concentrations are high enough, *secondary cracks* can be initiated and propagate in these melt rings as seen in caption (j), which corresponds to a reduced apparent shear rate of 0.055 s^{-1}. The pressure drop measured across the capillary was 14.1x10^5 Pa, equivalent to a τ_w of 0.58x10^{5}Pa.

For clarity, the inset in the caption shows the crack schematically. A small V-shaped front can be observed within the white circle. This caption will be studied in more detail in section 5.2. This secondary fracture propagates between two successive rings through the polymer core. Caption (k) shows the same crack as presented in caption (j), but a later stage. Multiple fractures may eventually propagate in the same ring. When this happens, as shown in captions (l) through (n), permanent flow splitting occurs at the die exit.

Two situations may occur. In the case of 2 mm diameter capillaries, only the case presented in caption (n) was observed. The polymer exiting the die is highly distorted and loses its glossiness with increasing shear rate. The outer surface of the branches still contains the respective portion of the successive melt rings formed at the die exit. The inner surfaces are smooth. The number of branches observed seems to increase with apparent shear rate. As little as two and as many as four branches have been observed.

The case resembling a peeled banana presented in (l) and (m) was observed during experiments with the 50/5 capillary at 230 °C. Here, the diameter is large enough and the secondary cracks cannot merge. A stable central core free of defects emerges continuously from the center, cut into the extrudate by the primary crack tip. At the same time the outer part of the extrudate is split and falls into pieces. It appears that the primary crack tip propagates further upstream than the several secondary cracks tips do. To our knowledge, such an extrusion defect has not been previously reported. It should be noticed that under the same experimental conditions, 230°C and 50/5 capillary, both *flow split* and *continuous peeling* were observed successively. It seems that *continuous peeling* will be the more stable solution, but that uncontrolled perturbations may cause the melt to flip from *continuous peeling* mode to common *flow-split*. Caption (m) presents the point at which the central core becomes part of one of the exiting branches observed during *flow-splitting*.

The sequence of captions presented so far in Figure 9 explicitly shows that flow split is just a consequence of the severe surface cracking that will occur in the case of fluids with the appropriate crack propagation properties. Figure 9 also shows that the use of block copolymers is well suited to studying the origin of *flow split* during capillary flow.

Oscillating flows

When τ_w reaches $4x10^5$ Pa, oscillating flows are observed during mean flow-rate controlled experiments. Both the slipping phase and the adhesion phase are clearly identifiable in captions (o) through (q). These captions show that with macroscopic slip at the wall, stresses will be low enough not to create new cracking surfaces. However, nothing will stop existing secondary cracks from propagating through the melt that is slipping at the wall. A perfect example is caption (o), where the entire slipping rod has been cut in part by a secondary crack along one of its diameters. To a lesser extent, but still serving as a good illustration, captions (p) and (q) show cracks that are propagating into the slipping phase. Finally, the captions in oscillatory flow regimes as well as continuous peeling regimes enable the minimum thickness of the central polymer rod to be estimated. It is found to decrease from one half to one quarter of the capillary's diameter, which gives an idea of the primary crack tip diameter, in relation with the die exit singular stress field.

With increasing shear rate, oscillating flows stop and melt slips permanently at the wall, as seen in caption (r). At these regimes, and with higher shear rates as well, the upstream instability can be observed via the fluctuating shape of the extruded melt.

2.4.2 Other fluids

The defects observed at the die exit during the extrusion of SEBS-1 were very similar to those encountered during the extrusion of SEBS-2. Thus, they will not be covered in detailed. In the case of SEBS-3, which has a spherical morphology, the defects observed when it is extruded at 90°C through a capillary with L/D of 50/5 are shown in Figure 10. The development of extrusion defects observed with increasing shear stress is very similar to that observed in the case of homopolymers such as PB, PDMS or PE. At the low shear rates, the extrudate coming out of the die is smooth and transparent. Surface cracking is initially observed when $\tau_{w,app}$~$0.3x10^5$ Pa and it then propagates gradually to cover the whole surface of the extrudate as captions (b) through (f) show. Notice that these initial surface cracks shown in (b), (c) and (d), are also V-shaped just as in the case of SEBS-2. However, their depth relative to the radius of the die is about 1/10 of that observed in the case of SEBS-2. Initially, these transversal fractures occur around the die exit nearly as one, forming in this way a successive series of regular peaks and valleys. With increasing flow rate these fractures become more chaotic and progressively gain in depth as shown in the sequence of captions (c) through (f). The flow curve obtained in the case of SEBS-3 with a short orifice die of 5 mm at 90°C did not show the discontinuity characteristic of the viscoelastic upstream instability when these deeper cracks appear. The discontinuity is observed at shear rates corresponding to oscillating flow. Thus, it seems these deeper fractures are still a consequence of the singularity at the die exit.

Oscillating flow is triggered at shear stress of about $4x10^5$ Pa in the case of SEBS-3. Finally, with apparent shear rates greater than 1.8 s^{-1}, the oscillations stop and upstream instability with macroscopic slip at the wall is observed, as in the case of PE and other entangled polymers [2]. Slight waviness is observed, becoming more noticeable with increasing shear rate. This can be attributed to the viscoelastic instability that originates just upstream of the die. At the highest shear rates studied, peeling at the die exit is observed. However, with the dies used, it was not possible to determine whether this peeling is due to the singularity at the die exit or whether it occurs inside the die [5].

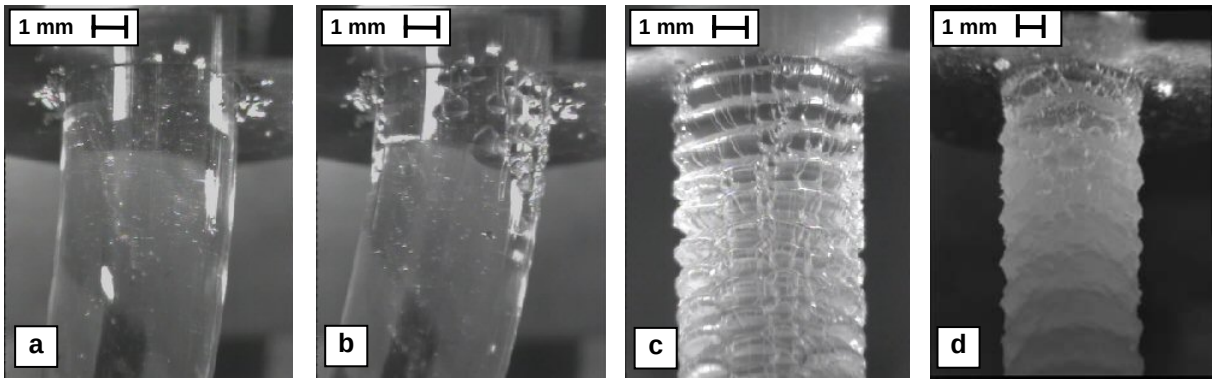

(a) $\dot{\gamma}_{app}$ = 0.005 s^{-1} τ_w = 0.22 **(b)** τ_w ~ 0.27 **(c)** $\dot{\gamma}_{app}$ = 0.009 s^{-1} τ_w = 0.36 **(d)** $\dot{\gamma}_{app}$ = 0.08 s^{-1} τ_w = 2.1

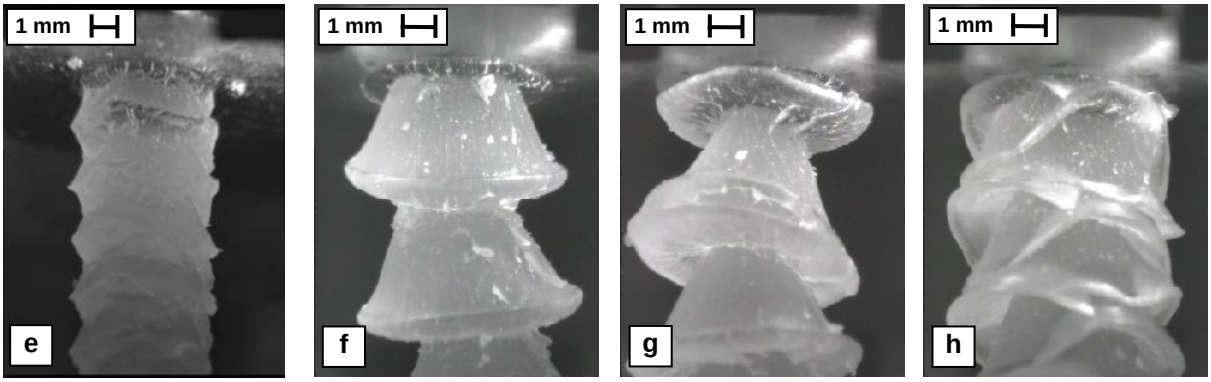

(e) $\dot{\gamma}_{app}$ = 0.11 s^{-1} τ_w = 2.4 **(f)** $\dot{\gamma}_{app}$ = 0.18 s^{-1} τ_w = 3.03 **(g)** $\dot{\gamma}_{app}$ = 0.55 s^{-1} τ_w = 4.03/08 **(h)** $\dot{\gamma}_{app}$ = 0.9 s^{-1} τ_w = 3.78/83

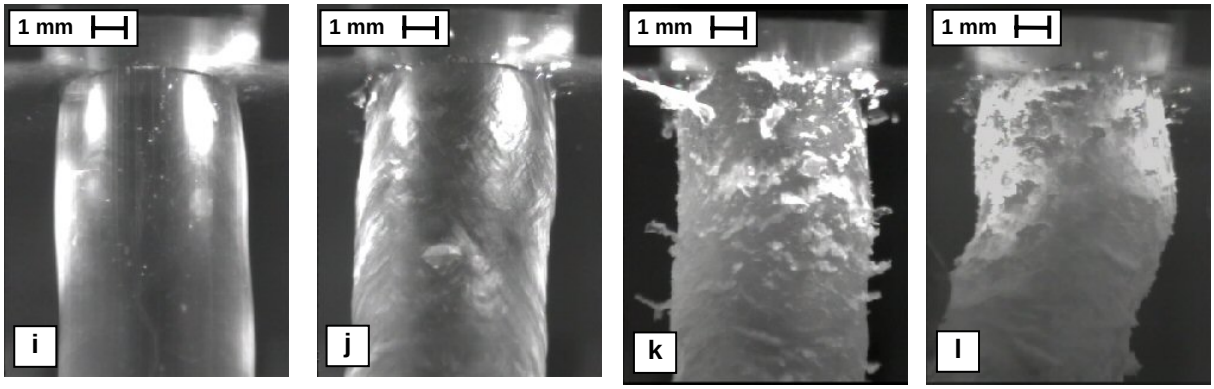

(i) $\dot{\gamma}_{app}$ = 1.8 s^{-1} τ_w = 3.7 **(j)** $\dot{\gamma}_{app}$ = 9.2 s^{-1} τ_w = 3.96 **(k)** $\dot{\gamma}_{app}$ = 18.4 s^{-1} τ_w = 4.85 **(l)** $\dot{\gamma}_{app}$ = 55.3 s^{-1} *τ_w = 4.4*

*Figure 10: Extrusion at 90°C of SEBS 13%PS at die exit (*L/D *= 50/5). Apparent shear stress is expressed in 10^5 Pa.*

2.5 Crack propagation under extensional stresses in SEBS and PB

In this section, special attention is paid to two particular features observed during surface cracking of SEBS-2 extrudate. Firstly, the primary cracks. These differ slightly from the cracks usually observed on moderate to highly-entangled polymer melts. During extrusion of these SEBS, the primary cracks do not relax but continue to develop entirely outside the die. Secondly, we will focus on the birth phase of flow splitting, which occurs as a consequence of stress concentrations in the extending polymer rings formed around the die exit. Thus, flow splitting should be considered as a severe case of extrudate surface cracking, which may appear when two longitudinal cracks propagating in different directions combine.

In order to study these phenomena, different frames extracted from films of the extrudate coming out of the die were used. The time interval between two consecutive frames is 0.04 seconds. Since cracks propagate during several, ~10-20, seconds in SEBS-2, it is possible to follow their propagation in a nearly continuous manner.

2.5.1 Primary cracks

Figure 11 shows the development of the crack presented in caption (c) of Figure 9 obtained at 230°C and a piston speed of 10^{-3} mm s^{-1} (equivalent to an apparent shear rate of 0.012 s^{-1} at 190°C) with a capillary 10 mm in length and 2 mm in diameter. This sequence of frames extracted from the film clearly shows that primary cracks initiate at small surface defects (dimples) and that they open along the outer surface of the extruded rod. As it opens, the crack also propagates towards the center of the extruded melt. Moreover, in the sequence it is perfectly observable that, though the crack is initiated at the die exit, it will continue to propagate when the melt is flowing as a free-surface jet. This can be attributed to the long relaxation times of SEBS-2. To our knowledge, fractures that continue to propagate well outside the die have not been reported in the literature thus far.

An Labview-based software developed in-house and some simple geometrical considerations allowed the velocity of the advancing tip in primary fractures to be roughly determined. The analysis procedure performed in each frame is explained graphically in Figure 12. Measurements with the software gave access to the length d, which is equal to $R\sin(\theta)$ if it is assumed that the crack propagates perpendicular to the capillary's axis of symmetry. This assumption is easily justified from observation of the distance between the crack tip and the die exit between the different frames. R represents the radius of the extruded rod and is considered to be equal to 1 mm since swelling is negligible.

Once the angle θ is known for different frames, let us call them i and j, obtained at times t_i and t_j respectively, the speed of crack tip propagation into the extruded rod is calculated as

$$U_{pc,R} = \frac{R\left(\cos(\theta_j) - \cos(\theta_i)\right)}{t_j - t_i} \qquad (3)$$

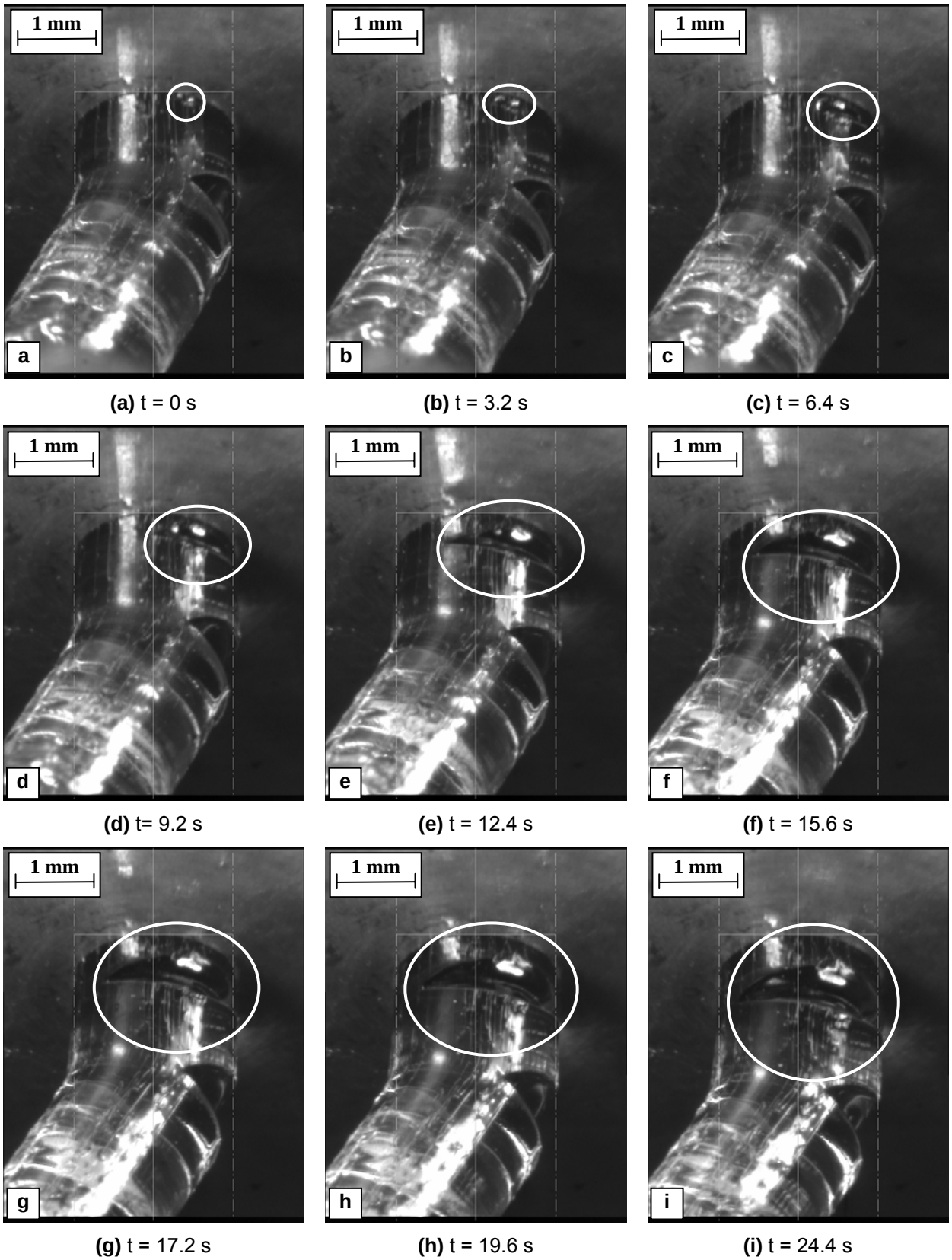

(a) t = 0 s **(b)** t = 3.2 s **(c)** t = 6.4 s

(d) t= 9.2 s **(e)** t = 12.4 s **(f)** t = 15.6 s

(g) t = 17.2 s **(h)** t = 19.6 s **(i)** t = 24.4 s

Figure 11: SEBS-2 same extrusion conditions as caption (c) in Figure 9. The experimental conditions were U_p *= 0.001 mm* s^{-1}*,* $\Delta P = 6.1 \times 10^5$ *Pa and* $a_T\dot{\gamma}_{app}$ *= 0.012* s^{-1}

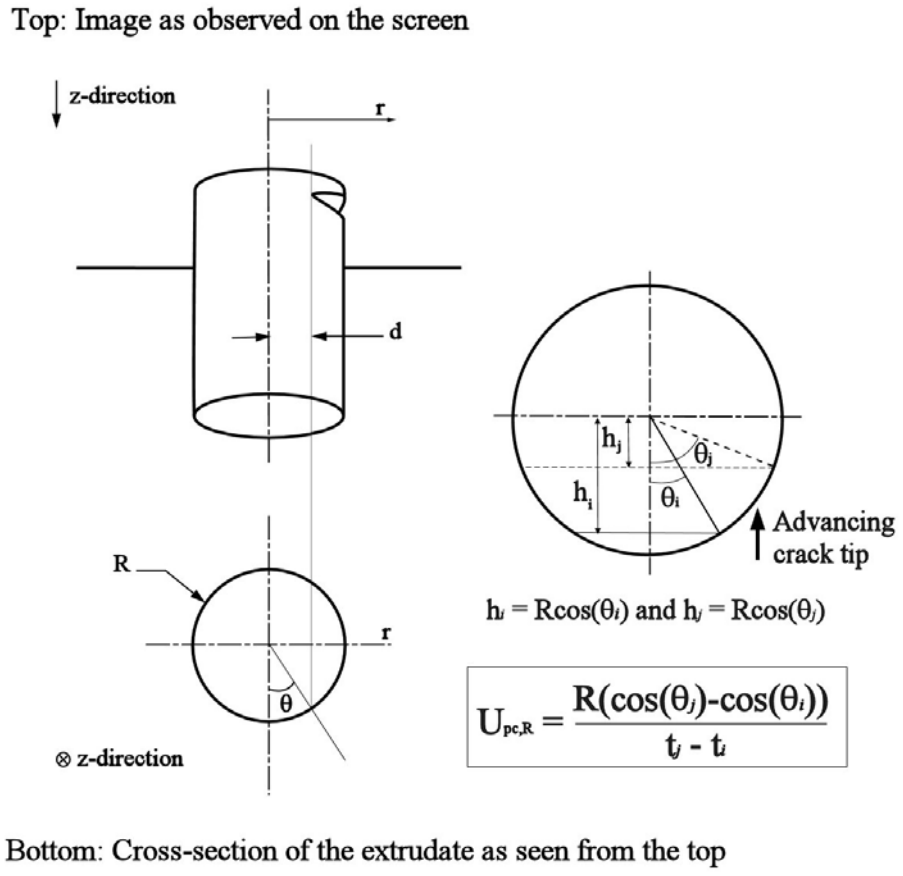

Figure 12: Geometric considerations and Image treatment used to determine primary crack-tip propagation speed.

Using this procedure, the crack tip propagation was calculated using a time interval of 0.8 seconds. This time interval allowed errors in the crack tip displacement measurement of the order of 10-15% to be kept. Figure 11 presents some, but not all, of the captions used for the calculations. It illustrates well how the crack is initiated at the die exit from a small surface defect. The sequence also shows that the crack continues to propagate when the trailing edge is no longer in contact with the die exit and is as a far as 0.7 mm from it.

Figure 13 is obtained if the radial crack tip propagation speed, $U_{pc,R}$, is normalized by the mean velocity in the capillary, defined by $\overline{U} = Up\frac{D_R^2}{D^2}$, where D_R is the reservoir diameter of 12 mm and U_p is the piston speed, and is plotted as a function of normalized time. The time was normalized by the percolation time, τ_p. τ_p was extracted from Figure 1 as the inverse of the lowest frequency where G'~G", which was then shifted to 230°C using the shift factors presented in the inset of Figure 2. τ_p is found to be ~8.3 seconds. Three different regions of radial crack tip propagation speed are observed during the life span of the crack. In region I the crack is initiated and its tip velocity increases. Region II corresponds to a continous deceleration of the crack propagation with time, which is explained by the relaxation of stresses within the polymer as time passes and the energy released by the propagation of the crack. Eventually the crack stops propagating (Region III) when no more stored

energy is available to drive the fracturing process. For this crack in particular, the die diameter is D=2 mm and propagation ceases with the tip being roughly at a distance of 0.7 mm from the die exit and 0.2 mm from the rod centre line. Notice that the length of time of region II is about twice the characteristic time τ_p. Keeping in mind that these are just gross estimates, and from measurements on other cracks, the normalized radial crack-tip propagation speed is within an order of magnitude from the mean velocity in the flow.

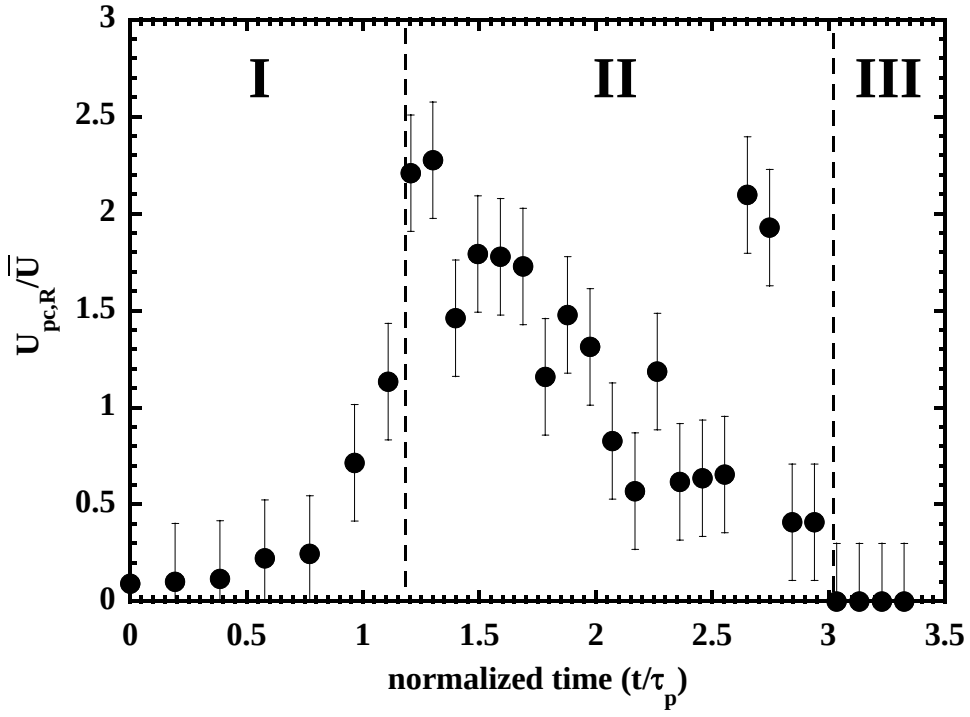

Figure 13: Primary crack tip propagation speed normalized by mean speed as a function of normalized time (t/τ_p). τ_p is the percolation time. These results correspond to the sequence presented in Figure 11 and in caption (c) Figure 9 (SEBS-2 at 230°C with L/D = 10/2, $\Delta P = 6.1x10^5$ Pa and $a_T\dot{\gamma}_{app} = 0.012\ s^{-1}$).

In order to gain a better understanding of why cracks continue to propagate outside the die, the magnitude of the extension rate at the die exit, where the melt passes from pipe flow to free-surface jet, was estimated. The extension rate was determined by monitoring the movement of impurities, or small surface defects, in the melt. Frames with a time interval of 0.4 seconds were used to allow the particles to move enough to obtain accurate measurements, but yet to track them clearly. Figure 14 shows the geometrical considerations that need to be taken into account to determine the velocity U_z. z' was the measured distance on each frame and is related to the real distance, z, as $z = \frac{z'}{\cos(\alpha)}$. The angle α was determined by means of the aspect ratio of two perpendicular radiuses on the die exit, knowing that when perpendicular to the die exit plane both values will be equal.

Particle velocities as a function of distance from the die exit, normalized by the die radius R, are presented in Figure 15 for apparent reduced shear rates of 0.0085 s^{-1} and 0.012 s^{-1}. These regimes are represented by captions (b) and (c) in Figure 9. The theoretical mean velocities (dashed lines) that should be achieved far enough downstream of the die have also been indicated on the plot. The

two filled marks represent average values obtained from all measurements performed for a given flow rate. In the case of U_p = 0.001 mm s^{-1}, the individual measurements are also presented (empty marks). The slope of these curves equals the extension rate acting on the fluid.

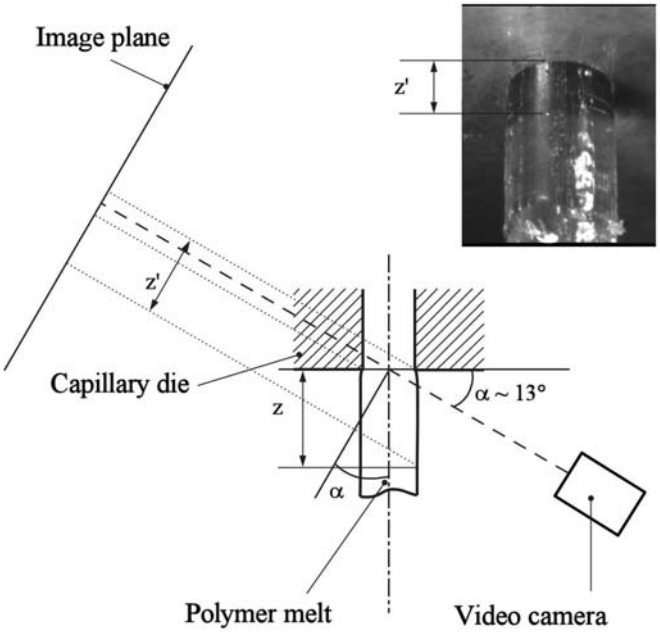

Figure 14: Geometrical considerations used to calculate Uz(z) of particles on the extrudate coming out of the die. Drawing not to scale.

In the case of 0.012 s^{-1}, corresponding to an extrudate with no severe defects, the results can be seen to agree well with the theroretical value of 0.025 mm s^{-1}. In the case of the higher flow rate, the values obtained are notably higher than expected by the theoretical prediction. This can be explained by the appearance of primary cracks that highly influence the flow field in the extrudate. When the crack occurs, the lower portion of the extrudate will accelerate while the crack is opening. At the same time, the trailing edge will decelerate. Particles A and B were the ones closest to a crack that was opening at the die exit, the crack examined in Figure 11, and show the highest velocity values. They were downstream of the leading edge, which accelerates. The other 3 particles studied were far from cracks during the measurements. It can be seen that these values are closer to the theoretical value of 0.036 mm s^{-1} than the values of particles A and B.

The slope of the curves gives an idea of the elongational strain rate at the die exit. Since the polymer adheres at the wall, thus having zero velocity in the die, and reaches the mean velocity $\overline{U}$ at about R/4 from the die exit, the elongational strain rate can be considered to be of the order of $4\overline{U}/R$.

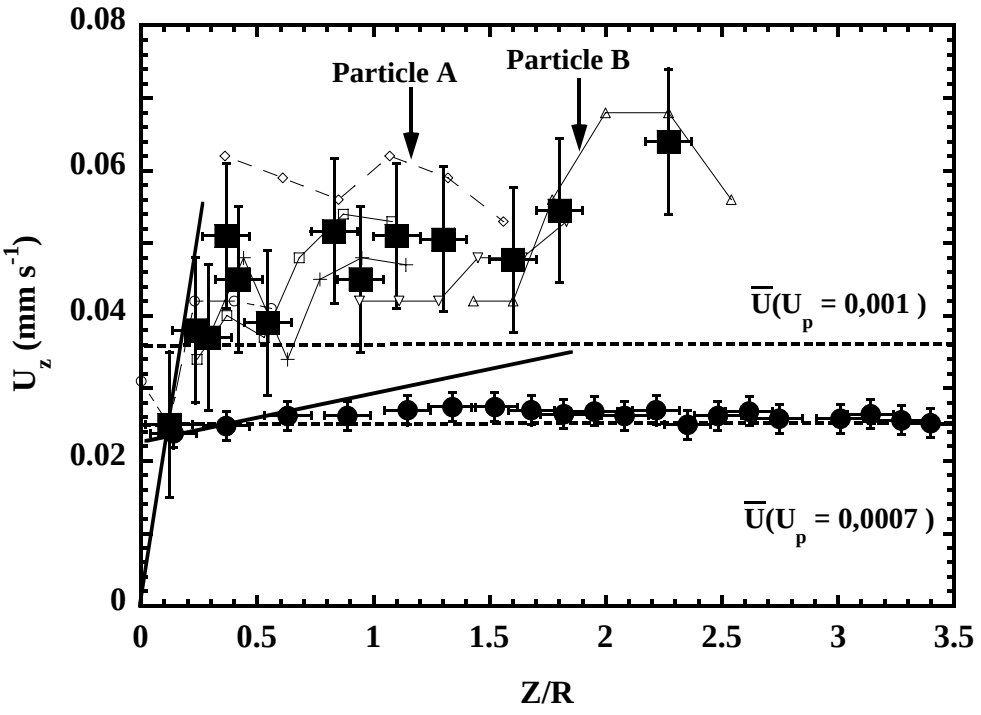

Figure 15: Axial velocity (U_Z) as a function of distance from the die exit using SEBS-2 extruded at 230°C through a die with L/D of 10/2. Solid round marks correspond to piston speed, U_p, of 0.0007 mm s^{-1} (Caption (b) in Figure 9). Solid square marks correspond to an average value for U_p = 0.001 s^{-1} (Caption (c) in Figure 9).

2.5.2 Secondary cracks and birth of flow split

The successive rings that appear at the die exit, captions (g) through (i) in Figure 9, are not free of stresses. Figure 16 presents frames extracted from a film of SEBS-2 coming out of the die at 230°C and at a reduced apparent shear rate of 0.055 s^{-1} through a die of L/D = 10/2. This is the same regime as captions (j) and (k) in Figure 9. Figure 16 shows see the birth of flow split.

In the case of captions (a) through (f), the area where the secondary crack is initiated has been circled for clarity. In addition, the advancing crack tip is indicated by the white arrow in captions (b) through (f) in the inset. The secondary crack starts its propagation on the surface of the polymer ring, as depicted in Figure 8. The initial propagation point seems to be where the original primary cracks initially opened before redirecting in the direction of extrusion. The sharp curvature and the extension of the polymer rings, due to their increasing diameter, induce stress concentrations that will favor the appearance of secondary cracks. The secondary crack tip propagates through the melt ring towards both the central polymer rod and the outermost diameter of the melt ring formed at the die exit. Within the white circular mark in the captions, crack tip propagation is observed as a triangular-shaped advancing front. Notice that the scratches in the central polymer rod coming out of the die are no longer parallel, which shows that the crack also propagates towards the axis of symmetry of the die.

Secondary crack propagation does not stop once the first ring is fully fractured. The ring is big enough for the crack to propagate continuously through the central polymer rod and then reach and break the following ring as shown in captions (e) through (o).

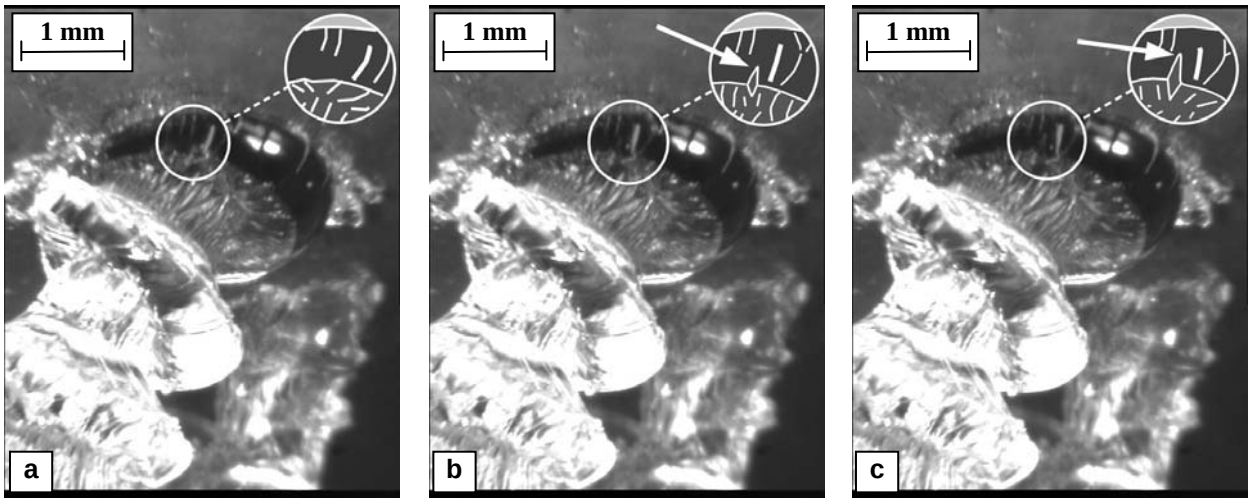

(a) t_0 = 0 s **(b)** t = 0.08 s **(c)** t = 0.12 s

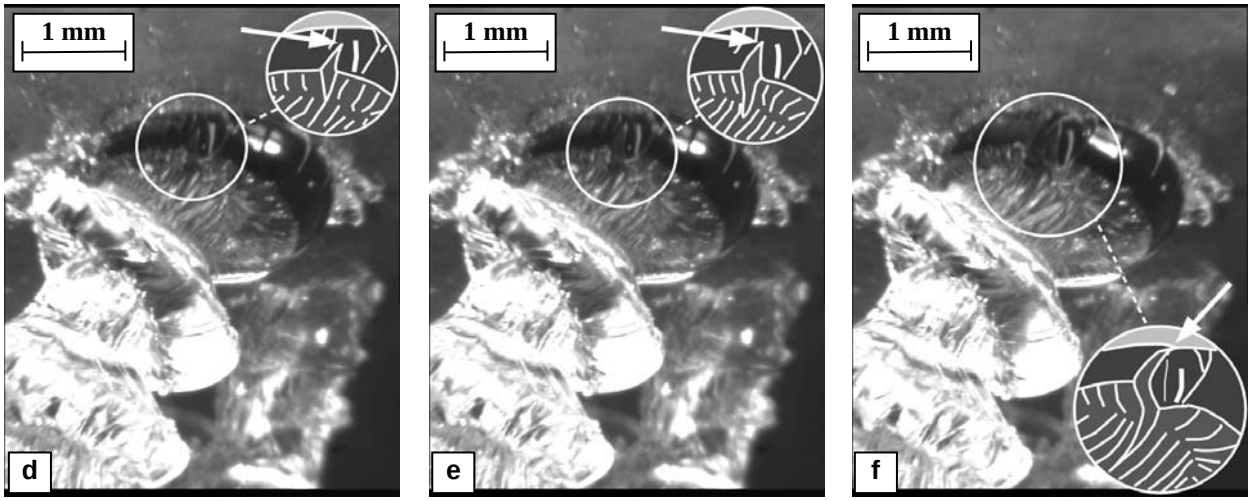

(d) t = 0.16 s **(e)** t = 0.2 s **(f)** t = 0.48 s

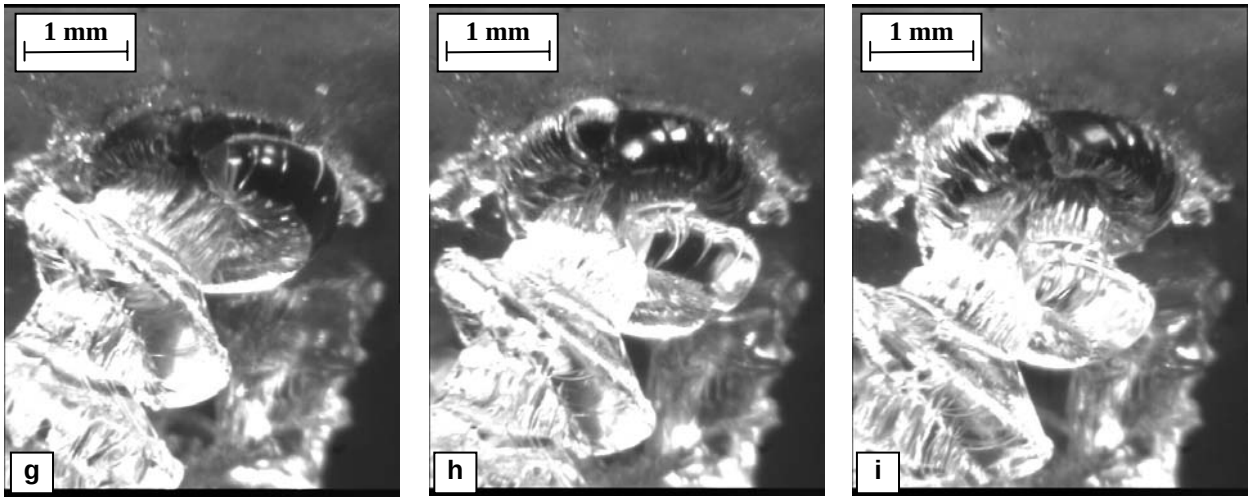

(g) t = 1.08 s **(h)** t = 3.48 s **(i)** t = 5.08 s

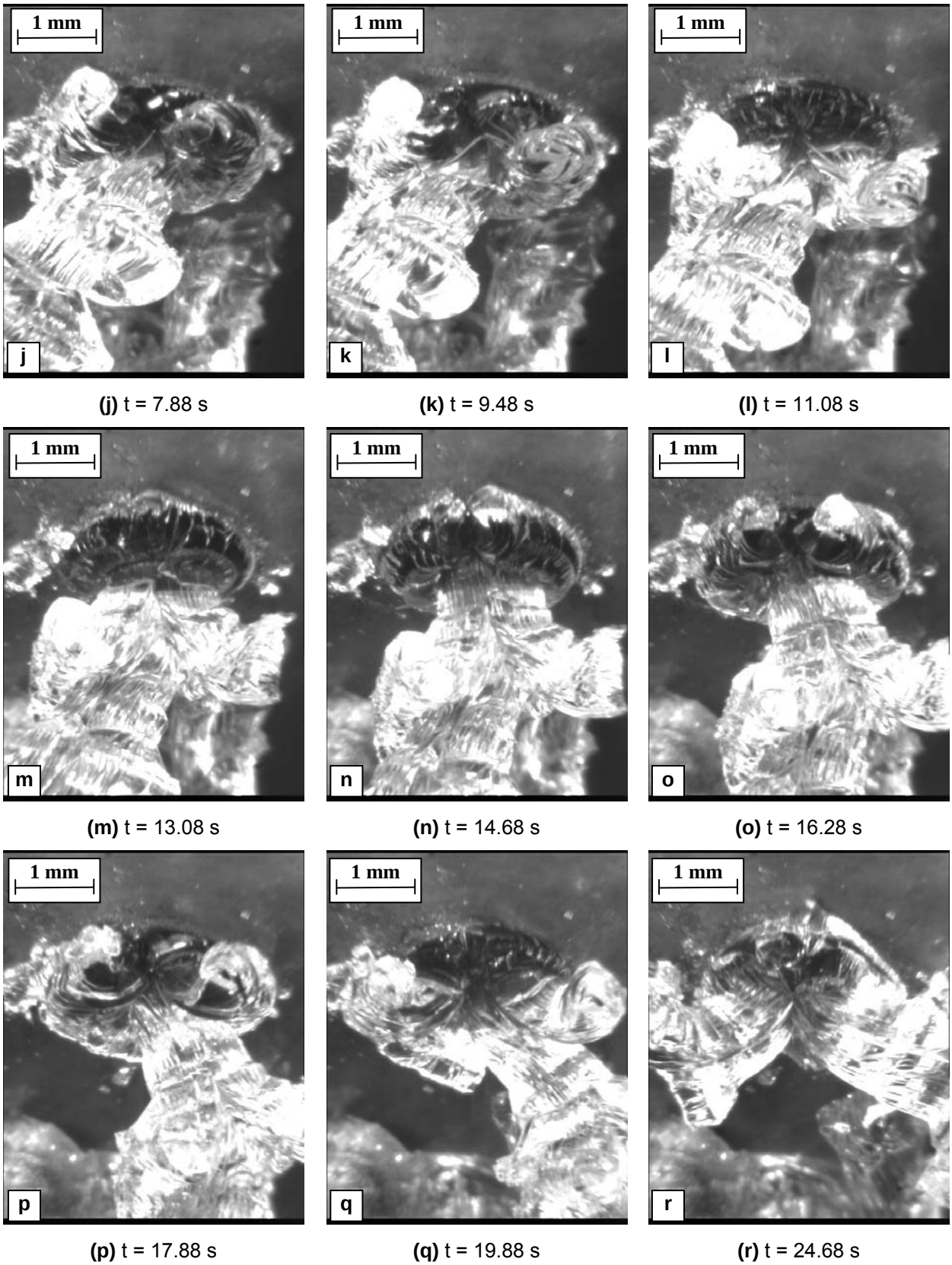

Figure 16: Birth of flow split at the capillary exit. Images taken at while extruding SEBS-2 at 230°C through a die with L/D = 10/2 and piston speed (U_p) of 0.0045 mm s^{-1}. Same conditions as captions (j) and (k) in Figure 9. The arrow indicates the position of the crack tip.

When two or more secondary cracks propagate on the same ring of polymer melt and penetrate into the core, the extrudate can split into different branches. Initially, as caption (q) shows, a principal branch conveying the majority of the polymer exiting the capillary is conserved. This main branch is then surrounded by secondary branches in the form of chips. Though measurements were not possible, visual observations show that the mean section area of the main branch is initially larger than that of the secondary ones.

When two cracks happen to occur opposite each other, the melt will split into two branches that are nearly equal, with each one having similar mean flow rates. This case is shown in caption (r).

With even higher flow rates, more than two cracks occur on the same polymer ring due to the higher state of stress built up in the melt. The different secondary cracks merge in the center of the melt, thus creating multiple branches. Examples are seen in captions (j) through (l) of Figure 9. The number of branches is not constant for a particular shear rate, though in the case of those rates showing continuous flow split it is always equal to or greater than 3. Four and five branches have also been observed but not regularly, making it difficult to extract quantitative conclusions regarding the number of branches and flow rate. It seems, though, that the number of branches increases with flow rate, since the number of secondary cracks increases due to higher stress levels in the polymer rings created at the die exit.

The sequence of images presented in Figure 16 shows that flow split at the capillary exit during extrusion of polymer melts is a consequence of severe surface cracking. Contrary to studies by Fernández *et al.* [13] and Zhu [26], no rotational movement of the branches was observed in the copolymers used in the present work. It may be noticed that right or left helicity of extrudates appears in relation to uncontrolled perturbations (initial conditions and boundary conditions) which may exist even inside apparently achiral experimental set ups.

A gross estimate of the mean crack tip velocity in the secondary crack can be determined though it is much more difficult than in the case of primary cracks. In order to calculate the mean crack tip propagation speed, $U_{sc,R}$, it is assumed that the cross-section of the polymer ring by a plane containing the die axis is half of a circle. Thus, the surface will trace half of a circumference. Moreover, the crack initiation point is considered to be at the zenith of this half circle. The height of the semi-circle is estimated to be of the order of 0.4 mm. The time needed by the crack to fracture the ring completely is about 0.5 seconds, as captions (e) and (f) in Figure 16 show. The path of the crack tip into the polymer ring will be 0.4 mm. Using these values, the path length and the change in time, an average crack tip propagation speed of 0.8 mm s^{-1} is obtained. The ratio $\frac{U_{sc,R}}{U_{pc,R}}$ is found to be of the order of 5.

This explains how different secondary cracks have time to merge near the center of the die and result in flow split.

The extension rate causing secondary fractures in the polymer rings was also estimated. The film from which caption (i) in Figure 9 were extracted, and which corresponds to a reduced apparent shear rate of 0.049 s^{-1}, was used. On different frames, we measured the increase in ring diameter between known time intervals. With the diameter value measured from the image, D_m, and the capillary diameter, D, the strain, equal to $(D_m–D)/D$, was calculated and then was plotted as a function of

normalized time. Again the percolation time τ_p was used as the normalizing factor. Figure 17 presents this curve, which represents the strain undergone by the polymer rings. Data for three successive rings are presented. It should be noticed that the first measurement was considered as time zero. Consequently, the development of the initial portion of the curve is unknown. This is due to the fact that the size of the previous polymer rings does not allow observation of the polymer ring studied. The period of two successive rings is of the order of 7 seconds, as the birth of the second and third rings shows in Figure 17. This is not far from the characteristic percolation time, τ_p, observed in dynamic rheometry experiments of 8.3 seconds for SEBS-2. Once the polymer ring is completely detached and is conveyed by the central polymer rod, its diameter no longer increases. The strain rate is obtained from the slope of the curves by using a linear fit and has been estimated at 0.024 s^{-1}. However, this value is underestimated as only the outer diameter of the polymer ring is considered. A better estimate is obtained by considering the place of the primary fracture crack tip delimiting the central polymer rod and the elongated upstream free surface of a crack. If the latter is considered, the original diameter will be of the order of 1.2 mm and the diameter of the point at which the fracture is initiated is of the order of 2 mm. Thus the strain will be 0.66 units, 5 times greater than initially considered. If we consider that the polymer at the upstream free surface of the crack travels with a velocity of 0.4 mm s^{-1} (mean velocity for a die for D = 1.2 mm) and that the length of the path traveled is 0.8 mm, a strain rate of 0.33 s^{-1} is obtained. Notice that this strain rate is of the same order of magnitude as the strain rate, estimated as $4\overline{U}/R$, exerted on the polymer at the die exit when primary cracks are initiated: 0.144 s^{-1}. Thus, it is quite likely that the same conditions, and mechanisms, take place for primary and for secondary cracks.

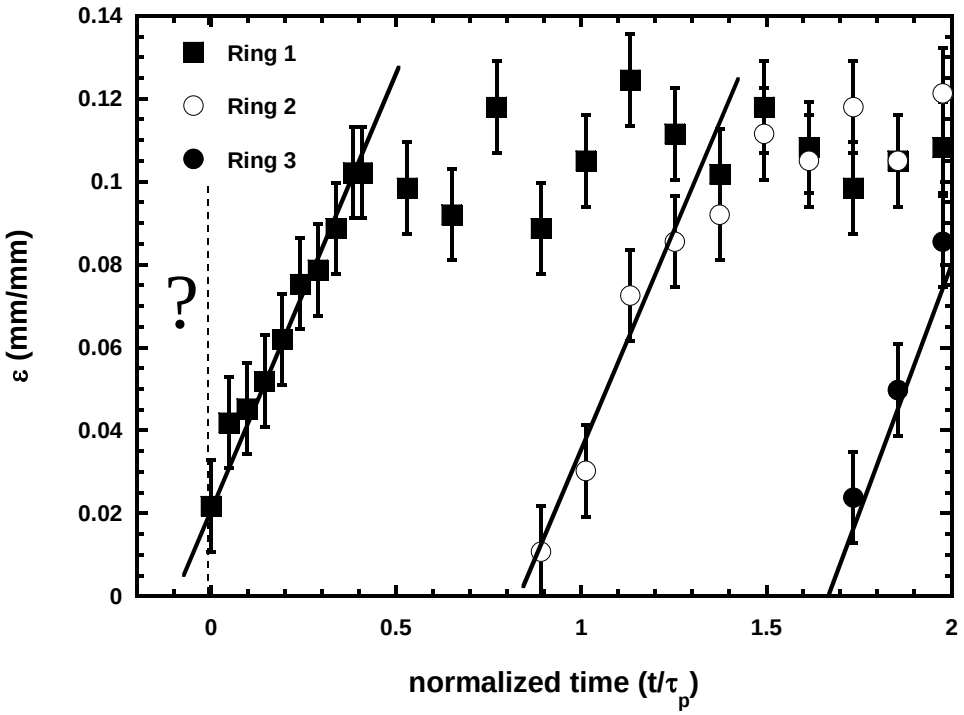

Figure 17: ring strain as a function of normalized time (t/τ_p) for SEBS-2 extruded at 230°C and an apparent shear rate of 0.049 s^{-1} (U_p = 0.004 mm s^{-1}) for three successive rings.

2.5.3 Linear high-molecular weight polybutadiene

Flow split at the capillary exit has been observed during the extrusion of ethene-propene copolymers [13], four-arm star PBs [26], and as the present study shows flow split also occurs with certain SEBS. The individual macromolecules constituting these fluids have different architectures and thus several aspects of molecular architecture which are important with respect to flow split need to be explored. Moreover, all fluids showing flow split reported in [13] and [26] have rather high molecular weights. The M_w values, as well as the polydispersity index (M_w/M_n) values given by the authors are tabulated in Table 3 together with the calculated ratio M_w/M_e. The values of M_e were extracted from [16].

Author	Product	Description	M_w (g/mol)	M_w/M_n	M_w/M_e
Fernandez *et al.* [13]	LM350	Ehtene-propylene copolymer *(Statistical)*	335000	4	< 98*
	LM118		375000	2.3	< 107*
	LM123		415000	2.3	< 120*
Zhu [26]	S-200K	4-arm star polybutadiene**	210000	1.11	140
	S-400K		455000	1.11	303

* M_e values used are for 100% PP (3500 g/mol). Thus, this is the smallest possible number of entanglements.

** For PB a value of 1500 g/mol was used[16].

Table 3: Principal characteristics of polymers reported in the literature that show flow splitting at the capillary exit during extrusion.

When in their microphase–separated state, block copolymers with sufficiently long end-blocks can be considered to be of quasi infinite molecular weight since the microdomains formed by the end-blocks act as stiff entanglement points in the flow conditions at hand. The assumption of an equivalent infinite M_w can be verified with the G' and G" curves: when both moduli are tangent and they vary with $\omega^{0.5}$, the fluid can be considered to be at its gelation point. Thus, the molecules can be considered to be interconnected, forming a percolated system. This case was only observed for SEBS-1 and SEBS-2. In the case of SEBS-3, G" overtakes G' in the frequency range of interest. Since dynamic rheometry experiments were performed on samples with randomly oriented domains at the macroscopic scale, the different behavior seems to be related to the entanglement of the PS blocks, proportional to their M_w, rather than the shape of the domains that they form.

An infinite molecular weight is not the only condition for the occurrence of flow split at the capillary exit. The fluid must also have good crack propagation properties, as PB does.

To verify the hypothesis of an infinite M_w causing flow split, a linear PB with M_w of 600000 g/mol was extruded at room temperature (~ 23°C) with a capillary rheometer. The ratio M_w/M_e is of the order of 400 for this PB. Notice that this M_w represents a 50% increase over the highest M_w value considered by Zhu [26]. Capillaries with L/D ratios of 10/2 and 50/5 were used in these tests. Extrusion was performed under fixed mean shear stress conditions since macroscopic slip at the wall had already been triggered with the lowest piston speed.

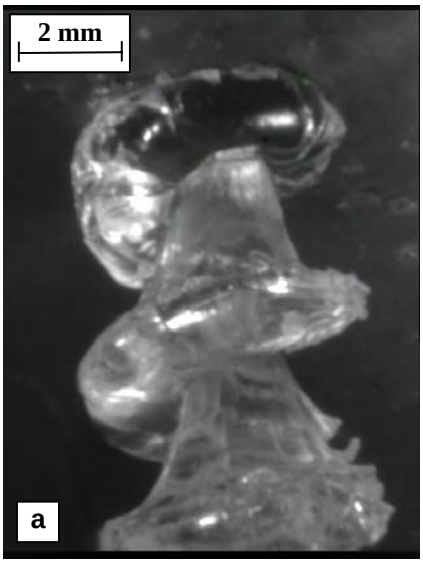

(a) L/D = 10/2, ΔP = 50x10^5 Pa

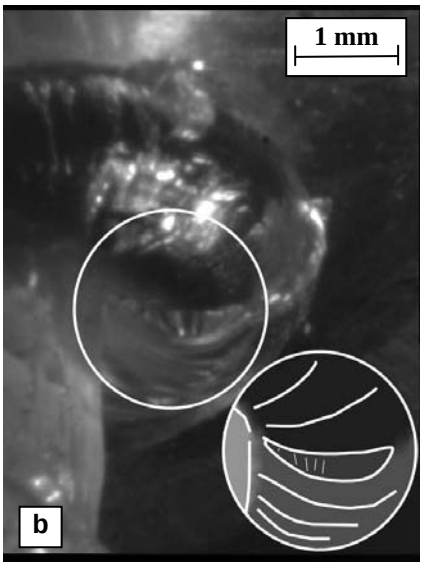

(b) L/D = 50/5 and ΔP = 80x10^5 Pa. t=0 sec

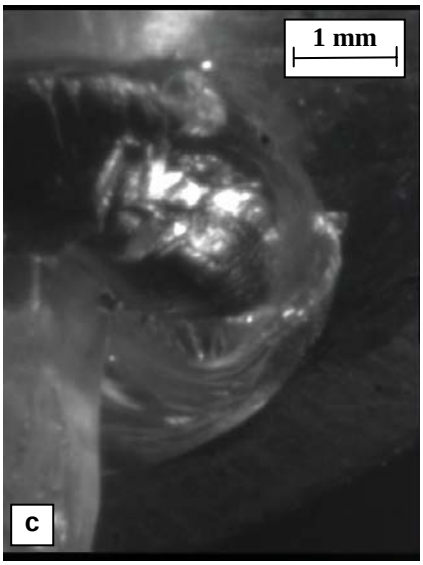

(c) L/D = 50/5 and ΔP = 80x10^5 Pa. t~40 sec

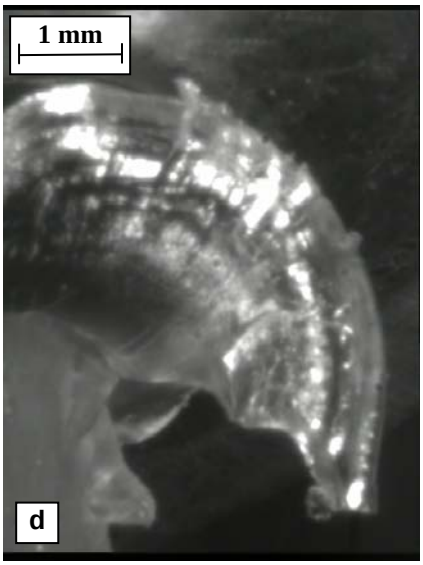

(d) L/D = 50/5 and ΔP = 80x10^5 Pa. t~200 sec

Figure 18: Polybutadiene of Mw = 600000 g/mol exiting the die during fixed mean shear stress experiments. Caption (a) L/D *= 10/2 and ΔP = 50x10^5 Pa. Captions (b) through (d)* L/D *= 50/5 and ΔP = 80x10^5 Pa.*

Extrusion defects of this PB are very similar in shape to those presented by SEBS-1 and SEBS-2, as can be seen in the captions presented in Figure 18. Caption (a) corresponds to the capillary with L/D of 10/2 and a pressure drop of 50x10^5 Pa. The successive polymer rings, similar to those presented in Figures 9(h) and 9(i), show the appearance of secondary cracks. However, stress concentrations in the ring are not yet large enough for these secondary cracks to propagate as much inside the core region of the extrudate. Propagation of secondary cracks that might lead to flow split at the die exit can be observed in captions (b), (c) and (d) of Figure 18. These captions were obtained with the 50/5 capillary and a pressure drop of 80x10^5 Pa. The images captions in Figure 18 are strong evidence that flow split at the capillary exit may also occur with PB homopolymers of sufficiently high-molecular

weight. However, in the case of SEBS copolymers, reinforcement due to PS microdomains and grain structure may lead to localized stress and strain concentrations that will magnify secondary cracks.

To understand the mechanism leading to secondary cracks better, the diagram on Figure 8 will be used. The arrows on the drawing roughly represent the flow field in the extruded polymer. Extensional stresses at the die exit, due to the change in velocity profile, create primary cracks that propagate well into the core of the extrudate. The polymer ring is formed from the accumulated polymer in the trailing edge of the primary crack. The polymer at the surface of the ring is stretched, as shown by the drawn concentric rings of increasing diameter. When the polymer is stretched too much, it will fracture in the radial direction. If there are multiple fractures in one polymer ring, they will eventually generate flow splitting at the die exit.

Secondary cracks are just a stress release mechanism equivalent to that for primary cracks. In both cases their appearance is periodical. Secondary cracks will occur radially because of the axisymmetric nature of the polymer rings, whereas flow at the surface of the extrudate at the die exit can be locally considered as 2-D, and thus primary cracks will initially be transversal to the extrusion direction.

With low stresses, a single secondary crack may be sufficient to release all excessive stresses in one ring. However as stress levels become higher, several secondary cracks will be necessary. The periodicity of these secondary cracks can be clearly seen in caption (p) of Figure 9.

2.6 Conclusions

This study examines flow distortions that are prone to occur during the extrusion of block copolymers and SEBS in particular. A linear high-molecular weight PB was also considered for comparison.

To elucidate this question, three different SEBS and a linear PB (M_w = 600000 g/mol) were considered. Two of the SEBS, SEBS-1 and SEBS-2, contain 30% PS and show a HPC morphology for the extrusion temperatures studied. The third one, SEBS-3, contains 13%PS and forms spherical (S) domains for the temperatures reported in the present paper.

The three SEBS were characterized using small-strain oscillatory shear rheometry experiments, differential scanning calorimety and size exclusion chromatography coupled to a multiple-angle scattering device. Our results, presented in section 2, agree well with those published elsewhere [14] for SEBS-2 and SEBS-3. Moreover, in the case of the viscoelastic functions G' and G" the master curves presented here extend on those already published by Daniel and Hamley [14] for the HPC morphology by nearly 5 decades of frequency.

Experiments at different extrusion temperatures revealed the best experimental window to catalogue the different distortions presented by these SEBS. They were filmed at the die exit.

Special attention was paid to the initiation of surface cracking, which can be severe enough in these fluids to cause the extrudate to split into several branches at the die exit, with or without a core rod being extruded.

Extrusion experiments showed that primary cracks appear initially and that the stresses in the newly formed surfaces can create secondary cracks. These secondary cracks propagate in the radial

direction at faster rates than the mean velocity of the polymer exiting the die. Thus, they can merge at the center of the die exit and split the melt flowing out of the die into several branches. In large diameter dies, or with high enough mean flow velocities, primary cracks can propagate deeper into the polymer than secondary cracks. In this case a smooth, transparent, polymer core, free of defects, is observed during the extrusion experiments.

Our films showed that when these SEBS and the linear PB of M_w = 600000 g/mol are extruded, secondary surface cracks can occur on the surfaces newly created by the primary cracks. Moreover, the films show that flow splitting is initiated by these secondary surface cracks occurring at the polymer melt rings that are formed at the die exit. A necessary condition, but probably not the only one, for these cracks to occur is a sufficiently high entanglement ratio M_w/M_e, or an equivalent infinite molecular weight. In addition, the polymer at hand must have good crack propagation properties.

In section 5, we were able to estimate the order of magnitude of crack propagation speeds for both primary and secondary cracks. Secondary cracks propagate faster than primary cracks.

The work presented in this paper has shown that flow split at the capillary exit can be considered as a very severe case of surface cracking. This study has also shown that at high shear rates, the behavior of the block copolymer is similar to that of the middle rubbery PEB block.

2.7 References

[1] M.M. Denn, Issues in viscoelastic fluid mechanics, Ann Rev Fluid Mech., 22 (1990) 13-34.

[2] J-M. Piau, N. El Kissi; F. Toussaint, A. Mezghani, Distortions of polymer melt extrudates and their elimination using slippery surfaces, Rheol Acta, 34 (1995) 40-57.

[3] M.M. Denn, Extrusion instabilities and wall slip, Ann Rev Fluid Mech., 33 (2001) 265-297.

[4] S.G. Hatzikiriakos and K.B. Migler, editors, Polymer processing instabilities-Control and understanding, Marcel Dekker, New York, 2005.

[5] J-M. Piau, Adherent and slippery walls for extrusion of entangled polymer melts and compounds. Macro98 world polymer congress, Gold Coast, 12-17 July 1998, Macromolecular Symposia, 1999, 269-289.

[6] F.S. Bates and G.H. Fredrickson, Block copolymer thermodynamics: Theory and experiment, Ann Rev Phys Chem., 41 (1990) 525-557.

[7] G.H. Fredrickson and F.S. Bates, Dynamics of block copolymers: Theory and experiment, Ann Rev Mater Sci., 26 (1996) 501-550.

[8] I.W. Hamley, The physics of block copolymers, Oxford Press, 1998.

[9] G.V. Vinogradov, V.P. Protasov, K.E. Dreval, The rheological behavior of flexible-chain polymers in the region of high shear rates and stresses, the critical process of spurting, and supercritical conditions of their movement at $T>T_g$, Rheol. Acta, 23 (1984) 46-61.

[10] N. El Kissi and J-M. Piau, The different capillary flow regimes of entangled polydymethylsiloxane polymers: Macroscopic slip at the wall, hysteresis and cork flow, J Non-Newtonian Fluid Mech., 37 (1990) 55-94.

[11] Piau JM, N. El Kissi, A. Mezghani, Slip-flow of polybutadiene through fluorinated dies, J. of Non-Newt Fluid Mech., 59 (1995) 11-30.

[12] Y.W. Inn, R.J. Fischer, M.T. Shaw, Visual observation of development of sharkskin melt fracture in polybutadiene extrusion, Rheol. Acta, 37 (1998) 573-582.

[13] M. Fernández, A. Santamaria, A. Muñoz-Escalona, L. Méndez, A striking hydrodynamic phenomenon: Split of a polymer melt in capillary flow, J. Rheol., 45 (2001) 595-602.

[14] C. Daniel. and I.W. Hamley, Extensional and shear rheometry of oriented triblock copolymers, Rheol. Acta, 39 (2000) 191-200.

[15] C. Daniel, I.W. Hamley, K. Mortenesen, Effect of planar extension on the structure and mechanical properties of polystyrene-poly(ethylene-co-butylene)-polystyrene triblock copolymers, Polymer, 41 (2000) 9239-9247.

[16] L.J. Fetters, D.J. Lohse, R.H. Colby, Chain dimensions and entanglements spacings. In: J.E. Mark (Ed.) Physical properties of polymers handbook,American Insitute of Physics, Woodbury, New York, 1996, Chapter 24.

[17] J.H. Rosedale and F.S. Bates, Rheology of ordered and disordered symmetric poly(ethylenepropylene)-poly(ethyleethylene) diblock copolymers, Macromolecules, 23 (1990) 2329-2338.

[18] J. Zhao, B. Majumdar, M.F. Schulz, F.S. Bates, K. Almdal, K. Mortensen, D.A. Hajduk, S.M. Gruner, Phase behavior of pure diblocks and binary diblock blends of poly(ethylene)-poly(ethylethylene), Macromolecules, 29 (1996) 1204-1215.

[19] M.B. Kossuth, D.C. Morse, F.S. Bates, Viscoelastic behavior of cubic phases in block copolymer melts, J. Rheol., 43 (1999) 167-196.

[20] C.Y. Ryu, M.S. Lee, D.A. Hadjuk, T.P. Lodge, Structure and viscoelasticity of matched asymmetric diblock and triblock copolymers in the cylinder and sphere microstructures, J. Polym. Sci.: Part B: Polym. Phys., 35 (1997) 2811-2823.

[21] J.D. Ferry, Viscoelastic properties of polymers, 2nd ed. John Wiley and Sons, 1970, Chapter 11.

[22] L.I. Palade,V. Verney, P. Attané, Time-Temperature Superposition and linear viscoelasticity of polybutadienes, Macromolecules, 28 (1995) 7051-7057.

[23] H.H. Winter and F. Chambon, Analysis of linear viscoelasticity of a crosslinking polymer at the gel point, J. Rheol., 30 (1986) 367-382.

[24] T. Kotaka, M. Okamoto, A. Kojima, Y.K. Kwon, S. Nojima, Elongational flow-induced morphology change of block copolymers part 1. A polystyrene -block-poly(ethylene butylenes)-block-polystyrene-block-poly(ethylene butylenes) tetrablock copolymer with polystyrene spherical microdomains, Polymer, 42 (2000) 1207-1217.

[25] D.V. Boger, Viscoelastic flows through contractions, Ann. Rev. Fluid Mech., 19 (1987) 157-182.

[26] Z. Zhu, Wall slip and extrudate instability of 4-arm star polybutadienes in capillary flow, Rheol. Acta, 43 (2004) 373-382.

CH. 3

Chapitre 3

Extrusion des copolymeres triblocs. Structure induite par l'ecoulement et defauts macroscopiques

[Version Abregee]

Les débits de production pendant la mise en forme des polymères, et en particulier pendant leur extrusion, sont souvent limités par les défauts susceptibles d'apparaître à la singularité en sortie de la filière quand les niveaux de contraintes sont trop élevés. Les contraintes élongationnelles présentes en sortie de filière peuvent générer des fissures sur la surface du matériau. Ce phénomène de fissuration est appelé, même si sans justification physique, défaut de *peau de requin*.
Pour certains polymères, les fissures peuvent être si sévères que l'extrudat se refente en sortie de la filière. Fernández *et al.* (2001) ont été les premiers à présenter un cas aussi sévère de fissuration pour deux copolymères statistiques d'éthylène et de propylène. Ils l'ont décrit par le terme *flow split* que nous avons traduit par *refente d'extrudat*. Plus récemment le même phénomène a été observé par Zhu (2004) pour deux polybutadiènes en étoile.
Les résultats présentés dans le chapitre 2 de ce mémoire ont permis d'identifier l'origine de la refente d'extrudat: la coexistence de deux systèmes de fissuration à la sortie de la filière. Ces deux systèmes de fissuration n'étaient observés que pour deux SEBS contenant 30% en polystyrène. Un troisième SEBS avec 13%PS en masse ne présentait pas la refente de l'extrudat.

L'objectif du chapitre 3 est de mieux comprendre pourquoi la refente d'extrudat a été observée dans le cas des SEBS avec 30%PS (SEBS-1 et -2), de morphologie cylindrique, et pas pour le SEBS 13%PS (SEBS-3) présentant une morphologie sphérique. Les deux morphologies sont représentées de façon schématique en Figure 1 (p. 109). Pour cela nous avons examiné en le comportement viscoélastique de ces copolymères dans leur domaine linéaire aux températures d'extrusion étudiés : 190°C dans le cas du SEBS-1 et -2 et 110°C dans le cas du SEBS-3. Ensuite nous avons couplé la diffusion de rayons X aux petits angles et l'extrusion des copolymères en développant un rhéomètre capillaire portable équipé d'une filière usiné en béryllium qui est transparente aux rayons X. Elle permet d'observer in-situ le polymère qui coule à l'intérieur de la filière.

Des essais en rhéométrie dynamique dans le domaine linéaire, et l'application du principe d'équivalence temps-température comme proposé par Ferry (1970), nous a permis de caractériser le comportement viscoélastique des copolymères utilisés aux températures d'extrusion. Les courbes maîtresses résultantes sont présentées en Figure 3 (p. 113) pour le SEBS-1 et en Figures 4 et 5 (p. 113-114) pour les SEBS-3. Pour les trois SEBS considérés, l'évolution du module élastique et du module de perte en fonction de la fréquence est caractéristique des copolymères à blocs dans leur état de séparation de phases à l'échelle micronique. Deux plateaux bien distincts sont observés. L'un aux « hautes » fréquences qui est caractéristique des blocs constituants la matrice. L'autre plateau est observé aux « basses » fréquences ou les temps longs. Il est représentatif des microdomains de PS submergés dans la matrice de PS qui sont organisées dans de grains de taille caractéristique de l'ordre des quelques centaines de microns.
En considérant seulement les températures pour lesquelles les SEBS présentent une séparation de phases à l'échelle micronique nous avons modélisé le comportement viscoélastique en combinant deux spectres dits de BSW+CW. Ces spectres sont empiriques mais ils s'avèrent adéquats pour un

grand nombre de polymères à chaînes flexibles et monodisperses. Le spectre dit de BSW est le résultat de la superposition de deux régions en loi de puissance qui décrivent le régime vitreux et le régime caoutchoutique à l'aide de deux pentes $-n_g$ et $-n_e$ respectivement. La contribution de CW tient compte d'une éventuelle réticulation du polymère. L'expression mathématique du spectre de BSW+CW est donnée par l'équation (1a) en p. 116. Comme les valeurs dans le Tableau 1 (p. 109) le montrent, la polydispersité de nos SEBS est inférieure à 1.12 et donc l'utilisation du spectre de BSW semble justifiée. Dans notre modélisation, le premier spectre tient compte de la réponse du PEB et le deuxième spectre apporte la contribution de l'ensemble des microdomaines de PS distribués dans des grains. Cette contribution est exprimée en terme de structure moléculaire des blocs de PS en fin de chaînes. Le poids de la contribution de chaque spectre a été déterminé empiriquement. Des paramètres qui donnent une bonne approximation sont présentés en Tableau 3 (p. 117). En Figures 7 et 8, (pp. 118-119) nous avons tracé les valeurs de G' et G'' calculées à partir de le spectre calculé ainsi que les données expérimentales. Un bon accord existe entre les deux pour la gamme de fréquences caractéristique du défaut de refente d'extrudat : 0.02-4 rad/s. D'après la valeur de la pente n dans le spectre de CW, nos résultats semblent montrer que les SEBS-1 et -2 ont un degré de réticulation plus avancé que le SEBS-3 et donc une masse molaire apparente plus élevée. De plus, es temps de relaxation peuvent être jusqu'à 300 fois plus longs que ceux prédits par la théorie pour des homopolymères de masse molaire équivalente à celle des blocs. Pour mieux comprendre la physique sous-jacente à la réponse viscoélastique des copolymères à blocs nous avons comparé la réponse expérimentale à celle prédite pour des homopolymères de masse molaire équivalente à la même température (Figure 9, p.120). Cette comparaison a permis de montrer que le plateau observé aux basses fréquences ne correspond pas à la réponse des blocs de PS en fin de chaînes, mais à l'ensemble des microdomaines de PS montrant un ordre cohérent dans un grain.

La caractérisation en écoulement a été faite avec deux rhéomètres capillaires différents : un Göttfert Rheograph 2001 et un rhéomètre capillaire conçu et développé au Laboratoire qui est équipé d'une filière en béryllium transparente aux rayons X et permettant des observations in-situ. La filière est un capillaire avec un rapport longueur sur diamètre de 10/2 et une épaisseur de paroi de 1.25 mm. Elle peut supporter des pressions maximales de 200 bars. Un schéma de ce rhéomètre et de la filière est présenté en Figure 2 (p. 111). Les courbes d'écoulement ont montré que le comportement aux grandes déformations et aux petites déformations diffère. Nous expliquons la différence par la disparition des jonctions entre grains lorsque ceux-ci s'orientent dans le sens de l'extrusion.

A l'aide de ce rhéomètre et des grands instruments de mesure disponibles à l'ESRF de Grenoble, nous avons suivi les changements structuraux subis par les copolymères au long du chemin d'extrusion. L'état du copolymère dans le réservoir a été modélisé par une phase de compression à l'état solide et une deuxième phase où le copolymère fond. La figure de diffusion caractéristique de cet état est présentée en Figure 14 (p. 126) pour le SEBS-1. Dans ces conditions, le matériau est isotrope aux échelles du volume examiné (0.3x0.3x1 mm^3).

La filière en Béryllium a été remplie à un régime instable (14.4 s^{-1} et 150°C), elle a été démontée du rhéomètre, laissée refroidir à température ambiante, et nous avons observé le copolymère à distances de l'entrée de la filière allant de 2.5 mm jusqu'à 9.5 mm par intervalles de 1 mm. Nous avons observé que sur toutes les distances examinées, les cylindres de PS du SEBS-1 étaient globalement orientés dans la direction de l'extrusion (Figure 15, p. 126). C'est-à-dire que l'orientation des domaines cylindriques se fait principalement au voisinage de la contraction en entrée de la filière. Une analyse plus détaillée de l'anisotropie des pics de diffusion sur ces images a révélé que les effets de la contraction d'entrée sur la déformation des domaines se propagent à des distances d'environ 3 diamètres en aval de la contraction. Nous avons constaté également que l'orientation des cylindres n'est pas la même sur toute la longueur de la filière. Des variations d'orientation irrégulières sont observées à des échelles de 1-3 mm. Ces tailles coïncident avec les défauts macroscopiques présentés par le copolymère. En effet, l'extrudat en sorite de filière semble couler par paquets successifs (Figure 18, p. 130). On les interprète comme les images publiées dans les travaux de Bergem (1976).

Finalement, on n'observe pas de différences importantes entre les images obtenues dans la filière et en sortie de filière.

La comparaison entre les essais de diffusion de rayons X faits avec le SEBS-1, avec des cylindres de PS, et le SEBS-3, contenant des sphères de PS ont montré que les cylindres de PS s'orientent dans le sens de l'extrusion mais que leur diamètre moyen ne change pas. Par contre, nous avons observé que dans le cas du SEBS-3, les domaines sphériques deviennent ovales. Le manque de déformation des cylindres induit des concentrations locales de contraintes au voisinages des jonctions des grains qui sont riches en PEB. Dans le cas du SEBS-3 les microdomaines de PS se déforment à l'intérieur de la filière et donc, le champ de contraintes est plus homogène et les fissures se propagent de la même façon que pour un polybutadiène.

CHAPTER 3

BLOCK COPOLYMER EXTRUSION: FLOW INDUCED STRUCTURE AND MACROSCOPIC DEFECTS.

ENRIC SANTANACH CARRERAS, NADIA EL KISSI, JEAN-MICHEL PIAU[A)], AND FRÉDÉRIC PIGNON
Laboratoire de Rhéologie[**], B.P. 53, Domaine Universitaire, 38041 Grenoble cedex 9 (France)

PIERRE PANINE
Beamline ID02, ESRF, BP 220, 38043 Grenoble (France)

Key words: *Block copolymer, extrusion, structure, macroscopic defect, dynamic rheometry, SAXS*

PROVISIONAL VERSION. THE FINAL MANUSCRIPT, TO BE SUBMITTED FOR PUBLICATION, IS IN PREPARATION.

a) Author to whom all correspondence should be addressed. Electronic mail: jmpiau@ujf-grenoble.fr

** *Université Joseph Fourier-Grenoble I, Institut National Polytechnique de Grenoble, CNRS (UMR 5520*)

Abstract

This paper proposes an explanation in terms of structural changes for the appearance, or not, of flow split at the capillary exit during the extrusion of three SEBS block copolymers in their microphase separated state. We present a possible relaxation time spectrum for these block copolymers as a combination of two BSW+CW spectra; one corresponding mainly to the PEB matrix and the other one corresponding to the PS microdomains within organized grains. The terminal region is estimated to be at shear rates lower than about 10^{-2} s^{-1} at the extrusion temperatures considered. The long relaxation times have allowed to probe the evolution of PS microdomains structural changes during the extrusion process. For this, a capillary rheometer equipped wih a beryllium die, transparent to X-rays, has been developed.

SAXS experiments have shown that during the extrusion of the SEBS presenting flow split, the cylindrical PS microdomains in these copolymers align in the flow direction. Enhanced local stresses are thus created at vanishing grain junctions when the melt is elongated at the singular die exit. The spherical PS microdomains present in the SEBS that did not show flow split, deform and become oval-shaped inside the die. Thus, only limited changes in the stress field can be created by the PS microdomains.

3.1 Introduction

Throughput rates during polymer processing operations and in extrusion in particular are often limited by defects that are prone to originate at the singularity of the die exit when stresses in the fluid are sufficiently high. At this point, the velocity profile of the melt exiting the die passes from a parabolic one to a flat one, which leads to high tensile stresses in the fluid. These stresses can be so high, that the polymer surface cracks. This surface cracking phenomenon leads to what is generally known (though without physical justification) as sharkskin.

Surface cracking can be so severe that the polymer exiting the die completely splits. Fernández and co-workers (2001) initially reported on this extreme case of surface cracking and coined the term "flow-split" to describe it. Their observations were made on three statistical copolymers of ethene and propylene. More recently, Zhu (2004) also observed similar defects for two 4-arm star polybutadienes of molecular weights (M_w) of 200000 and 400000 g/mol. Not until recent work by Santanach Carreras *et al.* (2005) has the birth of flow split been detailed. By extruding different SEBS block copolymers in their microphase-separated states at various temperatures, the authors were able to identify the presence of two stress release systems coexisting at the die exit. The longitudinal cracks propagating in the extrusion direction of the secondary stress release system being responsible for flow split. Moreover, their work shows that these secondary cracks will appear for apparent infinite molecular weights as long as the fluid has good fracture propagation properties. Though SEBS of similar molecular weights were used, only the ones with 30% polystyrene (PS) in mass content showed flow split.

The intention of the present work is to explain better why the flow-splitting phenomenon is only observed for the SEBS with 30%PS and not for the SEBS with 13%PS presenting spherical PS microdomains. Starting from the structure of the melt inside the barrel, data has been obtained to describe the way the microstructure of the copolymer changes under flow conditions through the die until the extrudates are obtained. The results presented will show that the cylindrical microdomains are likely to enhance local stresses in the fluid. On the other hand, the more mobile and shorter spherical microdomains of the SEBS with 13%PS can deform and allow smoother stress fields to develop within the fluid.

The work is divided in five sections. In the following one, section II, the material used, the experimental means that have been utilized, and the experimental procedures are presented. As a novelty, we present a capillary rheometer that has been developed in-house and that is equipped with a capillary die machined out of Beryllium (Be), which allows for Small Angle X-ray Scattering observations inside the die.

The results are described in section III that is divided in three subsections. The first subsection shows that the small strain oscillatory shear response can be modeled in terms of two BSW+CW spectrums that account for the response characteristic of the polystyrene microdomains. The agreement between experimental data and the fits obtained from the model spectra is good.

In the second subsection the flow curves corresponding to the two SEBS used, and the macroscopic defects of interest for the present paper, are presented. In this subsection the use of the in-house developed capillary rheometer is verified by comparison of the flow curves obtained with it and those obtained with a Göttfert Reograph 2000, a commercially available capillary rheometer.
The third subsection focuses on the observations performed using SAXS experiments on Beamline ID02 of the ESRF, Grenoble. The changes in organization and deformation of the PS microdomains through the different stages of the extrusion process will be followed by replicating the conditions in the melt barrel, by performing experiments in the Be die, and finally by probing the structure in relaxed extrudates. Our results will show that the orientation is mostly due to the flow field near the die entrance. In addition, SAXS experiments will evidence that the cylindrical PS microdomains are oriented by the flow field. However, they do not change in diameter. On the other hand, the spherical microdomains will be deformed and oriented by the flow field.
Section 3.4 presents the discussion of the results. It shows that both the space distribution and the deformation of the PS spherical microdomains permit surface cracks to propagate in a way similar to the case of polybutadiente melts, i.e. not as far as in the case of the SEBS with 30%PS and cylindrical microdomains. Since the cylindrical microdomains do not seem to break-up into small segments, the only way for the fluid to relax stresses is to fracture severely along vanishing grain boundaries.
Finally, some concluding remarks are presented in section 3.5.

3.2 Experiments

3.2.1 Materials

Three SEBS {polystyrene-*block*-poly(ethylene-*co*-butylene)-*block*-polystyrene} have been considered in their microphase-separated state. The three of them have similar overall molecular weights (M_w) but two of them, SEBS-1 and SEBS-2, contain about 30%PS in mass whereas SEBS-3 has 13%PS in mass. At the extrusion temperatures considered, SEBS-1 and SEBS-2 showed PS cylindrical microdomains in a rubbery matrix of PEB that are hexagonally packed for the processing temperatures considered. SEBS-3 microphase separated into PS spherical microdomains at 90°C. In Figure 1, a schematic representation of the morphologies at rest and room temperature and pressure conditions is shown. The systems are formed of polymer chains that form the PS microdomains and the matrix. These microdomains are in turn organized within grains with characteristic scales of about 1000 nm.

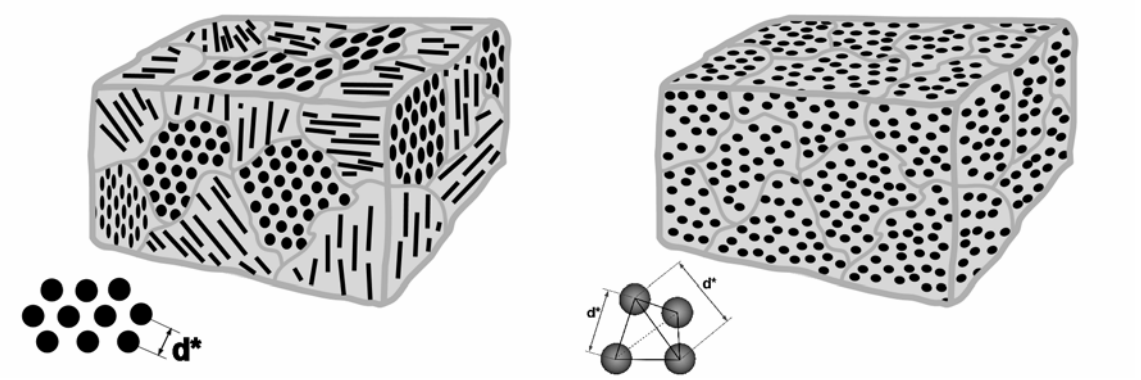

Figure 1: Morphologies presented by the different SEBS considered in this study. Left: cylindrical microdomains of PS hexagonally packed in a matrix of PEB (SEBS-1 and -2). Right: spherical microdomains of PS with no long range order in the PEB matrix (SEBS-3). In both cases the PS microdomains (d~20-30 nm) are organized within grains of ~1000 nm in length.*

The different morphology transitions of these block copolymers have been determined by means of DSC and small-strain oscillatory shear experiments. Table 1 reports the transition temperatures altogether with the principal characteristics of the fluids used.

	Material	Producer	PS weight content (%)	M_w* (g/mol)	M_w/Mn *	$T_{g,PS}$ (°C)	$T_{g,PEB}$ (°C)	Morphology		
								Room T	OOT	ODT
SEBS-1	SEBS 30%PS	Polimeri Europa SpA	~30	44400	1.09	100	-40	HPC	~280 °C	N/R‡
SEBS-2	G-1650	Kraton® Polymers	30	*75000*[‡‡]	*1.12*[‡‡]	*96*[‡‡]	-42**	HPC	~280 °C	N/R‡
SEBS-3	G-1657	Kraton® Polymers	13	37600 *70000*[‡‡]	1.10 *1.05*[14]	*75*[‡‡]	-42**	S	-	140 °C

* Values obtained with LALS measurements

** Values obtained from manufacturer

‡ N/R stands for "Not Reached" before thermal degradation of the copolymer

‡‡ Values from Daniel and Hamley (2000)

Table 1: Principal characteristics of the ABA triblock copolymers used in this study.

3.2.2 Small-strain oscillatory shear experiments

All oscillatory shear experiments were carried out on an ARES rheometer using parallel plate tooling of 25-mm and 10-mm diameter. The height of the gap varied between 1 and 2 mm. Firstly, the linear response viscoelastic regime was determined with isochronal, isothermal, strain sweeps. Then, isothermal frequency sweeps were carried out at different temperatures. For all temperatures, the range of frequencies covered was 10^{-1}-10^{2} s^{-1}, but points at frequencies as low as 10^{-3} s^{-1} were measured exceptionally.

An air-heated oven was used to keep the sample at temperature during the experimental runs. In addition, a nitrogen purge was used to avoid thermal degradation of the samples at high temperatures: T>220°C in the case of SEBS-1, and SEBS-2 and T>190°C in the case of SEBS-3. The time needed to reach thermal equilibrium was monitored by performing time sweeps at fixed temperature and strain (within the linear viscoelastic response regime). A constant torque response was observed roughly 3

minutes after the platinum resistance thermometer, placed underneath the lower plate, indicated the desired temperature.

Samples were prepared by initially compressing the SEBS in its solid state and then melting it in a mold. The procedure was as follows: the mold was filled with SEBS and closed as tight as possible at room temperature. The mold was then placed in an oven for approximately 45 minutes and the copolymer was allowed to melt and flow within the mold cavity. Sheets between 1 and 2 mm thick were obtained, from which disk-shaped samples were cut and used for dynamic rheometry experiments. This sample preparation method produced macroscopically isotropic samples as observed in SAXS experiments.

No pre-shearing of the samples was performed before the isothermal frequency sweep tests, thus the storage (G') and loss (G") moduli measured are characteristic bulk properties of a randomly oriented sample that can be considered as isotropic at volumes scales characteristic of the samples.

3.2.3 Capillary rheometry

Two different capillary rheometers were used.

On one hand, a Göttfert Rheograph 2000 was used for the capillary rheometry experiments. Both fixed piston speed and fixed pressure drop experiments were performed, allowing a flow curve spanning over 5 decades to be plotted. Fixed pressure drop experiments were used to obtain data at mean flow rates lower than 5.65×10^{-11} m^3 s^{-1}, attainable at the lowest piston speed. During the fixed pressure drop experiments, a small floating PTFE piston was placed between the molten copolymer and the nitrogen gas used to force it through the die. This piston ensured that the pushing force was applied uniformly over the entire cross-section of the melt in the reservoir of 12 mm diameter. The pressure was fixed with a valve and was read on a manometer. In addition, the output voltage of a class 0.5 Dynisco PT420 pressure transducer, placed near the capillary entrance, was traced as a function of time by means of a recorder. Two pressure transducers were used, depending on the pressure drops measured: one was rated at 100×10^5 Pa and the other at 500×10^5 Pa.

The dies used had diameters of 1, 2 and 5 mm. Capillaries with length-to-diameter (L/D) ratios of 15, 10 and 5 were used to keep dissipative heating low yet allowing characterization in shear. In addition, short orifice dies of negligible length were used to correct for entrance effects, unless indicated otherwise.

On the other hand, an in-house developed capillary rheometer equipped with a beryllium die allowing for SAXS measurement inside the die was used. A schematic drawing of the rheometer is presented in Figure 2. This rheometer can work at both fixed mean piston speed or fixed mean pressure conditions. The maximum apparent shear rates attainable in the fixed piston speed mode are of the order of 500 s^{-1}. The piston is driven by a screw actuator that is coupled to a motorgearbox. The rheometer can work at temperatures as high as 150°C. The barrel, of 12 mm in diameter, and the die are kept at temperature by means of two independently-controlled heating coils. However, the most important piece in the rheometer is the die of length 10 mm, 2 mm inside diameter, and a wall thickness of 1.25 mm. The die was machined out of beryllium, which allows for Small Angle X-ray Scattering experiments of the polymer inside the die. This die permitted to observe the effects of the

flow as a function of the abscissa along the die axis. A Force transducer placed behind the test piston allowed to quantify the shear stress at the die wall after friction forces in the reservoir and entrance effects had been accounted for.

Before the experimental runs, the temperature of the melt was registered along the entire die axis and probed after inserting a thermocouple inside the capillary filled with polymer. The temperature was measured while the thermocouple and some polymer were extruded simultaneously. Thanks to the use of a controlled pulsed air heating system blowing at the die exit, temperatures were found to be within 3°C of the nominal temperature at the beginning of the experimental runs.

During the experimental runs, the melt coming out of the die was filmed with a Sony IRIS-CCD high-resolution video camera that was connected to a Wild M-540 macroscope.

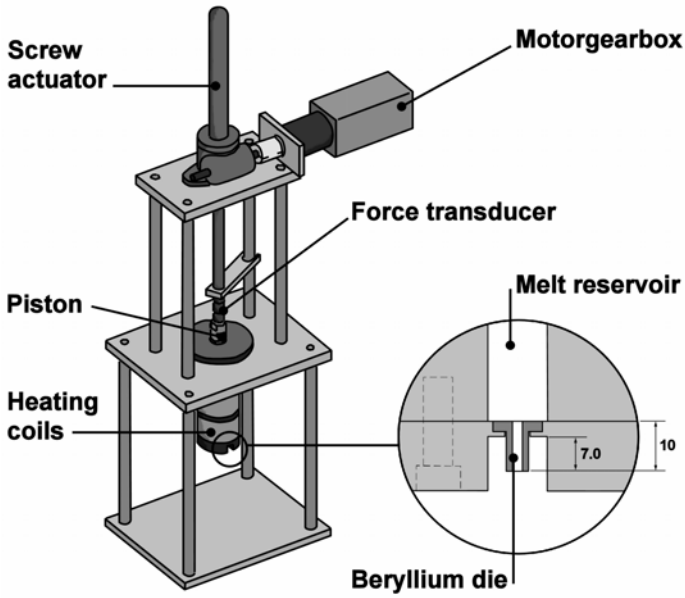

Figure 2: Schema of the capillary rheometer equipped with a die machined out of Beryllium and allowing for in-situ SAXS experiments in the die.

3.2.4 Small Angle X-ray Scattering (SAXS)

Small Angle X-ray Scattering experiments on both compression molded samples as well as cooled down extruded samples were carried out on the High-brilliance beamline (ID02) of the European Synchrotron Radiation Facility (ESRF), Grenoble, France. The capabilities of this line as well as the details on the detectors available have been described elsewhere (Narayanan ***et al.*** 2001).

A sample-to-detector distance of 3 meters was used for most samples, but to ensure no loss of information, some experiments were performed at both 1.2 and 10 meters. The incident X-ray wavelength, λ, was 0.0995 nm leading to a total range of scattering vector, Q, between 0.02 and 4.5 nm^{-1}. Q is defined as $(4\pi/\lambda)\sin(\theta/2)$ with θ being the scattering angle. The cross section of the beam was 0.3x0.3 mm^2.

Experiments were performed on three different types of samples. Firstly, on compression-molded samples that are characteristic the material in the melt barrel. For these tests, the incident beam was

parallel to the compression direction and passed through the center of the disk. Secondly, the Be die filled with polymer was removed from the rheometer and allowed to cool down. The structure as a function of the abcissa was then probed with the incident beam being perpendicular to the axis of symmetry of the die. Thirdly, relaxed extrudates obtained at different flow rates were used. In the case of the relaxed extrudates, experiments were performed with the incident beam both perpendicular and parallel to the extrusion direction.

3.3 Results and analysis

3.3.1 Small strain oscillatory shear and relaxation-time spectra

Figure 3 presents mastercurves of the storage modulus (G') and the loss modulus (G") for both SEBS-1 and SEBS-2 using 190°C as the reference temperature. The time-temperature superposition (TTS) principle was applied as described by Ferry (1970). A vertical shift factor b_T equal to T_{ref}/T was applied where T_{ref} is the reference temperature and T is the temperature at which experiments were performed. Variations in density caused by the temperature changes were neglected. The inset shows the empirical shift factor, a_T, used to reduce shear rates. The solid line represents a fit using the WLF-equation. The fit parameters C_1 and C_2 used are presented in Table 2. The high-frequency end viscoelastic linear response where the signature of the PS microdomains is not observed was matched at the different temperatures (Rosedale and Bates, 1990). Thus, one can expect TTS not to hold at low frequencies since the shift factor a_T used corresponds to the PEB block.

Mastercurves of the storage modulus (G') and the loss modulus (G") of SEBS-3 are presented in Figures 4 and Figure 5 using 110°C as the reference temperature. Two different figures have been used for clarity. The insets in both figures are the same and show the shift factors a_T used at the different temperatures. The solid line represents a WLF-fit and the fit parameters used are reported in Table 2. The lack of superposition at low shear rates for temperatures above 135-140°C is indicative of the order-disorder transition as discussed in work by Rosedale and Bates (1990). In addition, the order-disorder transition temperature agrees well with that one found for the same grade of SEBS in a paper by Daniel and Hamley (2000).

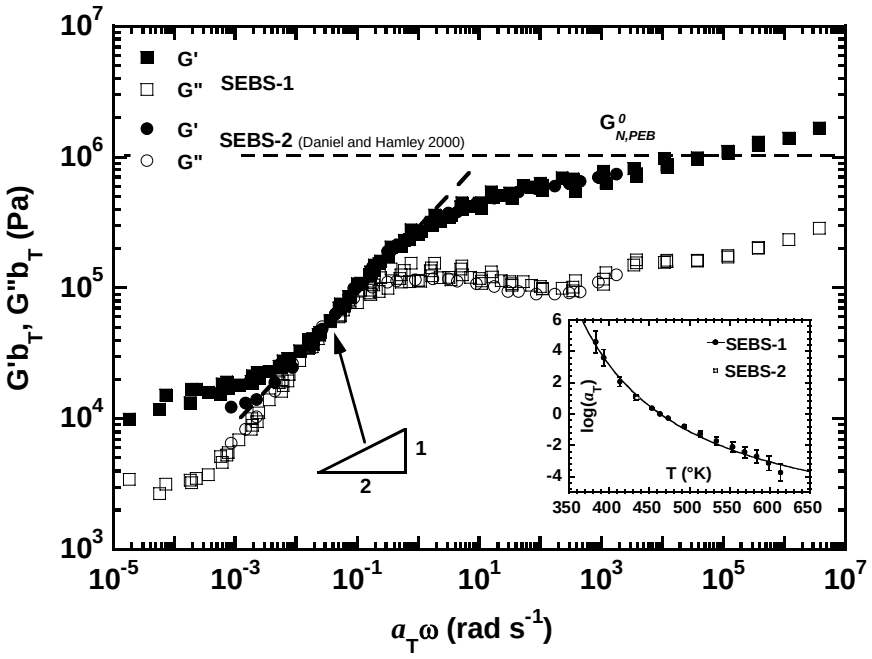

Figure 3: Reduced storage modulus (G'b_T) and reduced loss modulus (G"b_T) as a function of reduced frequency ($a_T\omega$) for SEBS-1 and SEBS-2 with cylindrical PS microphases using 190°C as reference temperature.

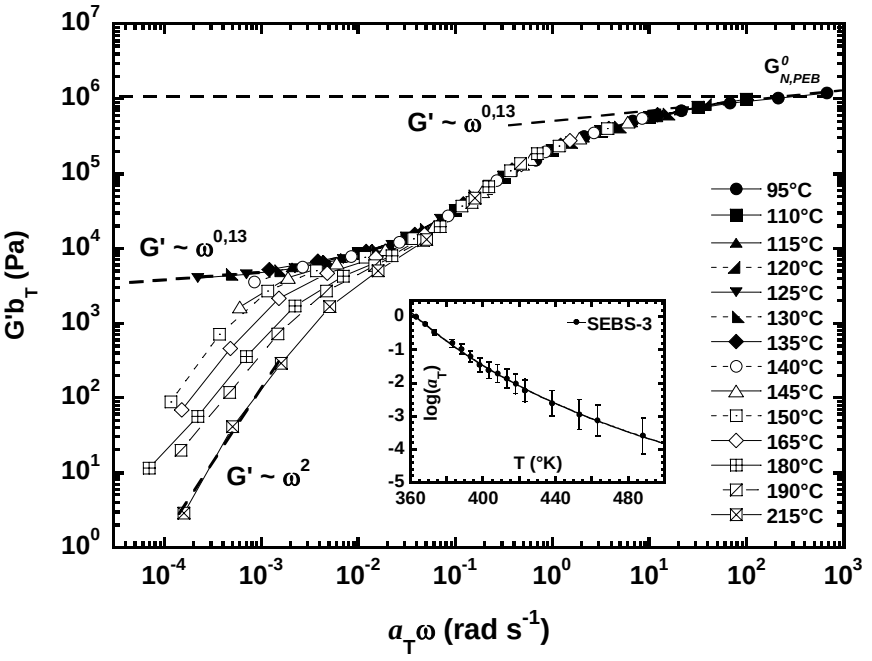

Figure 4: Reduced storage modulus (G'b_T) as a function of reduced frequency ($a_T\omega$) for SEBS-3 using 110°C as reference temperature.

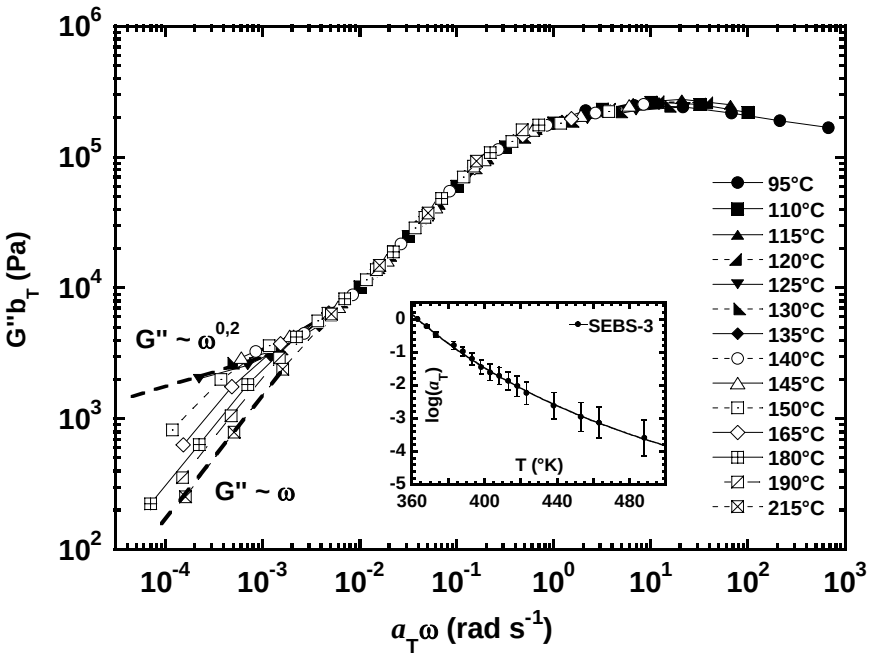

Figure 5: Reduced loss modulus ($G''b_T$) as a function of reduced frequency ($a_T\omega$) for SEBS-3 using 110°C as reference temperature.

	SEBS-1 (T_{ref} = 190°C)	SEBS-2 (T_{ref} = 190°C)	SEBS-3 (T_{ref} = 90°C)
C_1	8.2	7.1	6.6
C_2 (°K)	230.4	229.4	147.5
WLF-equation: $\log(a_T) = \frac{-C_1(T - T_{ref})}{C_2 + T - T_{ref}}$			

Table 2: WLF equation parameters used to fit the shift factor, a_T, for the three SEBS studied.

In the case of all three SEBS studied, the curves obtained are characteristic of block copolymers in their ordered-state with two plateaus as Kossuth *et al.* (1999) described. One at high frequencies that is related to the entanglement plateau of the species constituting the continuous matrix; PEB in our case. A second plateau is observed at low frequencies and it corresponds to the contribution of the PS microdomains formed by the end-blocks. Hereinafter, the term of lower plateau will be employed to describe it. It is well known that the PS microdomains can show a coherent order within grains of characteristic length scales in the order of 1000 nm. Thus, one could imagine that this lower plateau corresponds to molecular movements of lengths characteristic of the coherent grains. In this way, in the case of SEBS-3 when the order-transition temperature is reached, the different grains dissociate, their structure disappears and so does the lower plateau in the viscoelastic response.

A model of the time-relaxation spectrum of block copolymers can be obtained by borrowing ideas from earlier work by Winter and colleagues (Jackson *et al.,* 1994; Jackson and Winter, 1995; Mours and

Winter 1996) on the flow behavior of monodisperse flexible polymer chains, on bidisperse blends of polystyrene and polybutadiene, and on the relaxation patterns of nearly critical gels.

Figure 6a presents the model spectrum used for each block that is commonly known as a BSW+CW spectrum.

The BSW relaxation time spectrum is an empirical model that has been observed to work well for nearly monodisperse linear polymers. It results from the superposition of two power law regions describing the glass transition and entanglement regimes by means of two slopes $-n_g$ and n_e respectively. In the case of reticulating polymers a third power-law region of slope –n is added. This slope depends on the degree of reticulation of the system. For non-reticulated systems, n tends towards infinity and will reach a value of 0.5 at the gel point (Winter and Chambon, 1986).

Figure 6b presents the resulting spectrum obtained when two BSW+CW spectra are combined. One represents the PEB block and the other one represents the contribution of the PS microdomains in terms of the PS endblock characteristics.

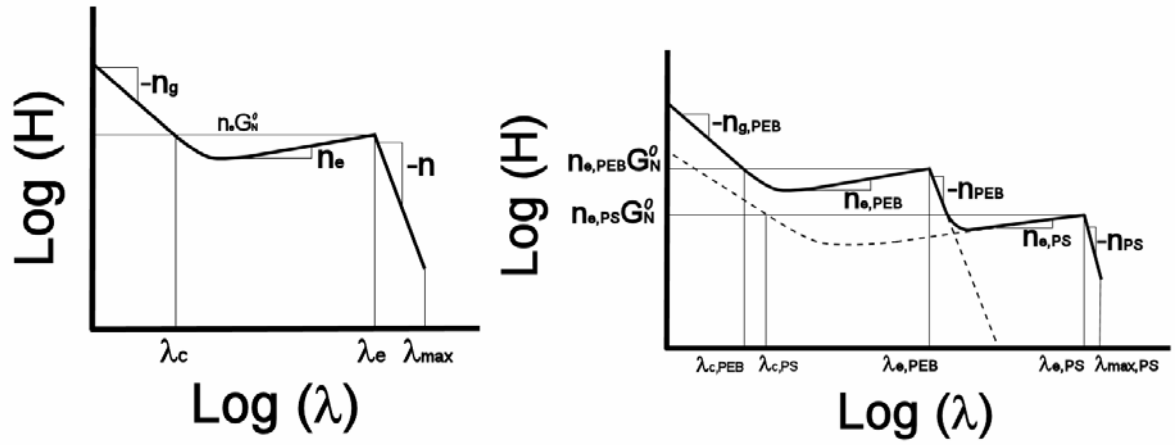

Figure 6: Time-relaxation spectrum used to model the viscoelastic response of block-copolymers in their microphase separated state. The BSW+CW model for monodisperse flexible polymer chains (left). This resulting spectrum when the PEB blocks and PS block are combined.

Mathematically, equation 1a describes the relaxation time spectrum for each block in the macromolecules. The overall spectrum of the block copolymer can then be described as the sum of the spectra of the *i* blocks conforming the macromolecule as expressed by equation 1b. The contribution of each species is weighted by the factor w_i. The sum of all weight factors must equal to 1. In the present case, *i* represents either the PS block or the middle rubbery PEB block following work by Jackson and Winter (1995).

$$H_i(\lambda)\begin{cases} n_{e,i}G^0_{N,i}\left[\left(\frac{\lambda}{\lambda_{c,i}}\right)^{-n_{g,i}}+\left(\frac{\lambda}{\lambda_{e,i}}\right)^{n_{e,i}}\right], & \text{for } \lambda \le \lambda_{e,i} \\ H(\lambda_{e,i})\left(\frac{\lambda}{\lambda_{e,i}}\right)^{-n_i}, & \text{for } \lambda_{e,i} < \lambda < \lambda_{max,i} \\ 0, & \text{for } \lambda \ge \lambda_{max,i} \end{cases} \quad (1a)$$

$$H(\lambda) = \sum_{i=1}^{N} w_i H_i(\lambda) \quad (1b)$$

From the function $H(\lambda)$, the storage (G') and the loss (G") modulus can be calculated (Ferry, 1970) as

$$G'(\omega) = \int_0^\infty H(\lambda)\frac{\omega^2\lambda^2}{1+\omega^2\lambda^2}\frac{d\lambda}{\lambda} \quad (2)$$

$$G''(\omega) = \int_0^\infty H(\lambda)\frac{\omega\lambda}{1+\omega^2\lambda^2}\frac{d\lambda}{\lambda} \quad (3)$$

Using equations (1) through (3) and a trial an error approach an adequate fit of the linear viscoelastic response can be obtained. The model used introduces many parameters due to the complexity of the system studied which makes the fitting procedure that much more difficult. Moreover, this is an inverse problem and many sets of solutions can lead to a relatively good fit of the experimental data. For this reason, we fix as many initial parameter values as possible beforehand. The initial parameter values that have been fixed were:

- Both entanglement plateau modulus (G^0_N): ~10^6-2x10^6 Pa in the case of PEB and 2x10^5 Pa in the case of PS (Fetters *et al.*, 1996). These values should be the same regardless of the SEBS considered.
- The power law slope of the entanglement region, n_e. In the case of the PEB, the initial value was determined from the slope of the curve G"(ω) in the entanglement regime as explained by the Jackson *et al.* (1994). A value in the range 0.10-0.20 was found from Figures 2 and 4. Data in the plateau characteristic of PS was scarce and a slope could not be determined precisely from neither data presented in Figure 2 nor in Figure 4. The values used come from work by Winter and co-workers (1994, 1995) on PS (n_e~0.23).
- The power law slope of the glass transition region, n_g. Our experimental data does not cover this region. Thus, values given in the work by Winter and co-workers for PS (n_g~0.67) and for PB (n_g~0.73) have been used.

Therefore the parameters that need to be evaluated are the different characteristic times $\lambda_{c,i}$, $\lambda_{e,i}$, and $\lambda_{max,i}$ and the near critical gel power law slope, n_{PEB}, for the PEB spectrum. For short and non-entangled PS macromolecules, the power-law slope n_{PS} for the second spectrum must tend towards infinity. However, in the case of PS micrdomain-dominated grains, no information is available about

the appropriate value of n_{PS}. Moreover, little influence of n_{PS}, if any, is expected within the experimental window. Hence, calculations below will be made assuming that n_{PS} equals infinity.

In Table 3, a range of parameters allowing for a satisfactory non-refined fit is given. Notice that the ranges of the different characteristic times can be in the order of a decade thus only upper and lower limits can be extracted. The fit was found to be most responsive to the parameters n, λ_{max}, and λ_e of the PEB blocks. These three parameters give the characteristic shape of the viscoelastic linear response at the rates where flow-split at the capillary exit occurs.

The parameter z presented in Table 3 is the scaling factor exponent of the viscosity-molecular weight relation. The values used in the case of PEB have been taken as those published by Jackson and Winter (1995) for PB. The PS end-blocks molecular weight is smaller than, or at most equivalent to, the entanglement molecular weight of PS, which is in the order of 13000 g/mol. Therefore, we have used a value of 1 for the scaling exponent z in the case of PS.

	SEBS-1 and SEBS-2		SEBS-3	
	PS block	PEB block	PS block	PEB block
Weight content (%)	30	70	13	87
Block M_w (g/mol)	12500	58000	4550	60900
w_i	0.1	0.9	0.05	0.95
G_N^0 (Pa)	$2\ 10^5$	10^6	$2\ 10^5$	10^6
n_g	0.67	0.73	0.67	0.73
n_e	0.16	0.12	0.16	0.18
n	-	**0.75±0.05**	-	**1.2±0.1**
λ_{max} (s)	$2\text{-}8x10^6$	**$>5x10^2$**	$4x10^5\text{-}10^6$	**$>8x10^2$**
λ_e (s)	$2\text{-}8x10^6$	**3-5**	$4x10^5\text{-}10^6$	**8-12**
λ_c (s)	$4x10^{-3}\text{-}10^{-2}$	$10^{-5}\text{-}10^{-4}$	$10^{-3}\text{-}10^{-1}$	$10^{-5}\text{-}10^{-4}$
z	1	3.5	1	3.5

Table3: Fit parameters used for modeling the storage modulus (G') and the loss modulus (G").

Figure 7 presents the modeled curves of G' and G" as a function of frequency (ω) for SEBS-1 and SEBS-2 along with the experimental data points reported at a reference temperature of 190°C. One can observe that the experimental curves for both SEBS-1 and SEBS-2 are nearly identical and the same fit curve can describe them both. The exact fit parameters used are presented within the plot. A good agreement between the experimental data can be observed for frequencies ranging between $4x10^3$ and $2x10^{-5}$ rad/s. We observe that that at high frequencies, the loss modulus experimental data presents a small shoulder that is not followed by the model. Since the corresponding dynamic rheometry experiments were performed at 110°C, one can expect this shoulder, and the subsequent extension of the entanglement plateau, to be representative of the glass transition of the PS microdomains. Work by Daniel and Hamley (2000a) had reported a T_g of 96°C for the PS microdomains of SEBS-2.

The model superposes well to the experimental data and allows estimating the stiffness of the PS microdomains and the upper and lower limits of the characteristic relaxation times. The stiffness of the PS microdomains can be estimated by the power law slope n and in the case of SEBS-1 and SEBS-2

a value of 0.75±0.05 has been considered to give a good fit. This value is not far from the value characteristic of a polymer at its gel point of 0.5 (Winter and Chambon, 1986).

The smallest value of λ_{max} giving an acceptable fit was 500 seconds. In work by Jackson *et al.* (1994) the molecular weight dependence of the longest relaxation time with respect to the critical time, λ_c, is given as $\lambda_{max}=\lambda_c(M/M_c)^z$ where M_c is the molecular weight for entanglement. In the case of PEB, M_c is of 3400 g/mol (Fetters *et al.* 1996). If the parameters presented in Table 3 are considered, a theoretical λ_{max} of 2 seconds can be calculated. This value is of the order of magnitude of the value of λ_e obtained from the fit. However, it is 250 times smaller than the estimate of λ_{max} from the model. Thus, the apparent infinite molecular weight assumption of Santanach Carreras *et al.* (2005) seems justified.

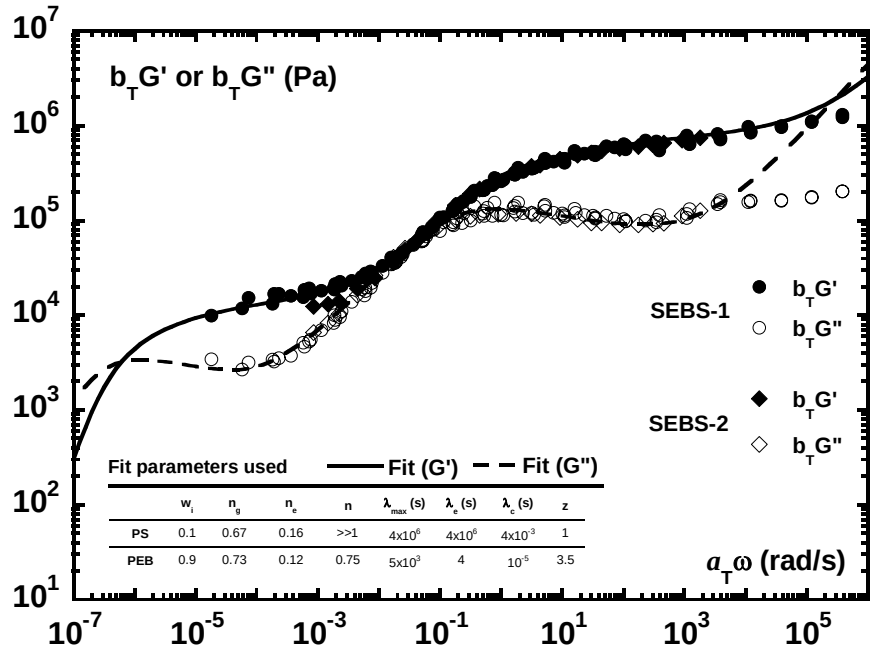

	w_i	n_g	n_e	n	λ_{max} (s)	λ_e (s)	λ_c (s)	z
PS	0.1	0.67	0.16	>>1	$4x10^6$	$4x10^6$	$4x10^{-3}$	1
PEB	0.9	0.73	0.12	0.75	$5x10^3$	4	10^{-5}	3.5

Figure 7: Experimental viscoelastic data (as presented in Figure 2) and viscoelastic response calculated using the spectrum model of Figure 5 and the parameters presented in Table 3. Reference temperature is 190°C

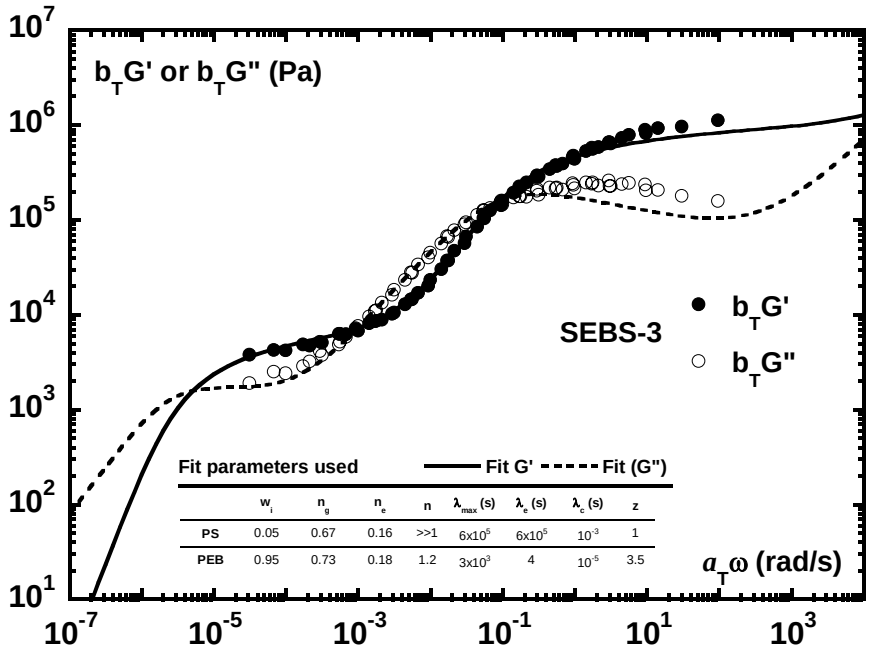

	w_i	n_g	n_e	n	λ_{max} (s)	λ_e (s)	λ_c (s)	z
PS	0.05	0.67	0.16	>>1	$6x10^5$	$6x10^5$	10^{-3}	1
PEB	0.95	0.73	0.18	1.2	$3x10^3$	4	10^{-5}	3.5

Figure 8: Experimental viscoelastic data (as presented in Figures 3 and 4) and viscoelastic response calculated using the spectrum model of Figure 5 and the parameters presented in Table 3. Reference temperature is 90°C

The modeled storage modulus and loss modulus for SEBS-3 are presented as a function of ω in Figure 8 altogether with the experimental mastercurve using a reference temperature of 90°C. Although the model represents all of the features of the experimental data, the fit of the loss modulus is not as good as in the case of SEBS-1 and SEBS-2 at high frequencies.

The model used is empirical, is based on a simple linear blending rule and on a trial an error approach. For this reason, in order to gain a better understanding of the physics behind the viscoelastic response of microphase separated block copolymers it is useful to compare their experimental response to that one of homopolymers of the constituent's species with molecular weight equivalent to the block molecular weight at the same temperature. Figure 9 graphically presents this comparison and allows determining whether the lower plateau is due to the PS blocks or some other characteristic length scale of the system.

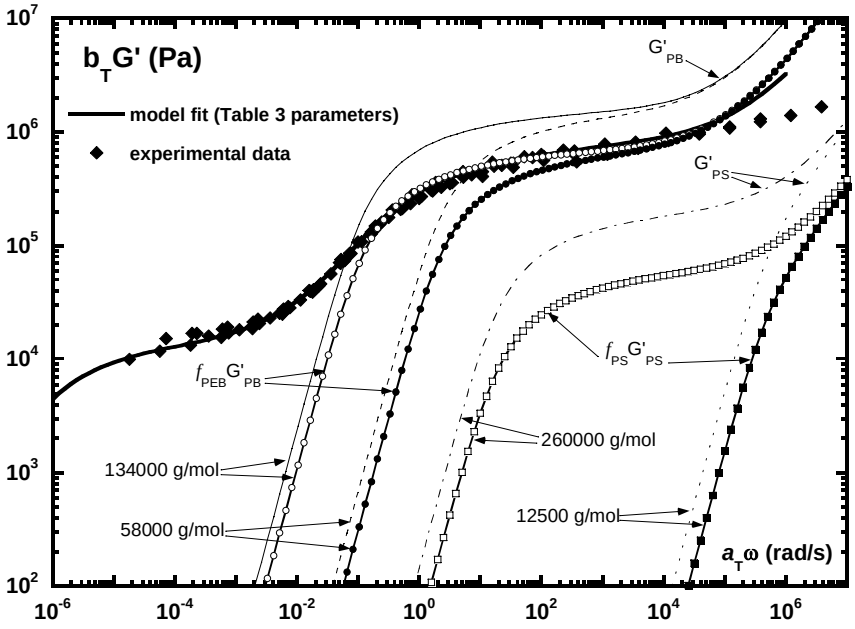

Figure 9: Comparison between the elastic responses of a microphase separated block copolymer (SEBS-1), the model fit, and the homopolymers constituting the different blocks based on values given by Jackson and Winter (1995). Reference temperature is 190°C.

Using the values for PB and PS given by Jackson and Winter (1995), we have calculated the elastic modulus representatives of homopolymers with the equivalent molecular weights: 58000 and 12500 g/mol in the case of the PEB block and the PS block respectively. Let us first look at the response of the middle rubbery block of PEB and that is represented by the PB curves. Initially we consider a M_w of 58000 g/mol equivalent to that one of the middle PEB block. The resulting curve, dashed line, presents an entanglement plateau that is shorter than the one presented by the experimental data by about 1.5 decades. Thus, the response of the PB homopolymer of molecular weight equivalent to that one of the middle block does not seem representative of the entanglement plateau observed for microphase separated block copolymers. When a molecular weight of 134000 g/mol, about 2.3 times greater than the block M_w, is considered, a plateau with a length similar to the one from the experimental data is obtained. Notice that the plateau of this curve, as well as that one of the curve corresponding to 58000 g/mol, is higher than the experimental curve by a factor of approximately two at the plateau. However, if the mass fraction of PEB in the block copolymer is taken into account, the curves superpose well on the plateau region; specially, the curve obtained with a M_w of 134000 g/mol. Let us examine now the response of a PS homopolymer of molecular weight equivalent to that one of the end-blocks in the copolymer: 12500 g/mol. The dotted line in Figure 9 represents the characteristic curve and as expected, it does not show an entanglement plateau. Indeed, the molecular weight for entanglement, M_c, in the case of PS is in the order of 13000 g/mol. One observes a change in regime, from glassy to viscous, at approximately $9x10^6$ rad/s and $3.75x10^5$ Pa. The elastic modulus obtained by modeling the response of a PS with M_w= 260000 g/mol, M_w/M_c = 20, has also been represented in Figure 9 to provide a better comparison with the lower plateau shown by the block copolymers studied. The times scales of the PS modeled curve with M_w=12500 g/mol and

those of the experimentally observed one are between 7-10 decades apart for a fixed stress level. Also, notice that the plateau of the modeled curve is a decade higher than the so-called lower plateau. Even when the mass fraction of PS in the copolymer is taken into account, the difference between the lower plateau of the copolymer and the entanglement plateau of the PS is significant: a factor 3 approximately. Thus, it seems that the PS endblocks, and their molecular length, does not suffice in order to explain the lower plateau.

The lower plateau occurs at times longer than approximately 350-400 seconds. Long times means that the solicited length scales must be long. In terms of the structure of block copolymers, the larger entities are the grains within which the polystyrene microdomains are coherent. Thus, the lower plateau can be considered to represent the global dynamics of these different grains.

If we perform the same molecular weight analysis as done in the case of SEBS-1 and -2, the ratio between the λ_{max} value from the model and that one calculated from the critical time λ_c, is 330. Thus, it seems that the apparent infinite molecular weight assumption is also justified in the case of SEBS-3. However, notice that in the case of SEBS-3 the slope of the power law region, n, is slightly greater than that found in the case of SEBS-1 and -2: 1.2 as opposed to 0.75. From this difference, we can induce that the spherical microdomains are less stiff than the cylindrical ones. Therefore, they will be deformed more easily by the flow field.

The model presented seems to describe well the viscoelastic response of both morphologies studied when the grains can be considered as randomly oriented in the sample. The problematic areas are at the high frequency end near the glass transition and the low frequency end in which only hypothesis of the PS microdomains and grains behavior can be made.

3.3.2 Capillary rheometry: flow curves and extrusion defects

Figure 10 presents master flow curves, wall shear stress as a function of apparent shear rate, obtained with SEBS-1 and SEBS-2 at different temperatures and by using different diameter and length capillaries. The shift factors, a_T, used for these curves agree with those presented in the inset of Figure 3 and can be modeled using the WLF equation with the coefficients C_1 and C_2 presented in Table 2.

The wall shear stress, τ_w, resulted from the measurement of pressure drops across different capillaries that were corrected for entrance effects. For a given flow rate Q, and a capillary of length L and diameter D, τ_w was calculated as

$$\tau_w(Q) = \frac{\Delta P_L(Q) - \Delta P_o(Q)}{4L/D} \qquad (4)$$

where $\Delta P_L(Q)$ and $\Delta P_o(Q)$ are the measured pressure drops across a die of length L and a short orifice of the same diameter and with negligible length.

The apparent shear rate that is a function of the flow rate, Q, and the die diameter, D, was given by

$$\dot{\gamma}_{app}(Q) = \frac{32Q}{\pi D^3} \qquad (5)$$

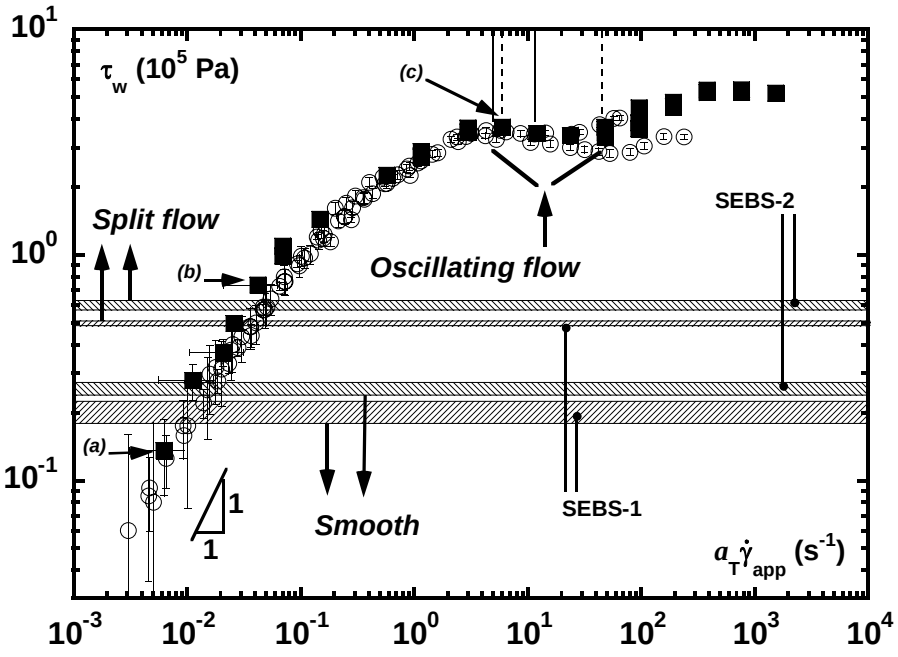

Figure 10: Wall shear stress (τ_w) as a function of reduced apparent shear rate ($a_T\dot{\gamma}_{app}$) for SEBS-1 and SEBS-2 using 190°C as reference temperature.

The behavior of both SEBS-1 and SEBS-2 is nearly identical, which should not come as a surprise since both of them have very similar molecular structure. Moreover, the shape of the curves is similar to those commonly encountered in the case of highly entangled polymer melts. One should notice that these flow curves seem to tend towards a slope of 1 at low shear rates. Thus, one would expect to observe slopes of 2 and 1 for the storage and the loss modulus in dynamic rheometry for these frequencies. This is not the case and can be explained by an effect of the large deformation on the PS microdomains and merging of grain boundaries rich in PEB. The macroscopic defects characteristics of these SEBS copolymers have been the subject of another paper by these same authors (Santanach *et al.* 2005). Thus, they will not be covered in detail here. Nevertheless, we should stress that SEBS-1, as well as SEBS-2, show the phenomenon known as *"Split flow"* that was first identified by Fernández and co-workers (2001) for three different copolymers of ethane and propylene. Zhu (2004) more recently reported the same phenomenon for two 4-arm star polybutadienes.

The three captions presented in Figure 11 show these defects characteristic of SEBS-1 and SEBS-2. The captions shown correspond to extrusion experiments with SEBS-1 at 190°C and through a capillary with L/D ratio of 10/1. The marks (a), (b), and (c) in Figure 10 show the placement of these extrusion regimes on the flow curve.

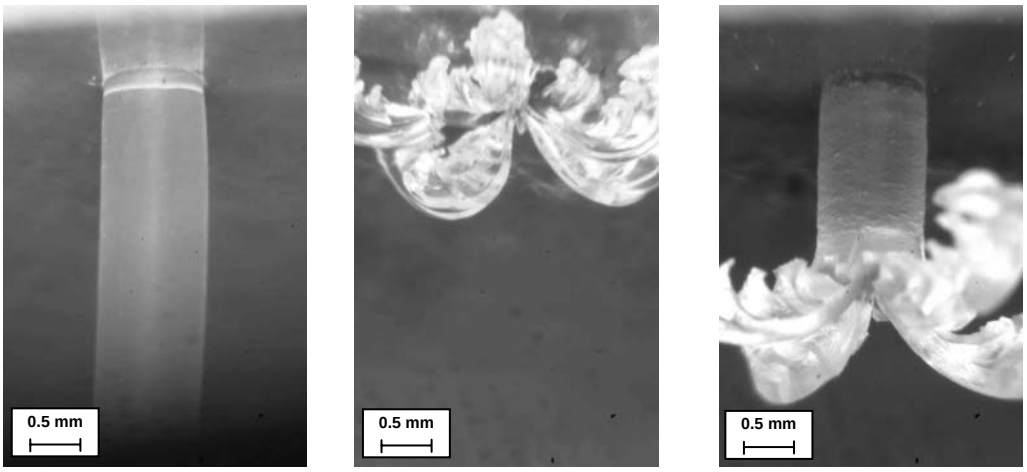

(a) $\tau_w = 0.1510^5$ Pa, $\dot{\gamma}_a = 0.006$ s^{-1} (b) $\tau_w > 0.5010^5$ Pa (c) $\tau_w \sim 4.1510^5$ Pa, 6 s$^{-1} \sim \dot{\gamma}_a < 48$ s^{-1}

Figure 11: SEBS-1 exiting a capillary with L/D of 10/1 at 190°C.

In the case of SEBS-3, the flow curves obtained with both the Götffert capillary rheometer and the in-house developed one with the Be capillary are presented in Figure 12. Within experimental uncertainties, both curves agree well for stable flow regimes with no-slip condition at the die wall. This condition is necessary to compare both sets of data since they were obtained with different diameter capillaries. This comparison validates the use of the in-house developed capillary rheometer. In the case of SEBS-3, just as in the case of the other two SEBS considered, the typical curve for moderate to highly entangled polymer melts is observed. Again, the difference between curves obtained by capillary rheometry and dynamic rheometry experiments is observed at low frequencies if Figures 8 and 12 are compared. SEBS-3, as discussed elsewhere by the same authors, does not show *"Split flow"* phenomena, although it shows very severe case of surface fracture as seen in caption (b) of Figure 13. Caption (a) in Figure 13 shows the extrudate obtained at the lowest flow rate accessible under fixed piston speed conditions using the Göttfert capillary rheometer and a capillary with L/D ratio of 50/5. The extrudate is smooth, transparent and no swelling is observable. Captions (c) and (d) show the extrudate obtained at two unstable extrusion regimes with permanent slip at the wall.

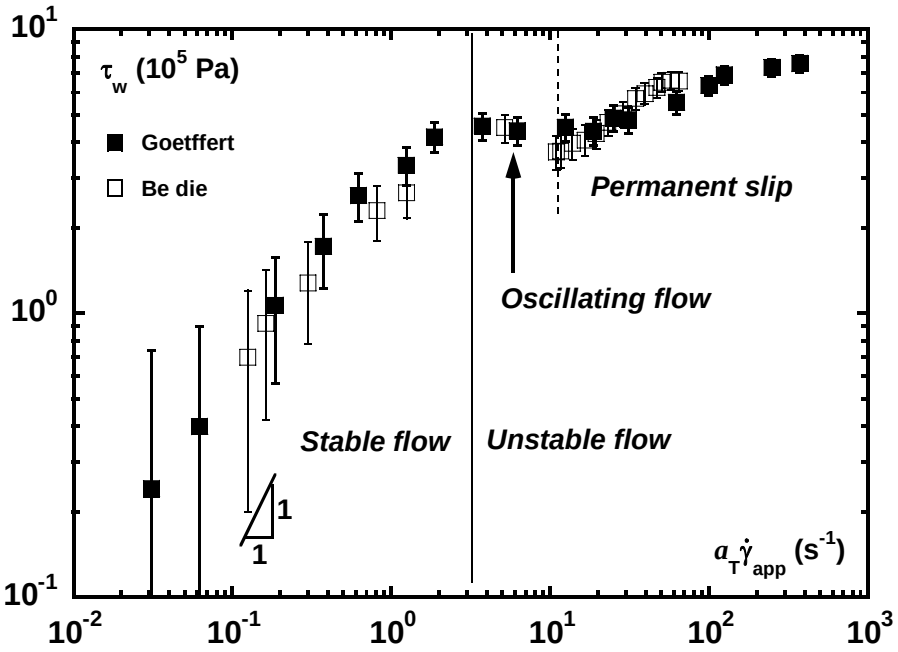

Figure 12: Wall shear stress (τ_w) as a function of reduced apparent shear rate ($a_T\dot{\gamma}_{app}$) for SEBS-3 using 110°C as reference temperature.

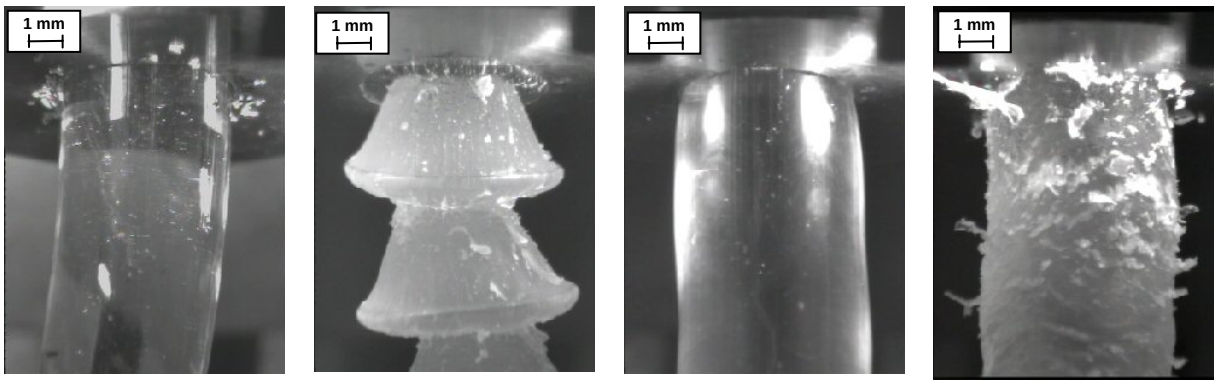

(a) 0.005 s^{-1}, 0.23x10^5 Pa ***(b)*** 0.184 s^{-1}, 3.03x10^5 Pa ***(c)*** 1.84 s^{-1}, 3.7x10^5 Pa ***(d)*** 18.4 s^{-1}, 4.4x10^5 Pa

Figure 13: SEBS-3 exiting a capillary with L/D of 50/5 at 90°C

The differences in the magnitude of the defects observed can be understood in terms of the different structures presented by SEBS-1 and SEBS 2 in the one hand and SEBS-3 in the other hand. As the next section explains, this difference in defects can be attributed in part to the damping effect of the spherical microdomains that are deformed with the flow field. In the case of the cylindrical PS microdomains align in the flow direction. The stresses in the fluid are only released by the severe surface cracks, which develop along vanishing grain boundaries, leading to "flow split".

3.3.3 SAXS experiments

Effect of the extrusion process on structure

In the melt barrel

During the filling process prior to extrusion, the barrel was filled with the copolymer that was initially compressed by the piston while still in the solid state. Then, the copolymer was allowed to melt inside the barrel. In-situ SAXS experiments inside the barrel to probe the structure in the material are not possible with the available rheometers. For this reason, and to model this state, samples were prepared by compressing some polymer in a mold at room temperature and then melting it in an oven at 230°C. The residence time in the oven was in the order of 40 minutes. At the compression molding temperature, cylindrical polystyrene microdomains in a rubbery matrix of ethylene-butylene are expected given the mass fraction of PS, small-strain oscillatory shear experiments results, and DSC analysis. Once the copolymer had melted, the mold was allowed to cool down to room temperature and a polymer sheet between 0.5 and 1 mm thick was extracted. Disk-shaped samples of 15 mm in diameter were cut from the sheet.

A temperature-controlled environment was used to hold the sample in place and at temperature during SAXS experiments. A homogenous temperature over the sample was ensured by wrapping it in aluminum foil. An area of about 2 mm^2 in the center of the sample was left uncovered for the incident beam, which was parallel to the compression direction, to pass. Scattering experiments were performed at temperatures ranging between 30°C and 305°C.

In all cases, the SAXS images were quite similar and even though we expected a change in structure at temperatures above 280°C, no significant differences were observed in any of the samples. The transition temperature of 280°C had been determined from DSC analysis.

Figure 14 presents a typical azimuthally averaged over 360° intensity curve obtained with compression molded samples. It corresponds to a temperature of 30°C. The 2D scattered intensity map shows that the sample can be considered as isotropic within the scattering volume (0.3x0.3x1 mm^3). Since the sample scatters the intensity nearly equally in all directions, one can imagine that we have a multitude of grains with organized PS cylinders within them, but that overall the grains are randomly oriented. As a recall, a 2D schematic representation is included in the plot.

A sharp peak is observed at a wave vector, $Q=2\pi/d$, of approximately 0.2 nm^{-1} which corresponds to a characteristic distance, d*, between the objects in the system of 32 nm. If an “ideal” hexagonal lattice formed by six equilateral triangles is considered, and the cylinders are considered to be long (L/D>>10), a cylinder diameter of 18 nm can be calculated from the main peak and the volume fraction of PS present in the block copolymer; for SEBS-1 about 30% PS. Notice that the interdomain distance and the cylinder diameter are of the same order of magnitude. Therefore, both the structure factor and the form factor will scatter at similar scales and wave vectors. It is for this reason that the intensity curve, I(Q), is rather smooth and only a main peak and a shoulder, spanning through wave vectors

between 0.5 nm^{-1} and 0.8 nm^{-1}, are observed. Had the scales been much different, we would have been able to see the peaks describing the structure in one hand (with ratios $1:3^{1/2}:4^{1/2}:7^{1/2}:9^{1/2}$) and the curve corresponding to a cylindrical rod in the other hand.

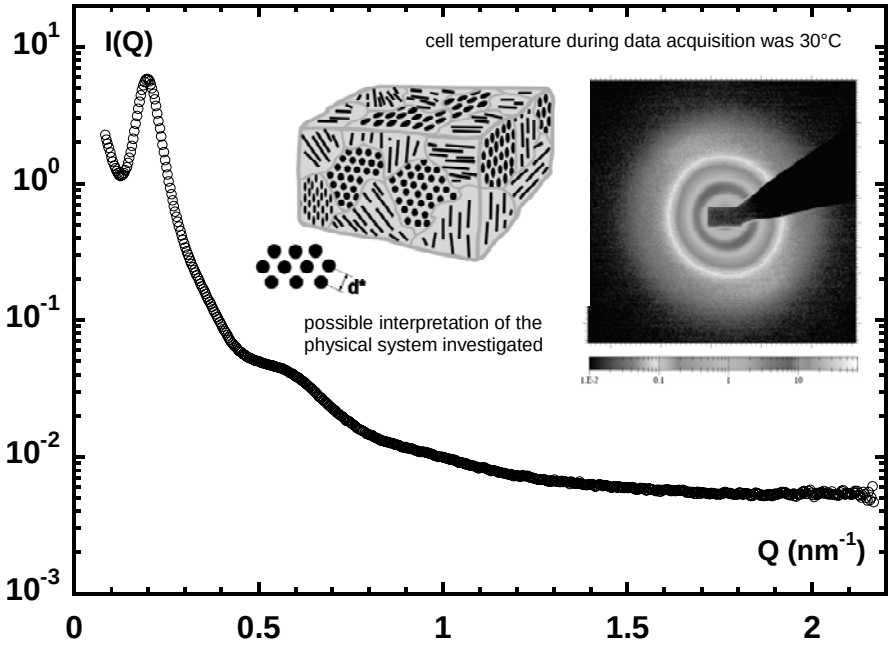

Figure 14: Scattered intensity curve of a SEBS-1 sample compression molded at 230°C. The test temperature was 30°C. The inset shows the 2D image which was integrated over 360°C to obtain the curve I(Q).

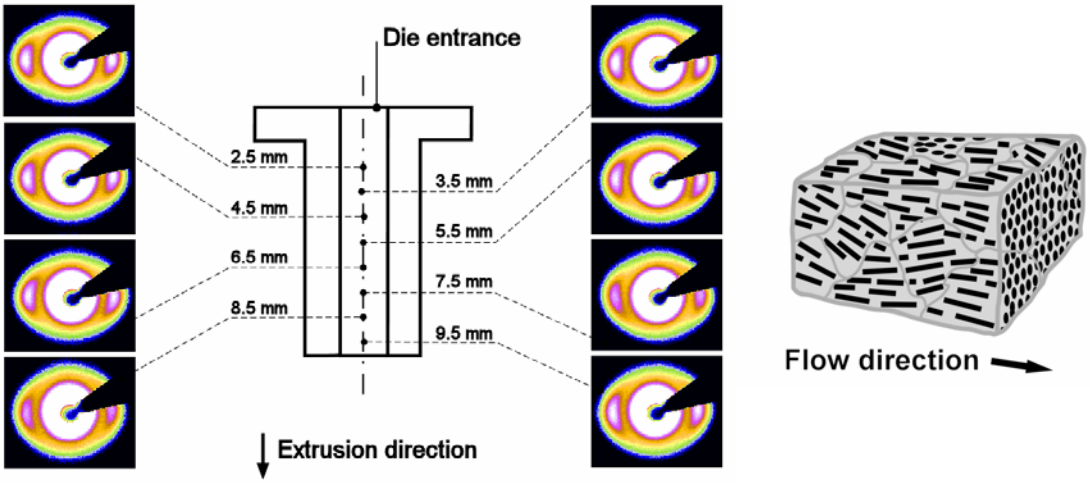

Figure 15: left: scattered intensity as a function of die length in the case of SEBS-1 extruded in the presence of the viscoelastic upstream instability. Right: the orientation of the different grains has taken place and the cylinders are oriented in the extrusion direction on average..

In the capillary

The Be capillary allowed to probe any changes in structure along the abscissa of the die. Measurements were taken along the axis of symmetry of the die at 1 mm intervals starting at a distance of 2.5 mm from the die entrance. The captions in Figure 15 show the images obtained when the capillary was filled at 14.4 s^{-1} and a temperature of 150°C, a regime showing the upstream instability and permanent slip at the wall. Once filled, extrusion was stopped and the die removed to perform SAXS experiments. Otherwise, the measurements at 2.5 mm from the die entrance would have been impossible to perform. The relaxation times of the PEB block are short and the rubbery matrix can fully relax while the polymer cools down at the capillary. However, the PS cylindrical microdomains have relaxation times in the order of some hundreds of seconds and hence, the PS cylindrical microdomains will only relax partially while the extrudate is cooling down outside of the die. Thus, the relaxed extrudate will conserve at least partially, the structural changes occurring during the extrusion process. In the figures, the central white circle corresponds to the contribution of the Be die.

The most noticeable difference between these images obtained in the beryllium capillary and the compression-molded sample is the appearance of anisotropy at the scale of the scattered volume that is of the order of 2x0.3x0.3 mm^3. In addition, these captions show that, in all cases, the PS cylindrical microdomains are aligned in the direction of the extrusion. However, no significant differences are observed among the images taken at different distances from the die entrance. Nevertheless, by probing along the abscissa of the capillary, we can conclude that the principal orientation of the PS domains occurs in the flow field near the die entrance and the orientation seems completed no more than 2.5 mm downstream of the die entrance.

If the images are observed more carefully, small differences in the shape and orientation of the peak characteristic of the PS domains can be noticed.

In order to quantify these differences, the anisotropy and the orientation of the peaks have been measured. To measure the anisotropy, and after taking into account the scattered intensity corresponding to the Be, integrations over azimuthal angular sections of ±15° about the vertical and the horizontal directions were performed. A measure of the anisotropy can then be obtained by the ratio of the scattered intensities in each direction for a given wave vector, Q. To correct for the Be contribution, the scattered intensity corresponding to a Be thickness of 2.5 mm was subtracted for the original I(Q) curve. The scattered intensity corrected for Be effect altogether with this measure of the anisotropy are reported in Figure 16 as a function of Q for different distances from the die entrance. It can be noticed that the maximum scattered intensity occurs at the same Q regardless of the distance from the die entrance. The maximum anisotropy occurs at Q=0.20 nm^{-1} that corresponds to an inter-cylinder distance of 32 nm since Q equals $2\pi/d^*$ where d^* is a characteristic length. In this case, and still considering an “ideal” hexagonal lattice and a volume fraction of 30% PS, one would obtain a cylinder diameter of 18 nm.

Work by Kotaka *et al.* (2000) had already showed in the case of the elongation that fast shear rates, it is the rubbery matrix that deforms. One the other hand, when the strain rates are low, the PS domains have time to flow and deform.

However, this is not the case of the maximum anisotropy, which varies by a factor of nearly two among the different measurements. The maximum anisotropy as a function of the distance from the die entrance has been reported in the inset on the upper right hand corner of Figure 16. The inset clearly shows a decrease in the maximum anisotropy with increasing distance from the contraction. A distinct slope change can be observed between the measurement corresponding to 5.5 and 6.5 mm. Two factors can contribute to this: on one hand, the decreasing effect of the elongational field near the die entrance combined to possible shear flow structural flip-flop.

The mean orientation of the peak was obtained by looking at the scattered intensity variations in a narrow Q range slab as a function of the angle theta. Figure 17 reports the angles at which the maximum intensity was recorded as a function of the distance from the die entrance for two different integration Q ranges. In the first case, denoted by the black square marks, a Q range of 0.17-23 nm^{-1} was used. In the second case, a narrower range was used (0.19 nm^{-1} < Q < 0.20 nm^{-1}). SAXS measurements are precise enough for these changes in direction to be taken into account.

The mean orientation inside the die varies between 179° and 184°. However, taking a closer look, two regions can be observed in the plot: one for distances from the die entrance below 6 mm and the other one from 6 mm and on. Notice that this cutoff distance is the same observed in the curve describing the maximum anisotropy as a function of distance from the die entrance. Near the die entrance, the mean orientation of the peak is rather constant around 181°. Then, the orientation changes by steps of 2 mm in length as we mover further from the exit. In this way, between 6 and 8 mm from the die entrance, the main peak is oriented at 182.5°. Between 8 mm and the die exit, the orientation of the main peak is at 184°.

Keeping in mind that the results presented in Figures 15-17 represent a still picture of the melt in the die, two interpretations are possible to explain the changes in anisotropy and in orientation.

One can think that these changes in orientation are due to the stretching and relaxation of the microdomains when passing through the contraction at the die entrance. The stretching and relaxation can be considered as an initial perturbation to a system of the elastic PS cylinders that degenerates into a global instability.

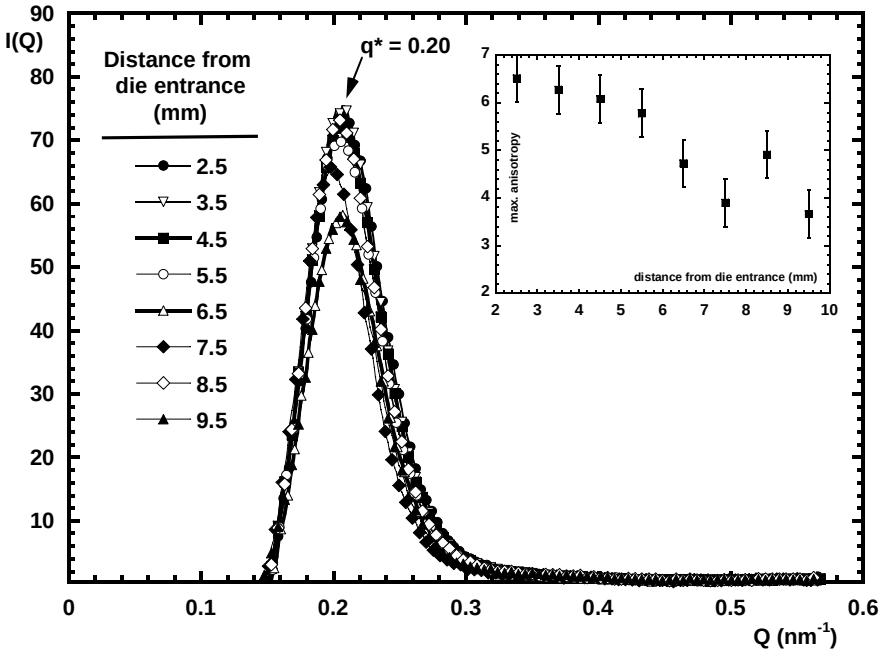

Figure 16: Main peak once corrected for the Be contribution as a function of wavevector at different distance from the die entrance in the case of SEBS-1 extruded in the presence of the viscoelastic upstream instability (14.4 s^{-1} and 150°C). The inset shows the maximum anisotropy as a function of distance from the die entrance.

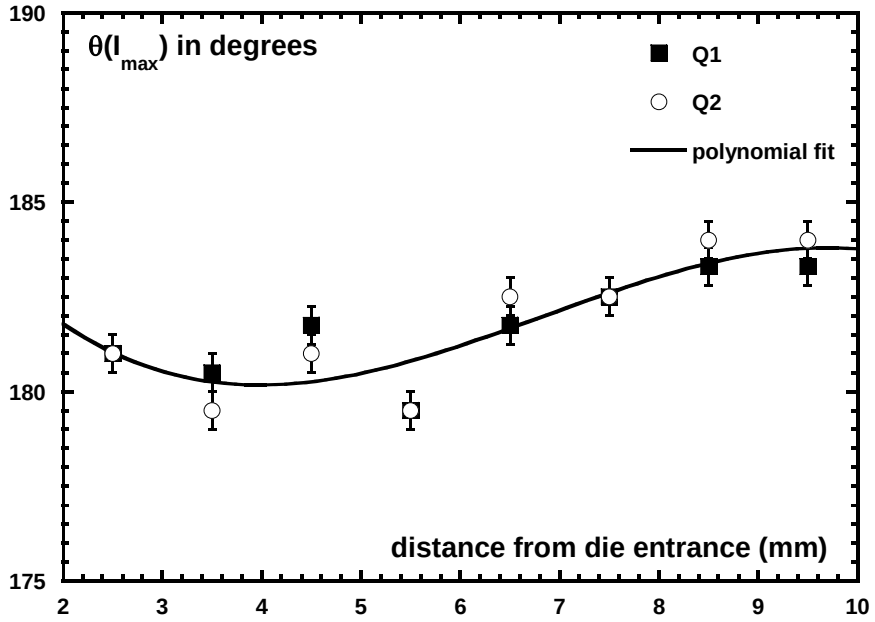

Figure 17: Angle at which scattered intensity is maximum as a function of distance from the die entrance.

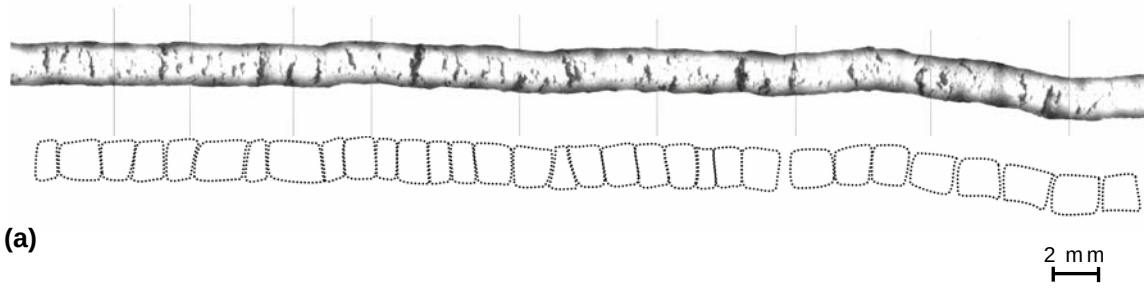

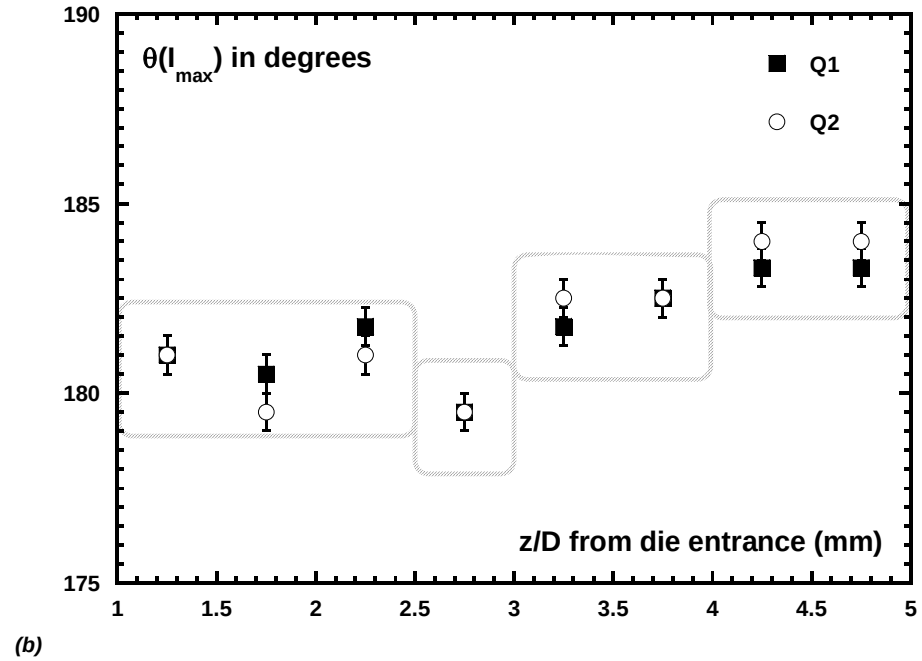

Figure 18: Relaxed extrudate obtained at the die exit when filling the Be die. SEBS-1, 150°C and 14.4 s^{-1}. (a) picture and decomposition in small polymer bulks. (b) reinterpretation of Figure 15 to account for these small bulks.

The second hypothesis, which considers the melt at a macroscopic level, is based on the work by Bergem (1976) and is presented in Figure 18. For unstable extrusion regimes, it is accepted that the polymer melt can flow as a series of successive small bulks with opposite flow orientations that are transported from the die entrance to the die exit. This type of phenomenon has already been reported for the extrusion of PB (Piau *et al.* 1995). Such type of flow may explain the changes in direction as the copolymer moves downstream of the die.

If this is the case, one can reasonably expect to observe a trace of the small bulks in the melt exiting the die. In particular since the die used is relatively short (L/D = 10/2) and the longest relaxation times in the PS domains are in the order of some hours as predicted by the models presented in section 3.3.1.

Figure 18a also presents a relaxed extrudate as observed through a macroscope with diffused white light behind. Several images, as marked by the grey vertical lines, have been combined to have a better overall view. This sample was obtained at the same conditions used to fill the Be die: 150°C

and 14.4 s^{-1}. At a first glance, the sample seems irregular with some changes in direction and some surface scratches (dark stains). A shallow undulation of the surface in the form of small changes in sample diameter is also present. The shaded region near the edges of the extrudate can be used to detect this undulation as well by the changes in tone. Moreover, these undulations seem to be coincident as a function of extruded length that permits to split the relaxed melt and to represent it as a connected series of small bulks of polymer. This representation of the melt is shown below the extruded samples by the different loops in dotted lines. The length of these bulks is not regular but go from 0.5D to 1.5D approximately, with most loops having a length in the order of the diameter of the capillary die (2mm).

Now the main orientations of the cylinders as a function of the distance from the die length can be reinterpreted as shown in Figure 18(b). Indeed, we observe that near the die exit, two distinct orientations are observed that can be explained in terms of two small bulks of bout 2 mm in length. As we approach the die entrance, the first three diameters in length, the orientation of the cylinders can be interpreted as three or four small bulks of either 2 or 1 mm in length. In any case, these lengths are in good agreement with those observed on the relaxed extrudate. This second hypothesis gives a consistent explanation of the phenomena observed by SAXS.

The relaxed extrudate obtained at the die exit

SAXS experiments were also performed on the final relaxed extrudates obtained at the die exit. The extruded samples were allowed to cool down at room temperature. The time necessary for the PS domains to undergo the glass transition being shorter than their relaxation times (cf. § 3.3.1), one can expect to conserve partially, at least, the internal structure characteristic of the extrusion regime. In Figure 17, we present the 2D image of the scattered intensity, as well as the integrations of these over two angular sectors of ±15° about the two principal directions, for an extrudate obtained within the slipping phase of the oscillatory flows. At this regime, the upstream viscoelastic instability is present. No significant differences are observed between the image presented in Figure 19 and the captions presented in Figure 15. The principal peak is at at Q= 0.2 nm^{-1}, the same position observed for the sample that was compressed and molded (cf. Figure 14). The strong anisotropic structure is related to the alignment of cylindrical PS microdomains in the extrusion direction. Measurements of the extrudate diameter with a caliper gave diameter values in the range 2.1-2.2 mm.

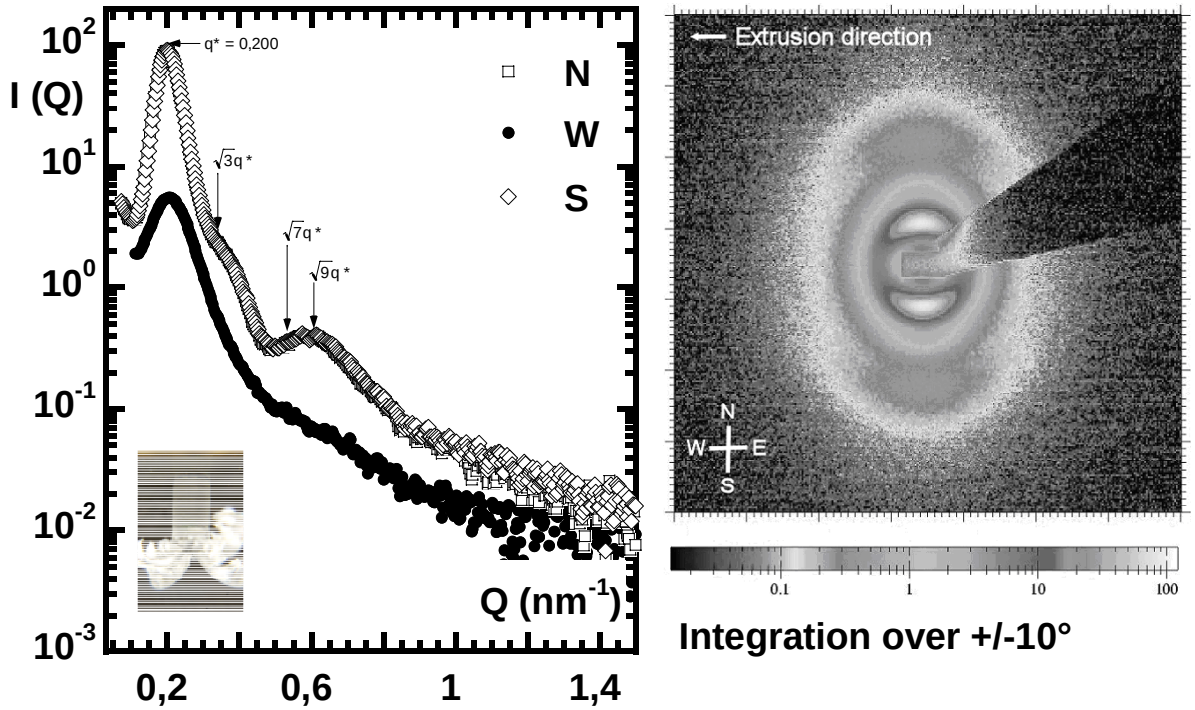

Figure 19: SEBS-1 extruded at 190°C – 6 s-1 through a capillary with L/D = 10/1. The beam was perpendicular to extrusion direction and focused on slip portion of sample.

Effect of the different extrusion rates on structure

Relaxed extrudates of hexagonally-packed cylinders (SEBS-1 and SEBS-2)

In the case of the hexagonally-packed cylindrical PS domains structure, two different extrusion regimes were analyzed by SAXS other than the compression-molded samples and the slipping phase of oscillatory flows: a smooth and transparent film extrudate, and an extrudate obtained with a short orifice die of negligible length and diameter of 2 mm and that showed flow split. Both samples were obtained by extruding SEBS-1 at 190°C. The shear rates were ~0.005 s^{-1} and 3 s^{-1} respectively. No significant differences were observed between the different regimes. The peak remained at Q=0.20±0.007 nm^{-1} meaning that the mean distance between the cylinders, and thus their diameter do not change with extrusion rate; the diameter of the PS cylinders being in the order of 18 nm.

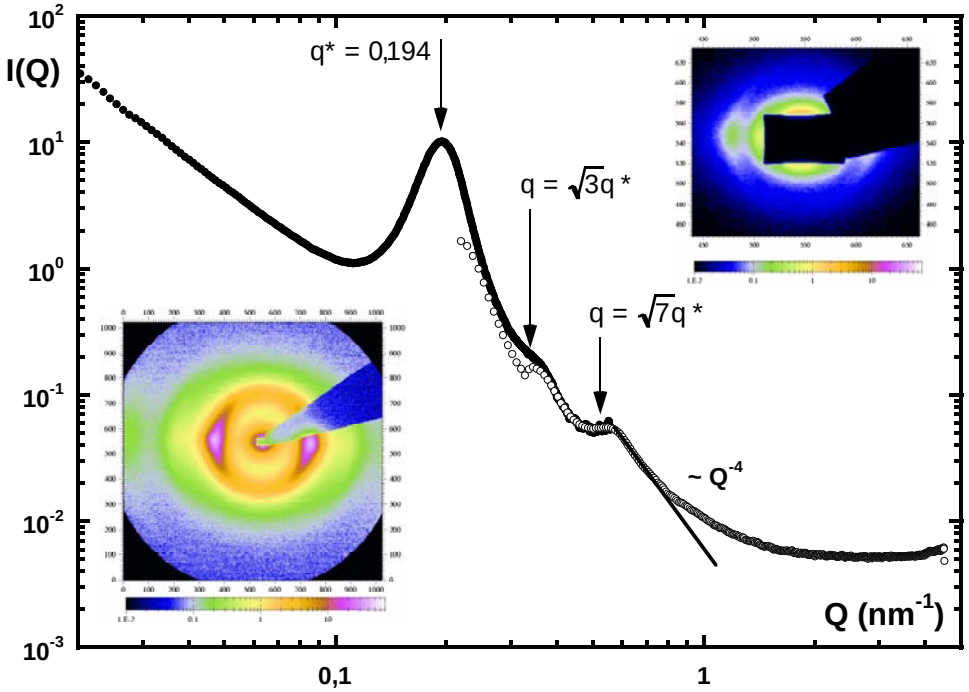

Figure 20: SEBS-1 extruded at 190°C – 0,005 s^{-1} – film (not shown). The arrows indicate the theoretical higher order peaks for hexagonally-packed cylinders. Incident beam perpendicular to the extrusion direction. (●) data obtained with a sample-to-detector distance (SDD) of 10 m. (○) SDD of 1.2 m

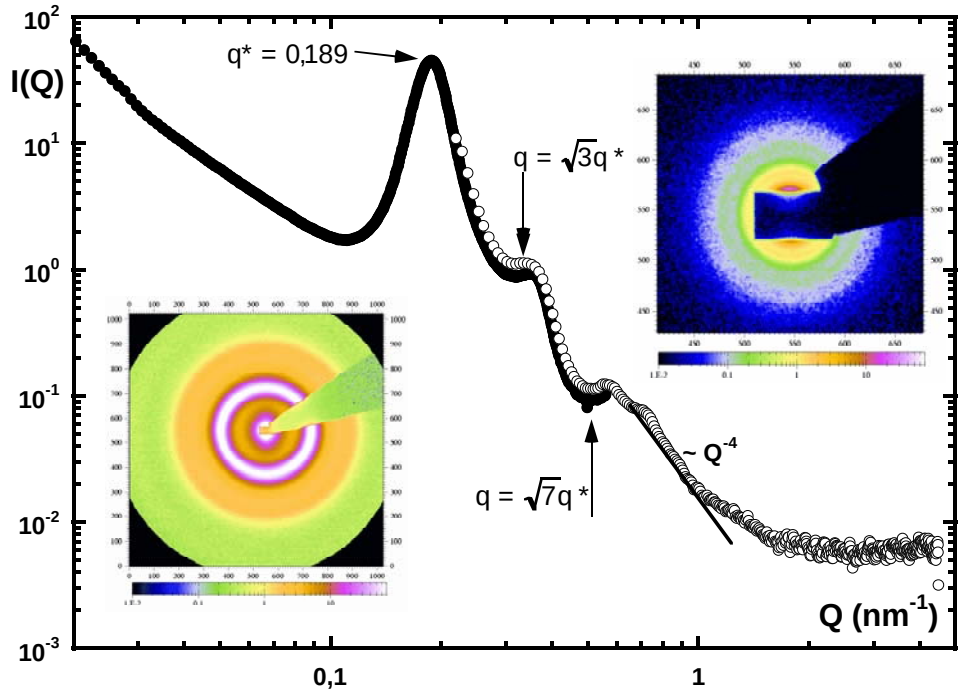

Figure 21: SEBS-1 extruded at 190°C – 0,005 s^{-1} – film (not shown). The arrows indicate the theoretical higher order peaks for hexagonally-packed cylinders. Incident beam parallel to the extrusion direction. (●) data obtained with a sample-to-detector distance (SDD) of 10 m. (○) SDD of 1.2 m

The film of SEBS-1 extruded at 190°C and ~0.005 s^{-1} through a slit die allowed to easily observe the structure in the copolymer with the incident beam both perpendicular (Figure 20) and parallel to the extrusion direction (Figure 21). In both cases, measurements with sample-to-detector distances of 1.2 and 10 meters were performed.

In the case of Figure 20, the anisotropy of the 2D images that is indicative of the alignment of cylinders in the direction of extrusion is clearly seen. The principal peak, with maximum at Q=0.194 nm^{-1}, corresponds to an average inter-cylinder distance of the order of 32.4 nm. The second and third peaks correspond to the long range order of the cylindrical PS domains. Also, notice that the intensity is scattered at a slope of Q^{-4} after the third peak. Such a slope is characteristic of smooth interfaces. Indeed, the SEBS used fall within the strong segregation limit at room temperature and one expects to have sharp changes in composition; PEB or PB..

Figure 21 was obtained with the incident beam parallel to the extrusion direction. In this case, the 2D SAXS images are isotropic and form a series of concentric rings. The principal peak give what is known as the liquid-order. If the PS cylinders were arranged in a perfectly hexagonal lattice with infinite long-range order, six distinct peaks would be observed on the SAXS image. Although a continuous ring is observed, the mean diameter of the circle passing through the axis of six PS cylinders can be determined from the maximum peak at Q=0.189 nm^{-1}. The diameter of the circle is 66.4 nm, and if a volume fraction of 30%PS is used and the cylinders are consider to be very long (L/D>>10), a cylinder diameter of about 19 nm is obtained. This diameter value is within 5% of that one obtained with the beam perpendicular to the extrusion direction.

The sample is not sheared homogenously. Near the die walls, the shear stress is maximum while it is nearly zero in the middle of the sample. Thus, misalignment of the cylinders, which is shear-induced, will be non-homogenous. Also, the copolymer only passes once through the die, which limits the amount of strain that the it undergoes. For this film in particular, the amount of strain is about 6, much smaller than those attainable in a Couette cell: Nakatani *et al.* (1996) went as high as 1600 strain units to obtain two well-defined peaks. On Work by Tepe *et al.*, (1995) and Winter *et al.* (1993) large-amplitude oscillatory shear, with strain comparable to that in the die, is used to orient triblock copolymers. However, the strain is applied several times (oscillations) and in the case of Winter *et al.* (1993), oscillation at 400% deformation were applied for at least two hours and in some cases for as long as 10 hours!

Spherical micro-domains (SEBS-3)

In the barrel equivalent state

The effect of the extrusion rate is more evident in the case of SEBS-3 extruded at 90 °C. Figure 22 presents the intensity scattered by a SEBS-3 sample that had been compressed in the disordered state and was allowed to cool down to room temperature. The signal is isotropic and with no apparent long-range order. The maximum intensity peak corresponds to a distance of 23.6 nm (Q=0.266 nm^{-1}).

To interpret this figure different hypothesis for a lattice were weighted. A cubic cell, a BCC cell and lattice formed of tetrahedral cells were considered. This last hypothesis results a system in which all particles are at the mean distance between two neighboring particles is the same for each pair of spheres. From the volume of fraction of PS (13%PS) and the characteristic size of 23.6 nm the sphere diameter was estimated for each hypothesis. Using these diameters and the form factor model of a polydisperse population of non-interacting spheres, the different modeled curves were fitted by changing the polydispersity factor $\Delta\phi/\phi_m$ and the mean sphere diameter ϕ_m. The better fit was obtained with the diameter given with the tetrahedral unit cell and it is represented in Figure 22 by the solid line. The size distribution of the spherical domains was considered to be described by a Schultzian curve. Thus, a possible interpretation of the image obtained is that of a population of polydisperse spheres of mean diameter, ϕ_m, 14.4 nm and a polidispersity factor, $\Delta\phi/\phi_m$ of 0.13. Gaussian chains form both spherical domains and the englobing matrix. Notice that the fitted curve matches the experimental curve for Q values greater than 0.44 nm^{-1}. The corresponding length scale is 14.3 nm, which is within 1% of the mean diameter value estimated. At length scales shorter than the diameter of the sphere, or Q > 0.44 nm^{-1}, the fit works because interactions between the different PS microdomains, which are neglected with the model used, do not play a role. However, the model does not work for Q<0.44 nm-1 because interactions between the different spherical microdomains exist. Indeed, we cannot forget that the different microdomains are connected by means of the PEB matrix that is constituted of the middle blocks that are covalently attached to the end-blocks forming the spherical PS microdomains.

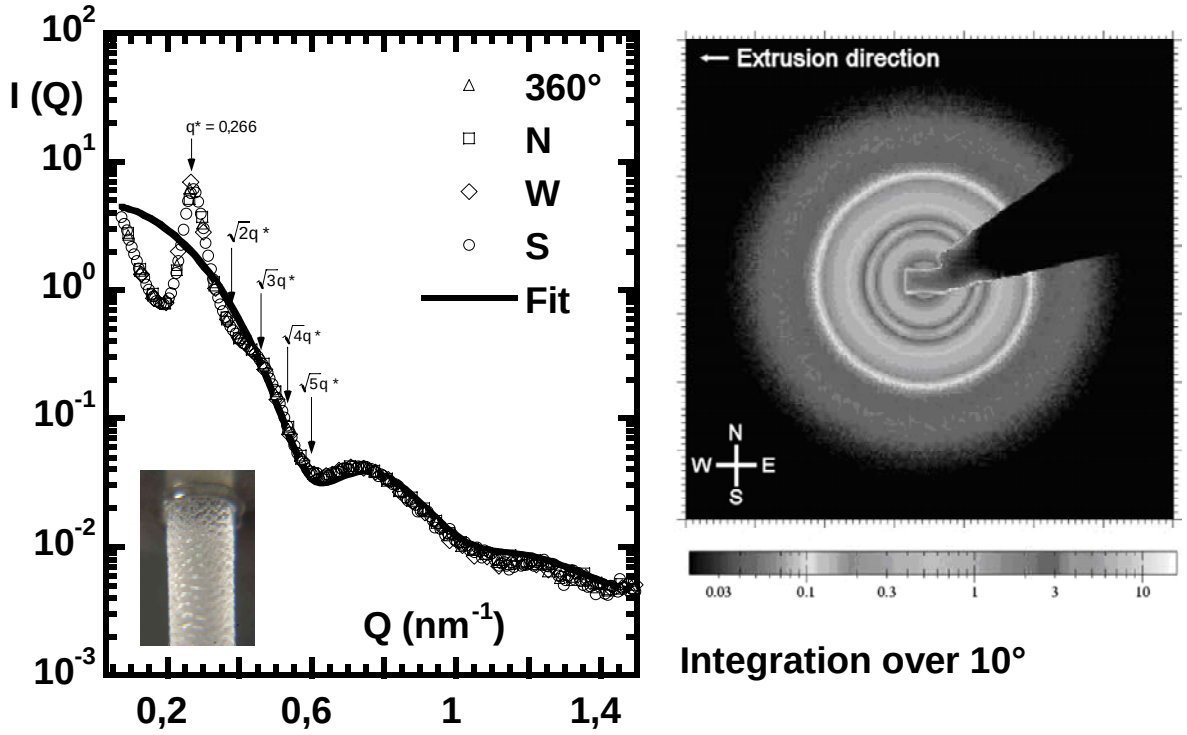

Figure 22: SEBS-3 (13%PS) at rest. Sample compressed with the rheometer in the disordered state and allowed to cool down to room temperature.

On relaxed extrudates

The spherical domains deform when the SEBS-3 is extruded as can be seen in three images presented in Figure 23. Caption (a) corresponds to the SEBS-3 extruded at 90°C and at a shear rate of 0.184 s^{-1} (cf. Figure 11b). At this regime, the wall shear stress of $3x10^5$ Pa and severe sharkskin occurs. The sample was obtained with a capillary with L/D ratio of 50/5 and it was cut longitudinally before being placed on the sample holder. The incident X-ray beam was perpendicular to the extrusion direction. An anisotropy corresponding to an alignment of the objects in the extrusion direction is observed. Moreover, notice that the outermost scattered intensity has lost its isotropy. In captions (a) and (b) a distinct oval-shaped continuous halo is observed. This area corresponds to large wave vectors, or lengths characteristic of the PS domains. Thus, allowing to conclude that the PS domains have deformed and have become oval shaped. A fit of the curve at large wave vectors yielded dimensions of 8.4 and 7.6 nm of a prolate ellipsoid. When the SAXS figures obtained with the SEBS-3 are compared to those obtained with the SEBS-1 one notices the difference in large wave vector range. In the case of the SEBS-3 the halo is continuous and the scattered intensity nearly uniform over all angles, whereas in the case of the SEBS-1 notice that at large wave vectors that the sample scatters mainly in one direction. This can be attributed to the higher anisotropy of the cylindrical domains with respect to the oval-shaped domains.

Captions (b) and (c) present the evolution of the scattered intensity with increasing flow rate. The incident beam was kept perpendicular to the extrusion direction in both cases. One can observe a gradual deformation of the main peak's shape. In caption (b), corresponding to a shear rate of 1.84 s^{-1} and an unstable flow, (cf. Figure 13c) the main peak is quarter-moon shaped, whereas in caption (a) it was nearly a half-moon. Increasing the flow rate by a factor of ten renders the flow highly unstable and results in the figure presented in caption (c) of Figure 23 (cf. Figure 13d for a picture of the extrudate exiting the die). On the 2D image, one clearly observes four intensity peaks; Two of them, in the N-S direction are 30° off the vertical, while the other two, E-W, are 40° off the vertical approximately. Thus, it seems that for highly unstable regimes the PS domains are oriented in two different directions. One can also depict an hexagonally shaped ring in the forming with two new peaks trying to appear in the equatorial point of the image. This is probably due to the unsteady flow field present just upstream of the die entrance and its strong elongational component. In both case, whether there are four peaks, or six peaks that are not yet fully formed, they can be attributed to a BCC organization of the oval shaped domains. Indeed, Daniel and Hamley (2000b) had been able this type of structure when elongated by means of compression flow with slippery walls.

However, in all of the three captions, the maximum scattered intensity is at a wave vector of Q=0.222 nm^{-1}. Thus, the mean spacing between domains in the direction perpendicular to the extrusion does not seem to change. Nevertheless, when the distance between spherical domains in the extrusion direction is considered, captions (a), (b) and (c) show a peak at Q of 0.244, 0.237, and 0.229 nm^{-1} respectively, hence the mean spacing between domains is no longer equal in both directions. However, in both cases the mean spacing between domains is larger than in the case of the melt at rest (Figure 20). Thus, we can conclude that the PS microdomains are deformed and that this

deformation at least partially holds when the extrudate cools down to room temperature. Moreover, the PEB matrix seems to be held in place by glassy domains.

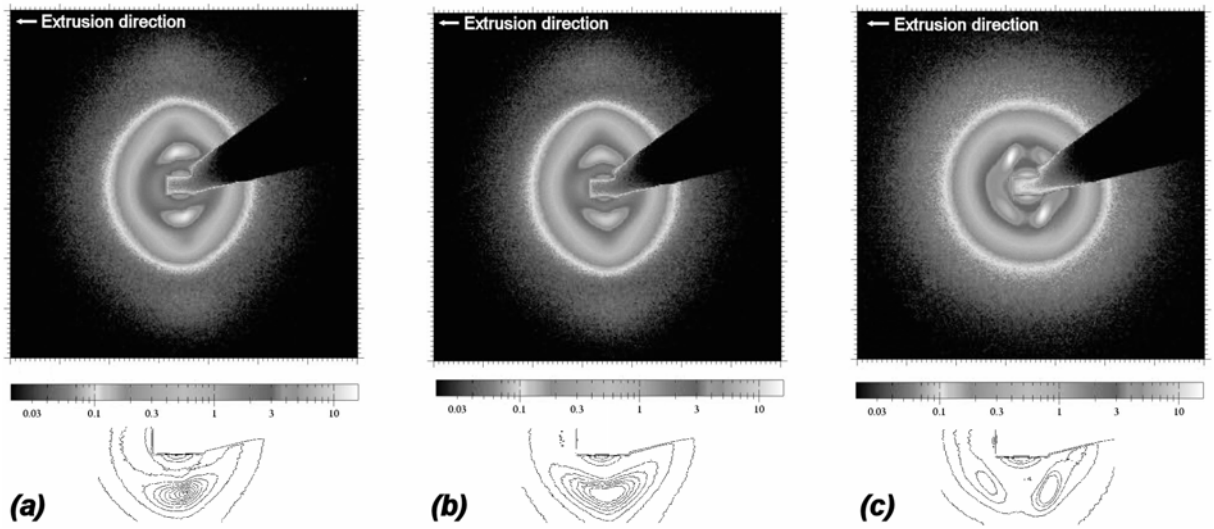

Figure 23: SEBS-3 extruded at 90°C 1 through a die with L/D ratio of 50/5 –SAXS images obtained with the incident beam perpendicular to the extrusion direction. (a) 0.184 s^{-1}, (b) 1.84 s^{-1}, (c) 18.4 s^{-1}.

3.4 Discussion

The effects of extrusion on the organization of microphase separated block copolymers have been studied since the 1970s. It was initially Keller and co-workers (1970) who reported that extruded rods of a Kraton SBS triblock copolymer with 25%PS formed nearly a single-crystal structure of hexagonally-packed PS cylinders aligned. In the case of lamellar structures, Geiger *et al.* (2002) considered two triblock copolymers of styrene and butadiene. One of them was linear while the other was a four arm-star architecture. In both cases the length of the blocks were highly asymmetric. They studied the long-range ordering of these block copolymers by measuring the birefringence in linear polarized light as a function of shear rate for different temperatures. Their results showed initially an ordering at long scales for shear rates below a critical value. For shear rates higher than this critical value that structure seemed to disorder. A possible interpretation of these could be the appearance of flow instabilities of viscoelastic nature. Unfortunately, the authors did not relate the structure at the mesoscopic scale to the macroscopic extrusion regimes. Still using two block copolymers forming a lamellar structure, in recent work by Phatak and co-workers (2005) the evolution of the bulk and surface morphology of a triblock and a pentablock copolymer is studied as a function of extrusion rate. Their results show that surface cracking is 10 times more severe in the case of the pentablock than in the case of the triblock due to the higher connectivity of the first one.

In this paper, we look at two triblock SEBS copolymers presenting different morphologies, cylindrical and spherical, and their effect on the macroscopic defects observed at the die exit.

Figures 4 through 6 showed that the three grades of SEBS were still on their lowerc plateau for rates as low as 10^{-5} rad s^{-1} at the extrusion temperatures used in the case of small strain oscillatory shear. In the case of large amplitude deformations, terminal behavior (slope of 1 in the flow curve) was observed for shear rates lower than 10^{-2} s^{-1} in the case of SEBS-1 and SEBS-2 and 10^{-1} s^{-1} in the case of SEBS-3.

The relaxation time spectrum of block copolymers in their ordered state can be modeled satisfactorily by adding two BSW+CW spectrums; a predominant one that accounts for the PEB blocks and a second one expressing the contribution of the ensemble of PS microdomains in grains in terms of the end-blocks molecular characteristics. The linear viscoelastic response of these SEBS is the one typically observed for microphase separated block copolymers. At high frequencies, an entanglement plateau characteristic of the rubbery matrix is most noticeable. The range of fit parameters giving an adequate superposition of the modeled viscoelastic response and the experimental data results in relaxation times that would be expected for PEB of molecular weight about between 2 and 3 times greater than the molecular weight measured with SEC experiments. In addition, the use of a power law region at the end of the spectrum to account for an apparent reticulation seems to validate the assumption of an apparent infinite molecular weight for flow split to occur at the capillary exit. However, it also proves that this is not the only condition that need to be satisfied. Indeed, a nearly infinite apparent molecular weight is calculated for the PEB block in the case of SEBS-3, but it did not show flow split. Thus it seems it seems an important parameter will be the stiffness of the PS microdomains whose response is observed at low frequencies in the form of the lower plateau and the local stress enhancements that these microdomains generate. As was shown in Figure 9, the lower plateau cannot be explained in terms of the PS chains in the end blocks as these are short and non-entangled. The lower plateau seems then to be the response of characteristic lengths larger than a single endblock. Therefore, we interpret it as being the contribution of the different grains within which the PS microdomains are coherently organized.

Kossuth and co-workers (1999) used the term of cubic plateau to describe the lower plateau. In our results, this plateau is also observed for cylindrical microdomains which are not in a cubic lattice. Actually, this lower plateau seems to be some measure of the matrix stiffness which depends on the nature of the endblock constituent, and its size and thus on the number of entanglements.

The relaxation times of the PEB matrix are short and the melt has time to relax while cooling down at the die exit. On the other hand the relaxation times of the PS blocks are in the order of several hundreds of seconds and the PS microdomains can only partially relax at the die exit. Therefore allowing to foresee that the structure of the extruded melts will remain partlyy unchanged while cooling down at the die exit before the PS domains solidify and “freeze” the microstructure. Thus, one can imagine that the SAXS figures obtained on “cooled down” extruded samples are representative of the effects of flow conditions on the PS mictrodomains.

By examining the path followed by the polymer during the extrusion process at different stages (in the reservoir, in the die, and at the die exit), it has been possible to determine that the alignment and deformation of the PS domains occurs near the die entrance. Indeed, it can be considered to occur in great part, just above the contraction where the flow field has a strong elongational component. In

Figures 16, 17, and 18, one can see that the sample is anisotropic with the PS cylinders oriented in the extrusion direction. From the position of the principal peak in the SAXS images, the intercylinder distance has been deduced and the cylinder diameter calculated from the volume fraction of PS. Our results show that the diameter of the cylinders does not change during the extrusion process, regardless of the extrusion rate. It seems that the different grains forming the material simply align on the mean direction of extrusion.

On the other hand, SAXS images show that deformation of domains is much more important in SEBS-3, thus stresses are released during the flow. This is clearly seen in the differences between the isotropic rings shown in Figure 20 and three captions presented in Figure 21. Moreover, when the distance of the principal peaks are compared parallel and perpendicularly to the extrusion direction, a change in characteristic distance is observed. In both directions, the distance between domains is greater than that one found in the case of the SEBS-3 at rest (Figure 20). Thus, indicating that the PEB matrix is also deformed.

In the case of SEBS-1 and SEBS-2 no significant deformation of the PS cylinders is observed in the case of stable or unstable flow rates. Thus, it seems all stress release occurs at the die exit leading to large surface fractures.

3.5 Conclusions

A possible relaxation time spectrum has been proposed that matches the viscoelastic response of three SEBS copolymers with two different microstructure. SEBS-1 and SEBS-2 presented hexagonally-packed cylinders of PS in a rubbery PEB matrix while in the case of SEBS-3 the PS microdomains were spherical.

The model proposed extends on a BSW+CW relaxation time spectrum by adding the contribution of the chains forming the PS microdomains in the form of a second BSW+CW. This model seems to work particularly well for low rates regimes and has allowed to estimate the crossover point of G' and G" to be in the order of 10^{-6} rad s^{-1} in the case of SEBS-1 and SEBS-2 and of $5x10^{-5}$ rad s^{-1} in the case of SEBS-3 at the extrusion temperatures considered.

Since these block copolymers have long PS microdomain relaxation times, SAXS experiments have been carried out on "cooled down" extruded samples. These experiments have permitted to obtain description of the microstructure alignment in SEBS-1 and SEBS-2 that are coherent with those published in the literature for other copolymer with same weight fractions of endblocks. Moreover, the SAXS experiments have allowed to see that in the case of SEBS-3, the PS microdomains deform significantly when the fluid is extruded, thus releasing in part the stresses in the fluid. On the other hand, no significant differences have been observed on the mean diameter of the cylindrical domains. Hence it is the apparent infinite molecular length of the elastomeric chain which combined with local stress reinforcement may explain crack propagation observed with SEBS copolymers. In the case of SEBS-1 and -2 primary cracks can be more severe. Secondary cracks can be related to the rotation of cylindrical PS microdomains in the diverging flow of polymer rings created by primar cracks at the die exit.

3.6 References

Bergem, N., "Visualization studies of polymer melt flow anomalies in extrusion". Proceedings of the VIIth International Congress on Rheology, Chalmers University of Technology, Gothenburg, Sweden, 50-54 (1976).

Daniel, C. and I.W. Hamley, "Extensional and shear rheometry of oriented triblock copolymers", Rheol. Acta 39, 191-200 (2000).

Daniel, C., I.W. Hamley, K. Mortensen, 'Effect of planar extension on the structure and mechanical properties of polystyrene-poly(ethylene-co-butylene)-polystyrene triblock copolymers", Polymer 41, 9239-9247 (2000).

Fernández M., **A. Santamaria, A. Muñoz-Escalona, L. Méndez**, "A striking hydrodynamic phenomenon: Split of a polymer melt in capillary flow", J. Rheol. 45, 595-602 (2001).

Ferry, J.D., Viscoelastic properties of polymers, 2nd ed. John Wiley and Sons, 1970, Chapter 11.

Fetters, L.J., **Lohse, D.J., and R.H. Colby**, Chain dimensions and entanglements spacings. In: J.E. Mark (Ed.) Physical properties of polymers handbook,American Insitute of Physics, Woodbury, New York, 1996, Chapter 24.

Geiger, K., Knoll, K. and M. Langela, "Microstructure and rheological properties of triblock copolymers under extrusion conditions", Rheol. Acta 41, 345-355 (2002).

Hamley, I.W., The physics of block copolymers, Oxford Press, 1998.

Jackson, J.K., **De Rosa, M.E. and H.H. Winter**, "Molecular weight dependence of relaxation time spectra for the entanglement and flow behavior of monodisperse linear flexible polymers", Macromolecules 27, 2426-2431 (1994).

Jackson, J.K. and H.H. Winter, "Entanglement and flow behavior of bidisperse blends of polystyrene and polybutadiene", Macromolecules 28, 3146-3155 (1995).

Keller, A., **Pedemonte, E., Willmouth, F.M**. "Macro-lattice from segregated amorphous phases of a three block copolymer". Nature, 1970 (225), pp. 538-539

Kossuth, M.B., Morse, D.C., Bates, F.S., "Viscoelastic behavior of cubic phases in block copolymer melts", J. Rheol., 43 (1999) 167-196.

Kotaka, T., M. Okamoto, A. Kojima, Y.K. Kwon, S. Nojima, Elongational flow-induced morphology change of block copolymers part 1. A polystyrene -block-poly(ethylene butylenes)-block-polystyrene-

block-poly(ethylene butylenes) tetrablock copolymer with polystyrene spherical microdomains, Polymer, 42 (2000) 1207-1217.

Mours M. **and H.H. Winter,** "Relaxation patterns of nearly critical gels", Macromolecules 29, 7221-7229 (1996)

Narayanan, T.,O. Diat and P. Bösecke, "SAXS and USAXS on the high brilliance beamline at the ESRF", Nucl. Instrum. Methods Phys. Res. A 467, 1005-1009 (2001)

Nakatani, A.I., Morrison, F.A., Douglas, J.F., Mays, J.W., Jackson, C.L., Muthukumar, M., Han, C.C., "The influence of shear on the ordering temperature of a triblock copolymer melt" Journal of Chemical Physics,, 1996 (104), pp. 1589-1599.

Phatak, A., C.W. Macoscko, F. Bates, and S.F. Hahn, "Extrusion of triblock and pentablock copolymers: Evolution of bulk and surface morphology", J. Rheol. 49, 197-214 (2005).

Rosedale, J.H. and F.S. Bates, "Rheology of ordered and disordered symmetric poly(ethylenepropylene)-poly(ethylethlene) diblock copolymers", Macromolecules, 1990 (23), pp. 2329-2338.

Santanach Carreras, E., N. El Kissi, and J-M. Piau, "Block copolymer extrusion distortions. Exit delayed transversal primary cracks and longitudinal secondary cracks. Extrudate splitting and continuous peeling", J. of Non-Newt. Fluid Mech. (2005) In press.

Tepe, T., **Schulz, MF., Zhao, J., Tirrell, M., Bates, FS., Mortensen, K., Almdal, K.** "Variable shear induced orientation of a diblock copolymer hexagonal phase" Macromolecules, 1995 (28), pp. 3008-3011.

Winter H.H.. **and F. Chambon**, "Analysis of linear viscoelasticity of a crosslinking polymer at the gel point", J. Rheol. 30, 367-382 (1986).

Winter, H.H., **Scott, DB., Gronski, W., Okamoto, S., Hashimoto, T.,** "Ordering by flow near the disorder-order transition of a triblock copolymer styrene-isoprene-styrene". Macromolecules, 1993 (26), pp 7236-7244

Zhao, J., **Biswaroop, M., Schulz, MF., Bates, FS., Almdal, K., Moretensen, K., Hajduk, DA., Gruner, SM.,** "Phase behaviour of pure diblocks and binary diblock blends of poly(ethylene)-poly(ehtylethylene)" Macromolecules, 1996 (29), pp. 1204-1215.

Zhu Z., "Wall slip and extrudate instability of 4-arm star polybutadienes in capillary flow", Rheol. Acta 43, 373-382 (2004).

CONCLUSIONS ET PERSPECTIVES

CONCLUSIONS ET PERSPECTIVES

Dans ce travail de thèse, nous avons étudié l'influence de la pression et de la structure de copolymères triblocs sur la stabilité en écoulement lors de la mise en forme par extrusion. La stabilité pendant l'extrusion de polymères fondus a fait objet de nombreux travaux. Cependant, ces deux aspects n'avaient pas été traités auparavant, d'où l'intérêt de ce travail. Pour l'étude des effets de la pression, 4 PE ont étés considérés. Dans l'étude des instabilités d'extrusion de copolymères triblocs, nous avons utilisés trois polymères de la famille de SEBS avec différentes fractions volumiques de polystyrène.

Les résultats obtenus dans la première partie de cette thèse concernant les effets de la pression sur la stabilité en extrusion et la viscosité des polyéthylènes sont les suivants :

Nous avons déterminé les conditions expérimentales nécessaires pour avoir des échauffements visqueux négligeables et ainsi isoler les effets de la pression. Dans le cas des PE en particulier et d'après nos résultats, les pertes de charge mesurées pendant les expériences ne doivent pas dépasser $200x10^5$ Pa environ.

Dans ces conditions expérimentales, nos résultats montrent que les instabilités d'extrusion observées à pression atmosphérique telles que les régimes oscillatoires, l'instabilité viscoélastique amont, ou le glissement ont aussi lieu à hautes pressions moyennes. De plus, ces instabilités apparaissent à gradients de cisaillement d'autant plus faibles que la pression moyenne augmente. Cependant, le niveau de contrainte critique au-delà duquel les instabilités se déclanchent reste indépendant de la pression moyenne. Les instabilités modifient la loi d'écoulement du fluide et en conséquent elles doivent être prises en compte lorsqu'on détermine les effets de la pression.

L'utilisation du principe de superposition temps-pression a permis de déterminer le coefficient de pression, β, en tenant compte des instabilités pour des écoulement de cisaillement (β_S) et des écoulement fortement élongationnels (β_E). Nos résultats ont montré que les valeurs du coefficient de pression pour le PEHD, le PEBDL, et le mPE-SCB peuvent être considérées comme étant égales aux incertitudes des mesures près. Elles sont dans la gamme 10-15x10^{-9} Pa^{-1} qui est en accord avec les valeurs rapportées dans la littérature pour les PE. Par contre, les coefficients en cisaillement et en élongation du mPE-LCB diffèrent de 30%, β_S étant plus grand que β_E. Cette différence ne peut pas être expliquée par des erreurs de mesure.

Finalement, nous avons proposé d'expliquer les désaccords entre les résultats existants dans la littérature pour un même PEBD par la nécessité de prendre en compte les instabilités d'écoulement.

Cette étude des effets de la pression sur la stabilité en écoulement et la viscosité a fourni de nombreux résultats. Cependant et à fin de l'affiner divers aspects devraient être étudiés plus en détail dans l'avenir :

Le premier point serait de comprendre quel est le rôle combiné de la structure moléculaire (longueur des ramifications, groupements caractéristiques de la chaîne principale…) et du type d'écoulement, élongation ou cisaillement. En effet, nos résultats obtenus avec le mPE-LCB sont à l'opposé de ceux rapportés par Couch et Binding en 2000 pour un polystyrène.

Pour aboutir à cet objectif il serait nécessaire d'observer la réorganisation des chaînes pendant les différents écoulements. Ceci pourrait être fait à l'aide des grands instruments de mesure par des expériences de diffusion aux grands angles. Un dispositif expérimental devrait être conçu. Un système à double piston, comme dans les travaux de Kadjuck et Van den Brule, de petite taille avec une fenêtre d'observation en Béryllium permetrait de faire les essais.

D'autre part, une meilleure précision de mesure avec les orifices minces pourrait être obtenue avec l'utilisation d'un capteur de pression différentiel au lieu des deux capteurs Dynisco.

Nous avons regardé les défauts macroscopiques d'extrusion de différents copolymères triblocs, de la famille de SEBS, et leur relation avec la structure des fluides, dans le deuxième chapitre de cette thèse.

Les résultats suivants ont été constatés :

L'évolution des défauts d'extrusion de ces copolymères est comparable à celle des polymères très enchevêtrés. A des débits très faibles, l'extrudat est lisse et transparent en sortie de filière. Lorsque le débit est augmenté la surface de l'extrudat est fissurée en sortie de la filière. A des débits suffisamment élevés l'instabilité viscoélastique amont apparaît. Si les polymères sont extrudés à débit moyen imposé, les régimes oscillatoires sont aussi observés. Aux plus grand débits, les oscillations de pression cessent et un glissement permanent à la paroi se déclenche.

Cependant, des différences existent, notamment, pendant la fissuration surfacique en sortie de filière. Pour les copolymères les plus réticulés, deux systèmes de relâchement de contraintes ont étés identifies. D'abord un système où les fissures naissent en sortie de filière et se propagent initialement transversalement par rapport au sens de l'extrusion. Ces fissures primaires sont similaires à celles observées avec des homopolymères. Ensuite, un système secondaire de fissures est observé. Les fissures secondaires se propagent dans le sens longitudinal. Elles sont à l'origine du phénomène dit de « refente d'extrudat ». Les travaux présentés ici ont montré pour la première fois que la refente d'extrudat est en fait un cas de fissure surfacique très sévère.

Nos résultats ont montré que les vitesses de propagation de fissures primaire et secondaires suivent différentes lois en fonction de la vitesse moyenne de l'écoulement à l'intérieur de la filière. Pour un niveau de contrainte donné, une augmentation de la vitesse moyenne dans la filière, le régime d'extrusion passe de la *refente d'extrudat* au *pelage continu*. Ce dernier régime d'extrusion n'avait pas été rapporté auparavant.

De plus, l'extrusion d'un polybutadiène de très haut poids moléculaire nous a permis de montrer que ces systèmes de fissures secondaires peuvent être aussi observés pour des chaînes linéaires, si le nombre d'enchevêtrements est suffisamment important. Ceci nous a conduit à conclure qu'une masse moléculaire apparente infinie est une condition sine qua non pour observer ces fissures secondaires.

Cette étude a abouti à de nombreuses conclusions. Cependant, certains points devraient être étudiés encore. Il serait intéressant de réussir à déterminer les contraintes d'élongation et les déformations locales au points d'initiation des fissures, et de les comparer à des résultats en essais de traction jusqu'à la rupture.

Pour montrer la relation entre la morphologie du copolymère bloc et l'apparition du système de fissures secondaires, des essais avec un SEBS 30%PS mais de faible masse moléculaire seraient envisageable. La basse masse moléculaire permettrait d'avoir des domaines cylindriques moins rigides que dans le cas des SEBS-1 et -2 utilisés. Une autre possibilité envisageable serait d'utiliser un SEBS13%PS mais avec une forte masse moléculaire. Dans ce cas, on aurait des domaines sphériques plus rigides que dans le cas du SEBS-3.

Finalement, il serait intéressant aussi d'étudier la structure présentée par les copolymères aux différents régimes d'extrusion et de voir comment les microdomaines s'orientent aux régimes des différents défauts d'extrusion. Ceci serait possible par l'utilisation de la microscopie électronique à balayage haute résolution. Les échantillons devraient être marqués avec de l'OsO_4 et cryofracturés.

Cette étude par microscopie électronique à balayage serait utile aussi pour vérifier les hypothèses faites lors de l'interprétation des figures de diffusion présentées dans la troisième partie de cette thèse.

Le Chapitre 3 de cette thèse fait apparaître les résultats suivants.

La réponse viscoélastique dans le domaine linéaire des copolymères blocs peut être modélisée par la combinaison de deux spectres de temps de relaxation du type BSW+CW. L'un des deux représente la matrice de PEB tandis que l'autre représente les domaines de PS. Un bon accord entre la prédiction du modèle et les donnés expérimentales a été observée. Néanmoins, ce modèle devrait encore être raffiné. Pour cela il serait nécessaire de caractériser des homopolymèrès, PS et PEB, de tailles équivalentes à celles des blocs et pour ainsi obtenir les paramètres à introduire dans le modèle. Une étude plus poussée permettrait de mieux comprendre comment les différents paramètres interviennent. En particulier il serait intéressant de comprendre la loi de mélangeage et quelle est la relation entre le poids du spectre de chaque constituant et sa fraction volumique.

Grâce aux grand instruments disponibles à l'ESRF, à Grenoble, nous avons pu suivre les effets du procédé d'extrusion sur la microstructure de copolymères blocs. Pour cela nous avons développé un rhéomètre capillaire équipé d'une filière usinée en Béryllium permettant des essais de rayonnement in-situ. Même si des essais ont été faits off-line, nos résultats ont montré que l'alignement des domaines de PS a lieu en entrée de filière. Cependant, des essais en ligne seront nécessaires pour bien comprendre le processus d'orientation de microdomaines.

ANNEXES

Annexe A

Extrusion de copolymères blocs :

Photographies d'extrudats en sortie de filière

A.1 SEBS–1 extrudé à 190°C à travers d'une filière avec rapport longueur sur diamètre (L/D) de 10/1

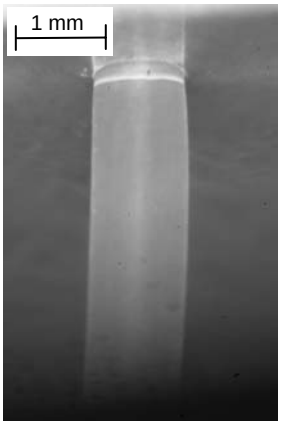

$\tau_w = 0.15 \text{x} 10^5$ Pa
$\dot{\gamma}_a = 0.006\ s^{-1}$

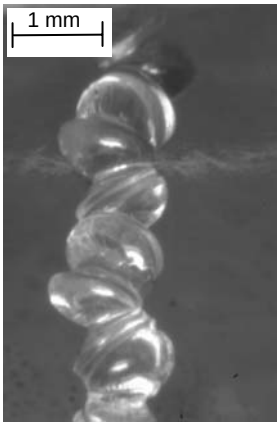

$\tau_w = 0.25 \text{x} 10^5$ Pa
$\dot{\gamma}_a = 0.011\ s^{-1}$

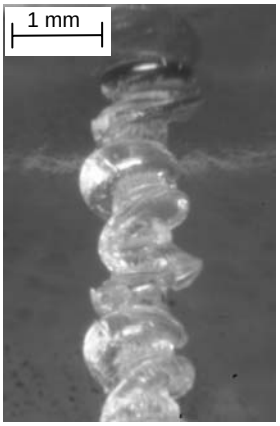

$\tau_w = 0.38 \text{x} 10^5$ Pa
$\dot{\gamma}_a = 0.02\ s^{-1}$

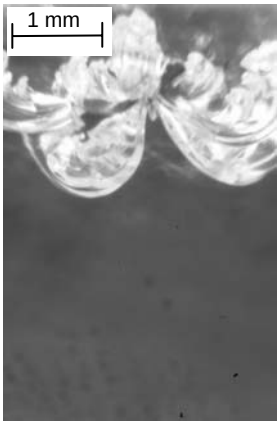

$\tau_w > 0.50 \text{x} 10^5$ Pa

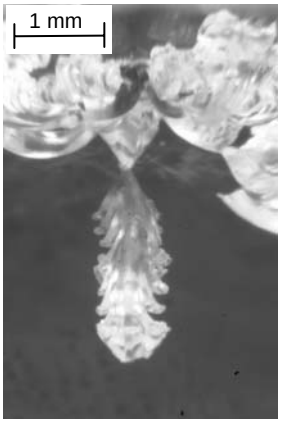

$\tau_w = 2.80 \text{x} 10^5$ Pa
$\dot{\gamma}_a = 1.15\ s^{-1}$

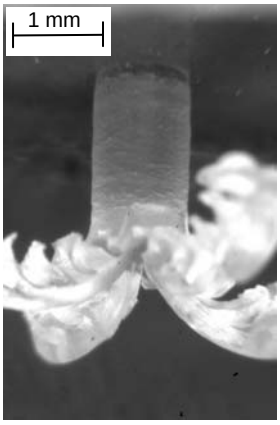

$\tau_w \sim 4.15 \text{x} 10^5$ Pa
$6\ s^{-1} \sim \dot{\gamma}_a < 48\ s^{-1}$

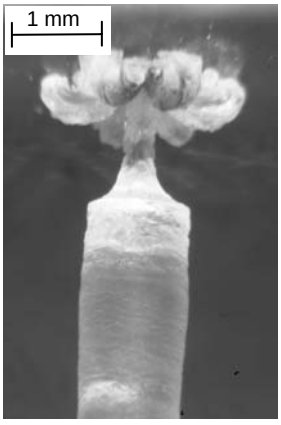

$\tau_w \sim 4.05 \text{x} 10^5$ Pa
$6\ s^{-1} \sim \dot{\gamma}_a < 48\ s^{-1}$

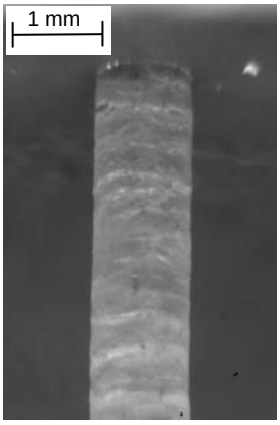

$\tau_w = 3.37 \text{x} 10^5$ Pa
$\dot{\gamma}_a = 48\ s^{-1}$

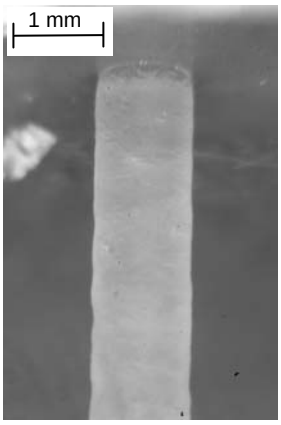

$\tau_w = 3.75 \text{x} 10^5$ Pa
$\dot{\gamma}_a = 96\ s^{-1}$

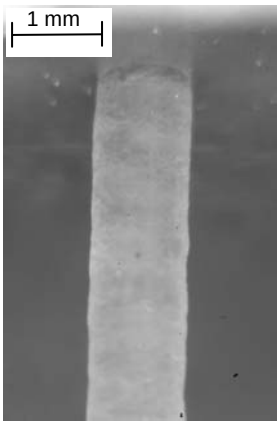

$\tau_w = 4.64 \text{x} 10^5$ Pa
$\dot{\gamma}_a = 192\ s^{-1}$

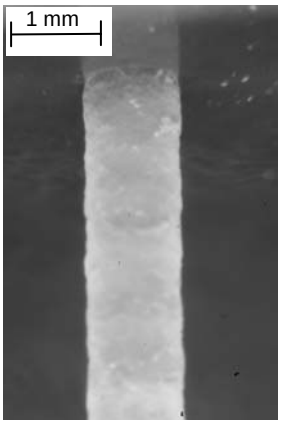

$\tau_w = 5.33 \text{x} 10^5$ Pa
$\dot{\gamma}_a = 384\ s^{-1}$

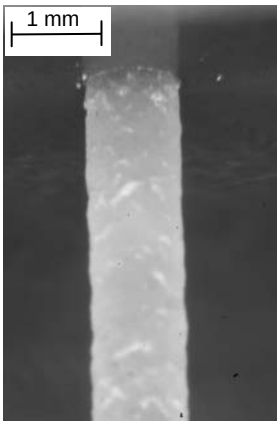

$\tau_w = 5.33 \text{x} 10^5$ Pa
$\dot{\gamma}_a = 768\ s^{-1}$

A.2 SEBS–1 extrudé à 190°C à travers d'une filière orifice mince de diamètre 1 mm (L/D~0)

$\Delta P = 4x10^5$ Pa

$\Delta P = 4.5x10^5$ Pa

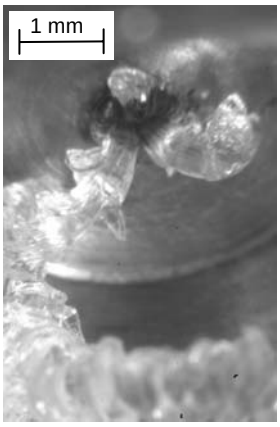

$\Delta P = 7x10^5$ Pa

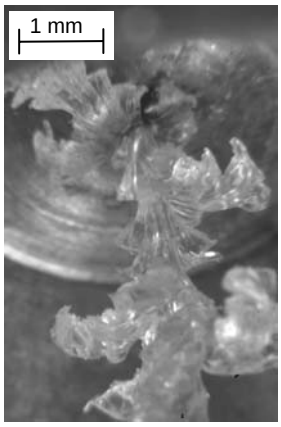

$\Delta P = 10x10^5$ Pa

$\dot{\gamma}_a = 1.15\ s^{-1}$

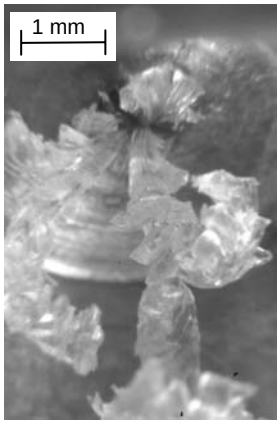

$\Delta P = 18x10^5$ Pa

$\dot{\gamma}_a = 6\ s^{-1}$

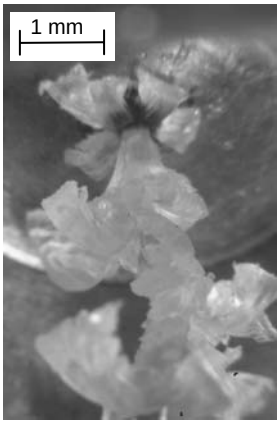

$\Delta P = 27x10^5$ Pa

$\dot{\gamma}_a = 12\ s^{-1}$

$\Delta P = 38x10^5$ Pa

$\dot{\gamma}_a = 24\ s^{-1}$

$\Delta P = 50x10^5$ Pa

$\dot{\gamma}_a = 48\ s^{-1}$

$\Delta P = 80x10^5$ Pa

$\dot{\gamma}_a = 192\ s^{-1}$

$\Delta P = 95x10^5$ Pa

$\dot{\gamma}_a = 384\ s^{-1}$

A.3 SEBS–1 à 295°C avec une filière L/D=10/1

A.3.1 Photographies

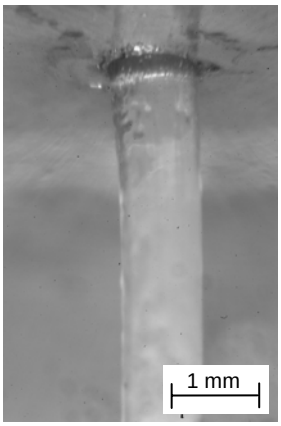

$\tau_w = 0.18x10^5$ Pa
$\dot{\gamma}_a = 3\ s^{-1}$

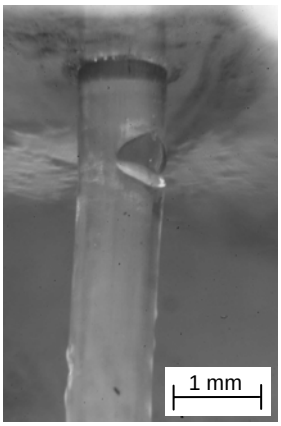

$\tau_w = 0.42x10^5$ Pa
$\dot{\gamma}_a = 6\ s^{-1}$

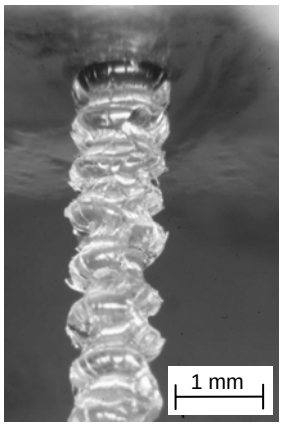

$\tau_w = 0.61x10^5$ Pa
$\dot{\gamma}_a = 12\ s^{-1}$

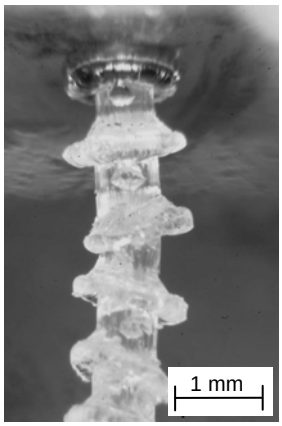

$\tau_w = 0.97x10^5$ Pa
$\dot{\gamma}_a = 24\ s^{-1}$

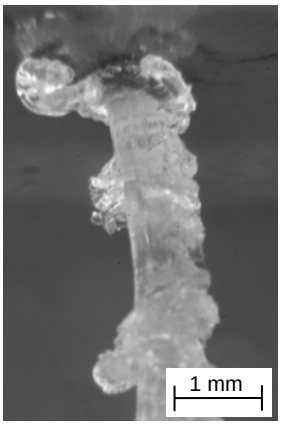

$\tau_w = 1.38x10^5$ Pa
$\dot{\gamma}_a = 48\ s^{-1}$

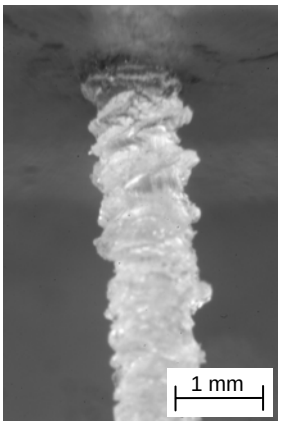

$\tau_w = 1.96x10^5$ Pa
$\dot{\gamma}_a = 96\ s^{-1}$

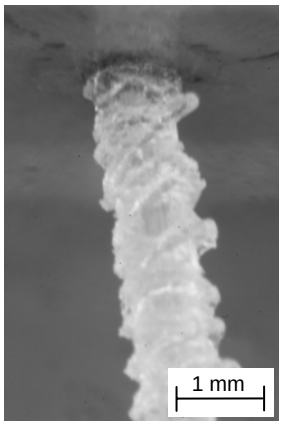

$\tau_w = 2.56x10^5$ Pa
$\dot{\gamma}_a = 192\ s^{-1}$

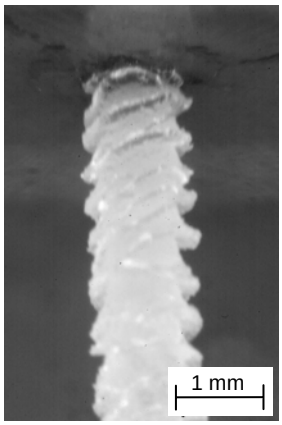

$\tau_w = 3.10x10^5$ Pa
$\dot{\gamma}_a = 384\ s^{-1}$

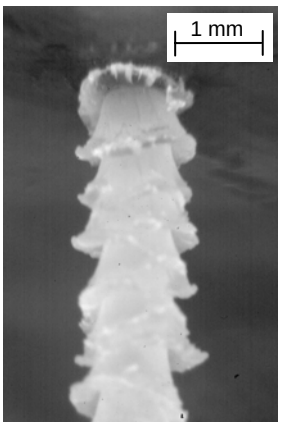

$\tau_w = 3.75x10^5$ Pa
$\dot{\gamma}_a = 768\ s^{-1}$

A.3.2 Images extraites à partir de films

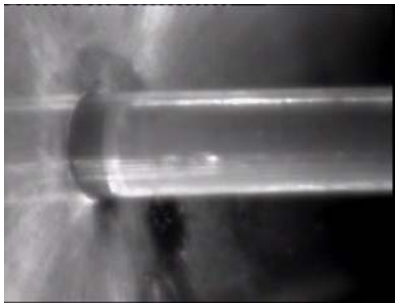

(10/1) **3 s^{-1}**/ 0.2x10^5 Pa

(20/2) **entre 6 et 12 s^{-1}**

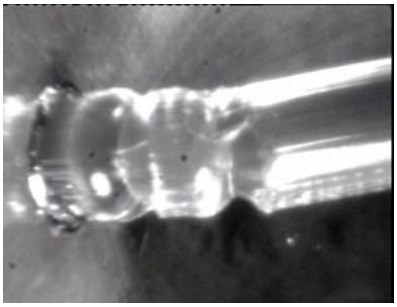

(20/2) **entre 6 et 12 s^{-1}**

(20/2) **12 s^{-1}**/ 0.65x10^5 Pa

(20/2) **48 s^{-1}**/ 1.5x10^5 Pa

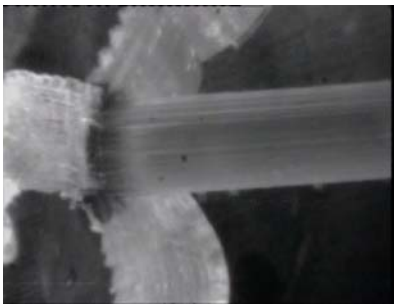

(10/1) **96 s^{-1}**/ 2.1x10^5 Pa

(10/1) **192 s^{-1}**/ 2.7x10^5 Pa

(10/1) **384 s^{-1}**/ 3.4x10^5 Pa (A)

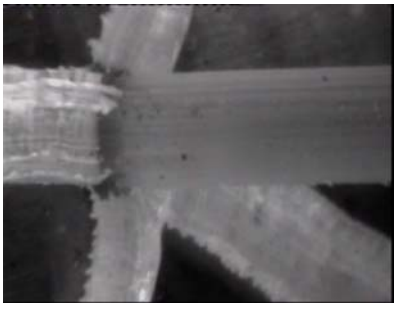

(10/1) **384 s^{-1}**/ 3.4x10^5 Pa (B)

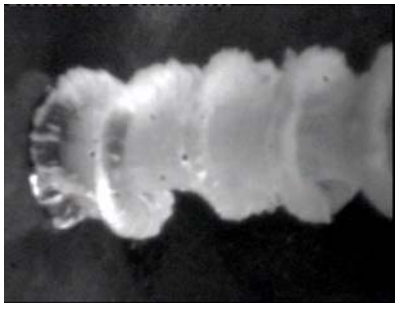

(10/1) **768 s^{-1}**/ 4.1x10^5 Pa

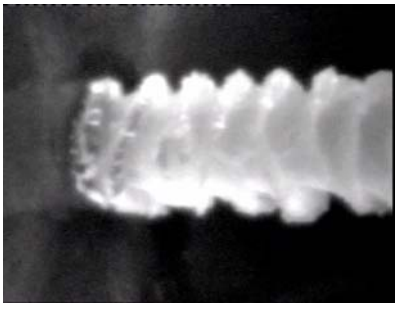

(10/1) **1536 s^{-1}**/ ~5x10^5 Pa

A.4 SEBS–1 à 295°C à travers d'une filière orifice mince de diamètre 1 mm (L/D~0)

$\Delta P = 1.88 \times 10^5$ Pa

$\dot{\gamma}_a = 24\ s^{-1}$

$\Delta P = 4.45 \times 10^5$ Pa

$\dot{\gamma}_a = 96\ s^{-1}$

$\Delta P = 6.7 \times 10^5$ Pa

$\dot{\gamma}_a = 192\ s^{-1}$

$\Delta P = 10.3 \times 10^5$ Pa

$\dot{\gamma}_a = 384\ s^{-1}$

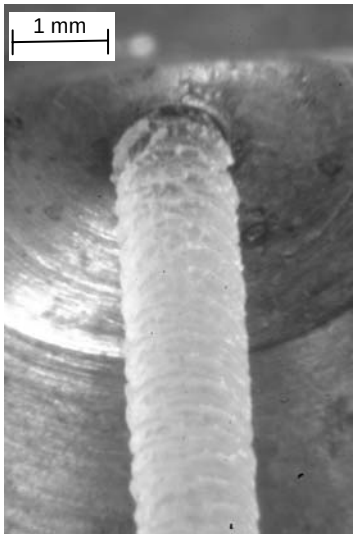

$\Delta P = 15.2 \times 10^5$ Pa

$\dot{\gamma}_a = 768\ s^{-1}$

A.5 SEBS–3 à 190°C à travers d'une filière L/D=10/1

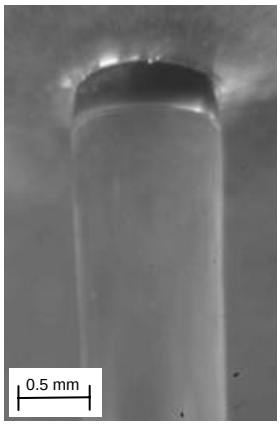

$\tau_w = 0.21x10^5$ Pa

$\dot{\gamma}_a = 6\ s^{-1}$

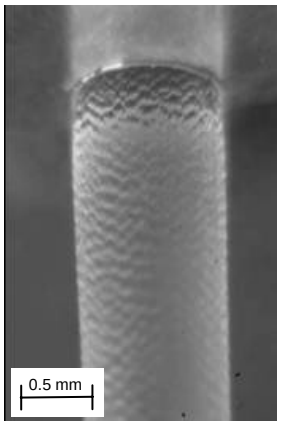

$\tau_w = 0.46x10^5$ Pa

$\dot{\gamma}_a = 12\ s^{-1}$

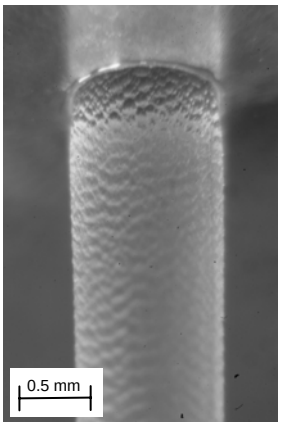

$\tau_w = 1.41x10^5$ Pa

$\dot{\gamma}_a = 48\ s^{-1}$

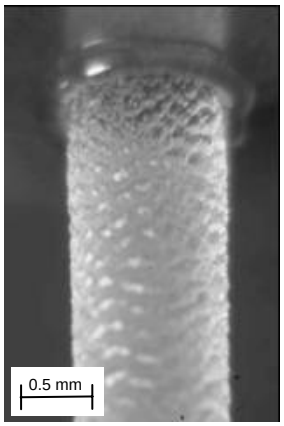

$\tau_w = 2.15x10^5$ Pa

$\dot{\gamma}_a = 96\ s^{-1}$

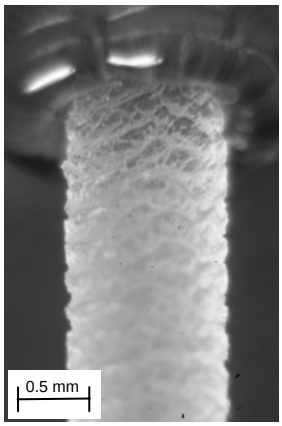

$\tau_w = 2.98x10^5$ Pa

$\dot{\gamma}_a = 192\ s^{-1}$

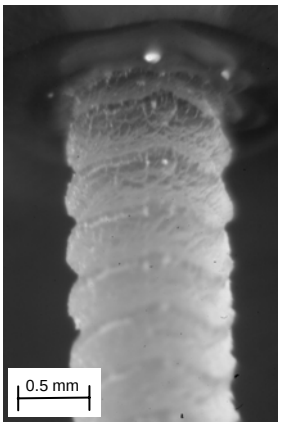

$\tau_w = 3.75x10^5$ Pa

$\dot{\gamma}_a = 384\ s^{-1}$

$\tau_w = 4.33x10^5$ Pa

$\dot{\gamma}_a = 768\ s^{-1}$

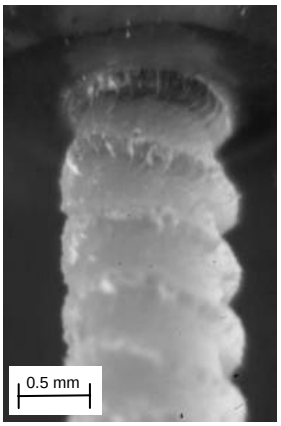

$\tau_w = 5x10^5$ Pa

$\dot{\gamma}_a = 1535\ s^{-1}$

Annexe B

Rheometre capillaire portable:

caracteristiques et fonctionnement

B.1 DISPOSITIF EXPERIMENTAL

Le rhéomètre capillaire « portable » a été conçu de façon à pouvoir faire des essais de diffusion de rayons-x aux petits angles in-situ. Pour cela il est muni d'une filière usinée entièrement en Béryllium de 2 mm de diamètre intérieur et 10 mm de longueur. L'épaisseur de la paroi est de 1.25 mm.
La pression maximale autorisée en entrée de filière pendant l'utilisation du rhéomètre portable est de 200 bar. Pour la sécurité de l'utilisateur sans pression de gaz, et du dispositif expérimental, on ne dépassera pas 200 bar pendant les essais. La température maximale d'utilisation est de 150°C.

PRESSION MAXIMALE : 200 bar

TEMPERATURE MAXIMALE : 150°C

IMPORTANT : la filière en Béryllium est très fragile (et chère). L'état de ses surfaces intérieure et extérieure doit être libre de toute rayure ou poussière, car celles-ci peuvent fausser les résultats.

Le dispositif expérimental peut être divisé en trois parties principales :

- les filières et le porte-filière
- le système de réglage en température
- le système de poussée

Les composants du système de réglage en température et de poussée sont indiqués en Figure 1. La filière n'est pas visible sur cette figure.

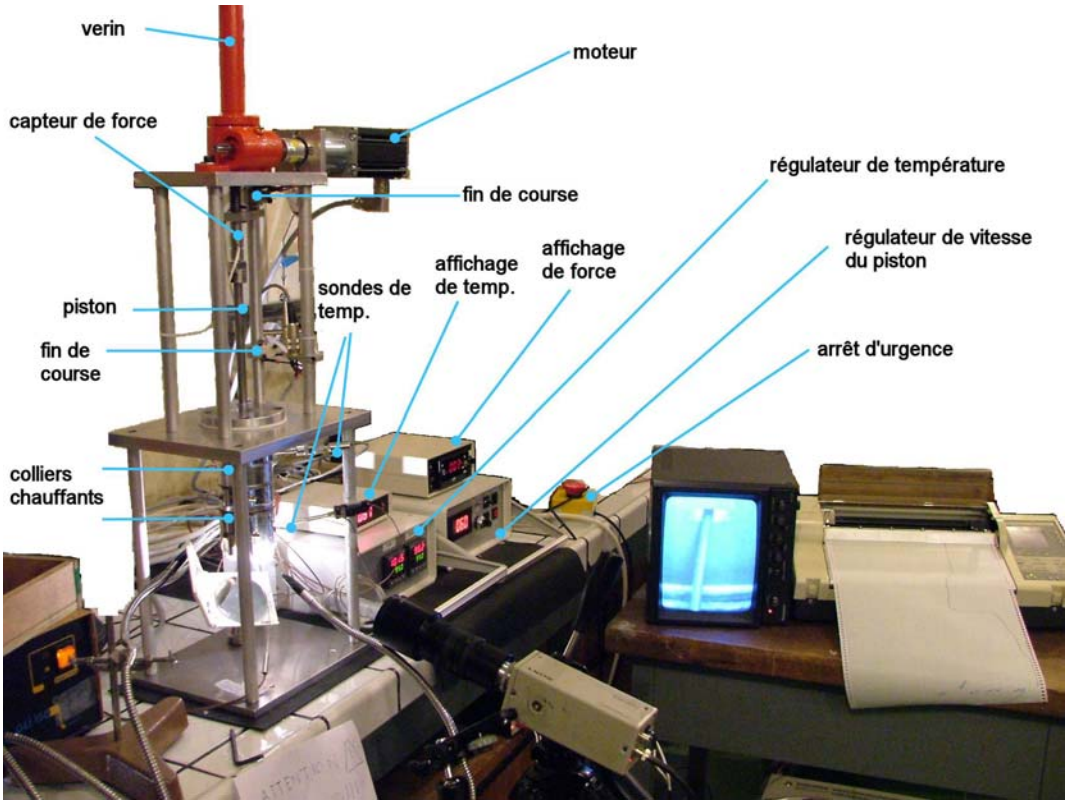

B 1: Vue de l'ensemble du dispositif expérimental. Pendant les essais, l'extrudat en sortie de filière est observé sur l'écran et enregistré par un magnétoscope. La mesure de force, ainsi que la mesure de température sur l'un des colliers sont enregistrées par l'enregistreur multivoie SEFRAM.

B.1.1 Les filières et le porte-filière

Le cœur du rhéomètre portable, et ce qui en fait son principal intérêt est la filière en Béryllium. Celle-ci est très délicate car un bon état de ses surfaces est primordial pour obtenir de bons résultats de diffusion.
A la différence de filières utilisées avec le Göttfert, la filière en Béryllium ne peut pas être nettoyée avec un fil de cuivre. Les poussières de cuivre que l'on risque de déposer sur les surfaces pendant le nettoyage introduiraient beaucoup de bruit sur les mesures, du fait de la grand absorption des rayons –X par le cuivre. Pour l'instant, on nettoie la filière en passant suffisamment de polymère.

IMPORTANT : la filière en Béryllium est très fragile (et chère). Les surfaces intérieure et extérieure doivent être vierges de toute rayure ou poussière, car celles-ci peuvent fausser les résultats.

NE PAS UTILISER UN FIL DE CUIVRE POUR NETTOYER LA FILIERE

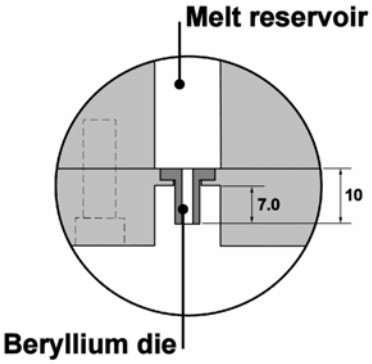

B.2. Détail du cœur du rhéomètre portable. La filière en béryllium et son porte filière.

Outre la filière en Béryllium, il existe aussi une filière orifice mince usinée en laiton. Elle est utilisée pour évaluer la perte de charge singulière due à la contraction entre le réservoir et la filière en Béryllium.

La filière utilisée est placée dans le porte-filière qui est attaché au corps du réservoir par quatre vis. Un joint torique en viton assure l'étanchéité entre le réservoir et le porte-filière.

B.1.2 Le système de réglage en température

Il est constitué de deux colliers chauffants, serrés autour du réservoir, qui sont contrôlés indépendamment par deux régulateurs de température. Deux sondes PT-100 et un thermocouple sont utilisés pour les mesures de température. Les réglages sont faits sur le boîtier principal (régulateur de température sur la Figure 1). Le petit boîtier donne accès à la mesure de température à distance, le câble faisant plusieurs mètres de long.
Les deux colliers ne sont pas identiques, l'un étant plus long que l'autre. Il faut placer le collier le plus long en haut, et le plus court en bas. La mesure de température pour la régulation est faite par deux sondes PT-100 qui sont placées à l'intérieur de deux trous dans le corps du réservoir. Les colliers et les sondes sont branchés sur la façade arrière du boîtier de régulation en température.

ATTENTION : quand on connecte les colliers chauffants et les sondes au boîtier, on doit s'assurer que la sonde placée sur le trou inférieur est bien reliée au collier chauffant placé en bas.

L'interrupteur pour alimenter le système de chauffage se trouve aussi situé sur la façade arrière du boîtier. Une fois le système allumé, il faut attendre quelques instants pour que les régulateurs s'initialisent. On peut changer la température d'extrusion lorsque les régulateurs ont fini leur initialisation. Les deux régulateurs fonctionnent de la même façon. Ils indiquent deux valeurs de température, une en rouge (la valeur réelle) et une en verte (la valeur programmée ou set point). Ils ont quatre touches sur leurs façades. On n'utilise que les trois de droite.

Pour rentrer la valeur de la température d'extrusion, on appuie sur la touche la plus à droite une fois. L'affichage en vert indique alors le message S.P. Ensuite on montera, ou descendra, la température d'extrusion (affichage rouge) avec les touches ▲ et ▼. Finalement, on appuie de nouveau sur la touche la plus à droite pour sortir. Ensuite on attend que le rhéomètre soit à température.

NOTE : pour chauffer à 150°C, il faut environ 35 min pour atteindre l'équilibre à partir de l'ambiante.

B.1.3 Le système de poussée et le capteur de force

Les différentes composantes du système sont :

- Le motoréducteur
- Le vérin
- Les capteurs de fin de course
- Le régulateur de vitesse
- L'arrêt d'urgence
- Le capteur de force
- Affichage de force

MESURES DE SECURITE : le rhéomètre est doté de différents dispositifs de sécurité pour éviter tout accident pendant les essais.

- Tout essai peut être arrêté en poussant sur **l'arrêt d'urgence** (boîtier jaune avec poussoir rouge). Cet action coupe uniquement l'alimentation du motoréducteur et de sa commande.
- Un **poussoir arrêt (rouge)** est aussi placé sur le boîtier de régulation de vitesse.
- L'arrêt du moteur se fait aussi par l'appui de n'importe quel poussoir différent de celui actionné.
- **Deux seuils de force (1 haut, 1 bas)**. Si la force mesurée par le capteur est au-delà de la gamme limitée par les seuils, le moteur s'arrête automatiquement.
- **Deux capteurs de fin de course** délimitent le parcours du piston. Ne pas les bouger. Ils sont réglés au mm près.

Le système est contrôlé par le régulateur de vitesse. Tous les contrôles se trouvent sur la façade avant du boîtier. La connectique se fait sur la façade arrière. Le boîtier est connecté à l'alimentation principale.

B.1.3.1 Connectique

Pour mettre en place le dispositif expérimental il faut brancher le câble du motoreducteur et le câble des fins de course. Il faut également connecter le câble correspondant aux seuils de force entre l'afficheur du capteur de force et le boîtier de régulation de vitesse.
Le capteur de force se raccorde à la face arrière de l'afficheur. De la sortie analogique de l'afficheur du capteur de force (câble BNC), on peut récupérer le signal en fonction du temps avec l'enregistreur multi voies.

B.1.3.2 Le capteur de force et son boîtier d'affichage

Le capteur de force est fait pour mesurer des sollicitations en traction et en compression, mais il *ne peut pas supporter de charges ni en torsion, ni en flexion (de plus il est cher)*.
L'étendue de mesure en traction et en compression est de 500 daN, sa précision étant de ±2,5 daN.

L'interrupteur de l'afficheur du capteur de force se trouve sur le coté gauche de la façade avant du boîtier. L'affichage du boîtier indique la force en daN.
Pour régler le zéro de l'afficheur il faut tourner le potentiomètre libellé « zéro » qui se trouve en bas à droite de l'affichage de façon à que le signe négatif clignote (ou disparaisse).

Les réglages de seuils se font aussi par des potentiomètres. Leur réglage se fait en appuyant sur l'un des poussoirs SH, ou SB, qui se trouvent à gauche, ou à droite, de l'afficheur. la valeur du seuil se règle à l'aide d'un tournevis, en maintenant le poussoir appuyé.

IMPORTANT : Pendant les essais d'extrusion, le capteur sera principalement sollicité en compression. Donc, le seuil haut (SH) doit être réglé à une valeur négative (qui correspond à la compression) et le seuil bas (SB) doit être régé à une valeur positive.

Le seuil haut, SH, ne peut pas être plus bas que -200 daN par sécurité !!!

B.1.3.3 Boîtier de régulation de vitesse

Tous les contrôles pour la vitesse de mouvement du piston se trouvent sur la façade avant du boîtier.

Le poussoir rouge sert à arrêter le moteur.

Le poussoir noir en haut à droite est utilisé pour faire remonter le piston une fois l'essai est fini. Une seule vitesse est disponible en montée, la vitesse maximale du moteur (~ 500 µm s^{-1}).

Un levier à bascule permet une descente rapide (~ 500 µm s^{-1}) du piston. Vers le haut, la commande est impulsionnelle. C'est-à-dire, qu'une seule touche est suffisante pour faire descendre le piston. Vers les bas, la commande est à action maintenue. C'est-à-dire, elle doit être maintenue appuyée pour que le piston descende. Si on relâche le levier, le moteur s'arrête.

L'option d'une descente de piston à vitesse réglée existe aussi. Pour cela il faudra appuyer sur le poussoir noir situé à gauche du bouton d'arrêt. Quand on utilise ce mode de descente, la vitesse est contrôlée par le potentiomètre. La valeur de la vitesse de descente, en µm s^{-1}, est affichée sur l'écran. La vitesse minimale est de l'ordre de 18 µm s^{-1}.

B.2 MISE EN ROUTE DU RHEOMETRE

Pour mettre en route le rhéomètre, il faut simplement connecter tous les câbles comme expliqué précédemment et allumer les alimentations. Lorsque la température d'extrusion est établie, on peut commencer les essais. La section qui suit explique le déroulement d'un essais type.

B.3 EXPERIENCE TYPE

On remplit le réservoir et on attend que le polymère soit fondu et à température. La température du polymère fondu peut être mesurée en introduisant un thermocouple dans le réservoir.

Quand le polymère est fondu, on descend le piston jusqu'à ce que le polymère commence à couler.

On note la hauteur initiale du piston à l'aide de la regle millimétré placé à gauche du rhéomètre, et on lance l'essai en appuyant sur le poussoir de vitesse contrôlée. En même temps qu'on lance l'essai, il faut démarrer l'enregistreur pour avoir et conserver une trace de la mesure de force en fonction de la hauteur.

NOTE : Il est conseillé de commencer avec la vitesse la plus faible et ensuite, quand le réservoir est un peu moins plein, d'utiliser les vitesses élevées.

Idéalement on devrait vider un réservoir pour chaque vitesse étudiée, mais il est possible d'étudier plusieurs vitesses avec le même réservoir. Ceci permettra de gagner du temps. La Figure 2 montre des données expérimentales obtenues avec le rhéomètre.

NOTE : Quand on remonte le piston, le polymère risque d'entraîner la filière. Pour éviter cela, on peut la retenir avec des pinces revêtues de PTFE et couvertes avec du papier essuie-tout (pour éviter d'endommager la filière)

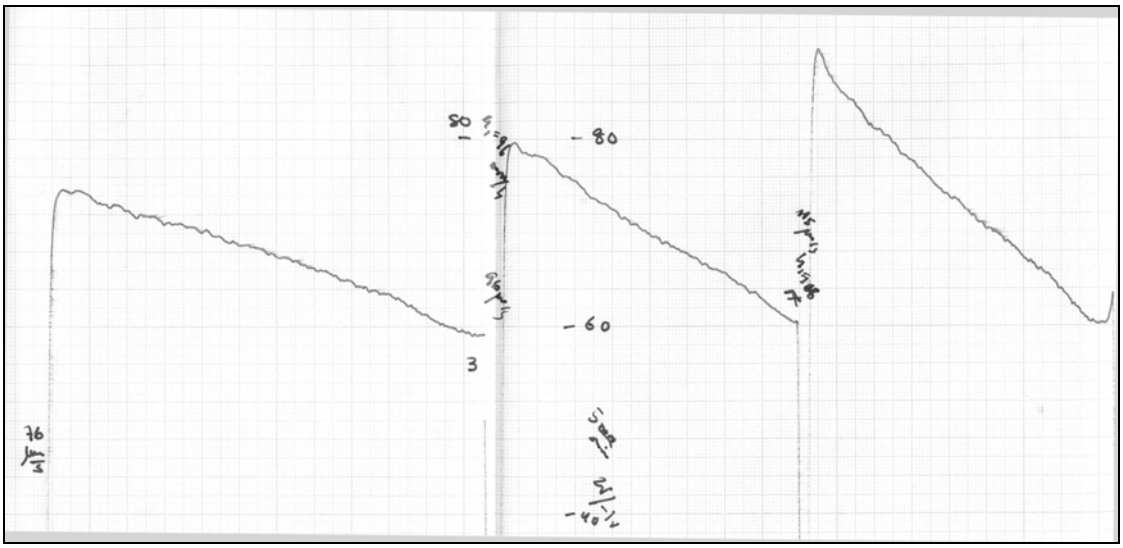

B. 3: Enregistrements de la Force en fonction du temps (proportionnel à la hauteur). Ces essais correspondent à un SEBS avec 13%PS extrudé à 100°C à travers un orifice mince usiné en laiton. Les vitesses étudiées sont 76, 96, et 115 µm s^{-1}. Un réservoir entier a été vidé pour chaque vitesse. Le papier de l'enregistreur défile à une vitesse de 5 mm min^{-1}. Verticalement, 50 mm représentent 20 daN.

B.4 TRAITEMENT DES DONNEES

L'objectif final est d'obtenir la courbe d'écoulement du fluide. Pour cela, il faudra traiter les données brutes de la façon suivante :

- Premièrement il faut passer les enregistrement du capteur F(t) à F(h). Ceci est fait à partir de la position initiale du piston, sa position finale, et la vitesse de déroulement du papier.
- Une fois les courbes F(h) tracées, on soustrait la courbe obtenue avec l'orifice mince à une vitesse U_p de celle obtenue avec la filière en Béryllium pour la même vitesse. La soustraction est faite entre points de mesure à hauteur de réservoir égale. Cette étape est équivalente à faire la correction de Couette-Bagley.
- La force résultante, théoriquement indépendante de la hauteur, est alors convertie en contrainte à la paroi de la filière. Pour cela, on fait un bilan de forces.

$$\left(F(h,U) - F_o(h,U)\right)\frac{d^2}{D^2} = \tau\pi dL$$

où d et D sont les diamètres de la filière et du réservoir respectivement. L représente la longueur effective de la filière. Elle est de l'ordre de 8,5 mm car l'orifice mince fait ~1,5 mm de longueur et celle de la filière en Béryllium est de 10 mm.

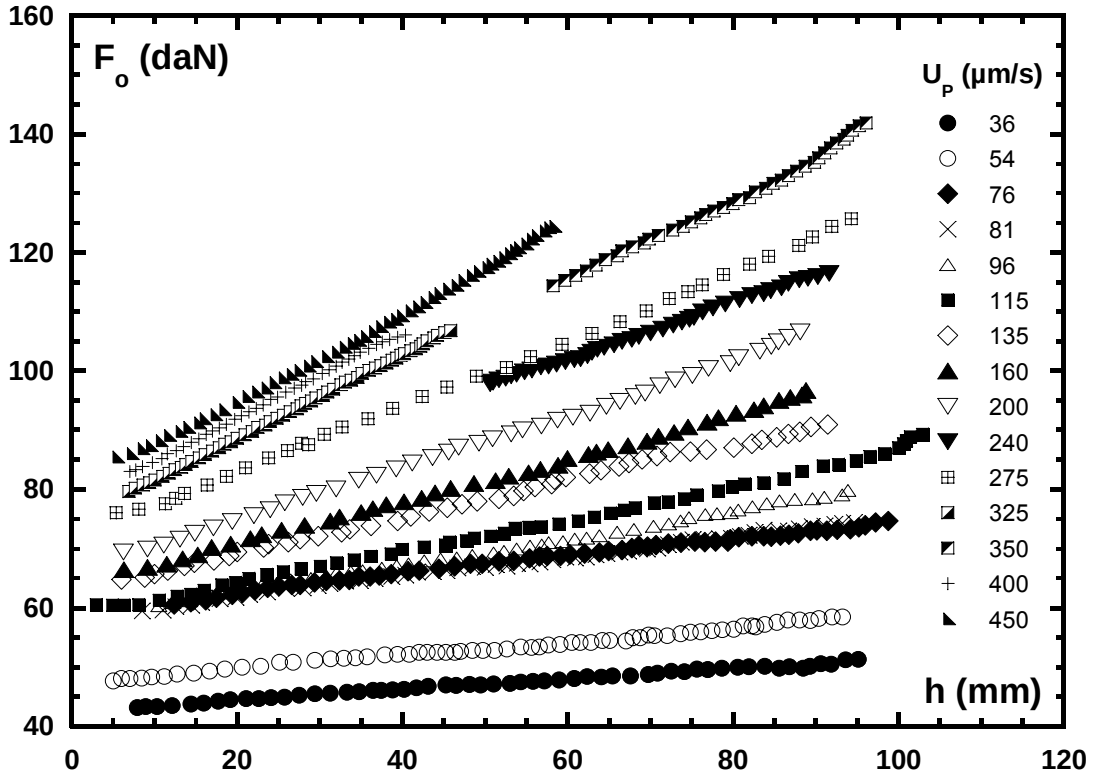

B.4: Force en fonction de la hauteur de polymère dans le réservoir pour différentes vitesses de piston. Le produit est du SEBS avec 13%PS. Il est extrudé à 100°C à travers la filière mince en laiton (L/D ~ 0).

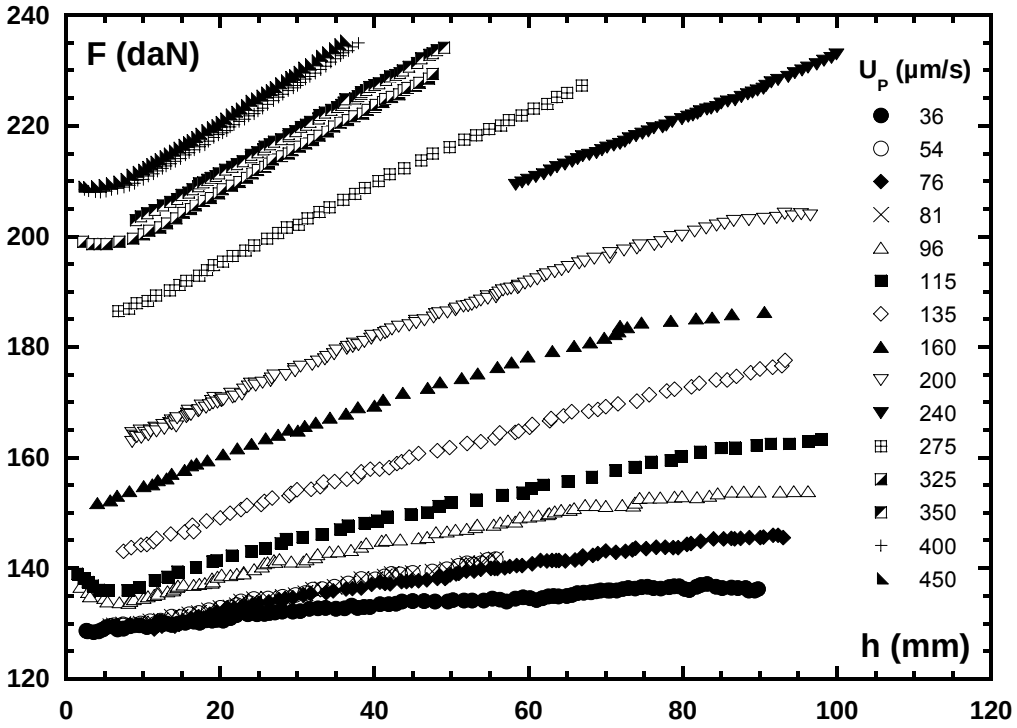

B.5: Force en fonction de l'hauteur de polymère dans le réservoir pour différentes vitesses de piston. Le produit est du SEBS avec 13%PS. Il est extrudé à 100°C à travers la filière en Béryllium (L/D = 10/2).

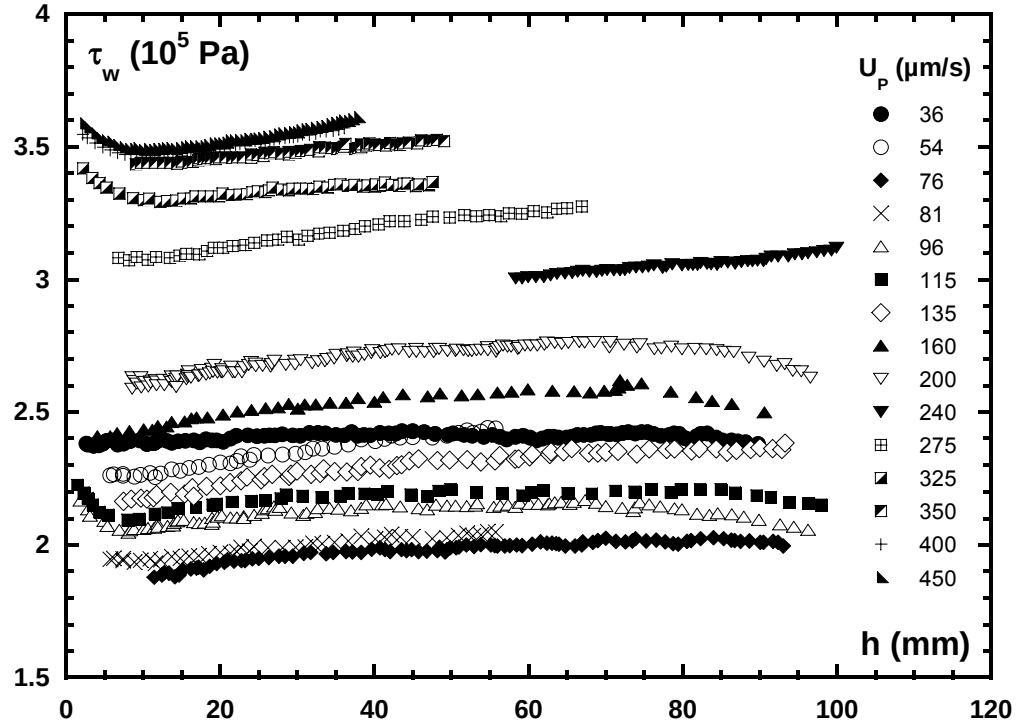

B.6: Force corrigée en fonction de la hauteur de polymère dans le réservoir pour différentes vitesses de piston. Le produit est du SEBS avec 13%PS. Il est extrudé à 100°C à travers la filière en Béryllium (L/D = 10/2).

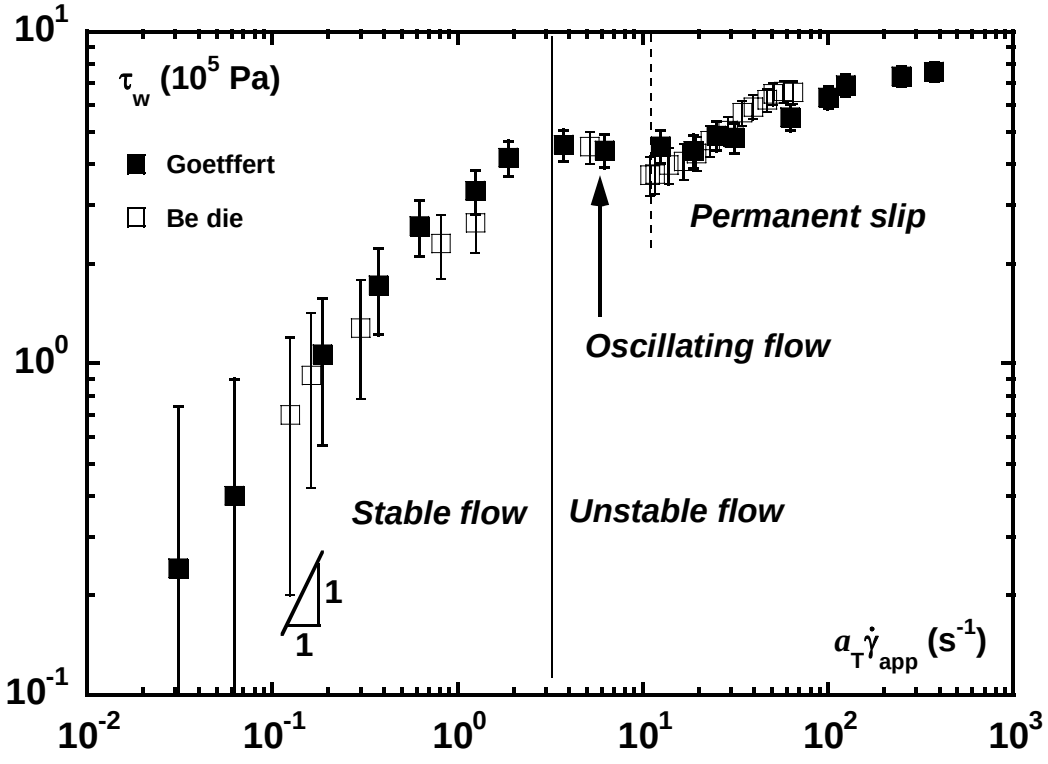

B.7: Comparaison des courbes d'écoulement obtenues avec le rhéomètre capillaire portable et avec le rhéomètre Göttfert pour un SEBS avec 13%PS à 110°C. Dans le cas du rhéomètre portable, la valeur moyenne de la contrainte pour chaque vitesse a été considérée.

Annexe C

Figures de diffusion de rayons X aux petits angles (SAXS) et analyse

Cette annexe présente les figures obtenues lors des essais de diffusion de rayons X aux petits angles à l'ESRF de Grenoble pour des échantillons obtenus par moulage à compression et avec des extrudats relaxés.
Les deux premières figures de diffusion correspondent aux échantillons obtenus par moulage en compression du SEBS-1.
Les figures de diffusions restantes correspondent aux extrudat relaxés. Une partie des essais ont été menés avec le faisceau incident étant perpendiculaire au sens de l'extrusion. D'autres échantillons ont été observés avec le faisceau incident étant parallèle au sens de l'extrusion. Les deux cas sont représentés dans la figure ci-dessous avec un schéma des éléments essentiels pour un essai de diffusion.

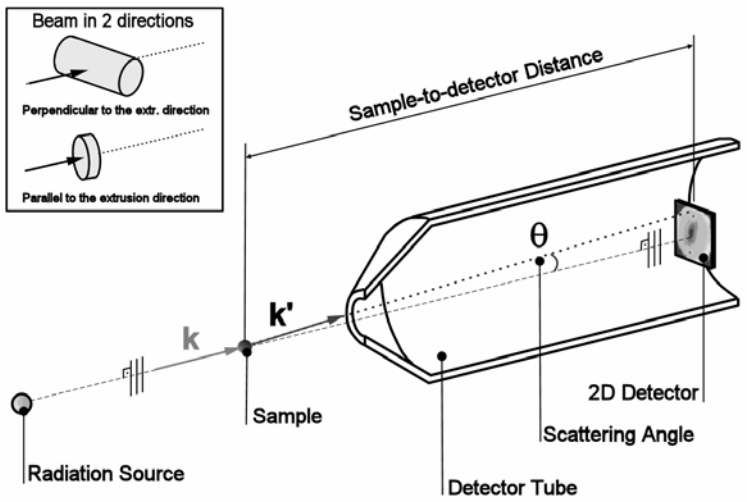

C.1: Schéma d'un essai de diffusion de rayons x aux petits angles Dans l'encadré, en haut à gauche, nous présentons les deux orientations utilisées pour observer les extrudats relaxés.

Les figures sont présentées pour les SEBS-1 d'abord et pour le SEBS-3 ensuite. Les SEBS-2 n'avait pas été utilisé pour ces essais, étant donné que sa structure chimique, son comportement en écoulement, et les défauts macroscopiques observés en sortie de la filière étaient très semblables au SEBS-1.

Ces essais nous ont permis de faire plusieurs hypothèses de travail pour mieux comprendre comment la structure à l'échelle mésoscopique du copolymère change avec le procédé d'extrusion. Pour les analyser et les interpréter, nous avons considéré plusieurs structures possibles pour chaque cas en nous appuyant sur les données existantes dans la littérature pour des copolymères similaires à ceux utilisés dans la présente étude. Ensuite nous avons calé des modèles théoriques du facteur de forme P(Q) des objets sur les courbes d'intensité expérimentales. Nos systèmes sont concentrés et les différents microdomains de polystyrène interagissent car ils sont connectés par la matrice de PEB. Ceci implique que la courbe expérimentale I(Q) contient des informations sur le facteur de forme P(Q)

des objets, mais aussi sur le facteur de structure S(Q) qui nous renseigne sur l'organisation spatiale des objets. La courbe I(Q) est égale au produit du facteur de forme et du facteur de structure.

Nous illustrons la méthode utilisée avec les cas du SEBS-3 avec 13%PS.

SEBS-3 (13%PS)

Détermination de la taille des domaines de PS

A partir de la fraction massique de PS, 13%, et des données existantes dans la littérature, on peut espérer que le SEBS-3 présente des microdomaines sphériques de PS dans une matrice de PEB. Des études ont montré que pour de fractions volumiques inférieures à 0.2, des copolymères comportent une phase liquide micellaire sans ordre apparent aux grandes échelles. Ceci est illustré par l'image de microscopie électronique à transmission en C.2. Elle a été reproduite des travaux d'Aggarwal (1976).

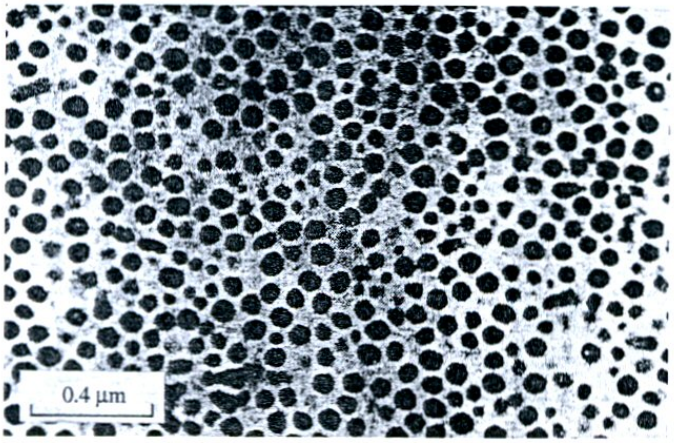

Fig. 2.18 TEM image of a PS–PB diblock with 10 wt% PB (Aggarwal 1976).

C.2 : Exemple d'une phase micellaire liquide. On observe la polydispersité de la taille des microdomaines sphériques ainsi que le manque d'ordre aux grandes échelles.

Pour le même grade de SEBS que nous avons utilisé, Daniel et al. (Polymer, 2000) expliquent dans leurs travaux qu'on doit avoir une organisation cubique centrée des sphères de PS. Cependant, sur les figures publiées, on observe clairement une organisation CC seulement pour des échantillons qui ont subi une forte élongation.

Indépendamment de la structure du matériaux, le vecteur d'onde, Q*, auquel le premier maximum est observé sur les courbes d'intensité, I(Q), donne une information sur une distance moyenne, d*, entre les domaines de PS. Q* et d* ont le rapport suivant

$$d^* = \frac{2\pi}{Q^*} \qquad (1)$$

Considérons d'abord le cas d'une phase liquide micellaire. La distribution dans l'espace des microdomaines sphériques de PS peut être modélisée par un réseau formé de tétraèdres réguliers. Ceci est schématisé en Figure C.3. Avec cette modélisation on fait l'hypothèse que toutes les sphères sont équidistantes de d_{ss} nm. Dans ce cas $d_{ss}=d^*$. Le volume du tétraèdre unité, en fonction de d_{ss}, est calculé par

$$V_{cell} = \frac{d_{ss}^{\ 3}\sqrt{2}}{12} \qquad (2)$$

Chaque sous élément de la cellule contient 1/32 du volume d'une sphère. Donc, le volume de PS dans une cellule est égal à un 1/8 de celui d'une micelle sphérique de PS. Donc,

$$V_{PS/cell} = \frac{1}{8}\frac{4\pi R_T^{\ 3}}{3} = \frac{\pi R_T^{\ 3}}{6} \qquad (3)$$

Le rapport entre $V_{PS/cell}$ et V_{cell} est égale à la fraction volumique de PS, f_{PS}. Etant donné que les masses volumiques des deux blocks ne diffèrent pas beaucoup (~10%), la fraction massique peut être considérée comme une approximation raisonnable de la fraction volumique. Si on combine les équations (2) et (3) avec la fraction volumique de PS, f_{PS}, on peut déduire le rayon de la micelle qui est

$$R_T = d_{ss}\left(\frac{f_{PS}\sqrt{2}}{2\pi}\right)^{1/3} \qquad (4)$$

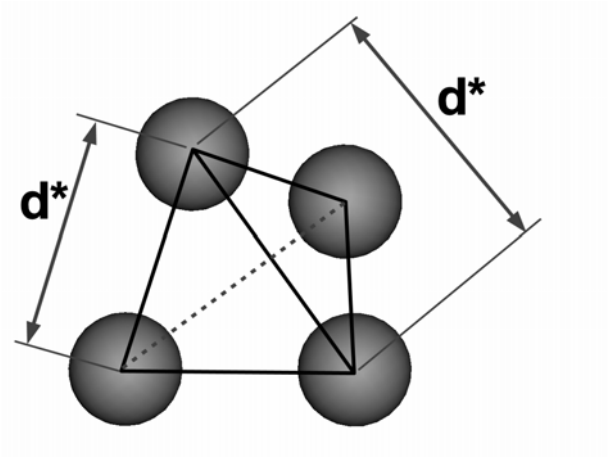

C.3: cellule tétraédrique où toutes les sphère sont équidistantes. Dans ce cas, la distance entre domaines, d_{ss} est égale à d.*

Pour une organisation cubique centrée, Figure C.4, La distance caractéristique obtenue à partir de Q* peut représenter trois échelles de longueur de la cellule. Elles sont représentés en Figure C.4. Le rayon des sphères de PS dépend alors de l'échelle de longueur à considérer. Nous examinons les trois cas, lorsque le volume de la cellule est égal à a^3. Une cellule contient deux sphères de PS et le rapport entre le volume des sphères et celui de la cellule donne la fraction volumique de PS.

1) Si la distance d* correspond à la longueur de l'arête de la cellule, alors le rayon de la sphère de PS est donné par

$$R_{BCC,a} = d^*\left(\frac{f_{PS}3}{8\pi}\right)^{1/3} \qquad (5)$$

2) Si la distance d* correspond à la distance la plus courte entre deux sphères dans le plan 110, alors le rayon de la sphère de Ps est donné par

$$R_{BCC,d_{110}} = d^*\left(\frac{f_{PS}3\sqrt{2}}{4\pi}\right)^{1/3} \quad (6)$$

3) Si d* représente la distance réelle entre la sphère centrale et une sphère placée sur un de vertex, la dimension d_d en Figure C.4, alors le rayon de la sphère de PS est donné par

$$R_{BCC,d_d} = d^*\left(\frac{f_{PS}}{\pi}\right)^{1/3} \quad (7)$$

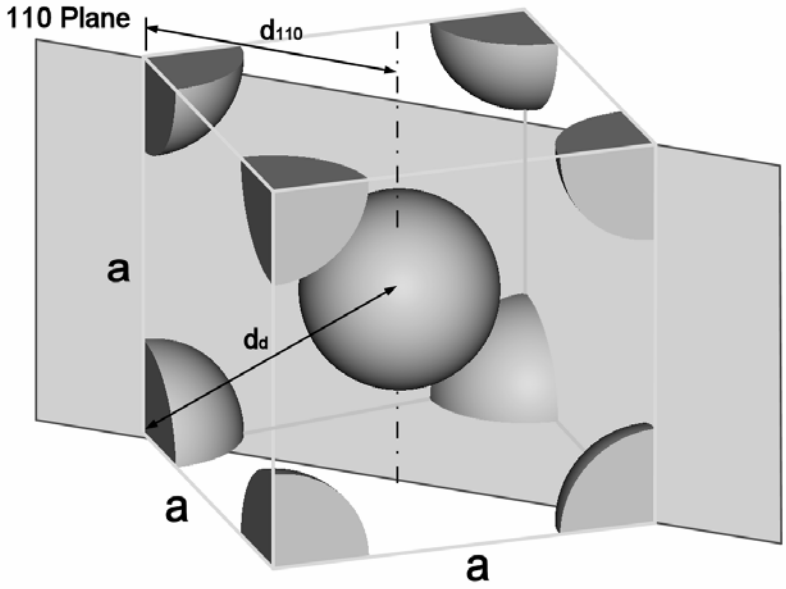

C.4: cellule cubique centrée représentant les différents façons de interpréter la distance d.*

Modélisation des courbes

L'intensité diffusée par un ensemble de particules sans interactions est proportionelle au volume des particules, V_o, à leur nombre, N, et au contraste électronique entre les particules et la matrice (δ_m-δ_o). L'intensité diffusée dépend aussi de la forme des particules. Cette dépendance est décrite par le facteur de forme, P(Q).

$$I(Q) \propto N^2(\delta_o - \delta_m)^2 V_o{}^2 P(Q) \quad (8)$$

D'après Rayleigh (1911), le facteur de forme d'une sphère isolée de rayon R peut être exprimée en termes du vecteur d'onde Q par

$$P_s(Q,R) = \Phi^2 \quad (9)$$

où

$$\Phi = \frac{3[\sin(QR) - QR\cos(QR)]}{(QR)^3}$$

L'équation (8) est valable pour des suspensions monodisperses. On peut tenir compte des écarts de la taille des objets par rapport au rayon moyen , R_0, autrement dit la polydipersité en introduisant une fonction de distributions de tailles dans le facteur de forme.

$$P(Q,C(R)) = \int_0^\infty C(R)P(QR)\left(\frac{R}{R_0}\right)^6 dR \qquad (10)$$

où C(R) est la fonction qui décrit la distribution des tailles. Pour un grand nombre de systèmes une distribution de Schultz semble aboutir à des résultats acceptables. Elle est exprimée par

$$C(R) = \int_0^\infty \frac{1}{Z!}\left[\frac{Z+1}{R_0}\right]^{(Z+1)} R^Z \exp\left[\frac{-(Z+1)R}{R_0}\right] \qquad (11)$$

avec

$$d = \frac{1}{\sqrt{Z+1}}.$$

La largeur de la distribution, $\Delta R/R_o$, est représentée par le paramètre d. La Figure C.5 montré l'effet du paramètre d. Le facteur de forme a été tracé en fonction de QR pour avoir des résultats adimensionnels. On observe que pour des valeurs de d supérieures à 0.2 touts les minima et maxima disparaissent.

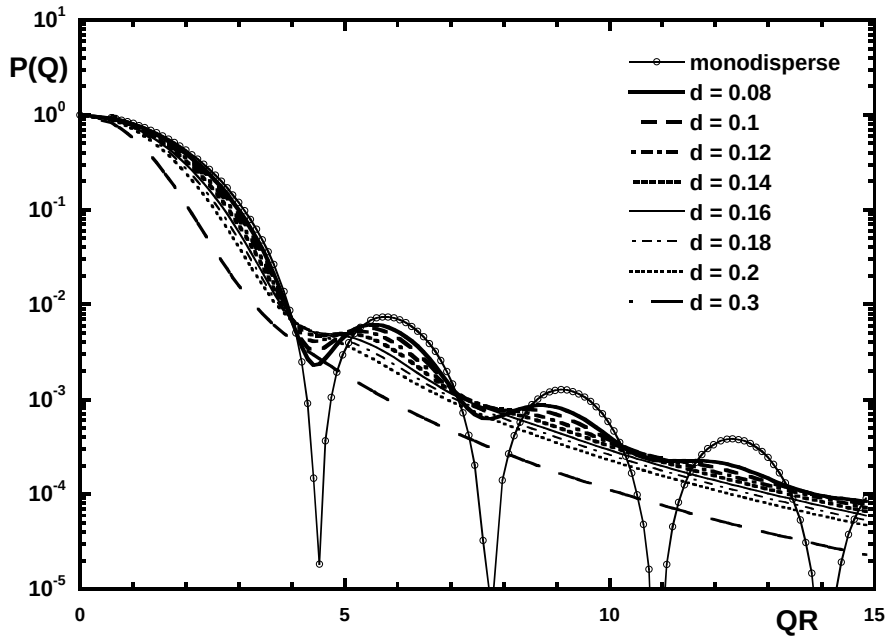

C.5 : Effet de la polydispérsité sur le facteur de forme d'un ensemble de particules sphériques isolées.

Application au SEBS 13%PS

Considérons la Figure C.15 obtenue avec un extrudat relaxé et le faisceau perpendiculaire au sens de l'extrusion. Les conditions d'extrusion étaient 190°C et un gradient de cisaillement apparent de 96 s^{-1}. A gauche nous avons des intégrations de l'intensité diffusé sur 360° et par secteurs (N,S, W). De la superposition des quatre courbes sur toute la gamme de vecteurs d'onde on déduit que l'organisation et la forme des domaines de PS sont isotropes. Donc, on peut s'attendre à avoir des domaines sphériques.

Q* est à 0,266 nm^{-1}, qui résulte en une distance caractéristique d* de 23,6 nm. Avec les équations (4), (5), (6), et (7) on calcule les rayons des sphères pour les différents cas de figures. Ils sont présentés dans le tableau ci-dessous.

d*	R_o (nm)
d_{ss}	7,22
a	5,85
d_{110}	8,27
d_d	8,11

Les facteur de forme pour des sphères isolées et monodisperses sont tracés pour les différents rayons et sont comparés avec la courbe expérimentale. On observe que le deuxième pic pour les facteurs de forme utilisant les rayons de 7,22, 8,11, et 8,27 nm semble être en bon accord avec la courbe expérimentale. Par contre, la courbe tracé avec un rayon de 5.85 nm ne coïncide pas avec la courbe expérimentale. Cette hypothèse ne semble pas être la bonne et on l'écarte.
Sur la courbe expérimentale, nous observons que le deuxième pic est atténué. Ceci indique que nous devons tenir compte de la polydispersité. On le fait en utilisant l'équation (10). Ensuite, on cherche le meilleur calage du modèle sur la courbe expérimentale sur le deuxième pic.
Nous avons observé qu'aux vecteurs d'onde supérieurs à (Q>1) le modèle utilisé n'était pas en bon accord avec les courbes expérimentales. Ceci à été résolu en rajoutant une composante au modèle pour tenir compte de la diffusion des chaînes de polymère qui forment notre système. Le résultat final est présenté par la courbe indiqué Fit en Figure C.15. Elle a été obtenue avec un rayon moyen des sphères de 7.22 nm, d=0.13, et la contribution de chaînes gaussiennes de rayon de giration de l'ordre de 4 nm.

On peut étendre cette méthode pour tenir compte des déformations subies par le copolymère pendant son extrusion.
Ainsi, pour l'image présentée en Figure C. 12, on observe une anisotropie pour toute la gamme de vecteurs d'onde étudiés. L'anisotropie aux grands vecteurs d'onde indique une anisotropie des objets, et donc on peut s'attendre à ce que les sphères de PS soient devenues ovales avec une certaine excentricité ε. Une façon possible de quantifier cette anisotropie est de faire le rapport entre la diffusion dans la direction N-S et la diffusion E-W. Avec cette méthode on trouve un rapport, d'excentricité, ε, d'environ 1.15-1.25.
A partir d'ε, on peut alors déduire un rayon caractéristique des domaines de PS déformés si on fait l'hypothèse que leur volume reste constant. Le rapport entre le rayon d'une sphère et d'un sphéroïde de volume égal est $R_s^3=\varepsilon R_{ov}^3$, où R_s est le rayons de la sphère et R_{ov} le rayon de l'ovale. Dans le cas du SEBS-3, pour R_s=7.22 nm et ε=1.25 nous obtenons une valeur de R_{ov} de 6.7 nm. La courbe qui en résulte est montrée dans la Figure C.12. Elle a été obtenue en considérant la même polydispersité

que dans le cas des sphères et avec une contribution de chaînes gaussiennes de 4 nm aussi. Dans le modèle nous avons aussi inclus une distribution normale de l'orientation des sphéroïdes avec une orientation moyenne alignée avec les sens de l'extrusion et un écart type de 10°.

Cette procédure d'analyse nous a permis de retenir les hypothèses suivantes :

- Les SEBS avec 30%PS présentent des microdomaines de PS cylindriques agencés de façon hexagonale. Les échantillons obtenus par moulage à compression sont macroscopiquement isotropes. Pour ces échantillons nous avons calculé un diamètre moyen des cylindres de PS de 18 nm. Quand le SEBS-30%PS est extrudé les grains s'orientent dans le sens de l'extrusion mais la taille du diamètre moyen reste toujours à 18 nm. Cette réorganisation des grains a lieu en entrée de la filière. A 2.5 mm de l'entrée, les grains sont déjà réorganisés et les microdomaines cylindriques orientés.
- Les SEBS 13%PS présente des microdomaines sphériques de PS sans un ordre aux grandes échelles et avec un degré de polydispersité d'environ 0.13. Le diamètre moyen de ces sphères est de 14.4 nm. Lorsque le produit est extrudé, les microdomaines de PS deviennent ovales avec un rapport entre le rayon long et le rayon court de 1.25. Les rayons des sphéroides sont de 6.7 et 8.4 nm. Ces microdomaines ovales s'orientent d'abord dans le sens de l'écoulement. Lorsque l'écoulement devient instable en amont de la filière, les microdomaines ovales de PS semblent passer à une organisation cubique centrée. Cependant leur excentricité ne semble pas changer.

C. 6: Scattered intensity curve of a SEBS 30%PS sample compression molded at 230°C. The test temperature was 30°C. The inset shows the 2D image which was integrated over 360°C to obtain the curve I(Q).

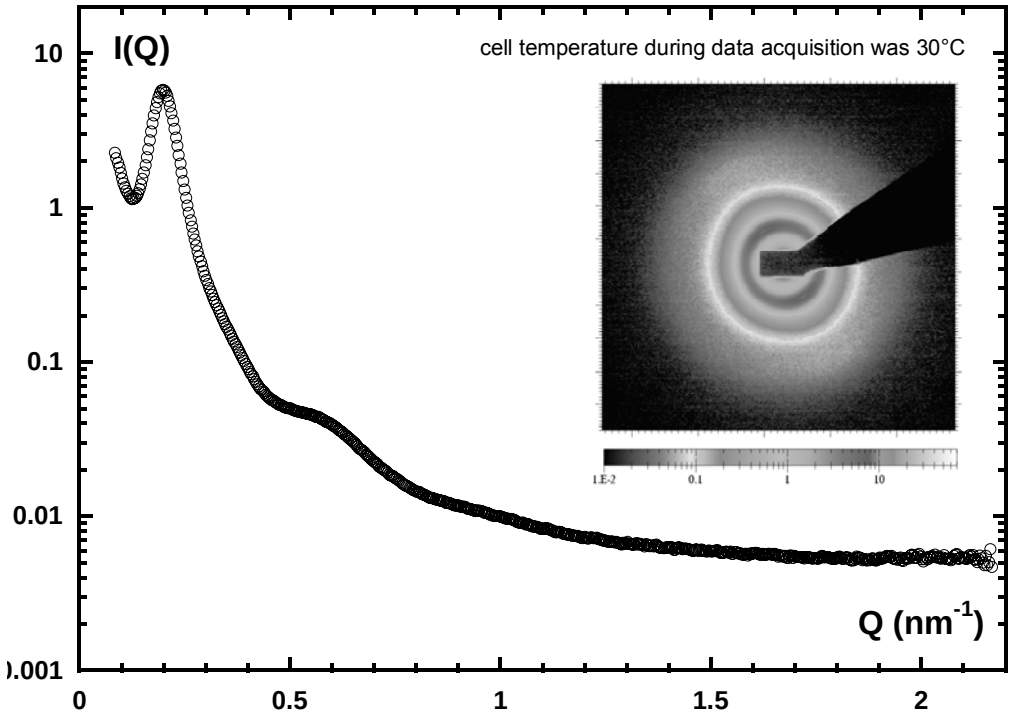

C. 7: Scattered intensity curves for SEBS 30%PS samples obtained by compression molding. Each curve represents a different test temperature.

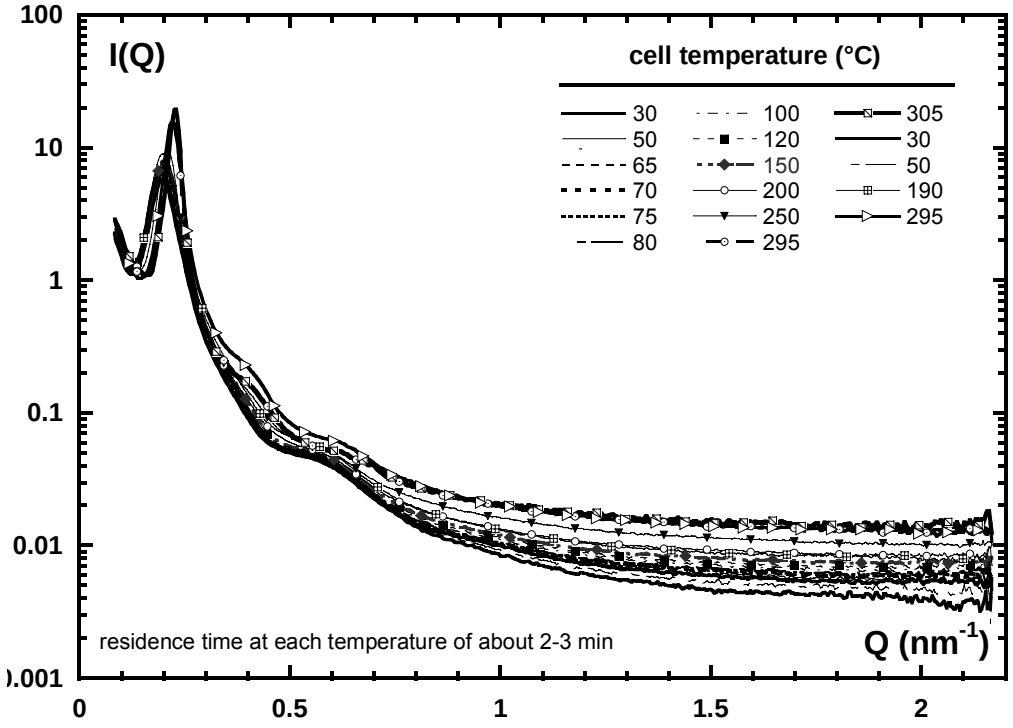

C. 8: SEBS 30%PS extruded at 190°C – 0,005 s^{-1} – film (not shown). The arrows indicate the theoretical higher order peaks for hexagonally-packed cylinders.

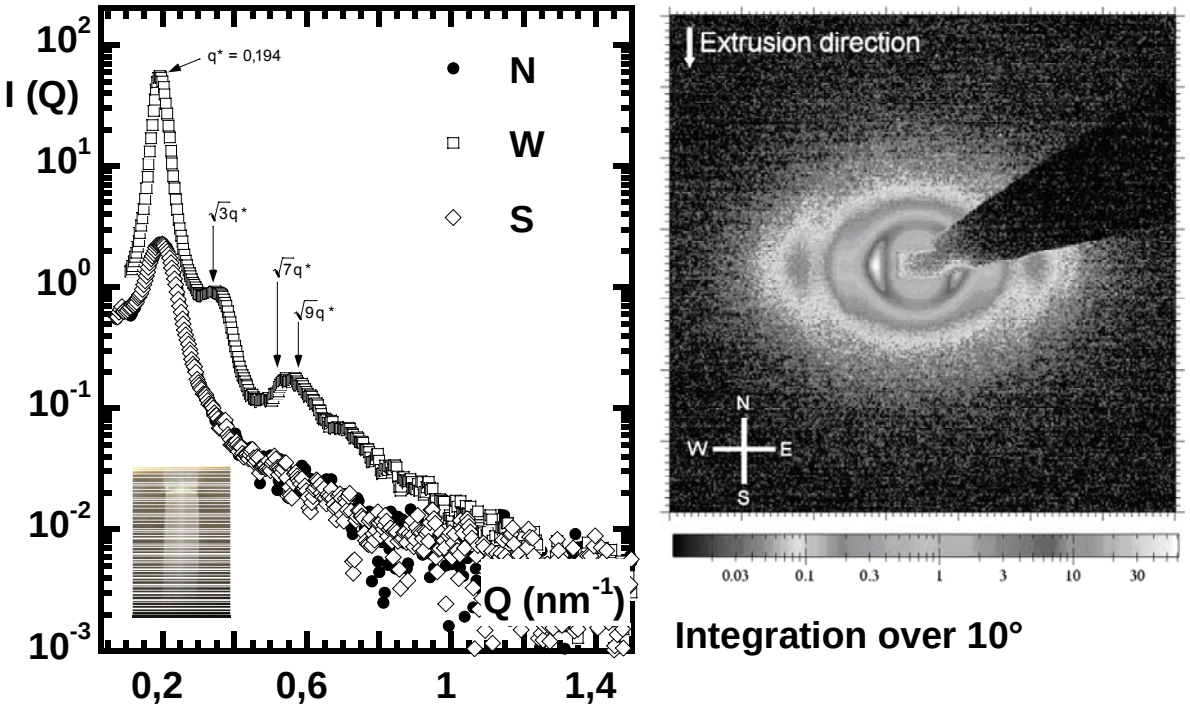

C. 9: SEBS 30%PS extruded at 190°C - 3s^{-1} through orifice die of 2mm diameter. The arrows indicate the theoretical higher order peaks for hexagonally-packed cylinders.

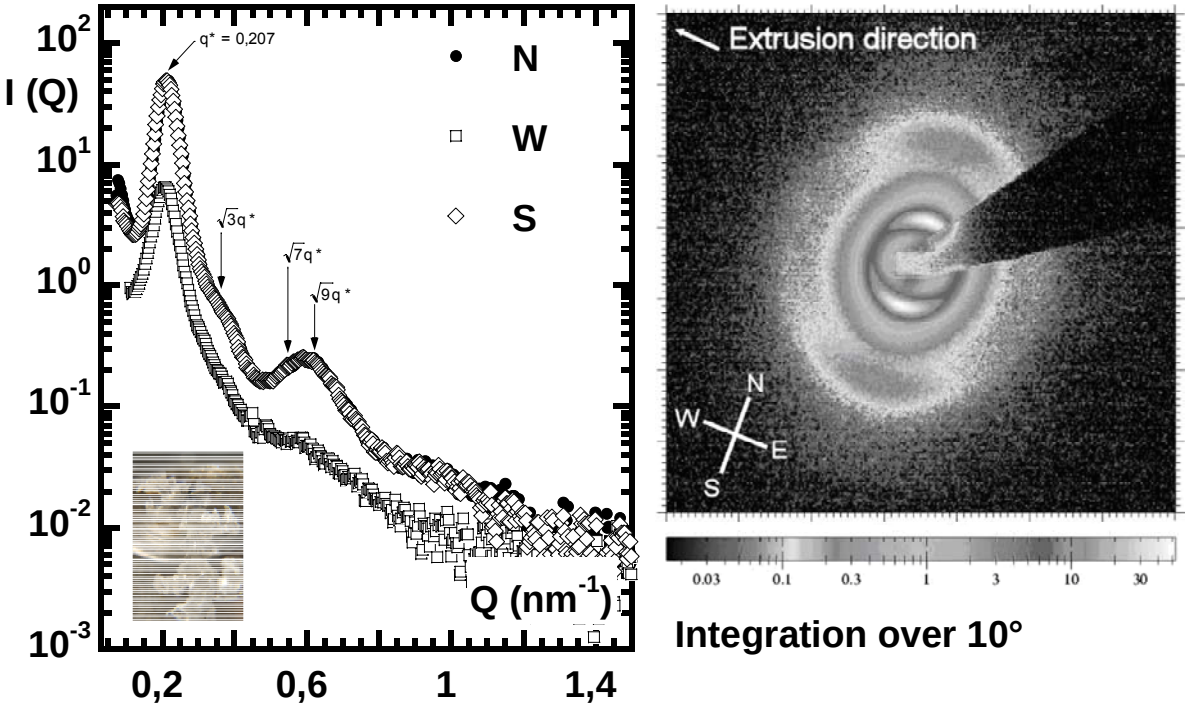

C. 10: SEBS 30%PS extruded at 190°C – 6 s-1 through capillary with L/D = 10/1. The beam was perpendicular to extrusion direction and focused on slip portion of sample.

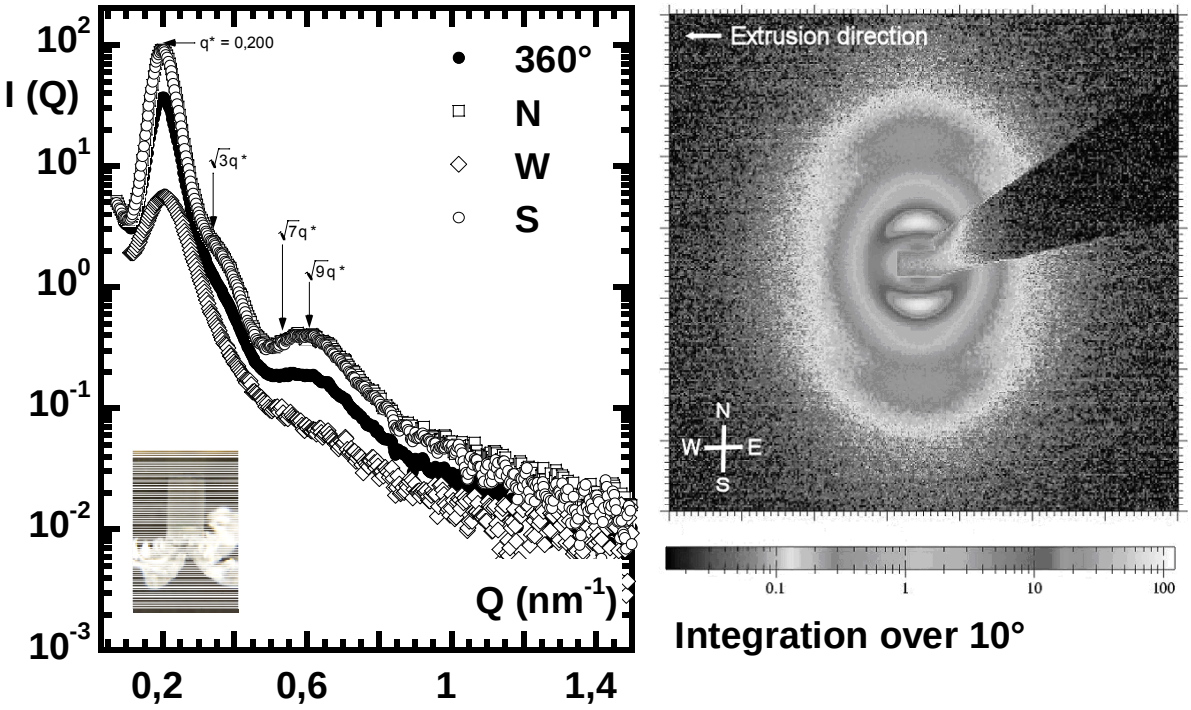

C. 11: SEB 30%PS extruded at 295°C and 6 s-1 through a die with L/D ratio of 10/1. The arrows show the theoretical higher order peak positions for spherical domains in a BCC lattice.

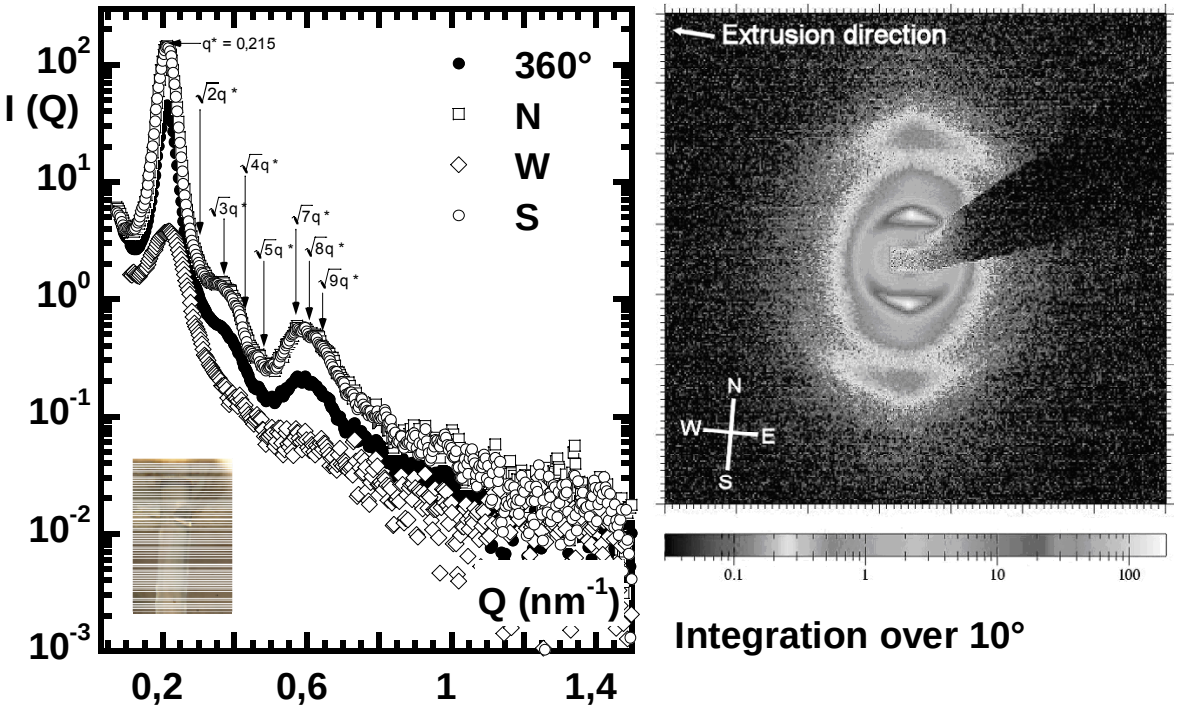

C. 12: SEBS 13%PS extruded at 90°C and 0,184 s^{-1} through a die with L/D ratio of 50/5 - beam perpendicular to extrusion direction. Arrows represent theoretical higher order peaks for BCC lattice organization of spheres

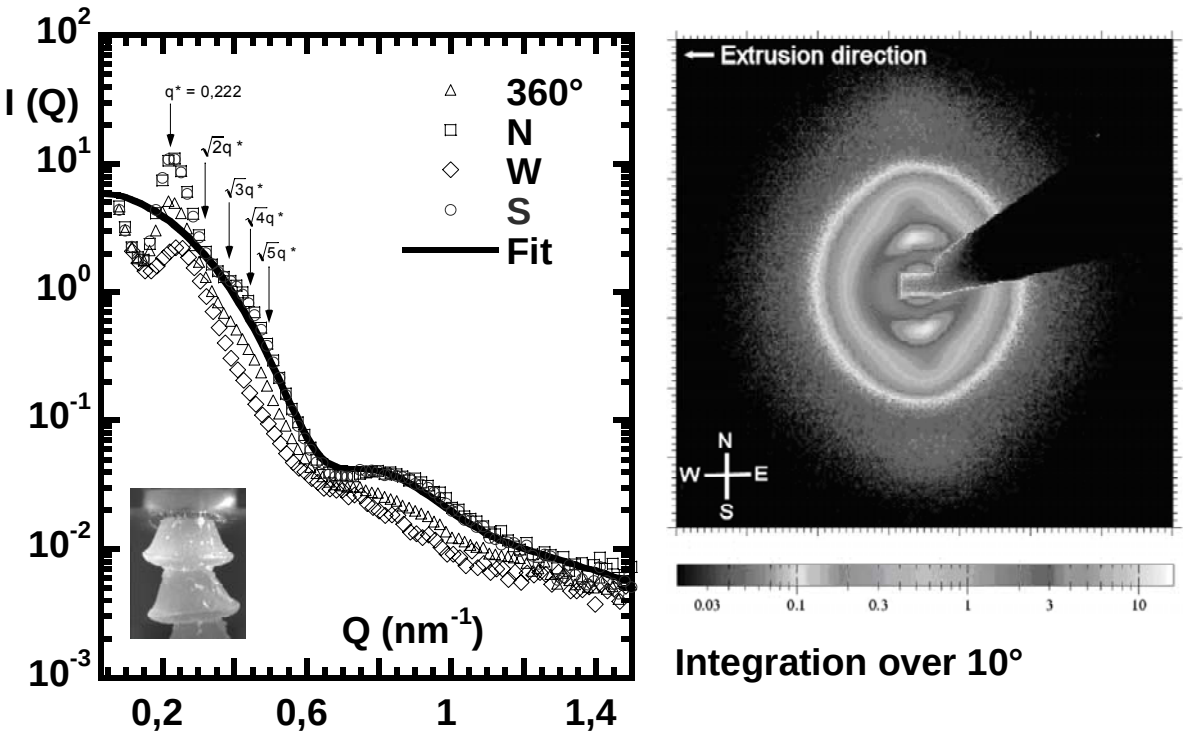

C. 13: SEBS 13%PS extruded at 90°C and 1,84 s^{-1} with die of L/D=50/5 – beam perpendicular to the extrusion direction. Definition of arrows in Fig 3.30.

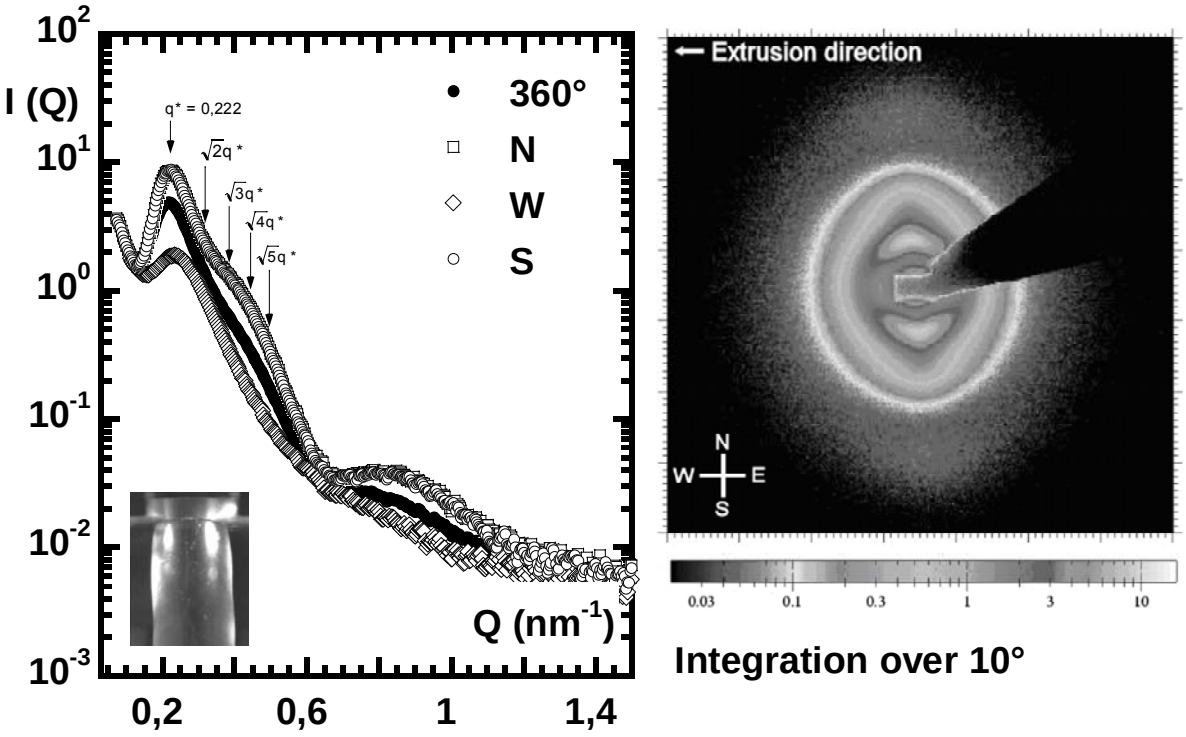

C. 14: SEBS 13%PS extruded at 90°C and 18,4 s^{-1} with a die of L/D = 50/5. Beam perpendicular to extrusion direction. Definition of arrows in Fig 3.30.

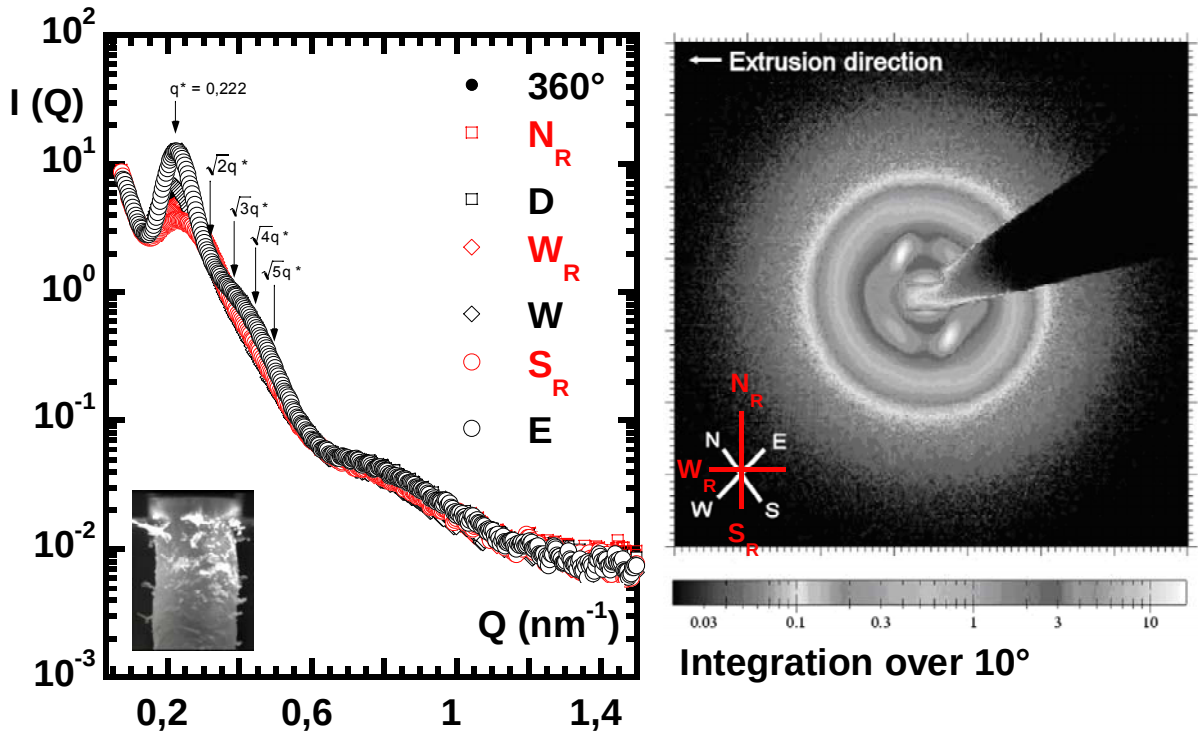

C. 15: SEBS 13%PS extruded at 190°C and 96 s^{-1} through a die with L/D = 10/1. Beam perpendicular to the extrusion direction. Definition of arrows in Fig 3.30.

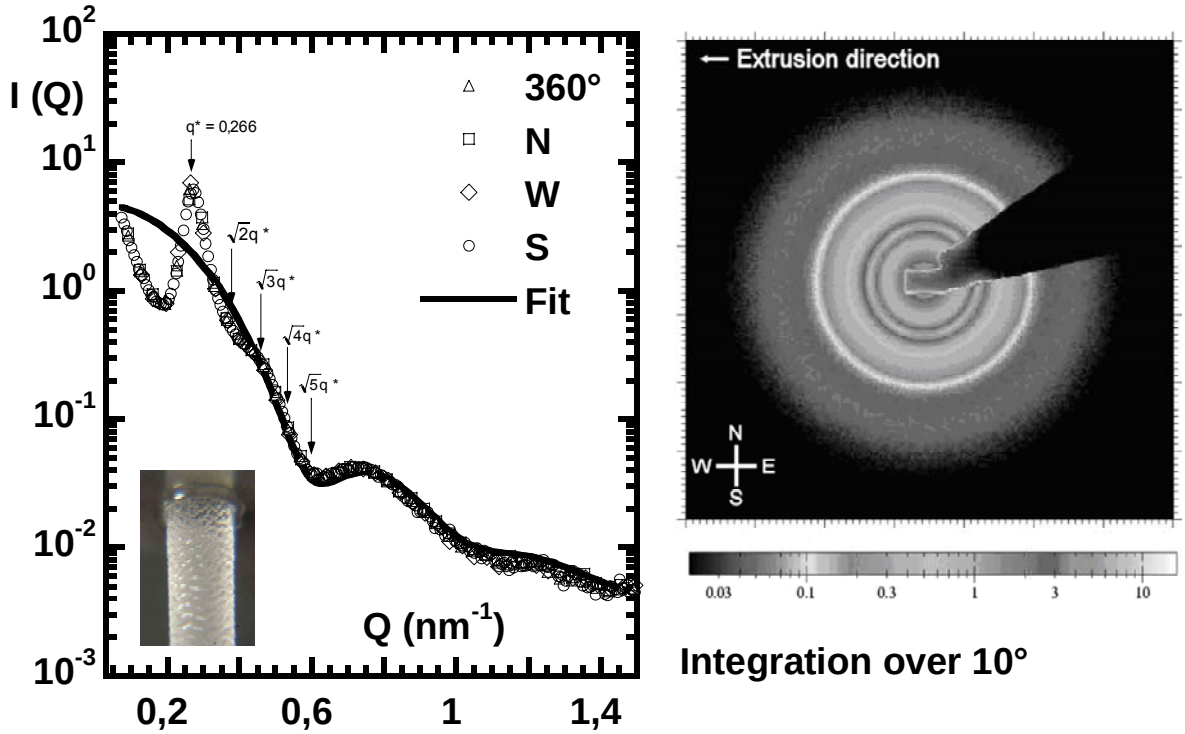

C. 16: SEBS 13%PS extruded at 90 °C and 0,184 s^{-1} - beam in the extrusion direction. Upper image: center of sample (x=0). Middle image, x= 1 mm. Lower image, x=1.25 mm.

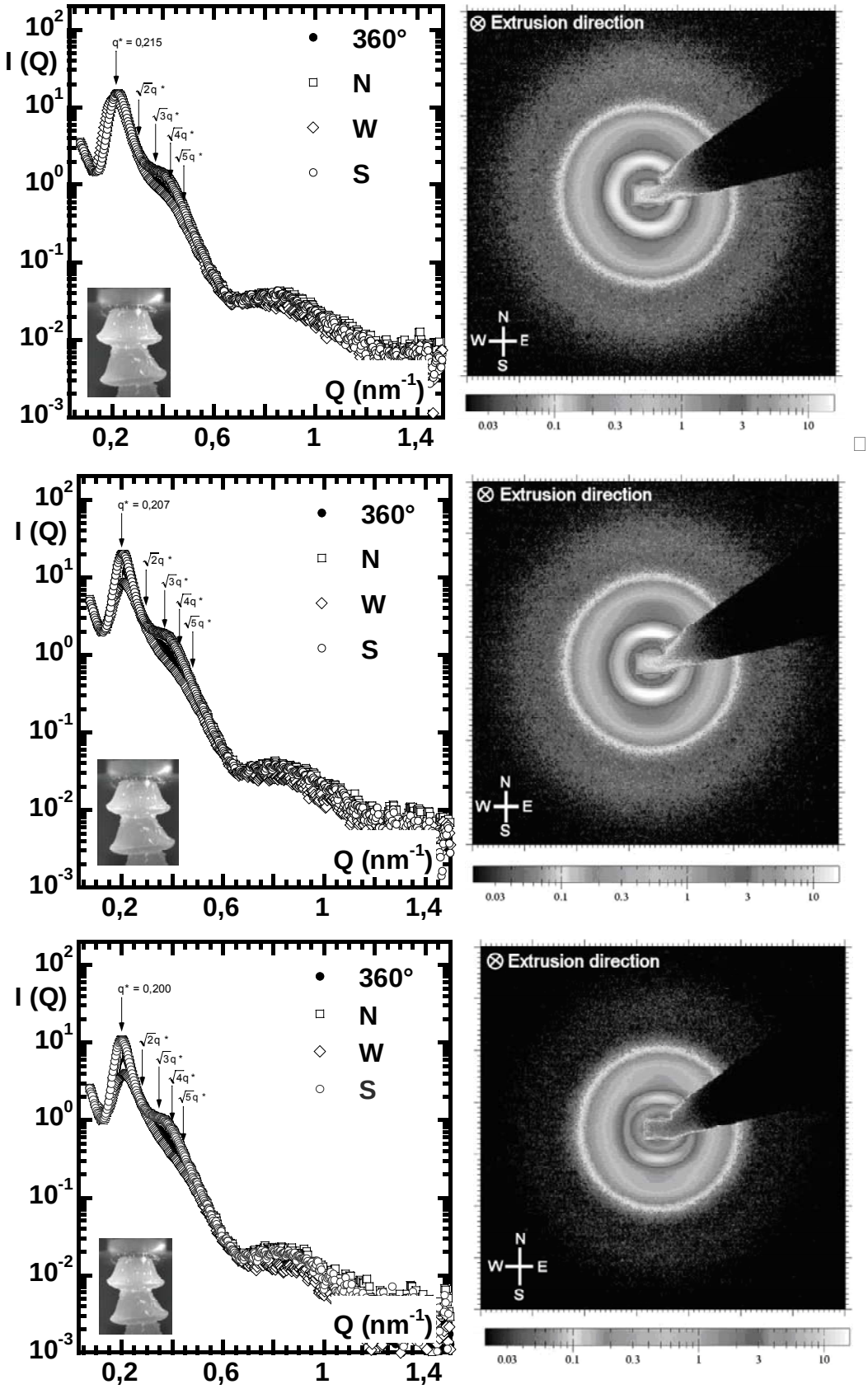

C. 17: SEBS 13%PS extruded at 90 °C - 18,4 s^{-1}. Beam parallel to extrusion direction. Upper image: center of sample (x=0). Middle image, x= 1 mm. Lower image, x=1.25 mm.

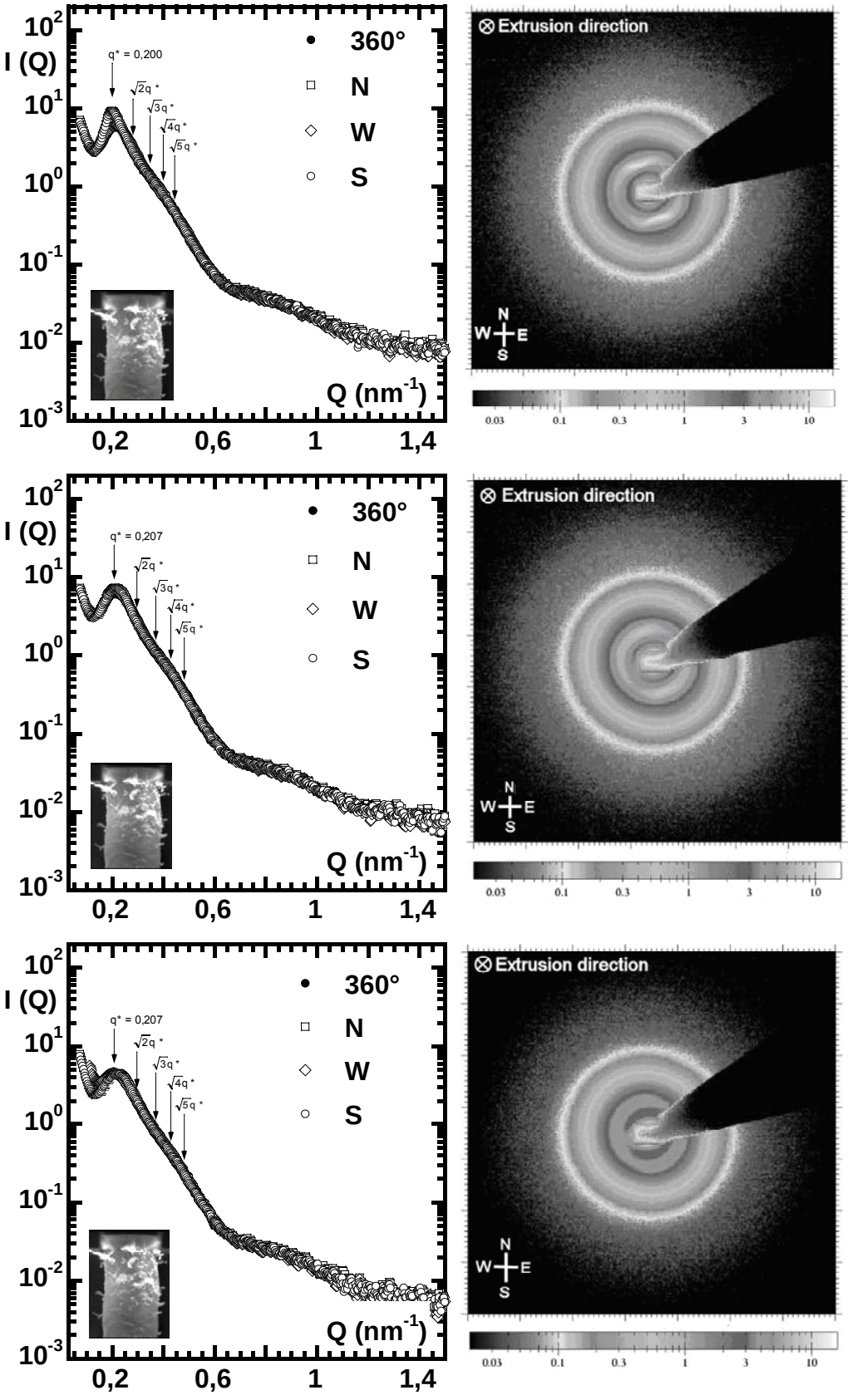

LISTES

LISTE DES FIGURES

CHAPTER 1

CHAPTER 2

CHAPTER 3

ANNEXE A

ANNEXE B

ANNEXE C

LISTE DES TABLEAUX

CHAPTER 1

CHAPTER 2

CHAPTER 3